

MOLECULAR DESIGN OF NITROGEN-DOPED  
NANOPOROUS NOBLE CARBON MATERIALS FOR  
GAS ADSORPTION

**DISSERTATION**

ZUR ERLANGUNG DES AKADEMISCHEN GRADES DOKTOR DER NATURWISSENSCHAFTEN  
(„DOCTOR RERUM NATURALIUM“, DR. RER. NAT.) IN DER WISSENSCHAFTSDISZIPLIN  
„KOLLOIDCHEMIE“

EINGEREICHT AN DER MATHEMATISCH-NATURWISSENSCHAFTLICHEN FAKULTÄT DER  
**UNIVERSITÄT POTSDAM**

VON

**RALF WALCZAK, M. SC.**

GEBOREN AM 05.06.1990 IN LANDAU AN DER ISAR

ORT UND TAG DER DISPUTATION: POTSDAM-GOLM, 13.09.2019

This work is licensed under a Creative Commons License:  
Attribution – Share Alike 4.0 International.  
This does not apply to quoted content from other authors.  
To view a copy of this license visit  
<https://creativecommons.org/licenses/by-sa/4.0/>

HAUPTBETREUER: PROF. DR. DR. H.C. MARKUS ANTONIETTI

BETREUER: PROF. DR. ANDREAS TAUBERT  
DR. MARTIN OSCHATZ

GUTACHTER: PROF. DR. DR. H.C. MARKUS ANTONIETTI  
DR. MARTIN OSCHATZ  
PROF. DR. BASTIAN J. M. ETZOLD

Published online at the  
Institutional Repository of the University of Potsdam:  
<https://doi.org/10.25932/publishup-43524>  
<https://nbn-resolving.org/urn:nbn:de:kobv:517-opus4-435241>

## Acknowledgement

First of all, I would like to express my very great appreciation to Prof. Dr. Markus Antonietti, my research supervisor, for scientific support and the opportunity to conduct my PhD thesis at the Max Planck Institute of Colloids and Interfaces in Potsdam/Golm.

I would like to acknowledge Prof. Dr. Andreas Taubert of the University of Potsdam as the second supervisor for supervising the thesis and supporting me for giving lecture courses at the University of Potsdam.

I would like to offer my special thanks to my group leader Dr. Martin Oschatz. The door to his office was always open whenever I ran into a trouble spot or had a question about my research or writing and he consistently supported me in my work. His willingness to offer his time so generously has been very much appreciated.

I would like to thank the following collaborators for their assistance with the collection of my data, evaluation, and discussion: Dr. Nadezda V. Tarakina and Dr. Tobias Heil for HRTEM, Dr. Johannes Schmidt for performing XPS measurements, Dr. Bogdan Kurpil and Dr. Aleksandr Savateev for the synthesis of HAT, Dr. Jan D. Epping for ssNMR measurements, Prof. Dr. Thomas D. Kühne for computational calculations, Michelle Wöllner for thermal response measurements, Carolin Selzer for TPD, and Dr. Alberto Riaño Carnerero and Prof. Dr. Aurelio Mateo-Alonso for the synthesis of CMP. Without their passionate participation and input, this research work could not have been successfully conducted.

I wish to acknowledge the help provided by the technicians of the laboratories of this institute who were involved in various aspects of this research project: Ines Below-Lutz and Regina Rothe for general support in the lab/BET lab, Antje Völkel and Ursula Lubahn for EA and TGA, Heike Runge and Rona Pitschke for SEM/EDX and TEM measurements, as well Bolortuya Badamdorj for help with collecting HRTEM images.

My PhD work was financially supported by the German Chemical Industry Fund (Fonds der Chemischen Industrie, FCI) with a Liebig Fellowship for the first two years.

My time at the MPI in Golm and Potsdam/Berlin was made enjoyable in large part due to the many friends and groups that became part of my life. I would like to thank for time spent with Baris, Amit, Max, Marius, Runyu, Paolo, Nina, Ivan, Daniel, Valerio, Jose, Francesco, Joao, and Markus, and many other people, for crazy clubbing tours, legendary Chez Briel nights,

successful football tournaments, relaxed barbecues and after-work-hours beer, and for other nice memories.

My Munich group of friends with Niklas, Juri, Peter, Flo, Alan, Tobi, Michi, Fionan, Nisi, Vera, Steffi, Eli, Sina, and Lara, gave me encouragement, suggestions, and support, over almost a decade. I am deeply grateful for all the unforgettable holiday trips to Croatia, weekend trips to Prag or Regensburg, enjoying life in summer (Westpark and Isar), and all the precious time spent together.

Lastly, I wish to express deeply gratitude to my parents Gabriele and Bernd, as well to my brother Stefan for all their invaluable support along my way and encouragement throughout my years of study. And my girlfriend Milena for her grateful support throughout the process of researching and writing this thesis is so appreciated. This accomplishment would not have been possible without them.

*Thank you all.*





---

# Table of Contents

<b>1</b>	<b>Motivation and Background .....</b>	<b>1</b>
1.1	Fundamentals of Porous Carbon Materials .....	4
1.1.1	The Element Carbon – Origin and Development .....	4
1.1.2	Different Synthesis Approaches towards Porous Carbon Materials .....	6
1.2	Nitrogen-containing Porous Carbon Materials .....	9
1.2.1	Fundamentals and Influences of Nitrogen Incorporation into Carbon Materials 9	
1.2.2	Different Synthesis Approaches towards Nitrogen-Containing Porous Carbon Materials .....	11
1.3	Unique Stability of Nitrogen-Containing Carbon Materials – The Concept of Noble Carbon Materials .....	12
1.3.1	Fundamentals of the Concept of Noble Carbon Materials .....	12
1.3.2	Rules and Guidelines of Different Carbonization Pathways .....	14
1.4	C <sub>2</sub> N-type Carbon Materials .....	15
1.5	Conjugated Microporous Polymers as Precursors Systems towards Porous Carbon Materials .....	18
1.6	Specific Interactions of Porous Carbon Materials with Guest Species .....	19
1.6.1	Porous Carbon Materials for Selective Gas Adsorption and Separation .....	19
1.6.2	Sodium-Ion Batteries with Carbon Anode Materials .....	25
<b>2</b>	<b>Outline .....</b>	<b>29</b>
<b>3</b>	<b>Results and Discussion.....</b>	<b>33</b>
3.1	Synthesis of Nitrogen-Rich Nanoporous Noble Carbon Materials from a Preorganized Hexaazatriphenylene Precursor.....	33
3.1.1	Background and State-of-the-Art .....	33
3.1.2	Template- and Metal-free Condensation of Preorganized HAT-CN.....	35
3.1.3	Structural Characterization of the HAT-CN-derived Carbon Materials.....	36
3.1.4	Structure-related Physisorption Properties of the HAT-Derived Carbon Materials .....	42
3.2	Towards Enhanced CO <sub>2</sub> /N <sub>2</sub> Molecular Sieving with Nitrogen-Doped Carbon Materials Prepared by Molecular Design .....	47
3.2.1	Background and State-of-the-Art .....	47

3.2.2	Structure Development during the Condensation Process of the HAT-CN-Derived Carbon Materials .....	48
3.2.3	Elaboration of a CO <sub>2</sub> /N <sub>2</sub> Molecular Sieving Effect .....	54
3.2.4	Theoretical Calculation of the CO <sub>2</sub> Adsorption on the C <sub>2</sub> N network .....	58
3.3	Structure-Related Properties of HAT-CN-Derived Carbon Materials for the Adsorption of H <sub>2</sub> O and NH <sub>3</sub> .....	60
3.3.1	Background and State-of-the-Art .....	60
3.3.2	Structural Classification compared to Reference Carbon Materials .....	62
3.3.3	Evaluation of Structure-Related Properties of HAT-CN-Derived Carbon Materials for the Adsorption of H <sub>2</sub> O Vapor .....	63
3.3.4	Evaluation of Structure-Related Properties of HAT-CN-Derived Carbon Materials for the Adsorption of NH <sub>3</sub> Gas .....	68
3.4	Nitrogen-doped Carbon Materials derived by Conjugated Microporous Polymer .....	72
3.4.1	Background and State-of-the-Art .....	72
3.4.2	Thermal treatment of Pyrazine-Fused Conjugated Microporous Polymer .....	73
3.4.3	Structural Characterization of the aza-CMP-derived Carbon Materials .....	74
3.4.4	Structure-related Physisorption Properties of the aza-CMP-Derived Carbon Materials .....	80
3.4.5	Aza-CMP-derived Carbon Anode Materials for Sodium-Ion Battery .....	81
<b>4</b>	<b>Summary, Conclusions, and Perspectives .....</b>	<b>89</b>
<b>5</b>	<b>Bibliography .....</b>	<b>93</b>
<b>6</b>	<b>Appendix .....</b>	<b>103</b>
6.1	List of Abbreviations .....	103
6.2	Characterization Methods .....	105
6.3	Experimental Part .....	124
6.3.1	List of used Chemicals and Gases .....	124
6.3.2	Synthesis of Materials .....	124
6.4	Supporting Figures and Tables .....	127
6.4.1	List of Figures .....	148
6.4.2	List of Tables .....	151
6.4.3	List of Schemes .....	152
6.5	List of Publications .....	153
6.6	Declaration .....	155





# 1 Motivation and Background

In the year 2050 the level of CO<sub>2</sub> in the atmosphere is expected to rise from today's 400 ppm with the current rate of growth to ~500 ppm, which is one among several scenarios.<sup>[1]</sup> The growing tendency of the 21<sup>st</sup> century economy, from agriculture, to manufacturing, and nowadays service-based economies,<sup>[2]</sup> is demanding more goods, needs, and services. The rapid development in numerous sectors, such as the increase in human activities (e.g., traveling by car, busses, or airplanes), is directly or indirectly correlated to a growing energy consumption.<sup>[3]</sup> Since the industrial revolution, fossil fuels in form of coal, oil, and natural gas, have been the main energy sources. The growing necessity of the combustion of carbon-based fossil fuels is inevitable but produces greenhouse gases, and in particular led to a substantial increase of the atmospheric CO<sub>2</sub> concentration (**Figure 1**).<sup>[4]</sup> Almost 90 % of the CO<sub>2</sub> emissions are due to fossil fuel combustion and are thus correlated to the increased energy production in power plants, transportation vehicles, and static or mobile machineries.

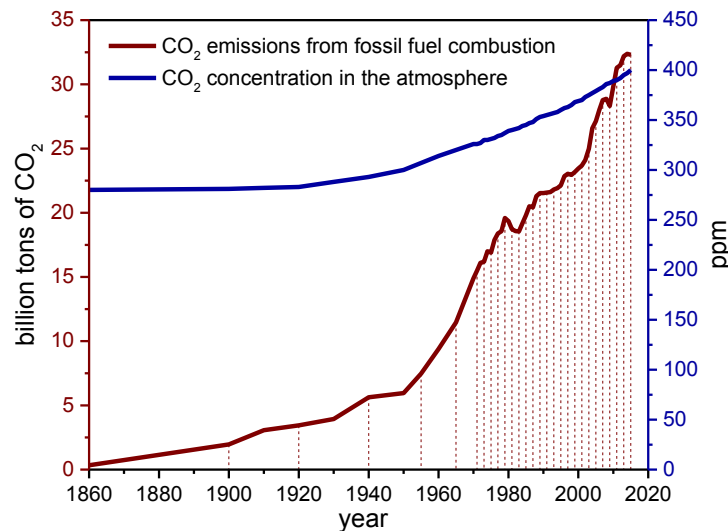


**Figure 1:** Development of the global CO<sub>2</sub> emission due to fossil fuel combustion and consequences on the CO<sub>2</sub> concentration in the atmosphere (adapted from reference<sup>[4]</sup>).

Recently, stronger efforts have been made to create carbon free alternatives, and to minimize the dependence on fossil fuels *via* sustainable energy sources, such as solar, wind, hydro, and

geothermal energy.<sup>[5]</sup> The serious limitation of solar- and wind-derived energy is the decoupling of production and storage. Storage and delivery of energy from these sources are crucial for a flexible, reliable, and decarbonized electric power system.<sup>[6]</sup>

To lower the CO<sub>2</sub> emissions, the capture of CO<sub>2</sub> from stationary sources (e.g., from pre- or post-combustion processes in power plants) is discussed, but this will only contribute to slowing down the rise of the atmospheric CO<sub>2</sub> concentration. On the long run, the technology of capturing CO<sub>2</sub> at low concentrations, such as the direct capture from air (DAC) itself will be a relevant application. The carbon capture and storage (CCS), or even more important the carbon capture and utilization (CCU), consider the CO<sub>2</sub> capture and reductive recycling of CO<sub>2</sub> to produce diverse useful materials and fuels. The environmentally safe utilization of CO<sub>2</sub> can be used for the production of regenerative synthetic carbon fuels, other hydrocarbon products, and in particular methanol as the most valuable C<sub>1</sub> chemical compound.<sup>[7]</sup> However, there are still massive challenges in these processes, for instance the low concentration of CO<sub>2</sub> in the air (400 ppm corresponds to 0.04 %). Moreover, the competitive adsorption of other gases (e.g., H<sub>2</sub>O, N<sub>2</sub>, or O<sub>2</sub>) remains a serious issue in accomplishing high CO<sub>2</sub> capacities and selectivities. As a consequence, a tremendous amount of air and capturing devices would be necessary to remove a meaningful amount of CO<sub>2</sub> from air at questionable energy consumption.

An additional approach to efficiently tackle the CO<sub>2</sub> problem is to avoid its production already at the emission sources. The refrigeration sector (including refrigeration, air-conditioning, and heat pump systems) is an important part of the global economy and energy management. Refrigeration is crucial in health, food, energy, and environmental fields. The refrigeration sector contributes significantly to CO<sub>2</sub> emissions, because of the consumption of around 17 % of the overall electricity used worldwide. Other global problems arise due to the possible leakage of ozone depletion gases (e.g., CFCs (chlorofluorocarbons), HCFCs (hydrochlorofluorocarbons), and HFCs (hydrofluorocarbons)).<sup>[8]</sup> Low global warming refrigerants (e.g., NH<sub>3</sub>) are needed in vapor compression refrigeration systems and activated carbon-NH<sub>3</sub> seems to be a promising adsorption working pair. NH<sub>3</sub> is stable over a wide range of temperatures (below 0 °C and at least up to 200 °C) and has a high latent heat. Considering its use as a cooling agent, the major advantage of NH<sub>3</sub> over H<sub>2</sub>O is the fact that it is a gas under standard conditions (i.e., at room temperature and atmospheric pressure) that can be directly adsorbed on porous materials in order to use the heats of adsorption and desorption for heat generation and cooling.

In the field of CO<sub>2</sub> capture, as well as in the field of refrigeration, the interaction of gas molecules with porous materials plays a crucial role. Such nanoporous solids are, for example, zeolites or metal-organic frameworks (MOFs). Zeolites have high thermal stabilities and CO<sub>2</sub> adsorption capacities, which is due to their basic character and the presence of electric charges in their cavities. These materials have narrow pore size distributions, which is resulting in high selectivities, but is limiting their adsorption kinetics.<sup>[9]</sup> MOFs can provide high surface areas, and high micropore volumes with uniform pore size, often in the range of the size of CO<sub>2</sub> molecules. They can be easily modified with functional groups and contain metal sites, which lead to high CO<sub>2</sub> affinity. Nevertheless, a low stability against heat or moisture (i.e., H<sub>2</sub>O) is often problematic for MOFs.<sup>[10]</sup> Porous carbon materials found their way in numerous applications due to their unique beneficial properties, such as tunable porosity (with high surface areas and pore volumes), electrical conductivity, as well as chemical (i.e., against H<sub>2</sub>O, acids, and bases) and thermal stability.<sup>[11]</sup> On the other side, in comparison to MOFs or zeolites, pristine carbon materials are by far less polar and thus reveal low affinity towards CO<sub>2</sub>. However, the chemical and electronic nature of carbon materials can be modified by heteroatom-doping, which results, for example, in nitrogen-containing carbon materials with an enhanced affinity towards polar or acidic guest molecules (e.g., CO<sub>2</sub>, H<sub>2</sub>O, or NH<sub>3</sub>). The performance of carbon materials is strongly dependent on their atomic construction and pore size/distribution to achieve optimal host-guest interactions, depending on the specific application. The difficulty herein, which is tackled within this thesis, is the introduction of a significant amount of nitrogen atoms homogeneously distributed and in similar bonding motives throughout the carbon framework.

In summary, a class of materials that can solve the aforementioned issues are porous (heteroatom-doped) carbon materials, as adsorbent materials for the removal of CO<sub>2</sub>. To tackle the modern problems of air pollutions, global warming, and energy demands, a synergy of different energy and environmentally sustainable concepts of energy production/storage and emission capture/utilization are necessary.

Within this thesis, a profound background on carbon materials, in particular nitrogen-containing carbon materials, concerning their application in gas adsorption and electrochemical energy storage with sodium-ion battery, is given. Novel nitrogen-doped carbon materials and their specific structure-related interactions with various energy and environmentally relevant guest species (especially CO<sub>2</sub>, H<sub>2</sub>O, NH<sub>3</sub>, and sodium) are elaborated with advanced gas sorption techniques (e.g., gas physisorption measurements,

thermal response measurements using the InfraSORP technique, and temperature-programmed desorption), as well as electrochemical methods.

## **1.1 Fundamentals of Porous Carbon Materials**

### **1.1.1 The Element Carbon – Origin and Development**

The chemical element carbon is possibly one of the most fascinating and alterable elements in the periodic table. *Carbo*, a word derived from the Latin language means “coal”. Carbon is being considered as “known to ancients”, in the form of charcoal. The universe creates this element in the center of the stars *via* the so-called triple-alpha process, which makes it the sixth-most abundant element in the universe. In old stars the accumulation of helium nuclei, with its two protons and two neutrons, under temperatures above 100,000,000 K leads to the fusion into a four-proton beryllium nucleus. The result of fusion of beryllium and helium is carbon – with its six protons and six neutrons.<sup>[12]</sup>

Carbon is abundant on earth, nonmetallic, mostly tetravalent, and a versatile element. It has a unique ability to form covalent bonds with other carbon atoms, thereby building for example polymer chains of various length and configuration, as well as to connect to non-carbon atoms (e.g., H, O, N, B, and metal atoms) forming organic and inorganic compounds with various chemical properties. Carbon can be found in stable form many different oxidations states. It can be present in methane with the oxidation state –IV and in CO<sub>2</sub> with +IV. The concept of hybridization of its orbitals in three stable bonding modes (i.e., sp, sp<sup>2</sup>, and sp<sup>3</sup>) serves as model to explain the molecular structure in organic compounds and it enables carbon to build up a large set of compounds. In other words, carbon offers a vast diversity. The element carbon is the key component in organic chemistry, and close to ten million carbon compounds has been discovered so far.<sup>[13]</sup>

The variety in properties of inorganic carbon materials is exemplified in its different allotropes, diamond (**Figure 2a**) and graphite (**Figure 2b**).<sup>[13]</sup> Diamond, known for its hardness (Mohs’ hardness = 10), is in its pure form clear and colorless, insulating, it possesses a wide bandgap. In diamond, sp<sup>3</sup>-hybridized carbon materials are packed in a cubic crystal structure.<sup>[14]</sup> In contrast, the soft graphite (Mohs’ hardness = 1.5), which is well-known as the “lead” in lead pencils, is a dark black, and electron conducting material.<sup>[15]</sup> In graphite, the carbon atoms are sp<sup>2</sup>-hybridized and arranged in hexagonal, honeycomb-type layers with  $\sigma$ - and  $\pi$ -bindings and these layers are stacked on top of each other. The special modification graphene is one monolayer of graphite. Like graphite, graphene is conductive due to the

delocalization of the electrons within the  $\pi$ -molecular orbitals. Nanostructured  $sp^2$ -based carbon materials can be subdivided in 2-dimensional (2D, graphene), 1-dimensional (1D, carbon nanotubes (**Figure 2c**)), or 0-dimensional (0D, fullerenes (**Figure 2d**)) compounds.<sup>[13]</sup> The combination of purely hexagonal binding with pentagons or heptagons of carbon atoms induces the bending of the sheets into spheres, ellipses, or cylinders. For example, fullerenes also have a graphene-like structure that forms hollow spheres (so-called “buckyballs”) by the substitution of carbon six-rings by carbon five-rings, where 60 or more carbon atoms are linked together ( $C_{60}$  or higher fullerenes). A porous carbon network is formed if the amount of the defects (e.g., pentagons and heptagons, as well as corners and edges in the graphene) is exceeding a certain limit (**Figure 2e**). Porous carbon materials are usually  $sp^2$ -rich frameworks and stand out by their high chemical/thermal stability, high electrical conductivity, abundant availability, and high porosity (i.e., high surface area and pore volume).<sup>[16]</sup> In consequence, these materials are extensively used in crucial fields of energy and environment, where a large interface area between the carbon material and the surrounding phase is required, like as electrode materials in supercapacitors, batteries and fuel cells,<sup>[17-20]</sup> in biomedical applications,<sup>[21]</sup> as sorbents in  $H_2O$  purification,<sup>[22]</sup> gas separation and storage,<sup>[23, 24]</sup> as well as supports for catalysts.<sup>[25]</sup> Porous carbon materials can be specified by their specific surface area (SSA) with a tunable pore size, geometry, and distribution, as well as the total pore volume ( $V_{total}$ ). Each application requires its unique porosity characteristics depending on the particular conditions and guest species. By adjusting these properties, an optimum in performance can be achieved.

A material can be called nanoporous if its pores have a size of up to 100 nm, according to the technical report of the International Union of Pure and Applied Chemistry (IUPAC).<sup>[26]</sup> A surface curvature can be defined as a pore if its cavity is deeper than wide. The nanopores are divided by their different sizes into macropores (pores of width  $d > 50$  nm), mesopores ( $d = 2-50$  nm), and micropores ( $d < 2$  nm). The micropores can be further divided into supermicropores ( $d = 0.7-2$  nm) and ultramicropores ( $d < 0.7$  nm).

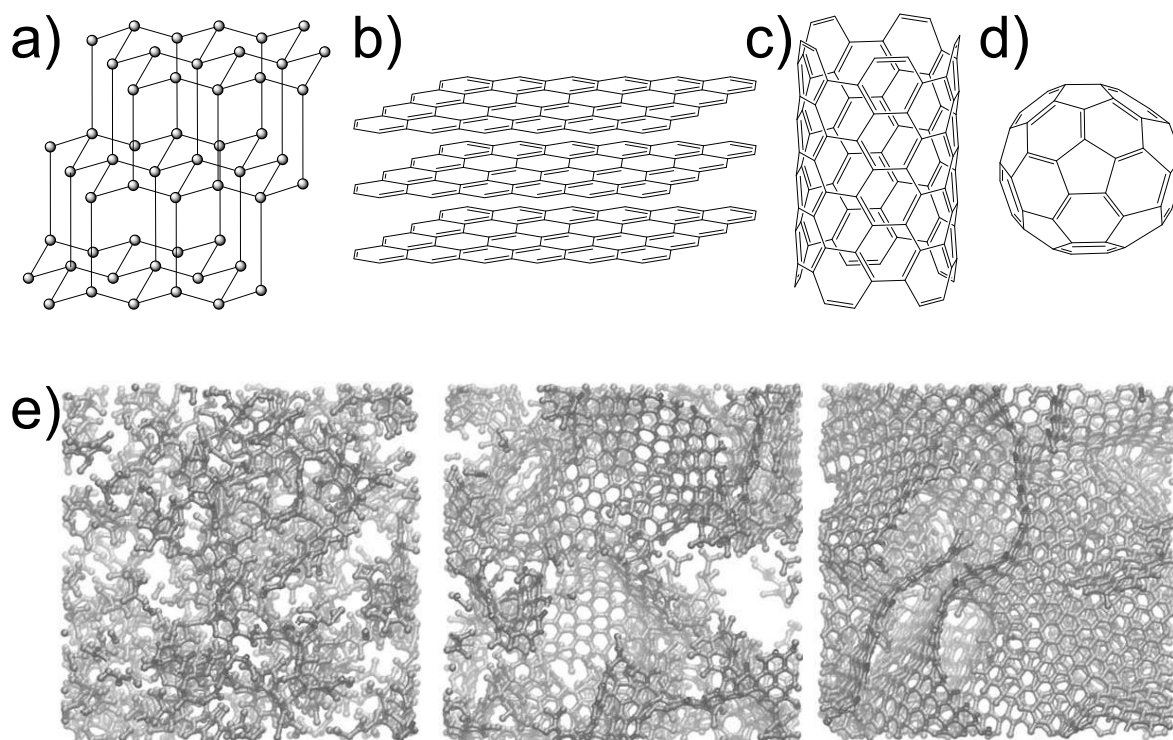


**Figure 2:** Structures of different carbon allotropes: Cubic diamond (a), graphite (b), carbon nanotube (c), and fullerene (d),<sup>[13]</sup> as well as model atomic construction of nanoporous carbon materials with different degree of carbon ordering (e). ((a–d) adapted from reference<sup>[13]</sup>, (e) adapted from reference<sup>[27]</sup>).

The importance of each porosity parameter varies with the targeted application. Thus, different approaches have been developed to implement various kinds of porosity into the carbon materials. In general, porous carbons are synthesized by pyrolysis of organic precursors at elevated temperatures, subsequently followed by physical or chemical activation. Ordered porous carbons can be further obtained by hard- or soft-templating approaches, as well as salt-templating methods.

### 1.1.2 Different Synthesis Approaches towards Porous Carbon Materials

Two aspects for the synthesis of porous carbon materials have to be considered. On the one hand, the carbonization of an organic carbon precursor material, and on the other hand, the implementation of porosity. A huge variety of precursors is suitable for carbonization ranging from phenolic-based resins (phenol-formaldehyde resins),<sup>[28]</sup> carbohydrates,<sup>[29]</sup> biomass,<sup>[30]</sup> metal organic frameworks (MOFs),<sup>[31]</sup> to ionic liquids (ILs).<sup>[32, 33]</sup> The introduction of porosity can occur during or after the carbonization step.<sup>[34]</sup> The physical or chemical activation follows the carbonization step for the production of activated carbon materials and is most widely used on an industrial scale. The physical activation is performed using CO<sub>2</sub>, steam, or air at elevated temperatures, which causes the etching of the carbon material and results in porosity.<sup>[35, 36]</sup> The chemical activation is mostly utilizing phosphoric acid (H<sub>3</sub>PO<sub>4</sub>), potassium

hydroxide (KOH), or zinc chloride (ZnCl<sub>2</sub>).<sup>[37, 38]</sup> Both kinds of activations result in micro- or mesoporous products with relatively broad pore size distribution (PSD). Most of these activated carbon materials are thus not suitable for size-selective applications and do not have a well-connected pore system, that is, they often contain bottle-neck-shaped pores.

As one method to achieve a more defined pore size distribution and the meso-/macropore range for carbon materials, templating approaches can be applied *in-situ* during the carbonization step.<sup>[39]</sup> The template is defining the pore size and structure of the carbon products and has to be removed during or after the carbonization step. Templating can be distinguished into hard- and soft-templating, as illustrated in **Figure 3**.

The hard-templating procedure is also called nanocasting, due to the infiltration of the carbon precursor (e.g., sucrose) into the pore network of a hard-template (the so-called “mold”, e.g., silica), subsequently followed by carbonization and template removal (**Figure 3a**).<sup>[40, 41]</sup> Sacrificial templates (e.g., poly(methyl methacrylate) (PMMA)) can be removed *in-situ* during pyrolysis.<sup>[42]</sup> Silica templates, or ordered mesoporous carbon materials can be divided by their pore geometry into 3D cubic ordered (e.g., KIT-6 (Korea Institute of Technology))<sup>[43]</sup> or CMK-1 (carbon mesostructured by KAIST (Korea Advanced Institute of Science and Technology)),<sup>[44]</sup> and 2D hexagonal ordered (e.g., CMK-3<sup>[45]</sup> or SBA-15 (Santa Barbara Amorphous Type Material)).<sup>[46]</sup> Disordered materials, such as activated carbons<sup>[47]</sup> or silica nanospheres,<sup>[48]</sup> are also widely applied. The precise control over the pore structure due to ordered templates results in ordered mesoporous replica carbon products with high surface areas. The soft-templating is based on the self-assembly of structure-directing amphiphilic molecules, such as surfactants or block co-polymers, that are forming soft-templates (e.g., micelles or liquid crystals) (**Figure 3b**).<sup>[49, 50]</sup> This approach allows the synthesis of ordered mesoporous materials and a famous example is the hexagonal ordered silica MCM-41 (Mobil Composition of Matter).<sup>[51]</sup> Although precise control over the pore structure of the resulting carbon materials can be achieved, the synthesis and removal of the template, as well as the infiltration step are huge drawbacks of the templating approach.

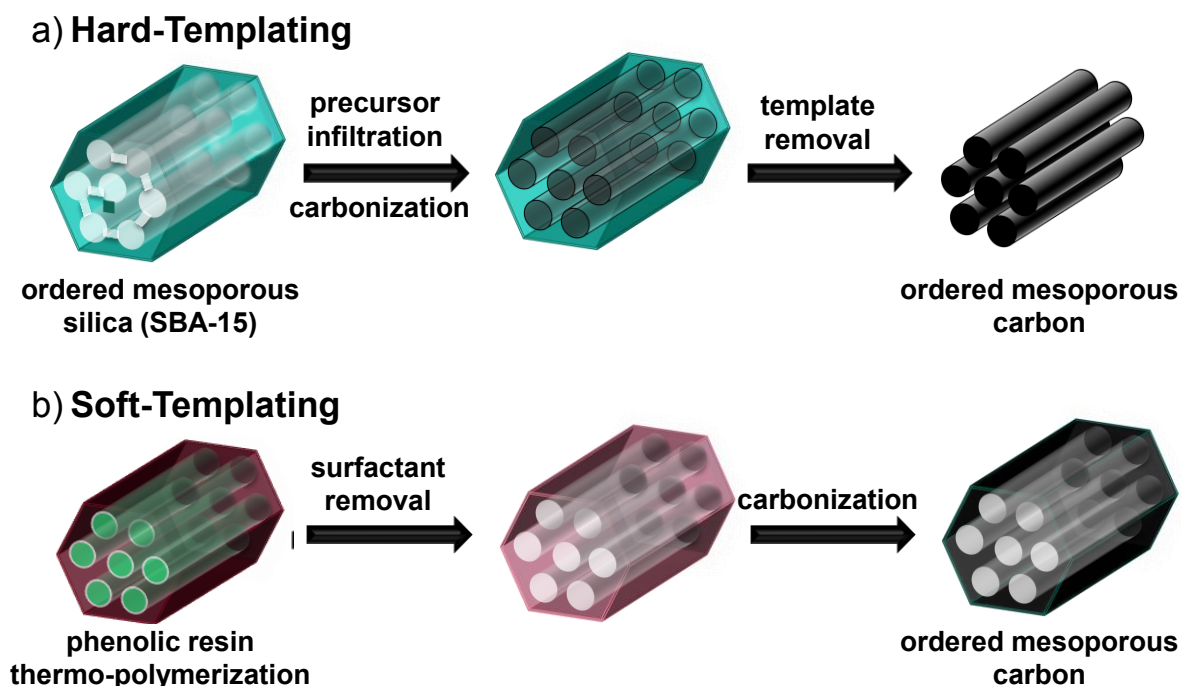


**Figure 3:** Hard- and soft-templating methods for the synthesis of ordered mesoporous carbon materials.

Other synthesis methods to obtain carbons with well-defined porosity are, for example, salt-templating<sup>[33, 52]</sup> or the removal of oxidic templates with reductive carbo-chlorination.<sup>[53, 54]</sup> Especially the salt-templating method avoids harsh conditions and enables the introduction of micropores. The pore size can be adjusted by using different salt mixtures, their ratios (e.g., LiCl/ZnCl<sub>2</sub>, NaCl/ZnCl<sub>2</sub>, or KCl/ZnCl<sub>2</sub>), and the ratio between salt templates and carbon precursors. The combination of several templating routes or a templating approach with activation step can lead to hierarchical carbon materials.<sup>[55, 56, 20]</sup>

A precise control over the porosity can also be achieved with carbide-derived carbons (CDCs). Mostly microporous carbons with very high SSAs (up to 3000 m<sup>2</sup> g<sup>-1</sup>) can be synthesized by high temperature chlorine treatment of (semi-)metal carbides (e.g., silicon carbide (SiC) or titanium carbide (TiC)), which results in the selective etching of the (semi-)metal atoms.<sup>[57]</sup> The micropore size can be controlled by the chlorination temperature and the choice of (semi-)metal carbide.<sup>[58]</sup> Performing the chlorine treatment on hard-templated ordered mesoporous metal carbides leads to hierarchically ordered micro-/mesoporous CDCs with fast diffusion pathways.<sup>[55]</sup> Nevertheless, this synthesis approach is quite expensive and ends up in low yields.

Besides the importance of porosity characteristics of porous carbon materials, the introduction of heteroatoms in form of chemical functionalities into the carbon framework can

significantly change the electronic structure of the material. Selective interactions of heteroatom-containing groups can result in stronger interaction with certain guest species, and thus lead to further control over their performances. A well-studied research field is nitrogen-containing porous carbons, which show improved selective gas adsorption,<sup>[59]</sup> higher energy storage capacities in electrochemical double-layer capacitors (EDLCs),<sup>[60]</sup> or properties as catalyst support (e.g., stabilization of metal clusters).<sup>[61]</sup> In consequence, it is noteworthy to introduce the fundamentals of structural/chemical influences of nitrogen-doping, as well as the corresponding preparation techniques for nitrogen-doped carbon materials (NdCs).

## **1.2 Nitrogen-containing Porous Carbon Materials**

### **1.2.1 Fundamentals and Influences of Nitrogen Incorporation into Carbon Materials**

The properties of porous carbon materials cannot only be influenced by their porosity, surface area, or structure, but also to a wide extent by their chemical features due to the doping with different heteroatoms (e.g., N, B, S, or P). The most widely studied heteroatoms for the incorporation into the carbon backbone are nitrogen and oxygen. The latter is usually present in carbon materials at the edges of the basal plane, and the oxygen-containing surface groups in most cases increase the acidic properties of the carbon materials.<sup>[62, 63]</sup>

The incorporation of nitrogen into the carbon lattice has some benefits compared to other heteroatoms. A similar atomic radius between nitrogen and carbon enables the introduction of large amount of nitrogen atoms into carbon materials without significant structural distortions. For instance, nitrogen-doped carbon materials can be as porous as pristine carbon materials. Nitrogen offers oxidative states and bonding multiplicities/schemes that can easily replace a carbon atom, and thus fit into the carbon framework. Nitrogen can be integrated by various synthesis approaches into carbon materials and this usually leads to stable compounds with different structures and properties. The electronic properties of nitrogen-doped carbon materials will be affected, as nitrogen has one valence electron more than carbon. In contrast to oxygen, (pyrazinic or pyridinic) nitrogen-containing functional groups introduce a basic character into porous carbon materials in most cases. The basic character of carbon materials is based on additional valence electrons provided by the nitrogen atoms, which contribute to the  $\pi$ -electron aromatic system. In consequence, the electron-withdrawing pyridinic or pyrazinic nitrogen atoms are inducing local positively charged carbon atoms.<sup>[64-67]</sup> The basic properties can be beneficial for enhanced interactions between carbon surface and acidic

molecules (e.g., CO<sub>2</sub>), due to dipole-dipole interactions, hydrogen bonding, or covalent bonding.<sup>[68]</sup> The basicity of nitrogen-doped carbonaceous materials leads to a higher affinity and capacity towards acid gases,<sup>[69]</sup> enables the materials to act as a catalyst for the reduction of oxygen in fuel cells,<sup>[70]</sup> can strengthen ion adsorption in supercapacitors,<sup>[71]</sup> and can increase the selectivity of membranes for gas separation.<sup>[72]</sup> The incorporation of nitrogen into the sp<sup>2</sup>-bonded carbon framework can improve the physical and chemical properties, especially basicity,<sup>[73]</sup> oxidative stability,<sup>[74]</sup> thermal stability,<sup>[75]</sup> and catalytic activity of carbon materials.<sup>[76]</sup> Nitrogen-doping can enhance the electrical conductivity, due to the formation of a localized electron-donor state near the Fermi level.<sup>[77, 78]</sup>

Nitrogen atoms can be implemented into the carbon lattice with different bonding configurations, as it is illustrated in **Figure 4**.<sup>[79, 80]</sup> This is including the two most stable configurations, namely graphitic (quaternary) nitrogen that is substituting an sp<sup>2</sup>-hybridized carbon in a hexagonal ring, and pyridinic nitrogen that is replacing a sp<sup>2</sup>-hybridized carbon at the edges of the structures (occurring at edges or defects). Sp<sup>2</sup>-hybridized pyrazinic nitrogen, which is incorporated in *para*-position in hexagonal rings, as well as sp<sup>3</sup>-hybridized pyrrolic nitrogen and pyridinic nitrogen oxides can be present in NdCs.<sup>[81]</sup> The content and the type of nitrogen in the carbon materials strongly depend on the applied precursor and the carbonization temperature. It is known that a lower overall nitrogen amount, predominantly graphitic nitrogen, is formed with elevated synthesis temperatures.<sup>[79, 80]</sup> The reason is that during the heating the pyridinic nitrogen atoms condensate to valley or central graphitic nitrogen atoms, as well as the on-going release of the pyridinic nitrogen atoms.<sup>[82]</sup> Thus, graphitic nitrogen atoms are thermally more stable than pyridinic nitrogen atoms.

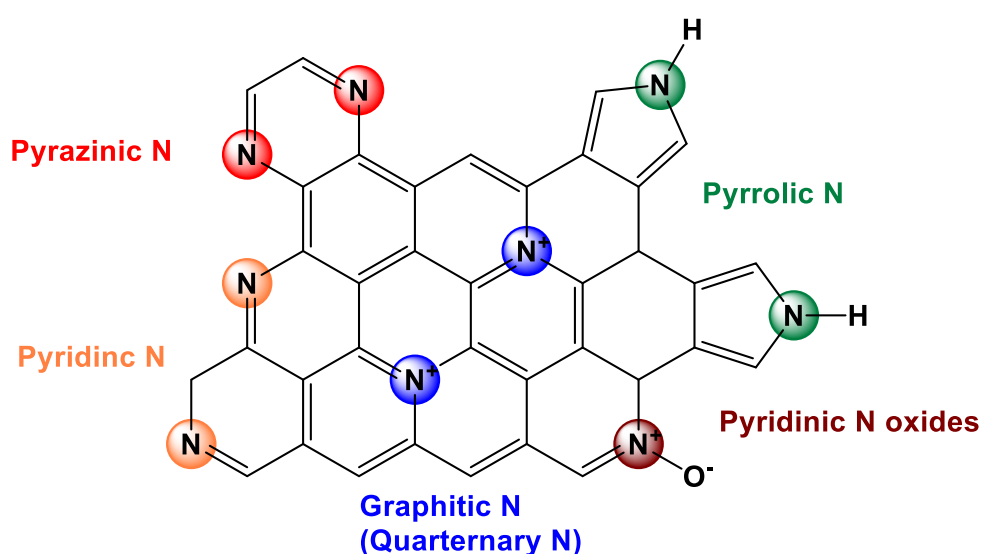


**Figure 4:** Different types of nitrogen-containing functional groups on porous carbon surfaces.

In general, nitrogen-containing carbon materials can be distinguished into nitrogen-doped carbon materials and nitrogen-rich compounds.<sup>[74]</sup> The latter are characterized by high nitrogen to carbon ratios ( $N/C \geq 1:1$ ), as for example, graphitic carbon nitride (g-C<sub>3</sub>N<sub>4</sub>) with a nitrogen content up to 61 wt%.<sup>[83]</sup> Their synthesis is based on thermal condensation of nitrogen-rich precursors ( $N/C \geq 1:1$ ), such as melamine or polyurea, at moderate temperatures (~500 °C).<sup>[84]</sup> In contrast, NdCs are synthesized either by *in-situ* carbonization or by post-treatment of the as-obtained carbon materials using nitrogen-containing precursors ( $N/C \leq 1:1$ ), like NH<sub>3</sub>, acetonitrile, or nitric acid.

### 1.2.2 Different Synthesis Approaches towards Nitrogen-Containing Porous Carbon Materials

The introduction of nitrogen-containing functional groups can either be realized by carbonization/activation of nitrogen-rich carbon precursors or the reaction of as-synthesized carbon materials with nitrogen-containing reagents. The latter is the post-treatment of porous carbon with nitrogen-containing reagents, like nitric acid, urea, melamine, dicyanodiamine, or most frequently used NH<sub>3</sub> (ammonoxidation) in liquid or gas phase.<sup>[85]</sup> Herein, the problem is the decrease of the surface area and pore volume of the porous carbons due to the ammonoxidation,<sup>[86]</sup> as well as the irregular distribution of nitrogen over the surface. The nitrogen-containing functional groups that are introduced in such an approach are also often unstable and low in number. To overcome these problems, the use of nitrogen-containing precursors with adjustable nitrogen content for the direct synthesis of nitrogen-containing porous carbons is beneficial.<sup>[87]</sup> Nitrogen-containing porous carbon materials with different structures can be obtained by templating approaches (e.g., zeolite 13X, SBA-15, MCM-48)<sup>[85]</sup> or physical/chemical activation (e.g., using steam, CO<sub>2</sub>, or KOH) of different nitrogen sources (e.g., acetonitrile, diaminobenzene, polypyrrole, amino-glucose, cyanamide, or polyacrylonitrile).<sup>[85, 88]</sup> The hydrothermal treatment of natural compounds, like amino acids or proteins with glucose or aminated saccharides (e.g., glucosamine or chitosan), led to the formation of stronger aromatized and nitrogenated products (8–10 wt.% nitrogen content).<sup>[89]</sup> This method was performed in pure H<sub>2</sub>O at mild conditions (< 200 °C) within closed autoclaves under autogenous pressure.<sup>[90]</sup> Physical/chemical activation leads to a high content and high stability of nitrogen, but reveals difficulties in the control of the pore structure of the carbon materials. The templating approach enables the synthesis of well-ordered nitrogen-containing porous carbons with defined pore size and structure, however this method is extensive and time consuming.

The facile preparation of highly nitrogen-doped porous carbon materials with a well-defined porosity and the homogenous distribution of nitrogen are still challenging, since the carbonization process is hard to control. A promising concept that helps to understand the carbonization pathway towards highly stable and desirable nitrogen-doped carbon materials is based on fundamental laws of thermodynamics and is further explained in detail in the following chapter by introducing the concept of noble carbon materials.

### **1.3 Unique Stability of Nitrogen-Containing Carbon Materials – The Concept of Noble Carbon Materials**

The challenge remains to introduce porosity and a significant amount of nitrogen atoms uniformly bonded and well-distributed into the carbon backbone. The insertion of heteroatoms, such as N, S, or O, has a stabilizing effect on carbon materials, which makes them resistant towards oxidation. In analogy to oxidation-resistant metals such as gold, these carbon materials can be called “noble”.<sup>[91]</sup> As already mentioned above, the direct carbonization of nitrogen-rich molecules is a well-established process for the homogeneous distribution of nitrogen atoms in carbon materials. One approach is to use suitable precursors for the carbonization process that are forming products which are well-defined in structure and in electronic properties. The understanding of the directed synthesis of such noble and heteroatom-doped carbons *via* the electronic band control of carbonization is a powerful concept.<sup>[92]</sup>

#### **1.3.1 Fundamentals of the Concept of Noble Carbon Materials**

In general, the resistance against oxidation is defined as nobility. This nobility can be quantified by ultraviolet photoelectron spectroscopy or cyclic voltammetry (CV). The former is describing the energy characteristics of photoelectrons emitted by a material after it has been bombarded with photons, and the latter is measuring the ability of a material to donate electrons by applying voltage.

The electrochemical potential can be calculated by using the Nernst Equation (**Equation 1**), which is dependent on the concentration of oxidized and reduced states of a mixture or a solid.

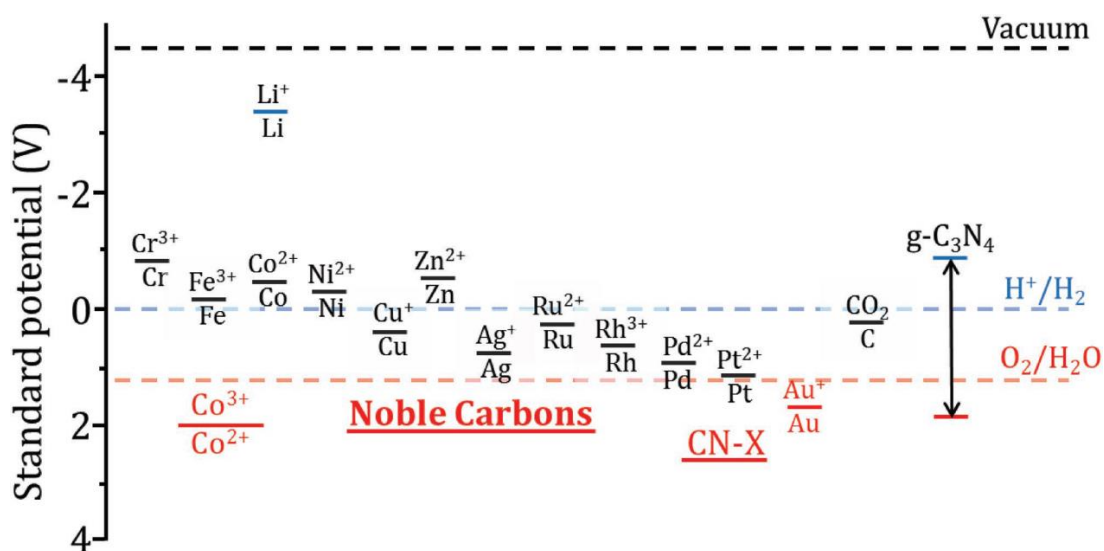
$$E = E^0 + \frac{RT}{nF} \ln \frac{[Ox]}{[Red]} \quad (\text{Eq. 1})$$

Furthermore, the relation of a change of the electrochemical potential and a change of the free energy of a system ( $\Delta G$ ) is defined by the bridging relation (**Equation 2**). In consequence, any spontaneous reaction between two materials will lower the electrochemical potential.

$$\Delta G = -n \times F \times \Delta E^0 \quad (\text{Eq. 2})$$

The CV-derived data is referred to a standard electrode potential, which is the reference hydrogen electrode (RHE) that is set to  $E^0_{\text{RHE}} = 0$ , and is schematically shown for some compounds in **Scheme 1**.<sup>[92]</sup>

By this definition and regarding **Scheme 1**, non-noble materials are considered to have a negative electrochemical potential relative to the RHE. This means, non-noble materials have a positive free energy concerning the hydrogen line and will thermodynamically corrode in  $\text{H}_2\text{O}$  and usually form oxides, which will be electrochemically below the RHE. In contrast, materials being more positive than the oxygen line ( $E^0(\text{O}_2) = +1.23 \text{ V}$ ) will not be easily oxidized (i.e., will not easily react exothermally with oxygen), and thus, materials that are located below the oxygen line are considered to be “noble”.



**Scheme 1:** Electrochemical potentials for some known materials (adapted from reference<sup>[92]</sup>).

Very electron-deficient materials are predestined to be noble materials, because they have a high affinity to their electrons. Some examples for molecules with high oxidation strength can be found in organic chemistry, including dyes (e.g., Fukuzumi dye with  $E_{\text{HOMO}} \approx +2.1 \text{ V}$ ; highest occupied molecular orbital (HOMO)),<sup>[93]</sup> nucleobases (e.g., Thymine  $E_{\text{HOMO}} \approx +2.1 \text{ V}$ ),<sup>[94]</sup> cations of ionic liquids (e.g., calculated with  $E_{\text{HOMO}} \approx +5.9 \text{ V}$ ),<sup>[95]</sup> or solid state organic materials (e.g., carbon nitride family  $E_{\text{HOMO}} \approx +1.6\text{--}2.1 \text{ V}$ ).<sup>[96, 97]</sup>

### 1.3.2 Rules and Guidelines of Different Carbonization Pathways

Two possible carbonization pathways can be distinguished towards the synthesis of noble carbonaceous materials, as illustrated in **Figure 5**. The first carbonization pathway describes the carbonization of precursors that have a slightly positive electrochemical position, such as carbohydrates (e.g., cellulose or sucrose). Carbohydrates do not react in  $\text{H}_2\text{O}$ , but they burn in air. During the carbonization of cellulose, for example,  $\text{H}_2\text{O}$  is eliminated with a higher potential (+1.23 V) and the resulting sugar coal must get upward in its internal energy according to the first law of thermodynamics. Thus, a non-noble and easily oxidizable carbon product is obtained. However, the choice of more electrochemically stable precursors results in a different carbonization pathway. The electrochemical potential of nucleobases, some dyes, or ionic liquids is below the  $\text{H}_2\text{O}$  line with +1.23 V. The carbonization of these precursors also comes along with the typical elimination products, such as  $\text{H}_2\text{O}$ ,  $\text{CO}_2$ ,  $\text{CO}$ ,  $\text{NH}_3$ , or  $\text{N}_2$ . The elimination products are more electrochemically negative than the applied precursors. In consequence, the resulting carbon materials have an even more positive electrochemical potential, according to the first and second law of thermodynamics, and have to be noble carbon materials, which are hardly oxidizable.<sup>[92]</sup>

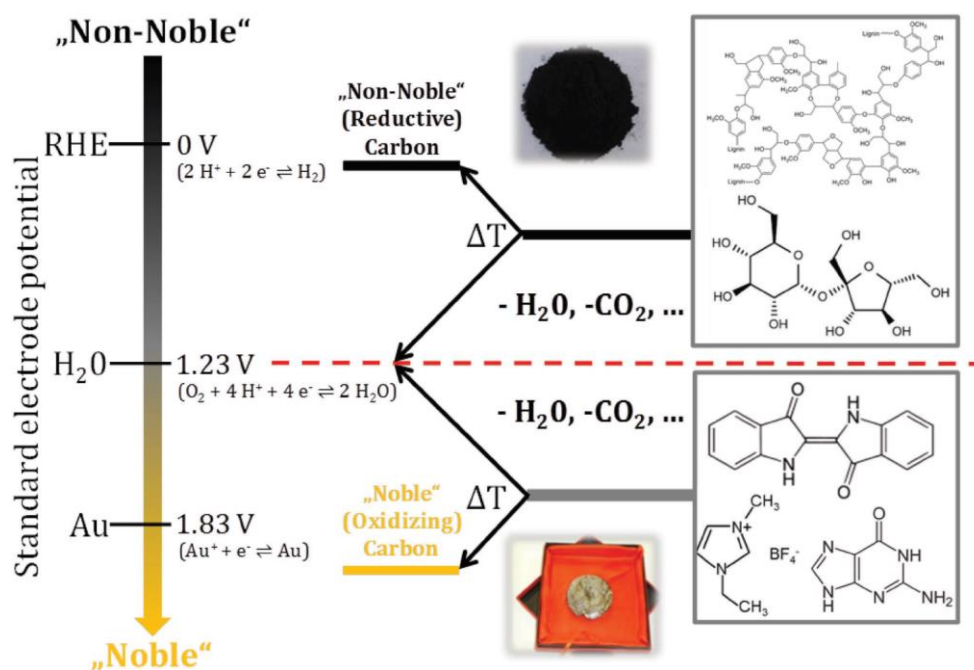


**Figure 5:** Concept of carbonization pathways to a non-noble and noble carbons (adapted from reference<sup>[92]</sup>).

This argumentation postulates that stable precursors, which have a more positive electrochemical potential than their elimination products, can only result in even more stable products. This allows more predictions on the properties of the resulting noble carbon materials, such as i) an energetically optimization of aromatic packing and aromatization, ii) a

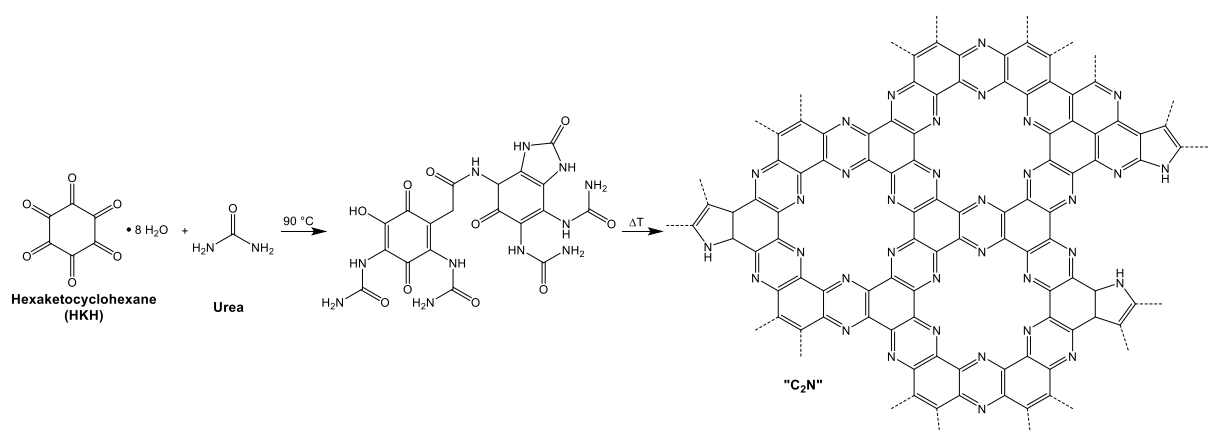
higher specific cohesion energy (i.e., increase in polarizability), and iii) an energetically favored distribution of heteroatoms within the carbon material. The latter is based on the stabilizing effect of heteroatoms (e.g., N, S, or O) that leads to positive HOMO levels.<sup>[92]</sup> Due to the “band confinements”, the heteroatoms will be located at energetically favored positions in an optimal distance to each other. This effect in electronically delocalized states is described in an experimental and theoretical paper.<sup>[98]</sup> This concept offers an approach to investigate simple organic solids as precursor systems to obtain novel noble carbon materials with unique properties regarding their application in catalysis, batteries or supercapacitors, and gas adsorption.

Taking the huge variety of nitrogen-doped carbon materials with specialized interactions for improved performances in numerous applications and an advanced approach from appropriate educts towards noble compounds into account, products with unique electronic properties and controlled structure can be realized. One nitrogen-doped carbon material that is of particular interest, but requires advanced synthesis approaches, has a C<sub>2</sub>N-type stoichiometry.

## 1.4 C<sub>2</sub>N-type Carbon Materials

The molecular-level design of carbon materials with a precise control of the local chemical composition and structure with a high homogeneity and regularity throughout the whole framework remains challenging due to the difficulties during carbon synthesis.

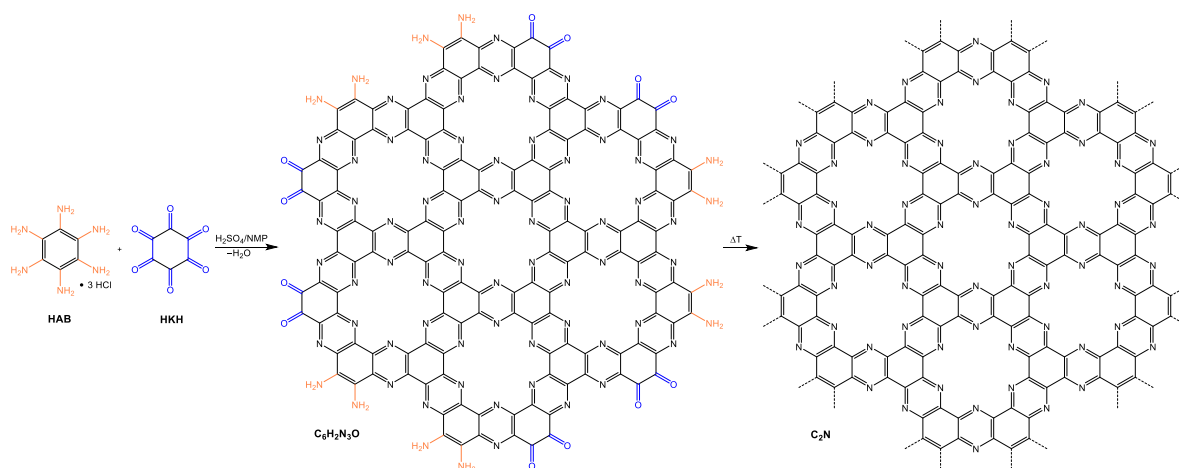
Recently, a synthesis approach towards a new nitrogen-containing carbon material was proposed using supra-molecularly preorganized precursor mixtures that consisted of oligophenol/ketones and urea (**Scheme 2**), investigated by Fechner *et al.* The precursors formed a deep eutectic mixture with a high homogeneity of liquids with a well-defined structure of prealigned liquid crystals, due to strong hydrogen bonds.<sup>[99]</sup> The structure of the phenol/ketone was implemented and expanded in the resulting carbon product, while urea acted as a melting point reducing agent and especially as nitrogen source. The study described the condensation as a structurally organized process between the two reactants. Nitrogen-containing aromatic carbon materials were obtained at 700–800 °C with high nitrogen content of 28 wt.%. This is according to a C<sub>2</sub>N-type structure with defects.<sup>[99]</sup>



**Scheme 2:** Synthesis pathway from cyclohexanone and urea as reactants, over a cross-linked intermediate state, towards a nitrogen-containing carbon material consisting of pyridinic and pyrazinic nitrogen in a defective C<sub>2</sub>N manner (adapted from reference<sup>[99]</sup>).

Some products that were synthesized at 500 °C exhibited a metallic gloss, which is very unusual at such a low temperature and is known for conducting polymers. To investigate the semi-metallic behavior, conductivity measurements were performed, which indicated a conductivity of 2 S cm<sup>-1</sup> at 423 K for a material synthesized at 800 °C, and Seebeck measurements exhibited the mainly *n*-character of the charge transport. The salt-templating approach using ZnCl<sub>2</sub> and cyclohexanone/urea resulted in high specific surface areas of ~1500 m<sup>2</sup> g<sup>-1</sup>. The nitrogen atoms were mostly present in form of pyrazinic nitrogen (20.7 at.% (67 %) at 500 °C), as well as some pyrrolic nitrogen (7.0 at.% (23 %) at 500 °C), on the surface edges and as defect structures. This C<sub>2</sub>N material formed a locally organized lamellar structure with tightly packed zeolite-like micropores that were lined with pyrazinic nitrogen.

Previously, the group of Baek *et al.* reported a layered 2D network structure, obtained by a so-called bottom-up wet-chemical reaction (**Scheme 3**).<sup>[100]</sup> The empirical formula for the entire molecule is C<sub>6</sub>H<sub>2</sub>N<sub>3</sub>O including the functional groups on the edges, and a C<sub>2</sub>N stoichiometry in its basal plane. This was obtained by the reaction of hexaaminobenzene (HAB) trihydrochloride and hexaketocyclohexane (HKH) in *N*-methyl-2-pyrrolidone (NMP) in the presence of acid (H<sub>2</sub>SO<sub>4</sub>). Subsequent heat treatment (700 °C) led to nitrogen-containing 2D C<sub>2</sub>N crystals.



**Scheme 3:** Bottom-up wet-chemical formation of  $C_2N$ - $h2D$  crystals via HAB and HKH in the presence of acid. The edge groups of the intermediate  $C_6H_2N_3O$  could be thermally (at 700 °C) removed in form of small molecules (e.g.,  $H_2O$ ,  $O_2$ , and so on) and resulted in the heat-treated  $C_2N$  holey structure (adapted from reference<sup>[100]</sup>).

The reaction was driven by the favored aromatization state of the product and is leading to the condensation of HAB and HKH into a crystalline layered 2D structure in form of a dark-black graphite-like solid. This network consisted of evenly distributed holes and nitrogen atoms and is thus stated as ‘ $C_2N$  holey 2D crystal’ (‘ $C_2N$ - $h2D$ ’). In addition to van der Waals interactions, the  $C_2N$ - $h2D$  crystal showed polar attraction, resulting in stronger interlayer interactions than those in graphite. In consequence, the interlayer distance ( $d$ -spacing) is narrower with 0.328 nm, compared to the  $d$ -spacing in graphite with 0.335 nm. A sharp peak at  $\sim 27^\circ$  in the powder X-ray diffraction pattern (PXRD) corresponded to the  $d$ -spacing. The ordered introduction of uniform holes and nitrogen atoms is proposed to widen the bandgap between valence and conduction band to form an ideal semiconductor material. And indeed, Baek *et al.* described an experimental semiconducting bandgap of 1.96 eV (close to the calculated value of 1.70 eV).<sup>[100]</sup>

Both synthesis approaches towards carbon materials with  $C_2N$  stoichiometry are contributing to the field of nitrogen-doped carbon materials.  $C_2N$  has a smaller bandgap with 1.96 eV than the semiconducting  $g$ - $C_3N_4$  with approximately 2.7 eV. In comparison, graphene with its fully  $\pi$ -conjugated electron system has an evanescent small bandgap and is thus a conductive material. In consequence, the unique electronic and geometric structure of  $C_2N$  can open up various electrochemical applications, where other materials offer inherent limitations.

## 1.5 Conjugated Microporous Polymers as Precursors Systems towards Porous Carbon Materials

On the search of tailor-made porous carbon nanostructures with pre-designed specific functional groups within the carbon network or on its surface, synthetic conjugated polymers arose to be promising carbon precursors.<sup>[101]</sup> Besides covalent organic frameworks (COFs) or porous organic polymers (POPs), a special subdivided class is conjugated microporous polymers (CMPs) which are also built up *via* a  $\pi$ -conjugated system of covalently bonded aromatic building blocks. The CMPs are synthesized by different coupling reactions and own an open nanoporous network and high surface areas.<sup>[102-104]</sup> Due to the integration of nanopores and a  $\pi$ -conjugated system, CMPs can be implemented in various applications ranging from light emitting<sup>[105]</sup>/harvesting<sup>[106]</sup>, heterogeneous catalysis,<sup>[107]</sup> sensing,<sup>[108]</sup> electrochemical energy storage,<sup>[109]</sup> as well as gas adsorption.<sup>[110]</sup>

The inherent carbon-rich CMPs with the robust  $\pi$ -backbone are predestined to act as promising carbon precursors due to following reasons:<sup>[101]</sup> i) The major advantage to other polymer precursors is the possibility for direct template-free carbonization of the tailor-made CMPs to the corresponding carbon materials; ii) a huge variety and flexibility in the molecular construction of nanopores and  $\pi$ -conjugated building blocks (e.g., phenyl units, extended arenes, heterocyclic aromatic units, large macrocycles) is leading to designable porous carbon nanostructures; iii) the *in-situ* incorporation of heteroatoms (e.g., nitrogen from polyaniline (PANI) or sulfur from polythiophene) is well-distributed into the carbon materials due to a precise control of the location of the heteroatoms on a molecular level in the CMPs, as well as the homogeneous doping with metals/metal oxides in the carbon materials using metal-containing CMPs;<sup>[111-113]</sup> iv) the aromatic  $\pi$ -conjugated system favors the graphitization of the carbon products that tends to contribute to a higher electrical conductivity, which is especially beneficial for electrochemical applications; and v) a high control over the chemical composition and different kind of nanostructures (i.e., zero to three dimensions and variable in size from several to hundreds of nanometers) *via* modern organic synthesis and polymerization techniques (e.g., Sonogashira, Yamamoto, or Oxidative coupling, as well as Schiff-base chemistry, or cyclotrimerizations).<sup>[101]</sup>

Recently, CMPs with their carbon-rich  $\pi$ -conjugated system and permanent nanopores have been used as outstanding precursors to produce porous carbon materials by direct carbonization. 1D microporous carbon nanofibers and nanotubes with surface areas up to  $900 \text{ m}^2 \text{ g}^{-1}$  were obtained by direct carbonization of tubular conjugated polyphenylene

networks,<sup>[114]</sup> which were synthesized by Sonogashira coupling using 1,3,5-tris-2'-biphenyl benzene. Nitrogen-doped holey graphitic carbon materials were fabricated by 2D conjugated polymers *via* Yamamoto polycondensation of nitrogen-containing organic complexes like porphyrin and triazine derivatives.<sup>[115]</sup> The structure and property of the polymeric precursors with precisely controlled locations of nitrogen and holes were transferred into corresponding carbon products. Membranes of conjugated frameworks were developed by acid-catalyzed trimerization of aromatic nitrile or acetyl groups. Accordingly, free-standing porous nitrogen-doped carbonaceous membranes were prepared, that show good CO<sub>2</sub> permeability and high CO<sub>2</sub>/N<sub>2</sub> permselectivity, because of the synergy of molecular sieving effect and an adsorption/diffusion mechanism.<sup>[116, 117]</sup> Finally, CMP-derived porous carbon materials can be fabricated by different preparation techniques, including direct templating (e.g., nanocasting or surface coating strategy), self-assembly, chemical activation, microwave irradiation, or template-free carbonization.<sup>[101]</sup>

## **1.6 Specific Interactions of Porous Carbon Materials with Guest Species**

### **1.6.1 Porous Carbon Materials for Selective Gas Adsorption and Separation**

Porous carbon materials are widely applied in the field of selective gas adsorption and separation. As a consequence of varying composition of different gases in a mixture, operating temperature, contact time, or costs, each application of gas separation defines its own need for specific materials. Numerous requirements towards the materials make their fabrication and modulation of their properties challenging. Especially nitrogen-containing porous carbon materials developed to a promising class of compounds due to their unique and tunable structural properties. In the following section, the research field of selective gas adsorption and separation using porous carbon materials and the influences of structure and electronic characteristics is elucidated in detail.

#### **1.6.1.1 General Overview of the Role of Porous Carbon Materials in Gas Adsorption and Separation**

Carbon nanomaterials found their way in many applications and one field of particular importance is gas sorption and separation processes. High specific surface areas and the tunability in pore size and distribution render carbon materials a good choice for the physical adsorption (so-called physisorption) of various gas molecules. Physisorption is a reversible process and has a smaller activation energy barrier, as compared to the chemical adsorption

(so-called chemisorption), where chemical bonds are formed. For example, the storage of hydrogen in porous carbon materials using physisorption is an intensively researched topic to enable energy supply for hydrogen powered fuel cells. Hydrogen storage *via* physisorption especially offers various benefits compared to compression (requires high pressures up to 70 MPa), liquefaction (needs low temperatures  $< 20$  K), or chemical storage (i.e., exothermal formation of metal hydrides or other hydrogen containing compounds; the storage tank would have to be heated to get hydrogen out as fuel).<sup>[118]</sup> In order to provide clean energy sources, the adsorption of methane or hydrocarbons is also important.<sup>[119]</sup> At the present time, the removal of environmentally harmful or toxic gases, such as CO<sub>2</sub>, SO<sub>2</sub>, NO<sub>2</sub>, H<sub>2</sub>S, or NO<sub>x</sub>, are of high interest.<sup>[23]</sup> Crucial parameters for efficient gas storage are high volumetric (cm<sup>3</sup> or mol gas per volume of adsorbent) and gravimetric (cm<sup>3</sup> or mol gas per mass of adsorbent) gas uptakes of porous materials.<sup>[120]</sup> The pressure at which the gas uptake occurs is of high importance, depending on the chosen application. Furthermore, the separation of gas mixtures by filtrating certain components or the removal of volatile organic compounds is crucial for industrial applications. For instance, in the pre-combustion process, CO<sub>2</sub> is separated from CH<sub>4</sub> during the purification of natural gas (~75–90 % CH<sub>4</sub>, ~8 % CO<sub>2</sub>, and 5 % N<sub>2</sub> at a pressure of ~5 bar) or landfill gas (CO<sub>2</sub>/N<sub>2</sub> in a 1:1 mixture at ~1 bar). The flue-gas (~3–15 % CO<sub>2</sub> and >70 % N<sub>2</sub>) purification from fossil-based power plants, so-called post-combustion process, requires the separation of CO<sub>2</sub> from N<sub>2</sub>.<sup>[9]</sup> What is often overseen in this context, is the difficulty of the similar presence of H<sub>2</sub>O and O<sub>2</sub> in the flue gas (~5–7 % H<sub>2</sub>O and ~3–4 % O<sub>2</sub>), which also tend to adsorb strongly on carbon materials.<sup>[121]</sup>

To date, industrial standards in CO<sub>2</sub> separation processes are mostly based on liquid amine absorption methods, also known as amine scrubbing.<sup>[122, 123]</sup> Aqueous solutions of monoethanolamine (MEA), diethanolamine (DEA), and methyldiethanolamine (MDEA)<sup>[124]</sup> or amine materials anchored on porous organic, inorganic, or organic-inorganic hybrid supports have been successfully applied to capture CO<sub>2</sub> on industrial scale,<sup>[125]</sup> as for example in post-combustion processes or direct capture from air (e.g., in submarines to purify breathing air).<sup>[10]</sup> In solid-supported amine materials, a chemical reaction between the amines and CO<sub>2</sub> creates covalent carbamate bonds, and is leading to significant CO<sub>2</sub> uptakes at low relative pressures.<sup>[126, 127]</sup> Their high selectivity towards CO<sub>2</sub> comes with a very high heat of adsorption (e.g.,  $Q_{st}$  for a MEA solution is  $>75$  kJ mol<sup>-1</sup>)<sup>[125]</sup> compared to physical adsorbents. Thus, the cycle ability in terms of recovering CO<sub>2</sub> and regenerate the sorbent is very energy and cost intensive.<sup>[128]</sup> The irreversible formation of carbamate, bicarbonate, or urea due to the

reaction with CO<sub>2</sub> lowers the sorption capacity, and once deactivated sorbents have to be regenerated by high temperature treatment under inert gas flow.<sup>[129]</sup> Other drawbacks are the corrosive properties of liquid amines<sup>[124]</sup> and the amine losses accumulated during the process.<sup>[128]</sup> In consequence, in recent years huge efforts were done to investigate alternative approaches for CO<sub>2</sub> capture, especially physical adsorption on porous solids.

The requirements for efficient gas filtration materials are diverse and ranging from i) high selectivities for one specific component out of a gas mixture, ii) high gas capacity under working conditions, iii) mild conditions for regeneration, iv) good stability against impurities and moisture, and v) sufficient sorption kinetics.<sup>[125]</sup>

A well-known and often industrially applied adsorbent is activated carbon (AC). ACs stand out due to their high specific surface areas and relatively low production costs, and is thus used, for example, as air filter in gas masks and respirators,<sup>[130]</sup> air purification, but also as storage material for methane or hydrogen.<sup>[131]</sup> The drawbacks of ACs are their limitation in gravimetric and in particularly volumetric storage capacities, as well as their broad size distribution, which margins their utilization in applications where a specific pore size is necessary. Furthermore, sufficient gas diffusion kinetics is especially important in gas separation or filtration due to limited contact time between adsorbent and adsorbate within these processes. Herein, hierarchical materials offer the opportunity for fast diffusion pathways with bigger meso-/macropores and high working capacities with micropores. In comparison, the polymer-based ordered-mesoporous silicon carbide-derived carbon (OM-SiC-CDC) consists of hierarchical micro- and mesopores, which leads to high gravimetric capacities and fast adsorption kinetics. Furthermore, OM-SiC-CDC has remarkable storage capacities for methane, *n*-butane, and hydrogen.<sup>[55]</sup>

### **1.6.1.2 Modulation of Host-Guest Interactions in Gas Adsorption**

*Which parameters are crucial for selective gas adsorption?*

The adsorption processes of porous materials that are designed especially for CO<sub>2</sub> gas storage at high pressures are mainly based on large micropores with predominant adsorbate-adsorbate interactions. In order to achieve selective capture of CO<sub>2</sub> at low relative pressures (for example CO<sub>2</sub> over other compounds present in air or in flue gas), strong adsorbent-adsorbate interactions and thus a high chemical affinity of the adsorbent towards CO<sub>2</sub> are crucial due to low CO<sub>2</sub> concentrations. Two inherent structure-related properties of porous carbon materials

can be engineered to optimize CO<sub>2</sub> selectivity, namely: pore size (corresponds to kinetic control) and polarizability (corresponds to thermodynamic control).<sup>[11]</sup>

The kinetic control is composed of the modulation of the pore size that should be apparent in high amount in the porous material. The optimal pore size is in the ultramicropore range (0.5–0.7 nm or even below), because of a strong van der Waals interaction between pore walls and CO<sub>2</sub>, which is leading to a larger adsorption potential for CO<sub>2</sub>.<sup>[125]</sup> This effect is less strong in supermicropores (0.7–2 nm) or mesopores (>2 nm). In general, the shape of a CO<sub>2</sub> adsorption isotherm should be rather convex and upwards-directed, because the crucial point for selective CO<sub>2</sub> capture from flue gas at ambient temperature is at pressures around 0.1–0.2 bar CO<sub>2</sub> (**Figure 6**).<sup>[132]</sup> In this context, it has to be considered that a smaller pore size also increases the adsorption potential regarding O<sub>2</sub> and H<sub>2</sub>O. An optimal isosteric heat of adsorption ( $Q_{st}$ ) is around ~35–50 kJ mol<sup>-1</sup> to favorably bind CO<sub>2</sub>. Below this lower limit, weak binding usually leads to low capacity. Whereas, above this upper limit, the cycling process gets energy intensive, and is thus resulting in additional heat needed in a CO<sub>2</sub> capture/release cycle.<sup>[125]</sup>

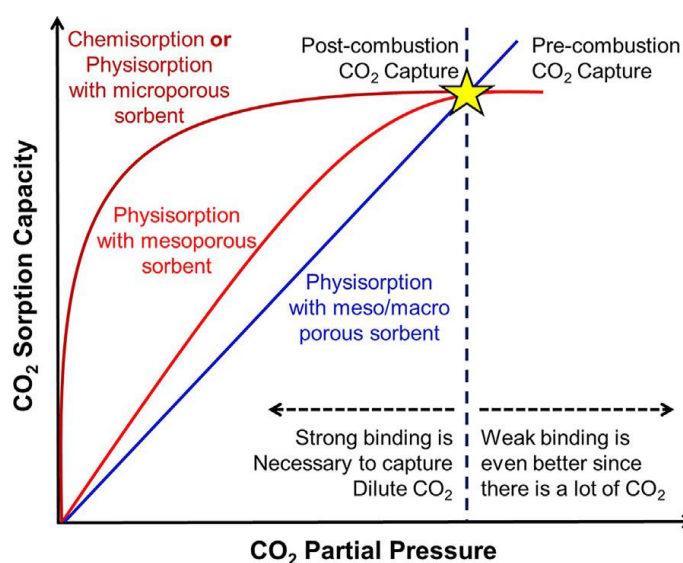


**Figure 6:** Different CO<sub>2</sub> sorption isotherms with similar uptake at 1 bar illustrate different working capacities for CO<sub>2</sub> adsorption at a relative pressure of 0.1 (adapted from reference<sup>[132]</sup>).

In an extreme case, the pore size of a material can be engineered that the pores are only accessible for one specific component out of a gas mixture. This principle is called “molecular sieving effect”, and is for example widely applied for the removal of H<sub>2</sub>O from organic solvents. In the field of CO<sub>2</sub> adsorption, it takes advantage of the kinetic diameter of CO<sub>2</sub> (0.330 nm), which is smaller than the kinetic diameters of N<sub>2</sub> (0.364 nm) or O<sub>2</sub> (0.345 nm).<sup>[133]</sup> In consequence, the selective separation of CO<sub>2</sub> from flue gas can occur *via* kinetic size exclusion from N<sub>2</sub> and O<sub>2</sub>. Again, H<sub>2</sub>O remains a challenging issue with its even

smaller kinetic diameter of 0.265 nm, as well as a high quadrupole moment, and has thus a competitive adsorption with CO<sub>2</sub>.<sup>[133]</sup> In addition, it has to be considered that the narrower a pore system gets, the more it limits the gas diffusion into the pores and the slower are the adsorption kinetics. To overcome diffusion limitations, the particle size of the adsorbent can be downsized or additional pores bigger in size can be introduced to enhance the gas transport, which will on the other hand decrease the selectivity. Van der Waals interactions alone are not discriminative enough to achieve high CO<sub>2</sub> selectivity, and thus kinetic control has to be maximized as long as high selectivity is the major goal.

The second approach to enhance CO<sub>2</sub> selectivity is to modify the polarizability of the adsorbent. This can be realized by the implementation of specific chemical interactions between adsorbents and adsorbates. Physisorption is based on weak van der Waals interactions between pore walls and adsorbate. To efficiently capture an adsorbate, additional stronger interactions such as hydrogen bonds or dipole-dipole interactions have to be introduced. A common approach is to functionalize the adsorbents with polar sites, such as polar functional groups, polar atoms, or ions within the material.

It was found that especially nitrogen-containing porous carbon materials exhibit outstanding adsorption properties for polar and/or acidic gas molecules. Nitrogen-doped ACs showed a significant difference in the H<sub>2</sub>O vapor sorption isotherm compared to AC without nitrogen-doping (**Figure 7a**).<sup>[75]</sup> The nitrogen-doped AC exhibits a convex-shaped isotherm and a higher adsorption capacity, whereas the pristine AC is concave-shaped at the onset point of adsorption. The reason is most likely the higher polarity (and thus stronger interactions between carbon materials and polar H<sub>2</sub>O molecules) in form of pyridinic nitrogen (as negative charge) or graphitic nitrogen (as positive charge). High CO<sub>2</sub> adsorption capacities were reported for nitrogen-doped microporous carbons with 5.7–6.4, 3.1–3.3, and 2.4–2.5 mmol g<sup>-1</sup> depending on the measurement temperature of 196, 273, and 298 K, respectively.<sup>[134]</sup> The nitrogen-doping of mesoporous carbon membranes leads to highly selective gas permeance of CO<sub>2</sub>/N<sub>2</sub>.<sup>[135]</sup> Significant nitrogen content in carbon materials contributes to the CO<sub>2</sub> capture abilities, as shown by a higher isosteric heat of CO<sub>2</sub> adsorption (**Figure 7b**).<sup>[136]</sup>

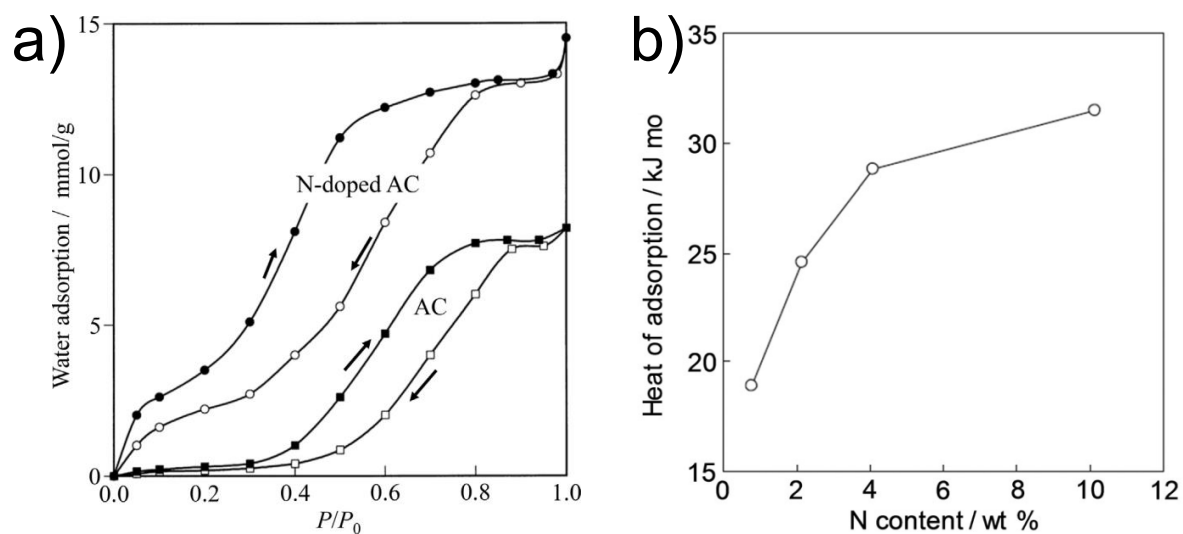


**Figure 7:**  $H_2O$  vapor physisorption isotherms of N-doped and non-doped ACs (a);<sup>[75]</sup> nitrogen-dependent change in isosteric heat of  $CO_2$  adsorption of N-doped polypyrrole-based porous carbons at a surface coverage of  $\sim 0.6 \text{ mmol g}^{-1}$  (b).<sup>[136]</sup> ((a) adapted from reference<sup>[75]</sup>, (b) adapted from reference<sup>[136]</sup>).

Fundamental aspects as the polarizability and the quadrupole moment of  $CO_2$  (with  $26.3 \times 10^{-25} \text{ cm}^3$  and  $13.4 \times 10^{-40} \text{ C m}^2$ , respectively), which is slightly higher than those for  $N_2$  (with  $17.6 \times 10^{-25} \text{ cm}^3$  and  $4.7 \times 10^{-40} \text{ C m}^2$ , respectively), should be kept in mind.<sup>[137]</sup> Due to the small difference in these values, more polar adsorbents are always attracting both molecules more than less polar adsorbents. The most promising approach is to achieve synergy effects of the binding interactions of the pore size, sufficient diffusion pathways, and a strong polarizing nature of the adsorbents. One impressive  $CO_2$  capture and release system is found in photosynthetically active plants with the enzyme Rubisco (ribulose 1,5-bisphosphate carboxylase/oxygenase) (**Figure 8**), which is the most abundant protein on earth.<sup>[138]</sup> The combination of two tethered capture moieties (that is the Lewis acidic  $Mg^{2+}$  site and the Lewis basic  $NH_2$  group of the lysine, which can beneficially interact with the negatively polarized oxygen atoms and the positively polarized carbon atom in  $CO_2$ ) is employed by nature to trap  $CO_2$  from air at a concentration of around 400 ppm in the presence of  $H_2O$ ,  $O_2$ , and  $N_2$ . This is leading to its outstanding IAST (ideal adsorption solution theory)  $CO_2/O_2$  selectivity of  $\sim 1500$ .<sup>[138]</sup>

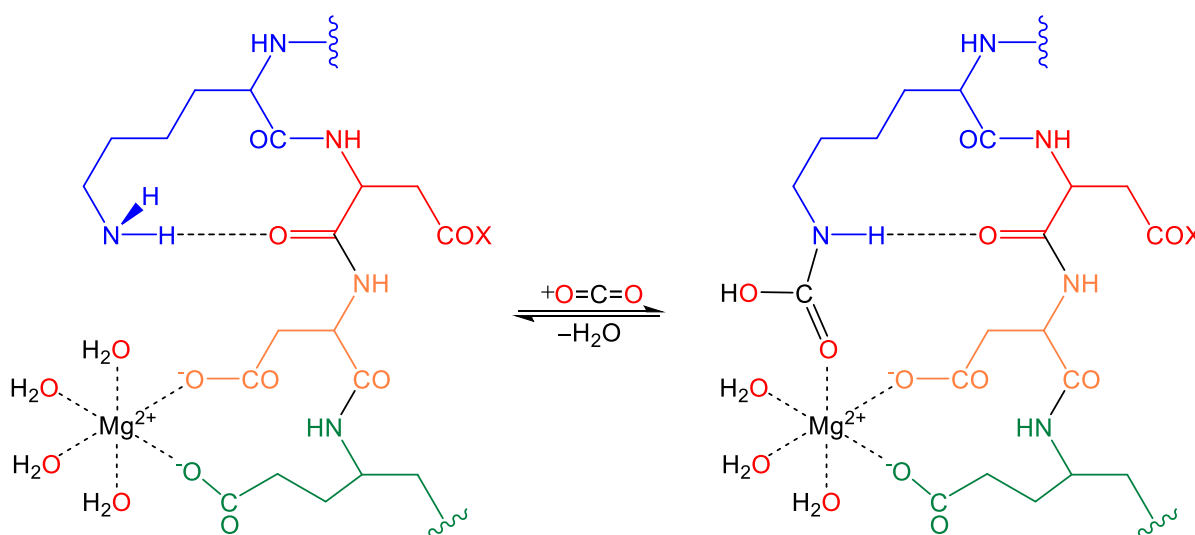


**Figure 8:** The  $\text{CO}_2$  capture system at the active sites of Rubisco between the  $\text{Mg}^{2+}$  and the lysine  $\text{NH}_2$  group (adapted from reference<sup>[138]</sup>).

Impressive synthetic examples with high  $\text{CO}_2$  selectivity are MOFs. Isostructural MOFs (SIFSIX-3-Zn and SIFSIX-3-Cu) constructed by silicon hexafluoride anions ( $\text{SiF}_6^{2-}$ , labeled as SIFSIX), pyrazine units, and unsaturated metal centers (Cu or Zn) result in favorable adsorption kinetics and reversible high  $\text{CO}_2$  uptakes ( $1.24 \text{ mmol g}^{-1}$ ) at low  $\text{CO}_2$  pressures relevant to air capture.<sup>[139, 140]</sup> Extremely high  $\text{CO}_2/\text{N}_2$  selectivities of 2000 and heat of  $\text{CO}_2$  adsorption of  $45\text{--}52 \text{ kJ mol}^{-1}$  touching chemisorption boundaries, are achieved. The synergetic effect of high charge density (thermodynamics, energetics) and optimal pore size (kinetics) led to strong and fast  $\text{CO}_2$  adsorption.<sup>[140]</sup>

### 1.6.2 Sodium-Ion Batteries with Carbon Anode Materials

Besides the use in gas adsorption processes, porous carbon materials play a crucial role in electrochemical energy storage devices. Lithium-ion batteries (LIBs) are the most common kind of rechargeable battery cells found in portable electronic devices and in electrifying transportation (e.g., hybrid electric vehicles and plug-in hybrid electric vehicles).<sup>[141, 142]</sup> The tremendous demands on lithium resources (especially with automotive batteries) will arise as a supply problem due to the limited global lithium resources (20 ppm in the earth cluster).<sup>[143, 144]</sup> Research work has been done in 1970–1980s in parallel to the LIBs with the concept of sodium-ion batteries (SIBs).<sup>[145, 143]</sup> Sodium is an abundant resource (23.600 ppm in the earth crust),<sup>[145, 146]</sup> low in cost,<sup>[147]</sup> and has a suitable redox potential similar to lithium ( $E_{(\text{Na}^+/\text{Na})}^0 = -2.71 \text{ V}$  and  $E_{(\text{Li}^+/\text{Li})}^0 = -3.04 \text{ V}$ ), respectively, versus the standard hydrogen reference electrode).<sup>[147]</sup> Sodium is the element below lithium in the alkaline metal group of the periodic table, and it is not surprising that both elements show similar physicochemical

properties, which results in comparable electrochemical principles of SIBs and LIBs.<sup>[148]</sup> One of the reasons for the stagnant research on SIBs was the lack of suitable anode materials. At any glance, carbonaceous materials were promising candidates for anode materials in LIBs. For example, graphite exhibits as anode a theoretical capacity of  $372 \text{ mA h g}^{-1}$  and a low potential plateau  $\sim 0.1\text{--}0.2 \text{ V}$  (vs  $\text{Li/Li}^+$ ).<sup>[148]</sup> However, sodium is not able to intercalate so easily into graphite layers due to its larger ionic radius (which leads to the formation of  $\text{NaC}_{70}$  with a theoretical capacity of  $31 \text{ mA h g}^{-1}$ ).<sup>[149]</sup> Recently, numerous materials have been explored to be applied as anode for SIBs, such as metal/alloys, metal oxide/sulfide/phosphide, as well as carbonaceous materials (e.g., expanded graphite, graphene, and amorphous carbon materials).<sup>[147]</sup> Amorphous carbon materials can be subdivided into soft and hard carbon materials. The first is usually obtained from pyrolytic aromatic compounds and polymers, whereas the latter is synthesized by pyrolysis of biomass with insufficient aromatic structures (i.e., disordered).<sup>[150]</sup> The metal and alloy suffer from the volume expansion during the charge-discharge process, resulting in poor cycle stability. Low initial coulombic efficiency, large hysteresis, also poor cycle stability is limiting the capability of metal oxide/sulfide/phosphide as anode materials. Various carbon-based anode materials were investigated involving expanded graphite, graphene, carbon spheres/fibers/tubes/sheets, and porous carbons,<sup>[150, 151]</sup> and capacities generally in the range of  $200\text{--}500 \text{ mA h g}^{-1}$  were achieved.<sup>[152]</sup> In consideration of the requirements of commercial batteries, including safety, cycling stability, non-toxic, durability, and low cost, and among the aforementioned materials, especially carbonaceous materials stand out due to stability, abundant resource, and low cost.<sup>[152]</sup>

During the charge process, the  $\text{Na}^+$  ions are migrating from the cathode to the anode and react with the anode materials. Accordingly, during the discharge process, the reverse process occurs with the simultaneous electron transfer in the external circuit to produce electric energy.<sup>[152]</sup> The sodium storage performances of carbon materials are strongly influenced by their microstructure. Especially, hard carbon materials seem to be the most suitable anode materials for sodium-ion storage. The large interlayer distance and amorphous structure of the disordered carbon materials can promote sodium insertion and extraction.<sup>[153, 154]</sup> Three different sodium storage mechanisms of hard carbon materials were proposed with regard to the slope and plateau capacity regions of the curve shape of sodiation/desodiation (**Figure 9a**).<sup>[152]</sup>

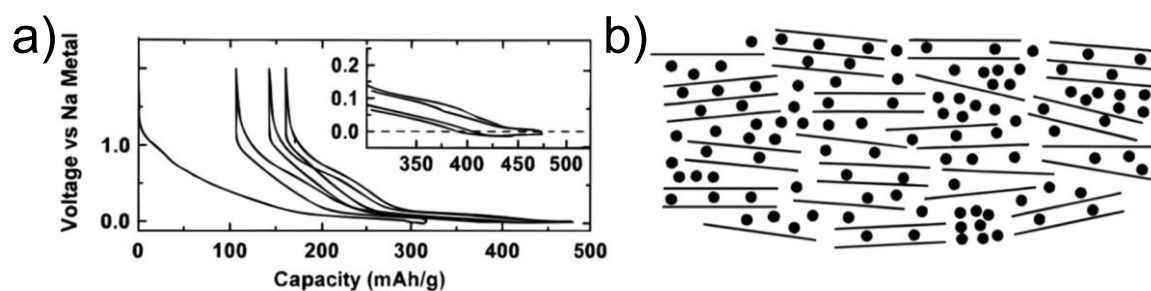


**Figure 9:** Charge-discharge curves of glucose-derived hard carbon in SIBs (a), and “house of cards” model for sodium storage in hard carbon (b). The “house of cards” model is built up by a big amount of randomly stacked microcrystalline carbon layers, several carbon layers are parallel ordered in order to form graphite microcrystals, and others are spread in a disordered fashion to form nanosized micropore areas.<sup>[155]</sup> ((a) and (b) adapted from reference<sup>[155]</sup>).

The first mechanism describes that the slope regions correspond to intercalation/extraction of sodium between carbon layers, according to the so-called “house of cards” model (**Figure 9b**). The plateau region comes from adsorption/deposition of  $\text{Na}^+$  ions in the micropores.<sup>[155]</sup> The second one claims that the slope area arises from absorption of  $\text{Na}^+$  ions on the carbon surface due to active/defect sites and functional groups. The plateau regions result from intercalation/extraction.<sup>[156]</sup> The last one proposes a mechanism without any sodium insertion.<sup>[157]</sup>

A common approach to effectively improve the electrochemical performances of carbon materials is through the modification of the electronic and chemical properties *via* heteroatom-doping.<sup>[158, 159]</sup> In consequence, introduction of heteroatoms (e.g., B, N, S, and P) into carbon anode materials of SIBs can improve the capacity, surface wettability, and electronic conductivity. This, in turn, can favor the charge transfer and electrode/electrolyte interactions.<sup>[160, 161]</sup> In this context, one of the most widely studied heteroatom-doped carbon materials, are nitrogen-doped carbon materials.<sup>[111, 162, 163]</sup> The first reported nitrogen-doped carbon nanofibers exhibited at a current density of  $0.2 \text{ A g}^{-1}$  a capacity of  $134 \text{ mA h g}^{-1}$  after 200 cycles, and at a high current density of  $20 \text{ A g}^{-1}$ , the reversible capacity reached  $73 \text{ mA h g}^{-1}$ .<sup>[164]</sup> 3D Nitrogen-doped graphene foams revealed high charge capacity of  $\sim 1057 \text{ mA h g}^{-1}$  at a current density of  $0.1 \text{ A g}^{-1}$ .<sup>[161]</sup> Free-standing electrospun carbon nanofiber films with high nitrogen content ( $\sim 7 \text{ wt.}\%$ ) showed significant electrochemical performances at a current density of  $0.1 \text{ A g}^{-1}$  and highly reversible capacity of  $\sim 1057 \text{ mA h g}^{-1}$  after 7000 cycles with a capacity retention of 99 %.<sup>[165]</sup>



## 2 Outline

The aim of this thesis is to gain deeper understanding of the structure-related characteristics of nanoporous carbon materials, especially nitrogen-containing nanoporous noble carbon materials, concerning their application in adsorption of different guest species, in particular in gas adsorption. The host-guest interactions in gas adsorption are influenced by the porosity characteristics of the adsorbents, such as pore size (distribution), pore connectivity, , as well as the atomic construction (**Chapter 1.6.1**). Thus, the precise design of a material on a molecular level plays a crucial role to achieve a more profound understanding, as well as enhanced performances in the field of gas adsorption. It is important to provide a facile synthesis pathway to implement a significant amount of homogeneously distributed nitrogen in well-defined structure motives within the carbon materials. This leads to essential changes in their chemical and physical properties, such as polarity, oxidation resistance, electrical conductivity, and acidity/basicity (**Chapter 1.2.1**).

In this context, the condensation of a preorganized organic precursor, hexaazatriphenylene-hexacarbonitrile (HAT-CN), for the synthesis of a set of nitrogen-rich microporous carbon materials will be presented (**Chapter 3.1**). Moreover, the special structure-related properties of these materials and their application in gas adsorption will be elucidated (**Figure 10**). The system of HAT-CN-derived carbon materials will be further examined concerning the enhancement of their CO<sub>2</sub>/N<sub>2</sub> selectivity (**Chapter 3.2**). In this regard, the accurate control of the condensation process of HAT-CN will be utilized to further optimize the nanostructure and the porosity of the resulting carbon materials on a molecular level. Gas adsorption studies on the nitrogen-doped carbon materials using CO<sub>2</sub> and N<sub>2</sub> will point out a potential molecular sieving effect of CO<sub>2</sub> over N<sub>2</sub>.

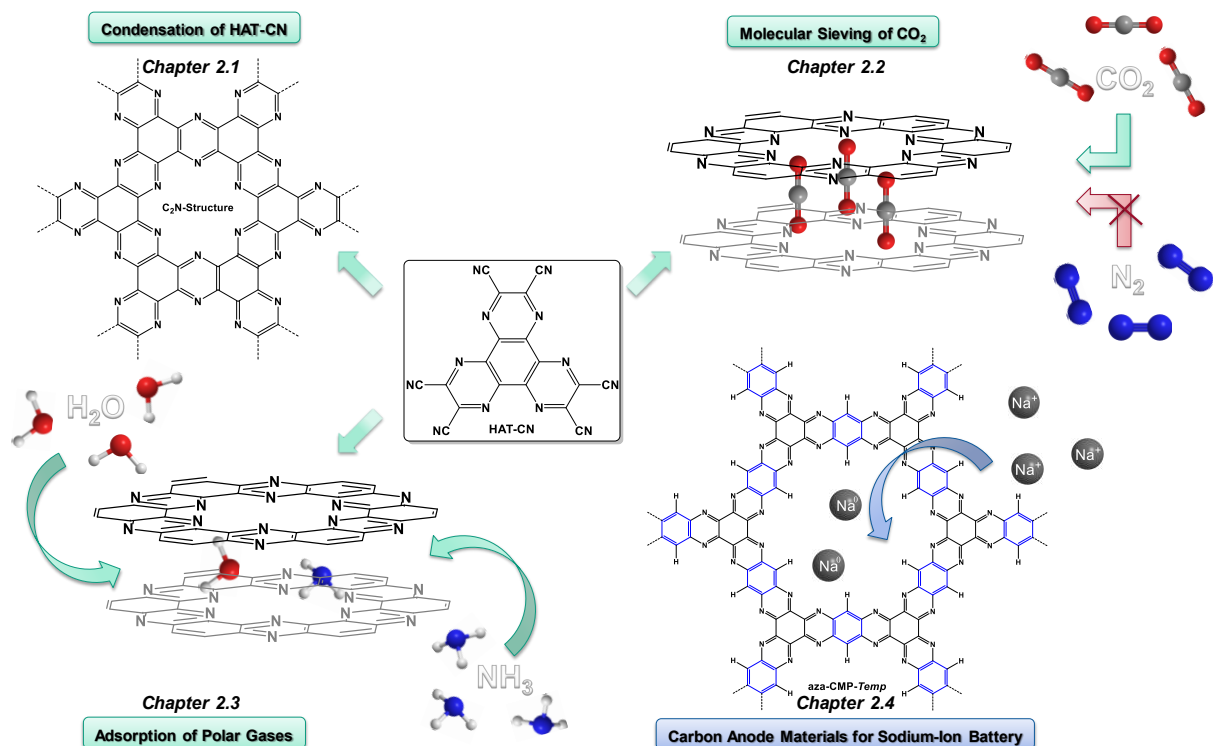


**Figure 10:** Nitrogen-doped carbon materials synthesized in this thesis and their pursued applications in gas adsorption and sodium-ion battery.

The structure-related performances of the nitrogen-doped carbon materials will be further investigated by adsorption using H<sub>2</sub>O vapor and NH<sub>3</sub> gas (**Chapter 3.3**). The combination of these guest molecules and porous adsorbents is widely applied in vapor compression refrigeration systems, and thus this chapter will be featured by gas adsorption studies related to this application. Another set of functional carbon materials, synthesized by using a conjugated microporous polymer as a precursor, will be introduced. In this regard, the beneficial properties of CMPs as precursors will be explained, and the structure-related performances of these functional carbon materials for electrochemical energy storage in sodium-ion battery will be elaborated (**Chapter 3.4**).





## 3 Results and Discussion

### 3.1 Synthesis of Nitrogen-Rich Nanoporous Noble Carbon Materials from a Preorganized Hexaazatriphenylene Precursor\*

#### 3.1.1 Background and State-of-the-Art

Sp<sup>2</sup>-based carbon nanomaterials<sup>[16]</sup> can be engineered in their geometrical structure *via* substitution of graphene six-membered carbon rings by structural defects or distortions (e.g., pentagons or heptagons carbon rings). Carbon materials have the smallest voxel size for chemical construction, and their properties can be adjusted over a wide range by tailoring their atomic framework construction. This leads to a random structural arrangement and finally to a porous carbon framework (**Chapter 1.1**). Besides geometrical structure engineering, carbon-based materials can be further tailored in terms of their electronic and surface atomic structure by heteroatom-doping.<sup>[111, 98]</sup> The incorporation of nitrogen into the carbon framework was explained in **Chapter 1.2**, which leads to nitrogen-doped carbon (NdC) materials with different stoichiometry. Heteroatom-doping makes the conjugated structure much stronger polarizing and can provide specific binding sites, both leading to significantly higher enthalpies of interaction between the adsorbent and the guest species, when compared to ordinary activated carbons. Thus, NdCs have significant advantages over traditional carbon materials in the field of adsorption from gas and liquid phase. For instance, enhanced interaction has been observed in CO<sub>2</sub><sup>[136, 167]</sup> and H<sub>2</sub>O vapor<sup>[168]</sup> gas adsorption, adsorption of ions from solution<sup>[169, 170]</sup> or ionic liquid ions<sup>[171]</sup> for carbons with substantial nitrogen content. In all those cases, heteroatom-doping leads to strong binding of the respective guest species (**Chapter 1.2.1**). In addition to their beneficial host-guest interactions, NdCs are much more “noble” than pristine carbons, that is, they oxidize matter rather than being oxidized due to the very positive working potential of their electrons

---

\* The results of this chapter are used with permission and are published by the author of this thesis as: R. Walczak, B. Kurpil, A. Savateev, T. Heil, J. Schmidt, Q. Qin, M. Antonietti, and M. Oschatz: “Template- and Metal-free Synthesis of Nitrogen-rich Nanoporous Noble Carbon Materials by Direct Pyrolysis of a Preorganized Hexaazatriphenylene Precursor”, *Angewandte Chemie, International Edition* **2018**, *57*, 10765–10770. (Reference<sup>[166]</sup>).

(**Chapter 1.3**).<sup>[92]</sup> NdCs are widely applied as stabilizers for metal catalysts<sup>[172, 173]</sup> or in energy storage applications<sup>[174, 169, 170]</sup> and typically provide beneficial properties as compared to pristine carbon materials obtained by established processes such as carbonization of carbohydrates.

In most cases, these significant advantages of NdCs over pristine carbon materials can only be accomplished if (i) the heteroatom-containing structure motives are well defined, large in number, and tailorable in chemical composition; (ii) the material provides a large surface area to allow for sufficient access to the entire atomic framework (or in other words to maximize the synergistic effect between surface heterogeneity and surface area); and (iii) the materials are free of any unwanted impurities such as metal atoms or metal ions.

One particular class of nitrogen-doped carbon materials with a high homogeneity and regularity throughout the whole framework that requires advanced synthesis approaches are NdCs with a C<sub>2</sub>N-type stoichiometry, as highlighted in **Chapter 1.4**. Recently, the synthesis of such C<sub>2</sub>N carbon materials by applying a prealigned precursor system consisting of oligophenol/ketones and urea mixtures was reported by Fechner *et al.* A salt-templating approach using ZnCl<sub>2</sub> allowed the synthesis of porous NdC products.<sup>[99]</sup> Simultaneously, the synthesis of a 2D layered structure with C<sub>2</sub>N stoichiometry in a bottom-up wet-chemical reaction was published by Baek *et al.*<sup>[100]</sup> HAB and HKH in NMP in the presence of acid (H<sub>2</sub>SO<sub>4</sub>) and consequent heat treatment led to the formation of nitrogen-containing 2D crystals. From a synthetic perspective it seems to be attractive to synthesize such NdC materials from precursors where the nitrogen atoms are already suitably preorganized.<sup>[175]</sup> In such molecules, the architecture of the heteroatom-containing structure motives already exists and their controlled carbonization leads to a more regular condensation towards nitrogen-rich noble carbon materials. This principle is already widely applied to address the above-mentioned point (i), but the introduction of porosity, and thus large available surface area in such materials remains template-based and thereby indirect.

Within this chapter, a template-free synthesis of highly microporous noble carbon materials with large and controllable nitrogen content and a stoichiometry close to C<sub>2</sub>N by direct condensation of the HAT-CN precursor is presented (**Figure 11a**).<sup>[176]</sup>

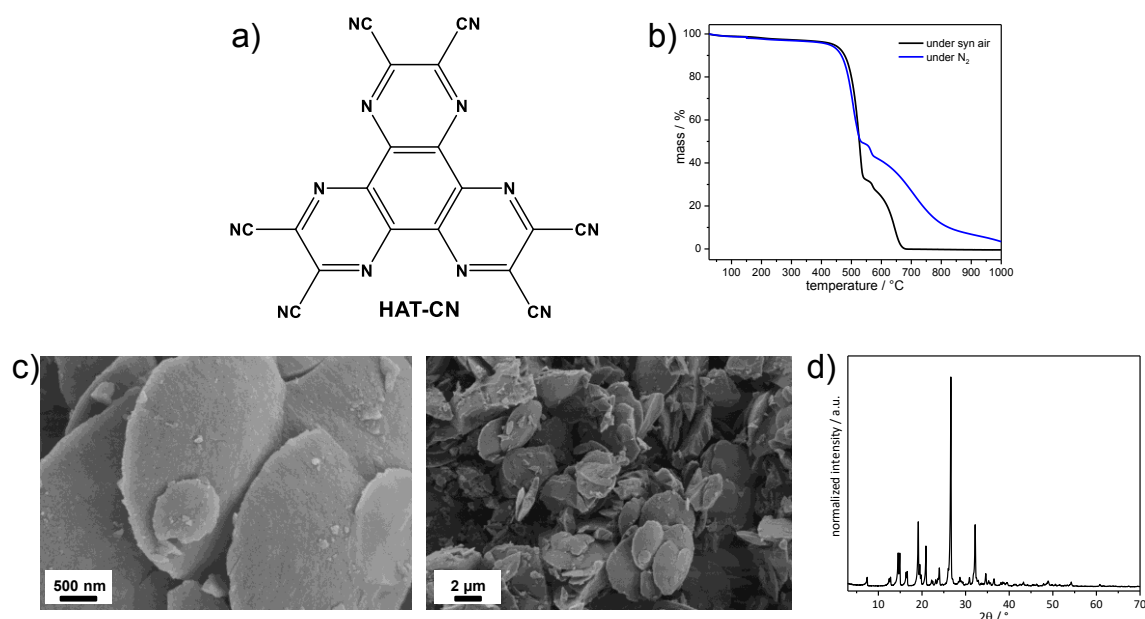


**Figure 11:** Molecular structure (a), thermogravimetric analysis (TGA) under air (black) and nitrogen (blue) atmosphere (b), scanning electron microscopy (SEM) images (c), and powder X-ray diffraction (PXRD) pattern (d) of the HAT-CN precursor used for condensation.

The HAT-CN precursor is an electron-deficient, rigid, planar, aromatic discotic system with an excellent  $\pi$ - $\pi$  stacking ability and remarkable oxidation resistance (**Figure 11b**).<sup>[177]</sup> Especially its strong supramolecular aggregation and the ability to self-assemble into crystalline structures (**Figure 11c** and **Figure 11d**) make it a promising material for the synthesis of noble carbon materials. The direct carbonization of HAT derivatives towards noble carbon materials has not been reported so far. In literature, photoelectron yield spectroscopy of pure HAT-CN determined the HOMO level to be approximately  $-7.50$  eV (against vacuum; corresponds to approximately  $+3.00$  eV against RHE).<sup>[178, 179]</sup> Compounds like HAT-CN being more positive than the oxygen line ( $E^0(\text{O}_2) = +1.23$  V) on the electrochemical scale relative to the RHE, will not be easily oxidized and can arrange in well-ordered oxidation stable carbon materials during carbonization, which is in agreement with the concept of noble carbon materials (**Chapter 1.3**). In other words, HAT-CN is a promising and suitable precursor towards the synthesis of noble carbon materials, which is investigated in detail in the following paragraphs (**Chapter 3.1.2** and **Chapter 3.1.3**), as well as their structure-related porosity characteristics (**Chapter 3.1.4**).

### 3.1.2 Template- and Metal-free Condensation of Preorganized HAT-CN

A series of porous carbon/nitrogen materials was synthesized *via* condensation of HAT-CN under N<sub>2</sub> flow (**Figure 11a** and **Figure 11b**). The nitrogen-rich (C<sub>18</sub>N<sub>12</sub>) organic molecule was heated to 550, 700, 850, or 1000 °C without any pre-treatment, and the resulting

condensed C-HAT-CN-X materials are labelled according to their condensation temperature.<sup>[166, 180]</sup> Nanoporous nitrogen-doped carbon materials can hence be obtained without the use of any template during synthesis, and no additional washing step after condensation is necessary due to the absence of residual inorganic porogen. Because already the HAT-CN precursor is fully  $sp^2$ -hybridized and free of hydrogen, further condensation can only take place by elimination of the nitrile groups, and thus is solely based on  $\pi$ -electrocyclic rearrangements, as proposed in **Figure 12**. Indeed, the investigation of the HAT-CN condensation mechanism by thermal analysis (under helium flow) coupled with mass spectrometry (TGA-MS) reveals that the main elimination products are CN-type species resulting from the splitting-off of nitrile groups from HAT-CN monomers (**Figure S 4**).

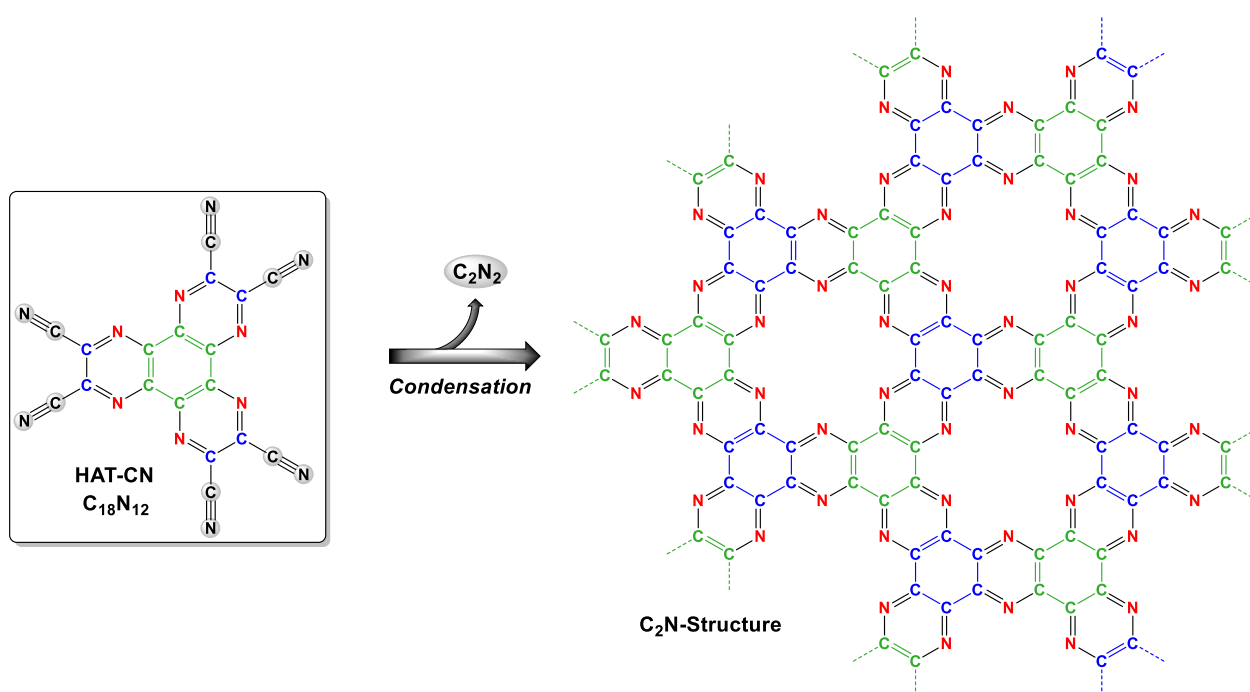


**Figure 12:** Idealized model for the proposed formation of a C<sub>2</sub>N structure by condensation of HAT-CN precursor.<sup>[166, 180]</sup>

### 3.1.3 Structural Characterization of the HAT-CN-derived Carbon Materials

The structural characterization of the as-synthesized C-HAT-CN-X materials can give insights into the condensation process. The as-synthesized materials show comparable microscale morphology to the primary HAT-CN crystals, that is, they appear as an accumulation of small flat plates exhibiting a smooth surface (**Figure 13a–d**). Thus, the macrostructure induced by the pre-organization of HAT-CN can be transferred to the condensed products. At higher temperature, condensation causes fracturing and several gaps (~100–200 nm in size) open evenly over the surface of the pallets (**Figure 13e** and **Figure**

13f). The fracturing of the flat plates reveals their set-up from small primary spheres which are randomly packed.

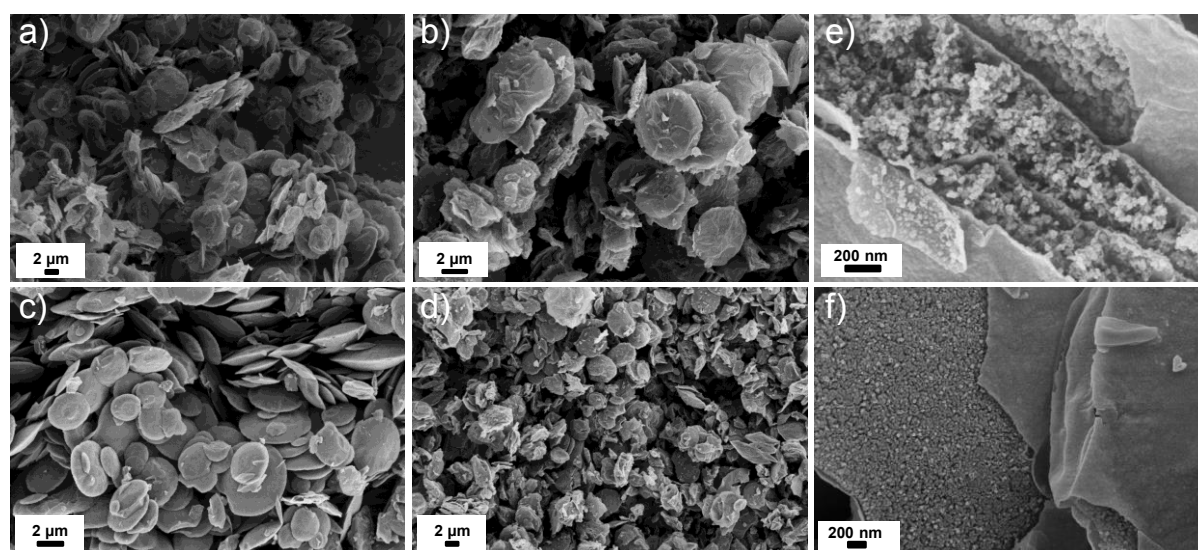


**Figure 13:** SEM images of C-HAT-CN-550 (a), C-HAT-CN-700 (b) and (e), C-HAT-CN-850 (c) and (f), and C-HAT-CN-1000 (d).

The results of the C/H/N elemental analysis (EA), energy-dispersive X-ray (EDX) spectroscopy, and the elemental compositions obtained by X-ray photoelectron spectroscopy (XPS) analysis show that lower synthesis temperatures results in higher nitrogen content in the C-HAT-CN-X materials (**Table 1**).

**Table 1:** EA, EDX, XPS, and Raman spectroscopy data summary, as well as experimental yield of C-HAT-CN-550, C-HAT-CN-700, C-HAT-CN-850, and C-HAT-CN-1000.

Material	C / at.%			N / at.%			O / at.%			$I_D/I_G$	Yield / %
	EA	EDX	XPS	EA	EDX	XPS	EA	EDX	XPS		
C-HAT-CN-550	48.3	58.9	64.0	29.4	39.7	32.7	-	1.4	3.3	0.58	50
C-HAT-CN-700	47.7	61.2	67.0	24.3	37.1	29.8	-	1.7	3.2	0.91	33
C-HAT-CN-850	51.3	62.4	69.9	20.0	35.9	24.6	-	1.7	4.7	1.37	27
C-HAT-CN-1000	67.8	96.5	90.1	4.9	-	7.4	-	3.5	2.6	1.80	25

Nitrogen contents of 24.3 at.% (EA) and 29.8 at.% (XPS) suggest a nearly perfect  $C_2N$ -type stoichiometry in C-HAT-CN-700, as previously reported by Fechler *et al.*<sup>[99]</sup> and Baek *et al.*<sup>[100]</sup> Thus, the stoichiometric composition pre-dictated by HAT-CN can be transferred to the  $C_2N$  products due to the controlled condensation mechanism. The homogeneous distribution of carbon and nitrogen is shown in the EDX mapping patterns independent of the

synthesis temperature (**Figure 14a–d**). The uniform porous nanostructure after HAT-CN condensation can be observed in high-resolution transmission electron microscopy (HRTEM; **Figure 14e–h**) images of C-HAT-CN-550 and C-HAT-CN-700. For C-HAT-CN-850 and C-HAT-CN-1000, structures are characterized by concentric spherical graphitic shells, which are interpenetrated and overlapping, thus revealing a structural rearrangement after condensation at higher temperatures due to transition from a noble carbon to a rather graphitic carbon phase poor of heteroatoms.

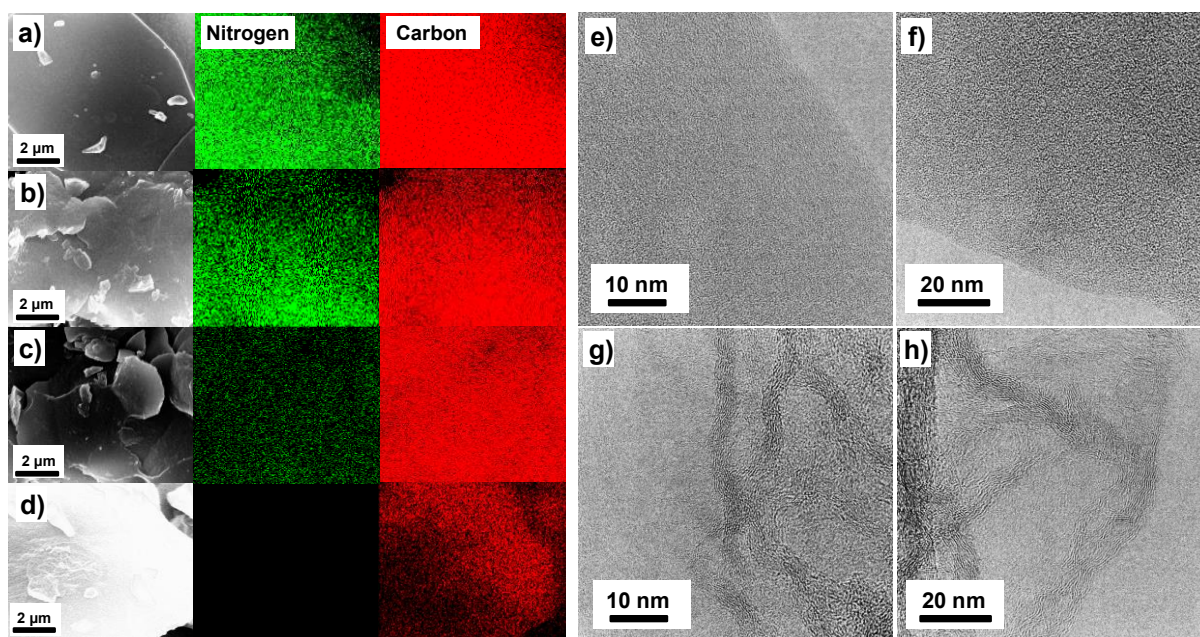


**Figure 14:** SEM images with elemental mapping (a–d) of N (green), and C (red), as well as HRTEM images (e–h) of C-HAT-CN-550 (a and e), C-HAT-CN-700 (b and f), C-HAT-CN-850 (c and g), and C-HAT-CN-1000 (d and h).

XPS spectra (**Figure S 5a–d**) were recorded to identify the different bonding characteristics of nitrogen and carbon atoms in these materials. Deconvolution of the N1s line scans (**Figure 15a–d**, **Table S 3**, and **Table S 4**) reveals the presence of cyano and pyrazine groups, corresponding to the signals at binding energies of  $\sim 398$  eV and  $\sim 399$  eV (i.e., electron-rich “anionic” nitrogen with weakly bonded electrons). The peaks at  $\sim 400$ – $401$  eV and  $\sim 402$ – $403$  eV correspond to quaternary nitrogen atoms and oxidized nitrogen atoms, respectively, (i.e., “cationic” nitrogen with strongly bonded electrons). The ratio between nitrogen atoms from cyano and pyrazine groups and quaternary nitrogen atoms can be controlled by the synthesis temperature since the decrease of nitrogen content at higher temperatures is mainly on the expense of cyano and pyrazine groups as present in HAT-CN (**Table S 3** and **Table S 4**). The amount of quaternary nitrogen atoms with higher binding energy in the nitrogen-doped carbon material increases at medium condensation temperatures and decreases again at  $1000$  °C. In contrast, the cyano and pyrazinic nitrogen content of the carbon materials

decreases continuously from 550 °C (25.5 at.%) to 1000 °C (1.8 at.%). Deconvolution of the C1s spectra (Figure S 6a–d, Table S 3, and Table S 4) reveals a peak at ~284 eV that belongs to electron-rich graphitic C=C carbon atoms, while two peaks at ~285 eV and ~286 eV correspond to electron-poor carbon atoms bonded to sp<sup>2</sup>-hybridized nitrogen atoms. The peak at ~289–290 eV can be assigned to oxidized carbon atoms. All single peaks, as well as the full line scan, are shifted to lower binding energy with increasing synthesis temperature, indicating a decrease of the noble character and less positive working potential of the electrons, i.e., the nobility is lost when heating to too high temperatures. Accordingly at 850 °C and 1000 °C common nitrogen-doped carbon materials are realized, while the most noble carbon materials of C<sub>2</sub>N-type are obtained at temperatures of around 550 °C or 700 °C.

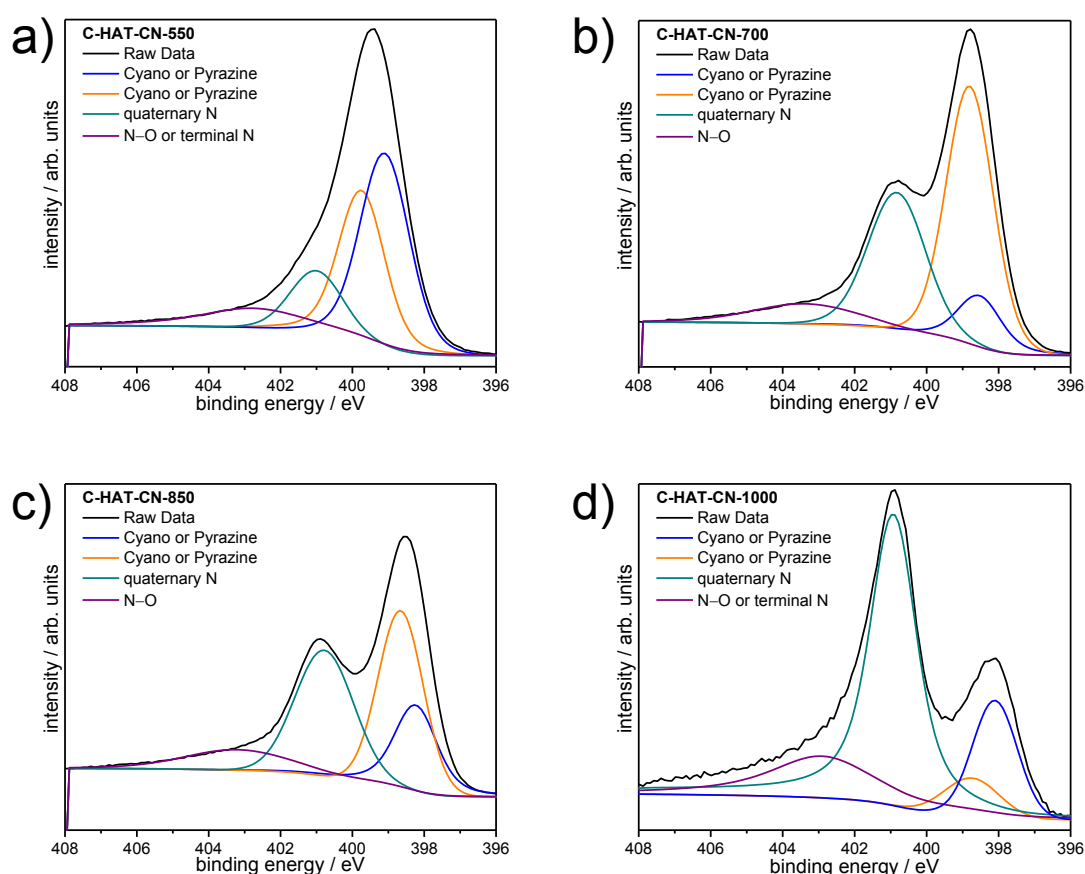


**Figure 15:** Fitted N1s XPS line scans of C-HAT-CN-550 (a), C-HAT-CN-700 (b), C-HAT-CN-850 (c), and C-HAT-CN-1000 (d).

The on-going development of a nitrogen-free graphitic-like carbon phase at higher synthesis temperature can be seen by the growing contribution of C=C bonds. In accordance to the results of the N1s spectra, the peak corresponding to sp<sup>2</sup>-nitrogen peak significantly decreases at higher condensation temperature. All in all, the XPS measurements underline the

comparably precise control over the atomic structure and the high nitrogen content that can be achieved in such nitrogen-doped carbon materials made from HAT-CN.

PXRD measurements (**Figure S 7**) confirm the absence of crystalline inorganic impurities and indicate an amorphous structure as it is typical for high surface area carbons such as the C-HAT-CN-X materials due to the absence of sharp peaks that correspond to graphitic stacking. Thus, such materials are characterized by a high local atomic ordering, but on the other side they do not have a distinct long-range ordering. However, the increasing intensity of the peak between 25 and 30 ° 2 $\theta$  suggests the reoccurrence of graphitic stacking at higher condensation temperatures in agreement with HRTEM investigations.

Raman spectroscopy (**Figure 16a** and **Figure S 8a–d**) is another useful tool to characterize sp<sup>2</sup>-based carbon structures by their so-called disordered (D) and graphite (G)-like bands with varying intensity, position, and width. It should be noted that the standard interpretation of Raman spectra as applied for pristine carbons cannot be strictly applied to nitrogen-containing carbons (as nitrogen-doping is a source of vibrational dissymmetry), but some interesting information on the progress of condensation can still be derived. The spectra have been fitted with a three-band model including the D-band (breathing mode of sp<sup>2</sup>-carbon atoms in aromatic rings), G-band (sp<sup>2</sup>-carbon organized in chains or rings), and the D2-band (assigned to *trans*-polyacetylene-like chains at layer edges). In this series of samples, the  $I_D/I_G$  ratio increases constantly from 0.58 to 1.80 with increasing synthesis temperature (**Table 1**) due to the favored organization of sp<sup>2</sup>-bonded carbon atoms in six-rings and a smaller amount of substitutional nitrogen atoms, that is, the on-going formation of a phase of pristine carbon. This, in combination with the cationic nitrogen atoms, will lead to a higher electrical conductivity of the samples prepared at higher temperatures. Higher carbon symmetry for the samples synthesized at higher temperatures is also suggested by the decreased intensity of the shoulder D2-band.

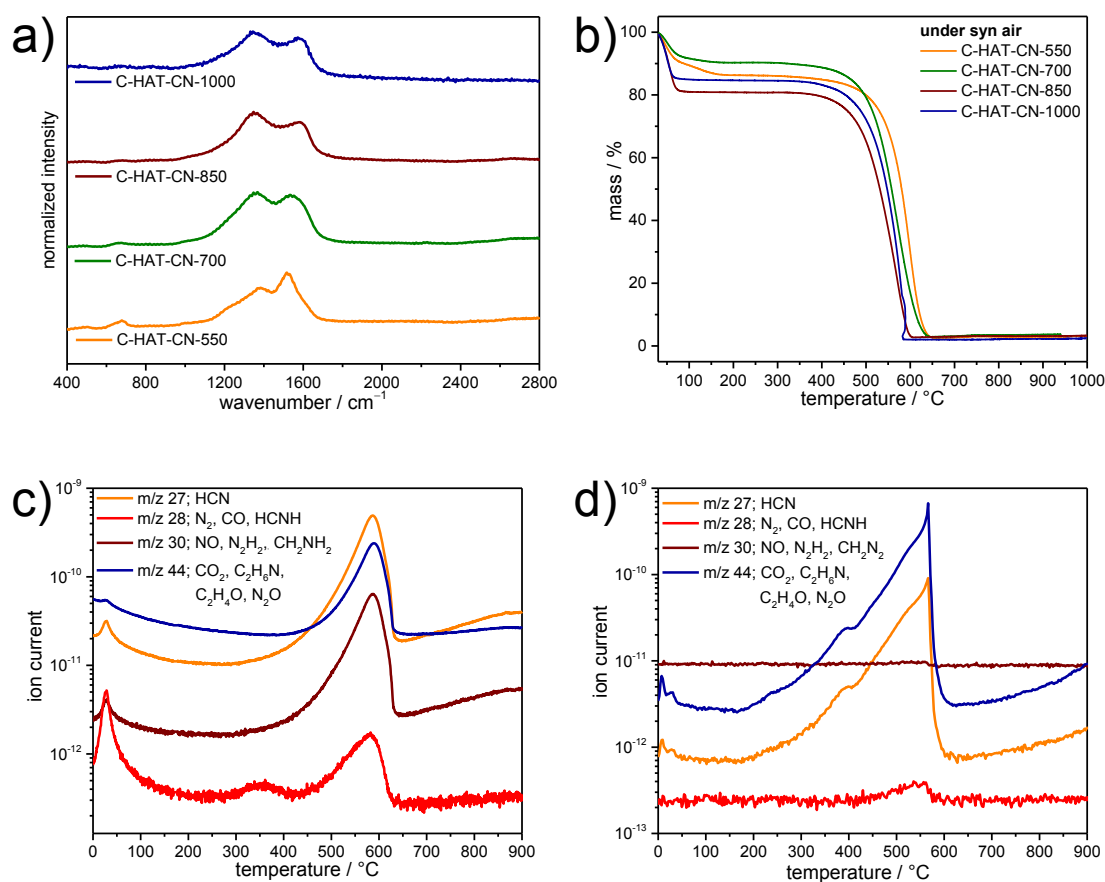


**Figure 16:** Raman spectra of C-HAT-CN-550, C-HAT-CN-700, C-HAT-CN-850, and C-HAT-CN-1000 (a), TGA measurements of C-HAT-CN-550, C-HAT-CN-700, C-HAT-CN-850, and C-HAT-CN-1000, measured under synthetic air with a heating rate of  $5 \text{ K min}^{-1}$  (b), and TGA-MS measurements of C-HAT-CN-550 (c) and C-HAT-CN-1000 (d) under synthetic air with heating rates of  $2.5 \text{ K min}^{-1}$ .

TGA under synthetic air (**Figure 16b**) show that C-HAT-CN-550 – the noblest compound with the highest nitrogen content – reveals the highest onset of the decomposition temperature in air of  $\sim 550 \text{ }^{\circ}\text{C}$ . The increase in onset temperature for the materials prepared at lower temperatures can be explained by the near-perfect  $\text{C}_2\text{N}$  stoichiometry and absence of a free carbon phase. Thus, C-HAT-CN-550 has the highest oxidation resistance. TGA-MS measurements (**Figure 16c** and **Figure 16d**) show that this sample shows a typical feature of noble carbons, which is its thermal decomposition into stable monomers rather than oxidation. Carbon-nitrogen compounds, such as HCN,  $\text{N}_2$ , and  $\text{N}_2\text{H}_2$  are the main products of sublimation, whereas  $\text{CO}_2$  is only a minor reaction product. In contrast, C-HAT-CN-1000 has a large contribution of free carbon and is thus combusted to  $\text{CO}_2$  while the remaining nitrogen is released as HCN. The high stability of the HAT-CN precursor leads to a thermal stability of the noble carbon structure which cannot be achieved by utilization of classical carbon precursors such as carbohydrates or biomaterials.

### 3.1.4 Structure-related Physisorption Properties of the HAT-Derived Carbon Materials

Argon (Ar) physisorption isotherms of the C-HAT-CN-X materials recorded at 87 K (**Figure 17a** and **Figure S 9**) are type Ia isotherms according to the IUPAC classification<sup>[26]</sup> with a large uptake of gas at low relative pressure and no further adsorption at  $p/p_0 = 0.1-0.9$ . The isotherms thus reveal the practically exclusive microporous character of the HAT-CN-derived carbon materials. In spite of the absence of any inorganic porogen, these materials provide high (multi-point) Brunauer-Emmett-Teller ( $0.005 < p/p_0 < 0.05$ ) specific surface areas ( $SSA_{\text{BET}}$ ; **Figure S 10a-d**) in the range of  $\sim 600-800 \text{ m}^2 \text{ g}^{-1}$ .  $SSA_{\text{BET}}$  determined by the quenched solid density functional theory (QSDFT) method are even slightly higher ( $\sim 1000-1150 \text{ m}^2 \text{ g}^{-1}$ ; **Table 2** and **Figure S 11**). Solely the condensation of the initially non-porous HAT-CN crystals ( $SSA_{\text{BET}} \sim 4 \text{ m}^2 \text{ g}^{-1}$ ) is responsible for the development of significant microporosity, which can be regarded as “structural”, i.e., typical for the geometry and angularity of the poly-condensed framework. This can also be seen in the structure of  $\text{C}_2\text{N}$ . With increasing condensation temperature, micropores are enlarged, and this is leading to the slight increase of micropore volume (**Figure 17b** and **Figure 17c**, **Table 2**). In particular, a large volume of accessible microporosity is created by condensation in the 550–700 °C regimes due to more well-defined arrangement and stacking in the C-HAT-CN-700 as supported by the rather open microstructure in HRTEM images (**Figure S 12a-d**). The Ar uptake at  $p/p_0 > 0.9$  is likely due to adsorption on the external surface of the small bullets within the flakes. This leads to a certain hierarchy into the pore system of the C-HAT-CN-X materials as well.

**Table 2:** Ar (87 K) and  $\text{CO}_2$  (273 K) physisorption data summary of C-HAT-CN-550, C-HAT-CN-700, C-HAT-CN-850, and C-HAT-CN-1000.

Material	$SSA_{\text{BET}} / \text{m}^2 \text{ g}^{-1}$	$SSA_{\text{QSDFT}} / \text{m}^2 \text{ g}^{-1}$	$V_{\text{CO}_2 (<1.5 \text{ nm})} / \text{cm}^3 \text{ g}^{-1}$	$V_{\text{Ar} (<2 \text{ nm})} / \text{cm}^3 \text{ g}^{-1}$
C-HAT-CN-550	627	1013	0.28	0.24
C-HAT-CN-700	785	1182	0.33	0.30
C-HAT-CN-850	814	1137	0.30	0.31
C-HAT-CN-1000	801	1148	0.32	0.31

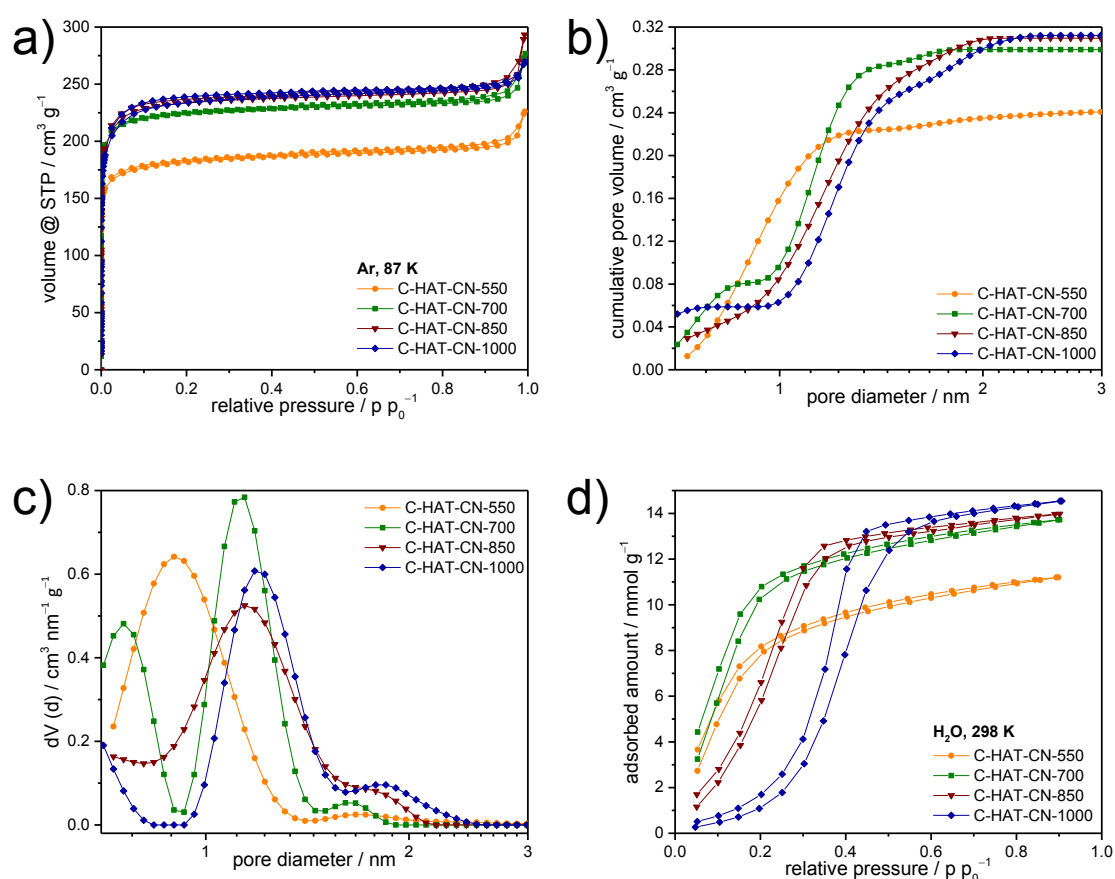


**Figure 17:** Ar physisorption isotherms (87 K) (a), corresponding cumulative (b) and differential (c) pore size distribution plots calculated with QSDFT (Ar on carbons with cylindrical/sphere pores at 87 K, adsorption branch kernel), and H<sub>2</sub>O vapor physisorption isotherms at 298 K (d) of C-HAT-CN-550, C-HAT-CN-700, C-HAT-CN-850, and C-HAT-CN-1000.

Due to their strongly polarizing surface structure in combination with narrow microporosity, the porous C<sub>2</sub>N materials show very high H<sub>2</sub>O vapor adsorption capability even at relative pressures below  $p/p_0 = 0.2$  (6000 ppm). All isotherms are of type I (Figure 17c). Considering the accessible pore volume of 0.35 cm<sup>3</sup> g<sup>-1</sup> (calculated by addition of the CO<sub>2</sub> pore volume below 1.5 nm and the Ar pore volume above 1.5 nm), the uptake (10.22 mmol g<sup>-1</sup>) of C-HAT-CN-700 translates to a density of 17–18 H<sub>2</sub>O molecules per nm<sup>3</sup>. In other words, the density of H<sub>2</sub>O would be more than 0.5 cm<sup>3</sup> g<sup>-1</sup> at a concentration of only 6000 ppm. To our knowledge, comparable strong affinity of carbonaceous structures to H<sub>2</sub>O molecules is so far only reported for a few highly nitrogen-doped materials produced by rather sophisticated methods using metal salts, solvents, and more synthesis steps.<sup>[168, 181]</sup> The packing density in the HAT-CN-derived samples is, however, still about 50 % higher, which is likely caused by their significantly higher nitrogen content at lower oxygen contribution and even more narrow micropores. A polar molecule such as H<sub>2</sub>O will find thermodynamically favored adsorption spots by interaction with electron-rich nitrogen atoms and electron-deficient carbon atoms as

present in C<sub>2</sub>N. The H<sub>2</sub>O vapor adsorption capacity of C-HAT-CN-550 is a bit lower at  $p/p_0 = 0.2$ , which presumably is caused by its lower microporosity and thus lower adsorption capacity in spite of its even higher affinity towards H<sub>2</sub>O due to the higher nitrogen content. With the increase of the condensation temperature the onset points of H<sub>2</sub>O vapor adsorption shift to higher relative pressures and the presence of a hysteresis in case of the nitrogen-poor C-HAT-CN-1000 shows the transition of the H<sub>2</sub>O adsorption mechanism to the one that is typical for microporous carbon materials with less polar sites. The comparable uptake of the materials produced at 700, 850, and 1000 °C and the slightly lower saturation volume of C-HAT-CN-550 are well in line with the pore volume trends observed in Ar physisorption experiments.

The strong polarization of gas molecules by the C-HAT-CN-X materials is also obvious in CO<sub>2</sub> adsorption experiments at 273 K (**Figure 18a**). Due to their higher nitrogen content, C-HAT-CN-550 and C-HAT-CN-700 show a CO<sub>2</sub> physisorption isotherm with a rather convex shape due to a high affinity to CO<sub>2</sub> at low pressure and thus very strong adsorption. Their uptake at 1 bar (5.09 mmol g<sup>-1</sup> for C-HAT-CN-550, 5.34 mmol g<sup>-1</sup> for C-HAT-CN-700) may not appear outstanding as such but in view of the low total pore volume, the volume of adsorbed CO<sub>2</sub> is very high. For microporous carbons without significant heteroatom content, the pore volume to achieve such high uptake must be around twice as high – even when the pore size is optimized for CO<sub>2</sub> adsorption.<sup>[182]</sup> Accordingly, thermal response measurements with the InfraSORP technique<sup>[183, 184]</sup> of CO<sub>2</sub> adsorption on the HAT-CN-derived carbon materials at 298 K and 1 bar (**Figure 18b**) show mass- and pore-volume-related thermal response peak areas between 22 and 41 mg<sup>-1</sup> cm<sup>-3</sup>. This is significantly higher than for microporous carbon materials with comparable pore size but without heteroatom functionalization.<sup>[185]</sup> This further indicates the very strong affinity and high binding enthalpy of HAT-CN-derived carbon materials to CO<sub>2</sub>.

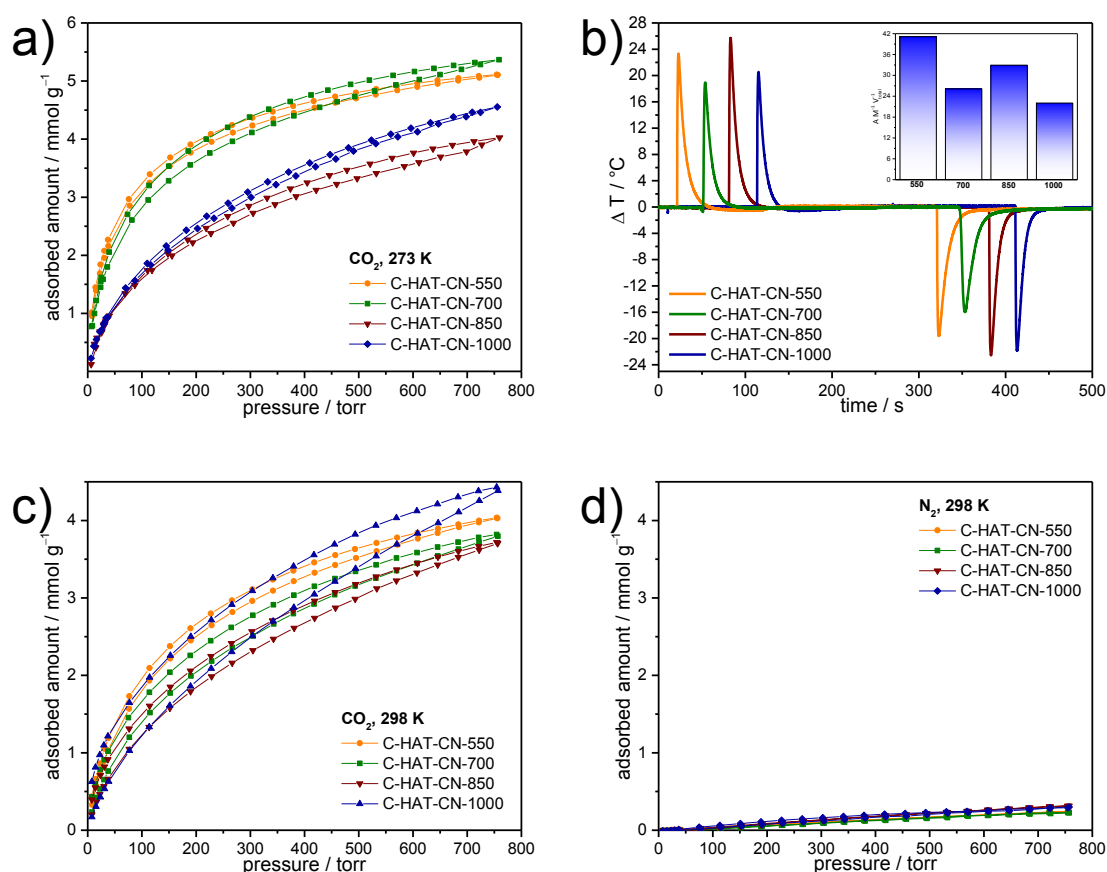


**Figure 18:**  $\text{CO}_2$  physisorption isotherms at 273 K (a), thermal response measurements of  $\text{CO}_2$  adsorption/desorption (1 bar, 298 K) with inset: Mass-related thermal response peak ( $A m^{-1}$ ) of the adsorption peak normalized by the  $V_{\text{total}}$  (b),  $\text{CO}_2$  physisorption isotherms at 298 K (c), and (d)  $\text{N}_2$  physisorption isotherms at 298 K of C-HAT-CN-550, C-HAT-CN-700, C-HAT-CN-850, and C-HAT-CN-1000.

C-HAT-CN-550 shows a  $\text{CO}_2$  uptake of  $3.24 \text{ mmol g}^{-1}$  at 273 K and  $p = 0.15 \text{ bar}$ . This value is in the range of the leading materials for  $\text{CO}_2$  capture which often have far higher micropore volumes.<sup>[11]</sup> Initially one could now assume that these HAT-CN-derived carbon materials are attractive materials for  $\text{CO}_2$  capture at low concentrations, e.g., for filtration of the molecule from flue gases. At 298 K and a  $\text{N}_2/\text{CO}_2$  ratio of 90/10, which are benchmark conditions for this application, the selectivity of C-HAT-CN-550 and C-HAT-CN-700 is 63.8 and 53.6, respectively (Figure 18c and Figure 18d). These values are very competitive, but not exceedingly high, and the likely reason for this is that the pores are still large enough to host significant amounts of  $\text{N}_2$ . Due to its significant quadrupole moment it will be attracted by the strong polarization inside the C-HAT-CN-X materials in a comparable way as  $\text{CO}_2$  as it was pointed out in a recent review article.<sup>[11]</sup> In other words, these materials are not really attractive for  $\text{CO}_2$  selective capture – especially if the similar high affinity to  $\text{H}_2\text{O}$  is taken into consideration, which will lead to less selective  $\text{CO}_2$  capture under real world conditions.

The strong CO<sub>2</sub> binding is more attractive for the activation of the molecule with regard to its catalytic conversion rather than its selective capture in the presence of other gases. Preliminary tests of the C-HAT-CN-700 in electrocatalytic CO<sub>2</sub> reduction (**Figure S 13**) show that there is a significant current enhancement in CO<sub>2</sub>-saturated solution in comparison to N<sub>2</sub>-saturated solution indicating its high catalytic activity.

To summarize the first chapter, a template-free synthesis approach towards microporous noble carbon materials with almost perfect C<sub>2</sub>N-type stoichiometry by controlled condensation of preorganized HAT-CN precursor molecule was presented. The significant amount of well-distributed pyrazinic nitrogen in these materials led to high thermal and oxidation stabilities are exceeding those of established porous carbons and outstanding adsorption properties so far only comparable to MOFs or zeolites. This is indicated by the high uptake in the CO<sub>2</sub> and H<sub>2</sub>O vapor physisorption isotherms, due to the high micropore volume and the strong polarization on specific adsorption sites. The precise structural control over the nanostructure of the HAT-CN-derived carbon materials on atomic level allows a more detailed investigation of the controlled condensation process. This facilitates further adjustment of their porosity characteristics and structure-related enhanced performances in gas adsorption, which is elucidated in the following chapter.

## 3.2 Towards Enhanced CO<sub>2</sub>/N<sub>2</sub> Molecular Sieving with Nitrogen-Doped Carbon Materials Prepared by Molecular Design \*

The system of HAT-CN-derived carbon materials was further examined concerning the enhancement of their CO<sub>2</sub>/N<sub>2</sub> selectivity. In this regard, the accurate control of the condensation process of HAT-CN was utilized to further optimize the nanostructure of the resulting carbon materials on a molecular level. Besides the atomic construction of the materials, the porosity can be precisely controlled *via* the condensation temperature. As it was already elaborated in the previous **Chapter 3.1**, increasing the synthesis temperature resulted in larger pore size (shown with Ar physisorption measurements in **Figure 17** and with HRTEM images in **Figure S 12**). In consideration of the different kinetic diameters of CO<sub>2</sub> and N<sub>2</sub> with 0.345 nm and 0.364 nm, respectively, a molecular sieving effect of CO<sub>2</sub> *via* kinetic size exclusion of N<sub>2</sub> could be achieved. In consequence, the optimized nanostructure of the HAT-CN-derived carbon materials was accurately analyzed by lowering the synthesis temperature close to the condensation spot, which, in consequence, narrows the pore size.

### 3.2.1 Background and State-of-the-Art

Selective CO<sub>2</sub> captures from post- and pre-combustion processes, as well as direct capture from air are an intensively studied field, due to the rapid increase of the CO<sub>2</sub> concentration in the atmosphere.<sup>[121, 186, 187]</sup> In contrast to currently industrially established energy-intensive amine scrubbing (**Chapter 1.6.1.1**), the physisorption of CO<sub>2</sub> is a less energy intensive alternative, but lacking of sufficient CO<sub>2</sub>/N<sub>2</sub> selectivity.<sup>[188, 189, 11]</sup> Typical physical adsorbents applied for selective CO<sub>2</sub> capture are nanoporous materials, such as carbon-based materials,<sup>[190, 136, 37, 9, 191]</sup> covalent triazine frameworks (CTFs),<sup>[192]</sup> covalent organic polymers (COPs),<sup>[193]</sup> zeolites,<sup>[194, 195]</sup> zeolitic imidazolate frameworks (ZIFs),<sup>[196, 197]</sup> and MOFs.<sup>[198-201]</sup> Common methods to increase their affinity towards CO<sub>2</sub> include the introduction of specific interaction sites (e.g., basic nitrogen sites, additional framework cations, or amine functionalities),<sup>[202-205, 167]</sup> as well as the tuning of the ultramicroporosity of the sorbents (**Chapter 1.6.1.2**).<sup>[136, 206, 207]</sup>

Narrowing of the pore size down to molecular dimensions of CO<sub>2</sub> will result in kinetic adsorption limitations. One approach to overcome this is by providing remarkable

---

\* The results of this chapter are used with permission and are published by the author of this thesis as: R. Walczak, A. Savateev, J. Heske, N. V. Tarakina, S. Sahoo, J. D. Epping, T. D. Kühne, M. Antonietti, and M. Oschatz: "Controlling the strength of interaction between carbon dioxide and nitrogen-rich carbon materials by molecular design", *Sustain Energy Fuels* **2019**, *accepted*.

surface polarity, and thus significant affinity to CO<sub>2</sub>. In consequence, MOFs and zeolites with strong ionic character have already been successfully utilized for CO<sub>2</sub>/N<sub>2</sub> separation with outstanding selectivities (**Chapter 1.6.1.2**).<sup>[208, 139, 140]</sup> However, MOFs usually suffer from stability limitations and zeolites from accurate adjustment of their crystal, and thus pore structures, as well as drawbacks concerning complex synthetic processes and the implementation of metals. However, carbon-based materials are still lacking the combination of narrow porosity and high polarizability, and thus selectivity that is needed for the separation of small molecules like N<sub>2</sub> and CO<sub>2</sub>. The aforementioned thermal condensation of HAT-CN towards nitrogen-doped carbon materials with high nitrogen content, well-defined structure motives, and narrow micropores could be adjusted by the synthesis temperature (**Chapter 3.1**).

In the following chapter, this concept is extended and a CO<sub>2</sub>/N<sub>2</sub> molecular sieving effect is realized by only partially condensing HAT-CN at temperatures below 550 °C. The structural changes at temperatures around the condensation step of HAT-CN are investigated in detail (**Chapter 3.2.2**), and a potential CO<sub>2</sub> molecular sieving effect in the metal-free carbon-based materials with narrow pores is elaborated (**Chapter 3.2.3**).

#### **3.2.2 Structure Development during the Condensation Process of the HAT-CN-Derived Carbon Materials**

The thermal condensation of HAT-CN at temperatures of 500 °C and 525 °C leads to the formation of nitrogen-rich carbon materials with a C<sub>2</sub>N-like stoichiometry. C-HAT-CN-500 and C-HAT-CN-525 show high nitrogen contents of 31–34 at.%, as determined by EA (**Table 3**). The significant amount of hydrogen and oxygen detected in these measurements likely arises from H<sub>2</sub>O adsorbed on the samples. Especially for the materials obtained at 550 °C and 700 °C, the ratio of Hydrogen/Oxygen at.% corresponds to 2:1. The greater amount of adsorbed H<sub>2</sub>O molecules is in agreement with the increasing surface area of the materials. The C/N atomic ratio of C-HAT-CN-500 (1.55) is only marginally higher than in HAT-CN (1.53), indicating no major condensation of the nitrile groups occurs at this temperature and that the HAT-CN is indeed an impressively stable molecule. After condensation at 525 °C and 550 °C the C/N ratios increase to 1.60 and 1.67, respectively. Finally, at 700 °C, the ratio reached 1.96 and a nearly perfect C<sub>2</sub>N-type material is obtained. According to the previous findings, condensation of the HAT-CN precursor molecule with a composition of C<sub>18</sub>N<sub>12</sub> releases cyanogen (C<sub>2</sub>N<sub>2</sub>) as the condensation product, and it can thus be assumed that the condensation proceeds according to the general equation  $C_{18}N_{12(s)} \rightarrow C_{12}N_{6(s)} + 3 C_2N_{2(g)}$ . In

agreement with TGA of HAT-CN under N<sub>2</sub> atmosphere (**Figure 11b**), there seems to be a sharp onset point of this condensation reaction located at 500 °C or slightly below. The experimental yield of nitrogen-doped carbon material after condensation at 500 °C is 70 % and drops significantly to 51 % after thermal treatment at 525 °C and to 33 % at 700 °C, which is in good accordance with the TGA experiment. These elemental compositions and yields do not only reveal that HAT-CN is a very well-suited precursor molecule for the synthesis of C<sub>2</sub>N materials, but also that the degree of condensation (and with it the chemical and textural properties of the resulting materials) is precisely adjustable *via* the condensation temperature.

**Table 3:** Elemental analysis data of HAT-CN and the condensed materials, as well as the corresponding condensation yields.

Material	C <sub>EA</sub> / at.% (wt.%)	N <sub>EA</sub> / at.% (wt.%)	H <sub>EA</sub> / at.% (wt.%)	O <sub>EA</sub> / at.% (wt.%)	Yield / %
HAT-CN	53.9 (55.8)	35.3 (42.6)	10.3 (0.9)	0.5 (0.6)	-
C-HAT-CN-500	52.5 (54.1)	33.9 (40.8)	10.6 (0.9)	3.0 (4.2)	70
C-HAT-CN-525	50.4 (53.3)	31.5 (38.9)	13.4 (1.2)	4.6 (6.5)	51
C-HAT-CN-550	43.7 (48.4)	26.2 (33.7)	19.3 (1.8)	10.9 (16.1)	50
C-HAT-CN-700	42.5 (50.5)	21.7 (30.1)	25.0 (2.5)	10.7 (16.9)	33

PXRD measurements (**Figure 19a**) and Fourier-transform infrared (FTIR) spectra (**Figure 19b**) further indicate a distinct structural change between 500 °C and 550 °C, resulting from condensation of the HAT-CN monomer. The PXRD pattern of C-HAT-CN-500 is still in nearly perfect accordance to the pattern of the untreated HAT-CN. The crystal structure is still intact after heating to 525 °C, but there is already a notable contribution of amorphous compounds, as can be seen by the obvious distortion of the baseline underneath the characteristic peaks in the 2 $\theta$  range 10–30 °. The contribution of amorphous scattering intensity at very low 2 $\theta$  values can be indicative for the development of porosity. This is not observed for HAT-CN and increases in intensity from C-HAT-CN-500 to C-HAT-CN-525. In accordance with the previous chapter 2.1, C-HAT-CN-550 and C-HAT-CN-700 have an amorphous structure, as it is typical for high surface-area carbon materials. The graphitic stacking reflection peak of minor intensity located between 25 and 30 ° 2 $\theta$  shifts to a slightly lower angle with increasing condensation temperature.

FTIR spectra of HAT-CN show sharp and narrow peaks, which disappear and get broader with increasing condensation temperature (**Figure 19b**). The intense peak at

$1339\text{ cm}^{-1}$  originates from C–N stretching vibrations. The C=N and C=C vibrations in the aromatic ring system appear at  $1708\text{ cm}^{-1}$  and  $1560\text{ cm}^{-1}$ , respectively. The peak at  $2240\text{ cm}^{-1}$  is attributed to the nitrile C≡N groups. This peak does not disappear as the condensation temperature increases. This might be related to the nitrile groups located on the edges of the carbon network. In accordance with EA and PXRD measurements, the spectra show that there is a continuous increase of the condensation degree with increasing synthesis temperature.

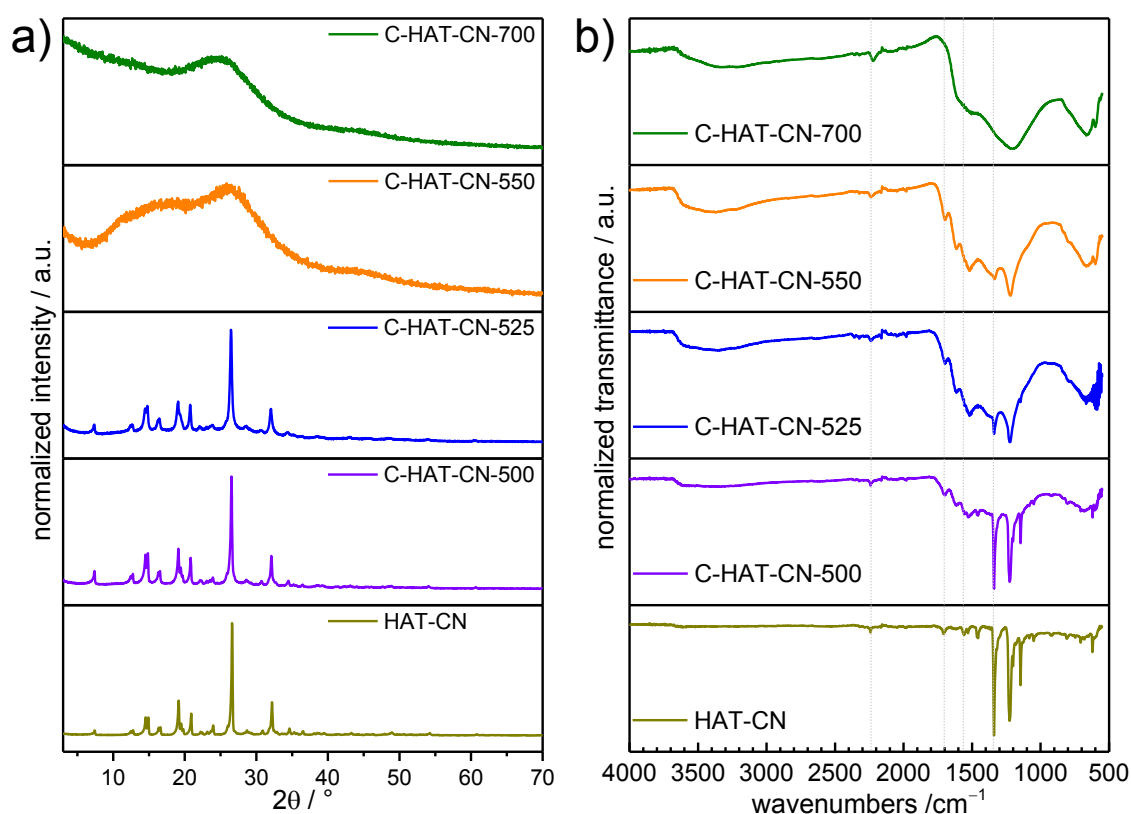


**Figure 19:** PXRD patterns (a) and FTIR spectra (b) of HAT-CN, C-HAT-CN-500, C-HAT-CN-525, C-HAT-CN-550, and C-HAT-CN-700.

The chemical environment of carbon atoms in HAT-CN and HAT-CN-derived carbon materials were investigated by  $^{13}\text{C}$  [ $^1\text{H}$ ] magic angle spinning (MAS) solid-state (ss) NMR experiments (**Figure 20**). Three characteristic peaks for HAT-CN are present. The peak at  $\sim 132$  ppm (marked with an orange circle) corresponds to the aromatic carbon atoms in the inner benzene ring of the HAT-CN molecule. The peak at  $\sim 139$  ppm (green circle) corresponds to the pyrazinic carbon atom, and the one at  $\sim 110$  ppm (blue circle) to the nitrile carbon atom.<sup>[209]</sup> As expected for well-crystallized organic molecule, the peaks for HAT-CN are sharp and well-separated. The condensation of the organic molecule towards a porous amorphous network clearly leads to broadening of the peaks, which gets more pronounced at

increasing temperature. The peak of the nitrile carbons remains for the C-HAT-CN-700. This is due to the surface termination of the porous network particles, as it was already shown in the FTIR spectra.

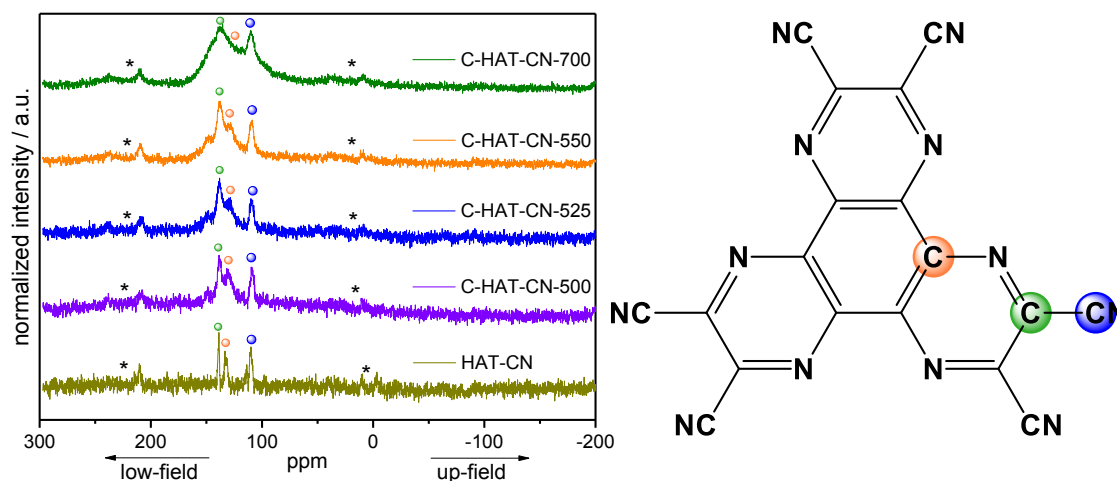


**Figure 20:**  $^{13}\text{C}$  CP-MAS ssNMR spectra of HAT-CN, C-HAT-CN-500, C-HAT-CN-525, C-HAT-CN-550, and C-HAT-CN-700, and the molecule structure of HAT-CN. Green circle is denoting aromatic carbon in the inner benzene ring, orange circle is the pyrazinic carbon, and blue circle is the nitrile carbon. Asterisks (\*) denote spinning sidebands.

Besides the atomic construction, the porosity of the HAT-CN-derived carbon materials is also controllable by the synthesis temperature. In the previous chapter 2.1, it was shown that (despite the absence of any additional porogen) condensation at 550 °C or above leads to the formation of structural microporosity.<sup>[166, 180]</sup> The Ar physisorption (87 K) isotherm (**Figure 21a** and **Table 4**) shows that the C-HAT-CN-700 material with near-ideal  $\text{C}_2\text{N}$ -stoichiometry has indeed a high  $\text{SSA}_{\text{BET}}$  and a significant  $V_{\text{total}}$  of  $785 \text{ m}^2 \text{ g}^{-1}$  and  $0.31 \text{ cm}^3 \text{ g}^{-1}$ , respectively.

**Table 4:** Ar physisorption (87 K) data summary, selectivity of  $\text{CO}_2$  over  $\text{N}_2$  (at 273 K and 298 K), and  $Q_{\text{st}}$  of  $\text{CO}_2$  of C-HAT-CN-500, C-HAT-CN-525, C-HAT-CN-550, and C-HAT-CN-700.

Material	$\text{SSA}_{\text{BET}} / \text{m}^2 \text{ g}^{-1}$	$\text{SSA}_{\text{DFT}} / \text{m}^2 \text{ g}^{-1}$	Selectivity / $\text{CO}_2/\text{N}_2$		$Q_{\text{st}} / \text{kJ mol}^{-1}$	
			Ar			
C-HAT-CN-500	13	13	0.01	-	-	
C-HAT-CN-525	82	172	0.03	72	121	52
C-HAT-CN-550	627	1013	0.24	34	65	36
C-HAT-CN-700	785	1182	0.31	23	53	42

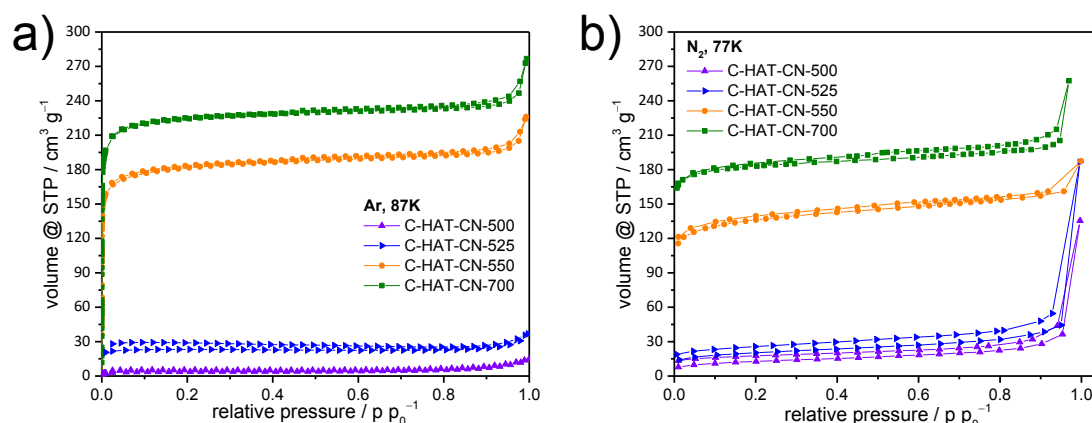


**Figure 21:** Ar physisorption isotherms (87 K) (a) and N<sub>2</sub> physisorption isotherms (77 K) (b) of C-HAT-CN-500, C-HAT-CN-525, C-HAT-CN-550, and C-HAT-CN-700.

Starting from the HAT-CN with no notable surface area, there is a step-wise increase of the porosity detected with Ar at 87 K with increasing condensation temperature. Whereas, the samples C-HAT-CN-500 and C-HAT-CN-525 do still not show any notable uptake of Ar, condensation at 550 °C forms a material with a  $SSA_{BET}$  of  $627 \text{ m}^2 \text{ g}^{-1}$  and a  $V_{total}$  of  $0.24 \text{ cm}^3 \text{ g}^{-1}$ . The larger pore volume of C-HAT-CN-700 is the consequence of further increasing pore size with increasing degree of condensation (**Figure 21a** and **Figure S 14**). The micropore volume ( $V_{micro}$ ) detected for C-HAT-CN-700 with Ar physisorption at 87 K ( $V_{micro}$  of  $0.30 \text{ cm}^3 \text{ g}^{-1}$ ) is comparable to the one detected with N<sub>2</sub> physisorption at 77 K ( $V_{micro}$  of  $0.27 \text{ cm}^3 \text{ g}^{-1}$ , **Figure 21b**). Notably, the difference for C-HAT-CN-550 is larger. In this material, Ar physisorption analysis detects a  $V_{micro}$  of  $0.24 \text{ cm}^3 \text{ g}^{-1}$ , whereas N<sub>2</sub> physisorption analysis only results in a  $V_{micro}$  of  $0.20 \text{ cm}^3 \text{ g}^{-1}$ . This indicates accessibility limitations for the slightly larger N<sub>2</sub> molecules with higher quadrupole moment at lower measurement temperature into the very small micropores of C-HAT-CN-550, which is still present but less pronounced in C-HAT-CN-700. Hence, these materials are possible molecular sieves, not only for CO<sub>2</sub>/N<sub>2</sub> adsorption, but also for Ar/N<sub>2</sub> adsorption, and the preferred adsorption is based on a kinetic exclusion at the expense of (the even stronger adsorbing) nitrogen molecules, that is, a (kinetic) molecular sieving effect. The uptakes of Ar and N<sub>2</sub> at relative pressures close to 1 bar are due to adsorption in the larger pores, which is in line with the HRTEM investigations as discussed below.

In order to utilize these materials for selective CO<sub>2</sub>/N<sub>2</sub> capture based on molecular sieving a pore size close to the dimensions of the CO<sub>2</sub> molecules, but smaller than for N<sub>2</sub> is required. On the other hand, the internal surface of the materials should be highly polarizing in order to have a high adsorption affinity towards CO<sub>2</sub>. H<sub>2</sub>O vapor (a

molecule with even higher adsorption enthalpy than CO<sub>2</sub>, and thus a well-suited probe for the presence of polar adsorption sites) physisorption isotherms of the samples show an extremely polar character of the pore walls in all HAT-CN-derived materials, as indicated by the significant H<sub>2</sub>O vapor uptake at low relative pressures (**Figure S 15**). The adsorbed volumes follow the available pore volumes detected with Ar physisorption.

HRTEM images of the condensed HAT-CN materials (**Figure 22a–h**) show the presence of an amorphous, covalent, carbonaceous microstructure without distinct stacking of layers in C-HAT-CN-550 and C-HAT-CN-700, which is typical for highly microporous carbon materials and in line with the previous findings (**Chapter 3.1**).<sup>[166, 180]</sup> This highly disordered structure likely result from the rapid condensation due to elimination of nitrile groups from HAT-CN, which does not allow the system to crystallize into a stacked structure. Besides in the zones of nitrogen-doped carbon, all materials show the presence of a secondary system of larger pores between the grains, resulting from the 3D network of the primary small flat spheres, as the crystals of the HAT-CN precursor look like.

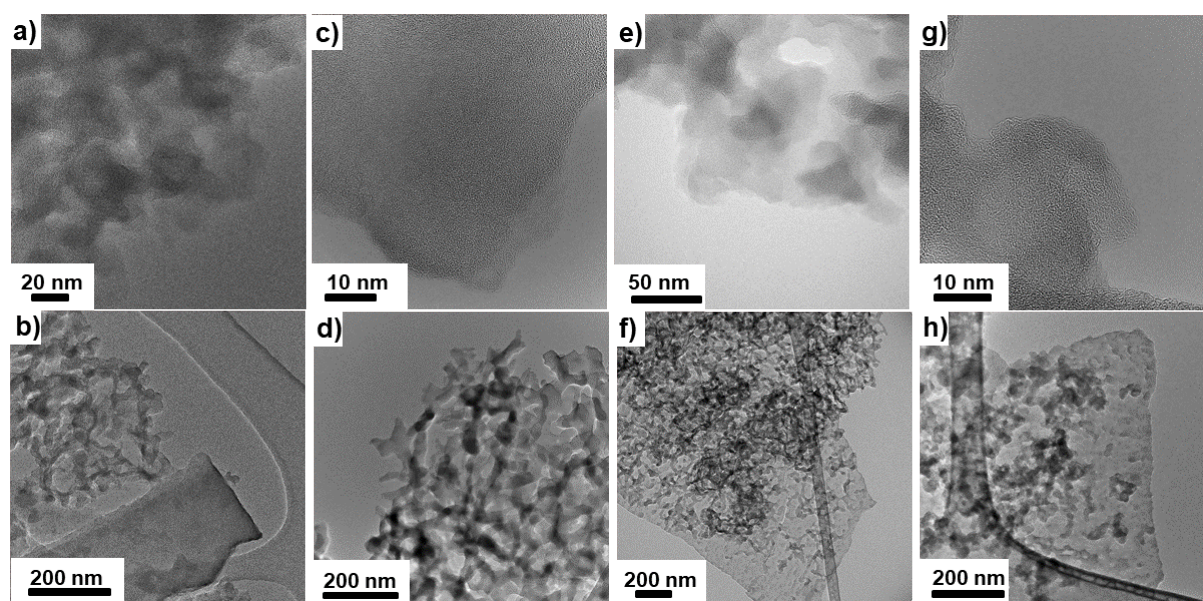


**Figure 22:** HRTEM images of C-HAT-CN-700 (a) and (b), C-HAT-CN-550 (c) and (d), C-HAT-CN-525 (e) and (f), and C-HAT-CN-500 (g) and (h).

More detailed annular dark field scanning transmission electron microscopy (ADF-STEM) images of C-HAT-CN-525 give insights into the construction of the characteristic discotic microscale morphology with an accumulation of small flat plates in different resolutions, as it is illustrated in **Figure 23a–h**. The flat plates are filled with small primary spheres in a random packed fashion, which was already shown in SEM images (**Figure 13e** and **Figure**

13f). Interestingly, the discotic plates are built up by a double-wall with only a few nanometers (10–20 nm) in distance in-between.

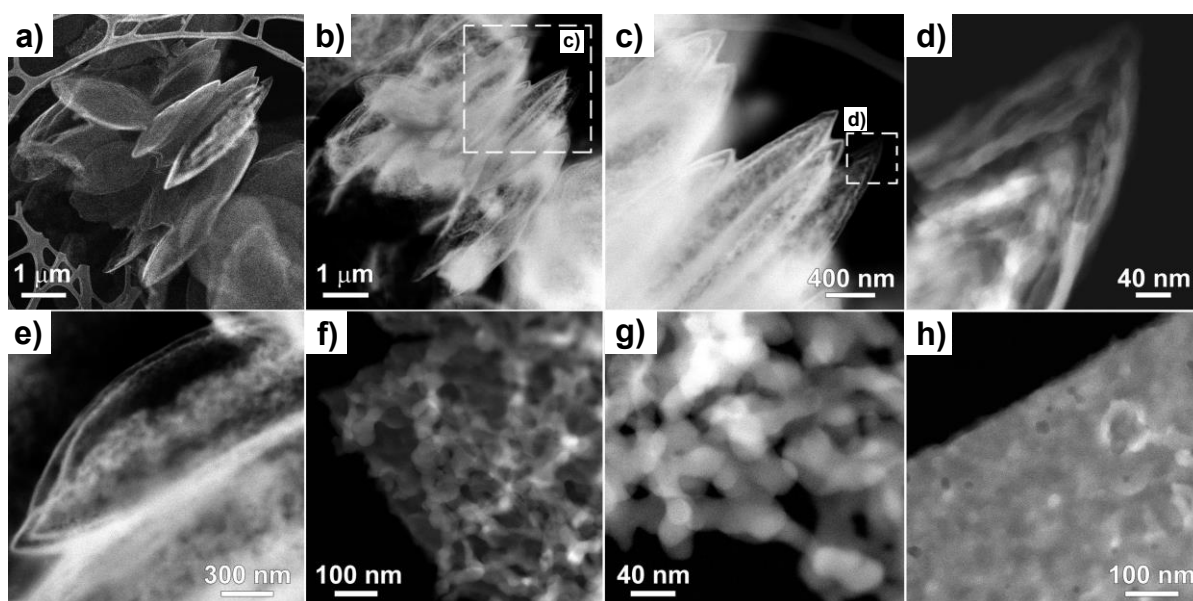


**Figure 23:** Backscattered electron image of the C-HAT-CN-525 sample (a), ADF-STEM images of the C-HAT-CN-525 sample (b–h), (b) shows the same areas as in (a), dotted lines in (b) and (c) indicate areas enlarged in (c) and (d), respectively. Images (f) and (g) shows inner morphology of the particles, (h) shows morphology of the outer layer of the particles.

### 3.2.3 Elaboration of a CO<sub>2</sub>/N<sub>2</sub> Molecular Sieving Effect

The narrow pore size of the HAT-CN-derived carbon materials can be rather precisely adjusted by the synthesis temperature and the materials generally have a very polar surface resulting from their high nitrogen content. On the one site, these pyrazinic nitrogen sites have basic and electron-donating properties, which are particularly strong in the C<sub>2</sub>N structure and are able to strongly bind to the electrophilic carbon in CO<sub>2</sub>. These properties render the materials attractive candidates for selective adsorption of CO<sub>2</sub> in the presence of N<sub>2</sub>. CO<sub>2</sub> and N<sub>2</sub> physisorption isotherms of the HAT-CN-derived carbon materials at 273 K and 298 K show a maximum IAST CO<sub>2</sub>/N<sub>2</sub> selectivity for C-HAT-CN-525 (**Figure 24a–d** and **Table 4**).

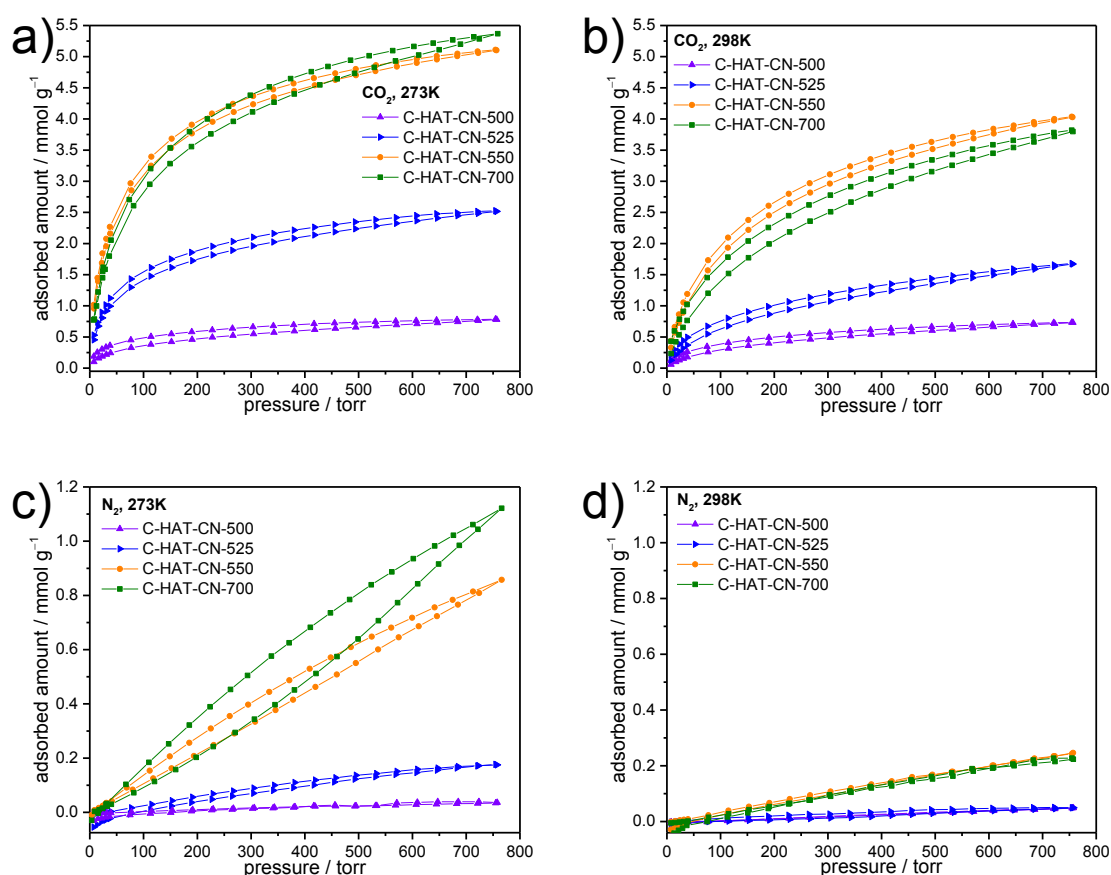


**Figure 24:** CO<sub>2</sub> (a) and (b), as well as N<sub>2</sub> (c) and (d) physisorption isotherms of C-HAT-CN-500, C-HAT-CN-525, C-HAT-CN-550, and C-HAT-CN-700 measured at 273 K (a) and (c) and at 298 K (b) and (d).

In this material, the pores are already large enough to adsorb significant amounts of CO<sub>2</sub>, but are not yet too large to take up high volumes of N<sub>2</sub>. At higher synthesis temperatures, CO<sub>2</sub> uptakes increase further as a result of the increasing pore volume, but the CO<sub>2</sub>/N<sub>2</sub> selectivity decreases. At the chosen measurement temperatures, the selectivity of C-HAT-CN-550 with smaller pores is still higher than for C-HAT-CN-700. This confirms the earlier discussion that the use of materials with a high N<sub>2</sub> surface area is useless for selective CO<sub>2</sub> capture, as long as high selectivity is required due to the increasing contribution of less discriminative van der Waals interactions. It is even more impressive considering that carbon-based molecular CO<sub>2</sub>/N<sub>2</sub> sieves where the pore size has to be precisely adjusted are rather difficult to synthesize due to the amorphous character of carbon materials compared to crystalline materials like MOFs or zeolites.

To put the IAST CO<sub>2</sub>/N<sub>2</sub> selectivities (at 298 K) into a comprehensible context, **Figure 25a** and **Figure 25b** show the comparison of the as-synthesized HAT-CN-derived carbon materials to state-of-the-art materials from literature, such as numerous nitrogen-doped carbon materials, aza-COPs, CTFs, zeolite, ZIFs, and MOFs (including SIFSIXs).<sup>[11]</sup>

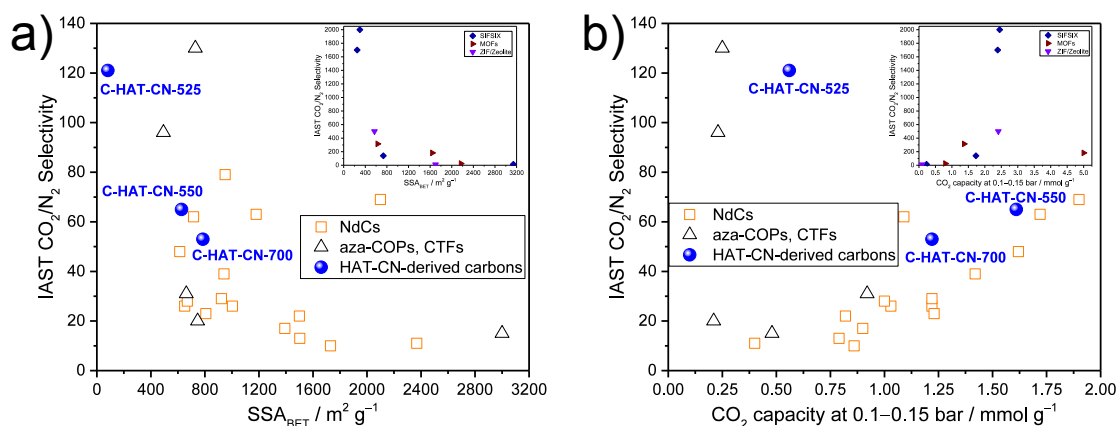


**Figure 25:** Comparison of  $SSA_{BET}$  (a) and  $CO_2$  capacities at 0.1–0.15 bar (at 298 K) (b) to IAST  $CO_2/N_2$  selectivities (at 298 K) of the as-synthesized HAT-CN-derived carbon materials (C-HAT-CN-525, C-HAT-CN-550, and C-HAT-CN-700) to nitrogen-containing porous carbon materials, aza-COPs, and CTFs from literature. Inset: SIFSIX materials, MOFs, ZIFs, and zeolite compounds from literature.<sup>[11]</sup>

In accordance to the nanostructure and nitrogen content, C-HAT-CN-525 shows a significantly higher  $Q_{st}$  of  $CO_2$  adsorption (Table 4 and Figure S 16) of  $\sim 52 \text{ kJ mol}^{-1}$  as compared to C-HAT-CN-550 ( $\sim 36 \text{ kJ mol}^{-1}$ ) and C-HAT-CN-700 ( $\sim 42 \text{ kJ mol}^{-1}$ ). Such a high  $Q_{st}$  is the result of the high nitrogen content, as well as the pore size, which is perfectly tuned for the molecular encapsulation of  $CO_2$ . Typically, isosteric heats of adsorption in this range are only achievable with metal-containing materials including coulomb charges.<sup>[202, 201]</sup> In this way, C-HAT-CN-525 indeed combines the necessary requirements for highly selective  $CO_2$  capture, which are molecular sieving and an atomic construction tuned for strong  $CO_2$  binding (i.e., separation of the electron density between carbon and nitrogen atoms), without the use of any metal.

Thermal response measurements of  $CO_2$  adsorption with the InfraSORP technology<sup>[183, 184]</sup> (Figure 26a–d) provide further information about  $CO_2$  adsorption capacities and kinetics of the HAT-CN-derived materials. In line with the volumetric measurements, the highest temperature peak areas are present for C-HAT-CN-700 and C-HAT-CN-550, due to their large micropores, and thus highest  $CO_2$  uptake at 1 bar (Figure 26a). Regarding their very low Ar and  $N_2$  accessible microporosity, the significant temperature signals of C-HAT-CN-525 and C-HAT-CN-500 are remarkable. According to their higher  $Q_{st}$  values, their normalized peak areas, which are divided by the mass and  $V_{total}$  determined with Ar physisorption, are significantly higher as compared to the materials obtained by HAT-CN condensation at higher temperatures (Figure 26b). The mass-related peak areas for adsorption and desorption are nearly similar for one and the same material, indicating no occurrence of irreversible binding

of CO<sub>2</sub>. Compared to a microporous carbide-derived carbon reference material (TiC-CDC, synthesized at 800 °C),<sup>[185]</sup> the presence of specific CO<sub>2</sub> binding sites is further indicated by minor asymmetry in the adsorption and desorption temperature signals in the cases of C-HAT-CN materials (**Figure 26c** and **Figure 26d**). The CO<sub>2</sub> desorption process by flushing with N<sub>2</sub> causes a slightly lower temperature decrease as compared to the temperature increase caused by adsorption of CO<sub>2</sub>. This is typical for materials with narrow pores and abundant nitrogen sites, and thus not observable for the heteroatom-free TiC-CDC with slightly larger micropores. The latter is showing rather symmetrical and “sharp” temperature signals in the thermal response measurements.

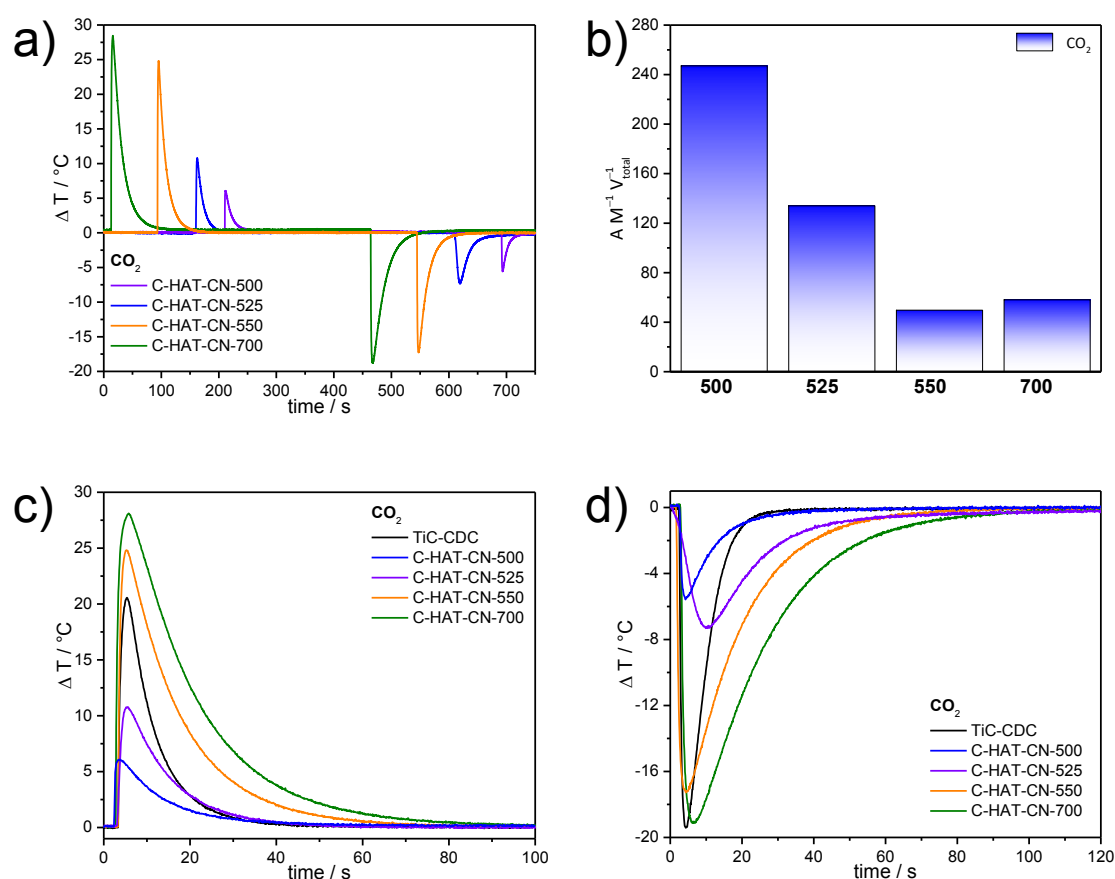


**Figure 26:** CO<sub>2</sub> thermal response adsorption and desorption measurements at 1 bar and 298 K (a), integrated adsorption temperature peak area normalized by mass ( $A\text{ m}^{-1}$ ) and  $V_{\text{total}}$  (b) of C-HAT-CN-500, C-HAT-CN-525, C-HAT-CN-550, and C-HAT-CN-700, as well as their adsorption (c) and desorption (d) thermal response curves at higher magnifications together with a microporous nitrogen-free carbon material (TiC-CDC) for comparison.

Despite the high CO<sub>2</sub> adsorption enthalpy of C-HAT-CN-525, the binding is fully reversible for 80 cycles by simple flushing with N<sub>2</sub> (**Figure S 17**). This means that this molecular

sieving concept is applicable to simple pressure swing adsorption without loss of CO<sub>2</sub> separation efficiency over time.

#### 3.2.4 Theoretical Calculation of the CO<sub>2</sub> Adsorption on the C<sub>2</sub>N network\*

An atomistic model of the adsorption site of CO<sub>2</sub> in idealized C-HAT-CN material with perfect C<sub>2</sub>N-type stoichiometry and AAA-type layer stacking has been obtained by dynamical simulated annealing<sup>[210, 211]</sup> using the second-generation Car-Parrinello molecular dynamics approach of Kühne *et al.*<sup>[212, 213]</sup> The computational details are described in the Appendix (**Table S 5** and **Table S 6**) and the resulting atomistic model is illustrated in **Figure 27a–d**. It can be seen that the CO<sub>2</sub> molecules are oriented orthogonal to the C<sub>2</sub>N-planes occupying every second hole in a checkerboard-like fashion (**Figure 27a** and **Figure 27b**). This energy minimization arises from collective stabilization effects from the nitrogen atoms in the C<sub>2</sub>N layers surrounding the carbon atom in the CO<sub>2</sub> molecule and from the electron acceptor properties of the carbon atoms from C<sub>2</sub>N in close proximity to the oxygen atoms in CO<sub>2</sub>. In simple words, all atoms of the gas molecule are surrounded in their electronically favorable environment. In the present supercell, which contains of four layers with four holes each, the insertion of eight CO<sub>2</sub> molecules entails adsorption energy of  $-232 \text{ kJ mol}^{-1}$ , which is equal to  $-29 \text{ kJ mol}^{-1}$  per molecule. This  $Q_{\text{st}}$  value is lower as compared to the experimental value determined for C-HAT-CN-700. In accordance with the gas physisorption data, this indicates that the pore size in the experimental sample is indeed lower than in a C<sub>2</sub>N material with pores resulting from perfect AAA-stacking, which contributes to CO<sub>2</sub> molecular sieving. In the corresponding nitrogen-free control system with C<sub>3</sub>H stoichiometry, all nitrogen atoms have been substituted by C-H groups (**Figure 27c** and **Figure 27d**). In this case, the adsorption energy is strictly positive being as high as  $+206 \text{ kJ mol}^{-1}$ , which corresponds to  $+26 \text{ kJ mol}^{-1}$  per molecule. No energetically favorable coordination of CO<sub>2</sub> takes place in this environment.

---

\* The computational calculations were performed by and the results were implemented with the permission of Prof. Dr. Thomas Kühne (Paderborn University, Theoretical Chemistry).

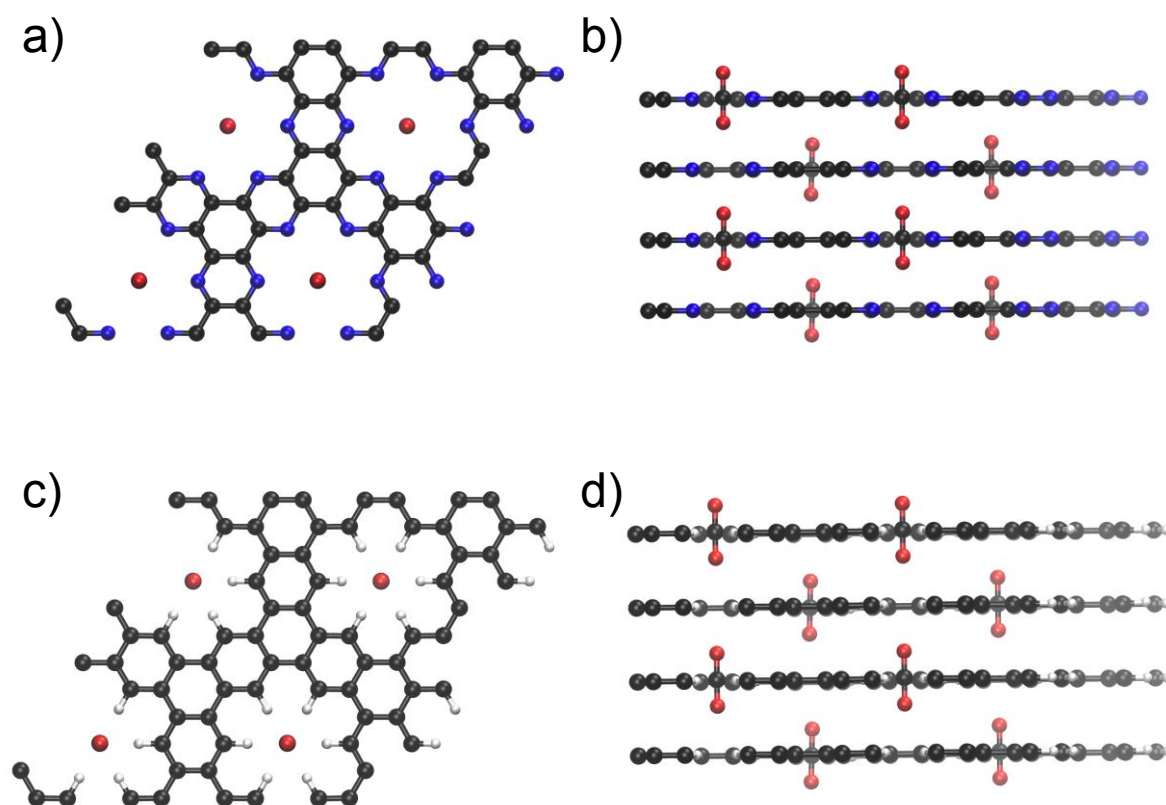


**Figure 27:** Lowest energy structure of the C<sub>2</sub>N network with maximum amount of CO<sub>2</sub> molecules adsorbed (a) and (b). For comparison, the considered control system with C<sub>3</sub>H stoichiometry is also shown (c) and (d). Left: top views; right: side views.

To recapitulate this chapter, the controlled thermal condensation of preorganized HAT-CN was further utilized to synthesize highly nitrogen-rich carbon materials with precise control over the molecular composition and nanostructure/porosity. A CO<sub>2</sub>/N<sub>2</sub> molecular sieving effect was established at a condensation temperature of 525 °C, where pores start forming, with a size too small for adsorption of N<sub>2</sub>, but large enough for adsorption of CO<sub>2</sub>. Until now, this is the first time that a metal- and hydrogen-free material with a Q<sub>st</sub> of CO<sub>2</sub> adsorption of up to 52 kJ mol<sup>-1</sup> and a CO<sub>2</sub>/N<sub>2</sub> selectivity of 121 has been obtained. These outstanding properties are related to the strong polarization of CO<sub>2</sub>, which is caused by negatively polarized nitrogen atoms and positively polarized carbon atoms. This synergy can be achieved due to the well-defined atomic construction of the C-HAT-CN materials. Tuning the pore size without appropriate polarization would end up in limitations in the adsorption kinetics, while a defined molecular construction with too large pores is limited by the dominating contribution of less discriminative van der Waals interactions. The previous chapter exemplified how paramount are interactions at the interface between solid materials and guest molecules to overcome performance limitations in different applications. The combination of narrow microporosity and strong polarization has even larger influence on the adsorption of more polar gases than CO<sub>2</sub>, such as H<sub>2</sub>O and NH<sub>3</sub>.

### 3.3 Structure-Related Properties of HAT-CN-Derived Carbon Materials for the Adsorption of H<sub>2</sub>O and NH<sub>3</sub>

The template- and metal-free preparation of carbon materials with a significant nitrogen content and narrow microporosity *via* the thermal condensation of preorganized HAT-CN was introduced in **Chapter 3.1**. The structure-related gas performance of a series of HAT-CN-derived carbon materials were revealed to show zeolite-like gas adsorption properties for CO<sub>2</sub> and H<sub>2</sub>O. The subsequent study took advantage of the high control over the porosity and the atomic construction of the materials depending on their condensation degree (**Chapter 3.2**). The gas physisorption performance of the molecularly-defined HAT-CN-derived materials was enhanced regarding CO<sub>2</sub>/N<sub>2</sub> selectivity, accomplishing molecular sieving of CO<sub>2</sub>. The synergistic effects of narrow microporosity and an ultrahydrophilic framework will be even more pronounced for guest molecules more polar than CO<sub>2</sub>. In this third constitutive chapter, the influence of the structural and chemical parameters of HAT-CN-derived carbon materials on their adsorption of H<sub>2</sub>O vapor (**Chapter 3.3.3**) and NH<sub>3</sub> gas (**Chapter 3.3.4**) will be described. These materials served as a suitable case example for a profound study on the influence of the structural and chemical parameters on H<sub>2</sub>O vapor and NH<sub>3</sub> gas adsorption on heteroatom-doped carbon materials.

#### 3.3.1 Background and State-of-the-Art

The interactions between H<sub>2</sub>O and solid materials with a large surface area are of utmost importance in energy and environmental applications, such as gas adsorption,<sup>[214]</sup> catalysis,<sup>[215]</sup> and in electrochemical energy storage and conversion,<sup>[216]</sup> as H<sub>2</sub>O vapor is in some cases present or the processes take place in aqueous environment. Materials known to have rather hydrophilic pores are zeolites, silica, or MOFs.<sup>[217]</sup> Nevertheless, silica and zeolites usually provide limitations in terms of achievable porosity and surface structures, whereas many MOFs suffer from their sensitivity for hydrolysis. Carbon materials can possibly overcome these limitations, due to their tunability in chemistry and porosity. However, pristine carbon materials are usually rather hydrophobic due to the inherent aromatic structure of sp<sup>2</sup>-hybridized carbon atoms.

The hydrophilicity, and thus the shape of H<sub>2</sub>O vapor physisorption isotherms of carbonaceous materials is determined by the concentration and type of functional groups, as well as their location and distribution in the materials, the pore size distribution, and pore interconnectivity.<sup>[218]</sup> H<sub>2</sub>O vapor sorption isotherms on hydrophobic carbon materials are generally S-shaped type V isotherms according to the IUPAC classification.<sup>[26]</sup> It is well

known that the introduction of nitrogen-containing functional groups as polar active sites into carbon materials shifts the onset point of adsorption due to partial electrostatic charges in the carbon framework, and thus enhances the uptake at low relative pressures. The mechanism of H<sub>2</sub>O vapor adsorption is proposed to start *via* interactions of functional groups (e.g., carboxylic or amine groups) on the carbon surface as primary adsorption sites initially adsorbing H<sub>2</sub>O. Once hydrogen bonds between H<sub>2</sub>O molecules and functional groups are formed, H<sub>2</sub>O becomes a secondary adsorption site, initiating the subsequent growth and merging of H<sub>2</sub>O clusters.<sup>[219]</sup> The  $Q_{st}$  of H<sub>2</sub>O adsorption can be calculated from H<sub>2</sub>O vapor physisorption isotherms at temperatures close to ambient. This allows one to conclude on the domination of H<sub>2</sub>O-carbon, H<sub>2</sub>O-functional groups, and H<sub>2</sub>O-H<sub>2</sub>O interactions during the sorption process at different relative pressures.

Interface effects between polar guest molecules and porous adsorbents play an important role in vapor compression refrigeration systems. Especially, zeolite-H<sub>2</sub>O or AC-NH<sub>3</sub> as adsorption working pairs with zero global warming potential<sup>[220]</sup> have gained great attention as an environmentally promising alternative to the obsolete use of CFCs and HFCs.<sup>[221]</sup> NH<sub>3</sub> can reach temperatures below 0 °C and is often used in the freezing sector, while H<sub>2</sub>O has the limitation of its freezing point at 0 °C, and is thus preferably used in air-conditioning systems. NH<sub>3</sub> also remains stable up to at least 200 °C, and is therefore feasible for application over a wide range of temperatures. The toxicity and corrosivity of NH<sub>3</sub> can be handled by engineered refrigeration systems without leakage and the ease of its detection is assured by its distinct smell (e.g., an already well-established approach are NH<sub>3</sub> detection systems in NH<sub>3</sub> refrigeration systems like ice rinks or fridges). The use of solid adsorbents faces big challenges such as low thermal conductivity, poor performance in heat and mass transfer, low adsorption capacity, or chemical and physical incompatibility with the chosen refrigerant. Crucial property of the adsorbent is its high adsorption capacity of the refrigerants combined with high heat of adsorption/desorption, which enhances its cooling effect.<sup>[222]</sup> Yet, ACs suffer from relatively low affinity and limited capacity for NH<sub>3</sub>.<sup>[223]</sup> To face these problems, recent studies concentrate on the introduction of Lewis or Brønsted acidic active sites into the adsorbent materials to achieve a higher affinity and capacity towards the basic NH<sub>3</sub>.<sup>[224, 225]</sup> An increase in NH<sub>3</sub> capacity and affinity comes often with slower sorption kinetics, in consequence leading to limitations in heat generation and release.<sup>[226]</sup>

Within this chapter, H<sub>2</sub>O vapor physisorption experiments at different temperatures allowed to study of the strength of the interactions between H<sub>2</sub>O and HAT-CN-derived materials. A

microporous carbon TiC-CDC was prepared as a rather hydrophobic reference material (**Chapter 3.3.2**). Different H<sub>2</sub>O environments between HAT-CN-derived materials and TiC-CDC were made evident by <sup>1</sup>H MAS ssNMR spectra (**Chapter 3.3.3**). The acceptor-donor interactions of the pyrazinic nitrogen moieties within HAT-CN-derived materials were investigated by NH<sub>3</sub>-temperature programmed desorption (NH<sub>3</sub>-TPD), which is usually applied for analyzing the acidic sites on solid zeolite surfaces (**Chapter 3.3.4**).<sup>[227]</sup> The kinetics and the temperature development upon NH<sub>3</sub> sorption are revealed by thermal response measurements using the InfraSORP technique.<sup>[184, 185, 228]</sup>

### 3.3.2 Structural Classification compared to Reference Carbon Materials

Ar physisorption measurements at 87 K reveal the microporous character with type Ia isotherms according to IUPAC classification<sup>[26]</sup> of the nitrogen-containing HAT-CN-derived carbon materials and the reference material TiC-CDC (**Table 5** and **Figure S 18a–c**). TiC-CDC has a significantly higher SSA<sub>BET</sub> of ~1700 m<sup>2</sup> g<sup>-1</sup>, than the C-HAT-CN materials with a SSA<sub>BET</sub> of ~600–800 m<sup>2</sup> g<sup>-1</sup>. TiC-CDC also has a more than twice as high V<sub>total</sub> with 0.66 cm<sup>3</sup> g<sup>-1</sup> than the C-HAT-CN materials with 0.25–0.32 cm<sup>3</sup> g<sup>-1</sup>. The micropore size distributions of C-HAT-CN is narrow, but the mean size increases with condensation temperature with the main peak located at a diameter of 0.90 nm, 1.12 nm, and 1.19 nm for condensation at 550 °C, 700 °C, and 1000 °C, respectively (**Figure S 18c**). A minor contribution of very narrow micropores with sizes below 0.8 nm is detected as well, but is negligible as compared to V<sub>total</sub> (**Figure 1d**). TiC-CDC has also a narrow micropore size distribution that is centered at 1.24 nm, which is comparable to C-HAT-CN-1000, but the former shows a significantly higher V<sub>micro</sub>.

**Table 5:** Ar physisorption (87 K) data summary of C-HAT-CN-550, C-HAT-CN-700, C-HAT-CN-1000, TiC-CDC, and CMK-3.

Material	SSA <sub>BET</sub> / m <sup>2</sup> g <sup>-1</sup>	SSA <sub>DFT</sub> / m <sup>2</sup> g <sup>-1</sup>	V <sub>total</sub> / cm <sup>3</sup> g <sup>-1</sup>	V <sub>micro</sub> / cm <sup>3</sup> g <sup>-1</sup>
C-HAT-CN-550	627	1013	0.25	0.24
C-HAT-CN-700	785	1182	0.31	0.30
C-HAT-CN-1000	801	1148	0.32	0.31
TiC-CDC	1725	2235	0.66	0.65
CMK-3	1101	1262	1.21	0.05

SEM analysis shows that TiC-CDC powders are composed of anisometric particles with smooth surfaces in the size range of ~1–10 μm and an average size of ~5 μm (**Figure S 19a** and **Figure S 19b**). EA illustrates the comparison of the nitrogen content of nitrogen-

containing materials C-HAT-CN-550 (27.1 at.%) and C-HAT-CN-700 (21.7 at.%) to C-HAT-CN-1000 (4.1 at.%), as well as to the nitrogen-free materials TiC-CDC and CMK-3 (**Table 6**). As already elaborated for the HAT-CN-derived materials at lower temperatures (see **Table 3**), the remarkable hydrogen and oxygen content according to EA measurements can be correlated to adsorbed H<sub>2</sub>O on the samples (**Table 6**). The C<sub>2</sub>N-type material C-HAT-CN-700 with higher surface area and significant nitrogen content reveals the biggest amount of adsorbed H<sub>2</sub>O molecules. The small amount of fluorine atoms (2.2 at.%) in CMK-3 derives from the silica template removal step using aqueous NH<sub>4</sub>F solution.

**Table 6:** Elemental analysis and EDX data summary of C-HAT-CN-550, C-HAT-CN-700, C-HAT-CN-1000, TiC-CDC, and CMK-3.

Material	C / at.%		N / at.%		H / at.%		O / at.%		F / at.%
	EA	EDX	EA	EDX	EA	EDX	EA	EDX	EDX
<b>C-HAT-CN-550</b>	44.7	58.9	27.1	39.7	20.6	-	7.6	1.4	-
<b>C-HAT-CN-700</b>	42.5	62.2	21.7	34.9	25.0	-	10.7	2.9	-
<b>C-HAT-CN-1000</b>	72.9	96.5	4.1	0.0	17.1	-	5.9	3.5	-
<b>TiC-CDC</b>	80.9	97.2	-	-	13.7	-	5.4	2.8	-
<b>CMK-3</b>	73.6	94.3	-	-	25.4	-	1.0	3.5	2.2

As expected, TGA under synthetic air revealed the nobility and oxidation resistance of C-HAT-CN-550 with an onset temperature of  $\sim 550$  °C, to be more pronounced than in comparison to the nitrogen-free TiC-CDC with a lower onset temperature of  $\sim 500$  °C (**Figure S 20**).

### 3.3.3 Evaluation of Structure-Related Properties of HAT-CN-Derived Carbon Materials for the Adsorption of H<sub>2</sub>O Vapor

The differences in the surface polarities of the samples were investigated by H<sub>2</sub>O vapor physisorption at 298 K (**Figure 28a**). High H<sub>2</sub>O uptakes at low relative pressures and a typical type I isotherm confirm the pronounced hydrophilic character of C-HAT-CN-550 and C-HAT-CN-700. At low relative humidity of 20 % (corresponding to  $\sim 6000$  ppm of H<sub>2</sub>O molecules) C-HAT-CN-550 adsorbs  $7.95 \text{ mmol g}^{-1}$  of H<sub>2</sub>O, whereas this value increases by a factor of 1.29 for C-HAT-CN-700. This relation matches well the ratio of their  $V_{\text{micro}}$ , which is 1.25. At the saturation pressure, both materials have a H<sub>2</sub>O uptake of  $\sim 46 \text{ mmol cm}^{-3}$ , normalized by their  $V_{\text{micro}}$ . This roughly corresponds to the density of liquid H<sub>2</sub>O. Although their pore size and volume are comparable, the lower nitrogen-content in C-HAT-CN-1000 leads to a significant shift of the onset point of H<sub>2</sub>O vapor adsorption to higher relative pressure. At a relative humidity of 0.2, the high temperature sample adsorbs  $1.08 \text{ mmol g}^{-1}$  of

H<sub>2</sub>O, indicating the significantly lower adsorption enthalpy in this material. At the saturation pressure, the density of H<sub>2</sub>O in this material is comparable to C-HAT-CN-550 and C-HAT-CN-700. Despite the comparable micropore sizes, the onset point of H<sub>2</sub>O vapor uptake is shifted to even higher relative pressures for TiC-CDC in comparison to C-HAT-CN-1000, due to the complete absence of heteroatoms, and thus polar binding sites. At a relative pressure of 0.2, the packing density of H<sub>2</sub>O molecules adsorbed in TiC-CDC and C-HAT-CN-1000 corresponds to 2.1 and 0.43 molecules per nm<sup>-3</sup>. Extreme densification of the adsorbed molecules occurs in C-HAT-CN-550 and C-HAT-CN-700; both have ~20 molecules per nm<sup>-3</sup> pore volume. C-HAT-CN-1000 and TiC-CDC further show a hysteresis loop, which is a typical feature for H<sub>2</sub>O adsorption on rather hydrophobic carbon materials. This is due to the nucleation enthalpy that has to be overcome to form liquid H<sub>2</sub>O in larger micropores (similar to the widely known capillary condensation of N<sub>2</sub> in mesopores). This phenomenon cannot be observed for C-HAT-CN-700 and C-HAT-CN-550, which indicates preferred interactions between H<sub>2</sub>O and pore wall rather than H<sub>2</sub>O-H<sub>2</sub>O interactions in these highly polar materials. Another possible reason for the absence of hysteresis may be their slightly smaller pore size, which does not provide enough space for the formation of an extended hydrogen bonding network between H<sub>2</sub>O molecules.

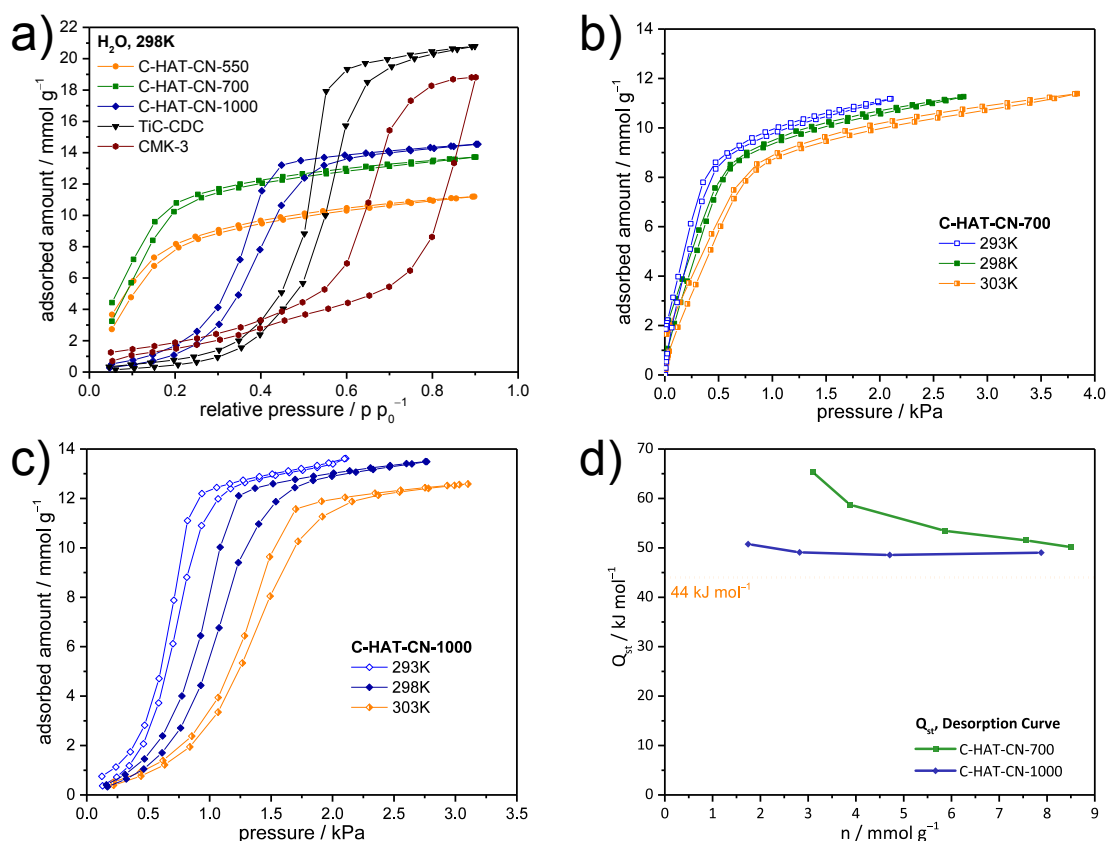


**Figure 28:** H<sub>2</sub>O vapor physisorption isotherms at 298 K of C-HAT-CN-550, C-HAT-CN-700, C-HAT-CN-1000, TiC-CDC, and CMK-3 (a), H<sub>2</sub>O vapor physisorption isotherms at different temperatures (293 K, 298 K, and 303 K) of C-HAT-CN-700 (b), and C-HAT-CN-1000 (c), as well as  $Q_{st}$  of H<sub>2</sub>O vapor adsorption (d). The orange dotted line indicates the heat of evaporation of H<sub>2</sub>O with  $44 \text{ kJ mol}^{-1}$ .<sup>[229, 230]</sup>

H<sub>2</sub>O vapor physisorption measurements were carried out at different temperatures (at 293, 298, and 303 K) for C-HAT-CN-700 (**Figure 28b**) and C-HAT-CN-1000 (**Figure 28c**). The  $Q_{st}$  of H<sub>2</sub>O adsorption was calculated using the desorption curve of the three H<sub>2</sub>O vapor isotherms. The standard enthalpy of H<sub>2</sub>O evaporation (i.e, the enthalpy summing up all the intermolecular interactions between the molecules in liquid H<sub>2</sub>O) of  $\sim 44 \text{ kJ mol}^{-1}$  (at 298 K)<sup>[229, 230]</sup> is shown for comparison by the orange dotted line in **Figure 28d**. As expected, the H<sub>2</sub>O vapor uptakes shift to absolute higher pressures with increasing measurement temperature in both cases, while no significant difference in the overall adsorption mechanism can be observed. Independent of the H<sub>2</sub>O vapor uptake, the corresponding  $Q_{st}$  of H<sub>2</sub>O vapor adsorption is higher in the stronger polarizing C-HAT-CN-700 (**Figure 28d**). Even at a rather high H<sub>2</sub>O vapor uptake of  $4 \text{ mmol g}^{-1}$ , this material shows an impressively high  $Q_{st}$  of  $\sim 60 \text{ kJ mol}^{-1}$ . The less polar C-HAT-CN-1000 also has  $Q_{st}$  values ranging above the enthalpy of liquid H<sub>2</sub>O over the entire range of adsorption. In other words, the hydrogen bonding interactions between the C-HAT-CN materials and H<sub>2</sub>O are stronger than the hydrogen

bonding interactions between H<sub>2</sub>O itself. This makes the C-HAT-CN a carbon-rich material the surface of which is more hydrophilic than liquid H<sub>2</sub>O. At lower loadings, the Q<sub>st</sub> would reach even higher values for both materials (**Figure S 21**), but it has to be considered that the measurement error at such low H<sub>2</sub>O uptakes will become increasingly high. The Q<sub>st</sub> values for C-HAT-CN-1000 with  $\sim 80 \text{ kJ mol}^{-1}$  for the H<sub>2</sub>O molecules first adsorbed on its surface, are therefore more realistic than those for C-HAT-CN-700 with  $\sim 100 \text{ kJ mol}^{-1}$ .

The differences in the physicochemical states and environments of H<sub>2</sub>O adsorbed in C-HAT-CN-550, C-HAT-CN-700, and C-HAT-CN-1000 were further determined by <sup>1</sup>H MAS ssNMR spectroscopy of samples after air exposure (**Figure 29a**) and samples filled with H<sub>2</sub>O according to their V<sub>total</sub> (**Figure 29b**). NMR spectroscopy has been widely applied as a tool for the investigation of the chemical environment of H<sub>2</sub>O molecules.<sup>[231-233]</sup> <sup>1</sup>H chemical shifts are a precise measure for the physicochemical state of H<sub>2</sub>O molecules adsorbed in pores of different size and polarity. In particular, the chemical shielding effect caused by the  $\pi$ -conjugated aromatic system has to be considered for carbon materials. In consequence, a characteristic low-field shift is observed for the <sup>1</sup>H ssNMR signals molecules adsorbed in narrow pores of carbon materials.

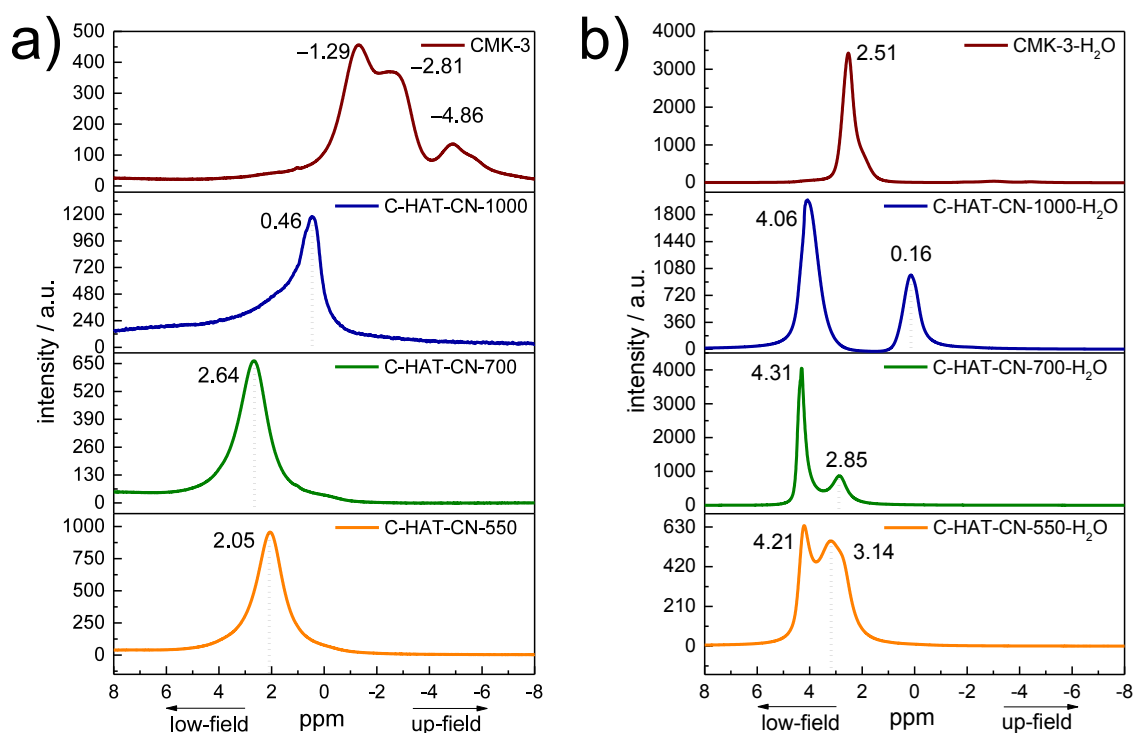


**Figure 29:** <sup>1</sup>H MAS ssNMR spectra of air exposed (a), and H<sub>2</sub>O impregnated (b) samples of C-HAT-CN-550, C-HAT-CN-700, C-HAT-CN-1000, and CMK-3.

An ordered mesoporous carbon (CMK-3) (**Table 5** and **Table 6**, **Figure S 18a–c**) was measured as a reference sample. CMK-3 is a nitrogen-free carbon material that has a mesopore size centered at  $\sim 4$  nm and low micropore content. The H<sub>2</sub>O vapor physisorption isotherm of CMK-3 shows a high uptake with an onset at high relative pressures due to the formation of liquid H<sub>2</sub>O in the mesopores after nucleation from H<sub>2</sub>O adsorbed in micropores or from polar functional groups on the surface of the mesopore walls (**Figure 28a**).

CMK-3 contains ordered mesopores and micropores of various sizes and thus shows multiple <sup>1</sup>H ssNMR signals for H<sub>2</sub>O molecules adsorbed after exposure to air (**Figure 29a**). The signal with low intensity located at  $-4.86$  ppm likely corresponds to H<sub>2</sub>O adsorbed in narrow micropores, whereas the more intense signals at  $-1.29$  ppm and  $-2.81$  ppm originate from H<sub>2</sub>O adsorbed in larger mesopores. The <sup>1</sup>H ssNMR signals of H<sub>2</sub>O molecules adsorbed in air-exposed C-HAT-CN materials appear at a low-field chemical shift as compared to the H<sub>2</sub>O molecules adsorbed in CMK-3. It can be expected that the H<sub>2</sub>O molecules of the C-HAT-CN materials that are located in the pores are more deshielded, and thus the proton signals will be low-field shifted. While H<sub>2</sub>O molecules in CMK-3 adsorbed on the external surface are shielded and accordingly up-field sifted. In consequence, the peak for H<sub>2</sub>O adsorbed in C-HAT-CN-1000 is the most up-field shifted chemical shift ( $0.46$  ppm) of all HAT-CN-derived carbon materials. The H<sub>2</sub>O molecules are more strongly bound in the HAT-CN-derived carbon materials prepared at lower temperatures and the absence of an extended  $\pi$ -conjugated system within the pores leads to the signals at  $2.05$  ppm and  $2.64$  ppm. The <sup>1</sup>H ssNMR signal of liquid H<sub>2</sub>O is located at  $\sim 5.5$  ppm and after loading of the pore system with H<sub>2</sub>O, the HAT-CN-derived carbon materials contain near-liquid-like H<sub>2</sub>O on the external surface, as indicated by the peaks at  $4.06$ ,  $4.31$ , and  $4.21$  ppm (**Figure 29b**). H<sub>2</sub>O adsorbed in the micropores of C-HAT-CN-550 and C-HAT-CN-700 has a chemical shift located at  $3.14$  and  $2.85$  ppm, respectively. These peaks are slightly low-field shifted as compared to the H<sub>2</sub>O molecules adsorbed due to air exposure.

As the shielding effect will remain similar in intensity, the artificial H<sub>2</sub>O loading is fully filling the pores with H<sub>2</sub>O, which are leading to the low-field shift. H<sub>2</sub>O molecules adsorbed in C-HAT-CN-1000 show a significant up-field chemical shift at  $0.16$  ppm, as compared to the C-HAT-CN materials prepared at lower synthesis temperature, due to a more pronounced shielded protons. H<sub>2</sub>O adsorbed in mesopores of CMK-3 is now located at a chemical shift of  $2.51$  ppm, while again the shielding effect of the fully developed  $\pi$ -conjugated aromatic system in CMK-3 leads to the up-field shift of the signal. Overall, the fact that the interactions

between H<sub>2</sub>O and C-HAT-CN-550 or C-HAT-CN-700 are strong enough that H<sub>2</sub>O is rather located in the pores, instead of the external surface, describes their strong hydrophilicity. This is in good agreement with the finding from the H<sub>2</sub>O vapor physisorption measurements (**Figure 28a**) and that the onset point of adsorption shifted to lower relative pressures.

#### 3.3.4 Evaluation of Structure-Related Properties of HAT-CN-Derived Carbon Materials for the Adsorption of NH<sub>3</sub> Gas

Due to the highly polarizing character of the HAT-CN-derived carbon materials, the NH<sub>3</sub> gas adsorption properties of these materials, which would be particularly interesting for heat pump applications, was further investigated. NH<sub>3</sub>-TPD is usually applied as a tool for analyzing the acidic sites on solid surfaces.<sup>[227]</sup> Herein, NH<sub>3</sub>-TPD is applied to characterize the hydrogen donor-acceptor interactions between NH<sub>3</sub> gas and C-HAT-CN materials (**Figure 30**). The strength of the N-H-N hydrogen bridge is bit weaker than the strength of the O-H-N hydrogen bridge, nevertheless it can be expected that these materials are outstanding hydrogen acceptors will also have a particularly high affinity to NH<sub>3</sub> gas. Interestingly, for all materials a rather broad signal of the thermal conductivity detector (TCD) over the temperature range of ~150–450 °C can be seen instead of sharp, distinct peaks that are common in TCD analysis. Thus, the analysis of the peak areas *via* integration in order to obtain the NH<sub>3</sub> uptake of the materials, and to gain knowledge about the nature and amount of donor-acceptor sites inside the materials, is not applicable for those curves. C-HAT-CN-1000 with low nitrogen content and the nitrogen-free TiC-CDC showed negligible TCD signals (~8 a.u.). The onset point of TiC-CDC is located ~50 °C higher than for the C-HAT-CN materials. This was expected due to the lacking hydrogen donor-acceptor sites, and thus, lower affinity towards NH<sub>3</sub>. C-HAT-CN-550 and C-HAT-CN-700 showed TCD signals up to 150 a.u. and 27 a.u., respectively, which corresponds to a higher amount of NH<sub>3</sub> bound in those materials as compared to TiC-CDC and C-HAT-CN-1000. Also, C-HAT-CN-550 still released NH<sub>3</sub> gas at higher temperatures of ~275–375 °C with a rather horizontal curve progression, which indicates strong donor-acceptor sites. Interestingly, C-HAT-CN-550 showed a five times higher TCD signal than C-HAT-CN-700, both having comparable nitrogen content. A possible argument to explain the stronger interactions of C-HAT-CN-550 towards NH<sub>3</sub> can be the smaller pore size of C-HAT-CN-550 (0.9 nm) compared to C-HAT-CN-700 (1.1–1.2 nm). This results in stronger interactions of the pore walls in C-HAT-CN-550 with the NH<sub>3</sub> gas molecules. The strength of the interactions between the C-HAT-CN materials and NH<sub>3</sub> gas follows a comparable capture mechanism as explained for CO<sub>2</sub> in

**Chapter 3.2.** The electron-deficient carbon atoms in the  $C_2N$  network can interact with the free electron pair located at the nitrogen atom of  $NH_3$ , while the hydrogens atoms of  $NH_3$  can interact with the electron-rich nitrogen atoms of the C-HAT-CN materials. The TCD signal at  $\sim 450\text{--}550\text{ }^\circ\text{C}$  corresponds to condensation or dimerization of  $NH_3$  in the pores. The condensation derives from the thermodynamic difference in adsorption and desorption of  $NH_3$  due to pore condensation. In consequence, high temperatures are required to remove  $NH_3$  from the pores.

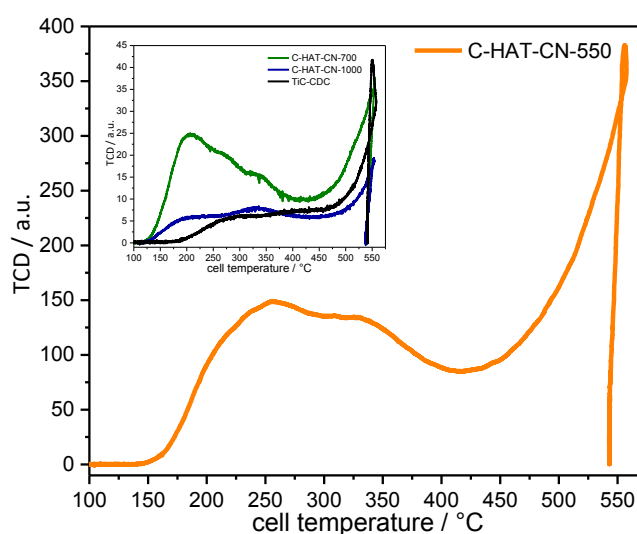


**Figure 30:**  $NH_3$ -TPD curve of C-HAT-CN-550. Inset:  $NH_3$ -TPD curves of C-HAT-CN-700, C-HAT-CN-1000, and TiC-CDC.

Thermal response measurements using the InfraSORP technique<sup>[184, 185, 228]</sup> using  $NH_3$  as test gas at 298 K and 1 bar gave insight into the heat of adsorption (**Figure 31a–d**). There is a significant temperature increase of  $\sim 60\text{ }^\circ\text{C}$  upon  $NH_3$  adsorption for C-HAT-CN-550 (**Figure 31a**), which is twice as high as for nitrogen-free TiC-CDC with  $\sim 28\text{ }^\circ\text{C}$  (**Figure 31c**). The cooling effect upon  $NH_3$  desorption reached up to  $-10\text{ }^\circ\text{C}$  and  $-15\text{ }^\circ\text{C}$  for C-HAT-CN-550 and C-HAT-CN-700, respectively.

The asymmetry between adsorption and desorption curve indicates that the adsorption mechanism of  $NH_3$  on the HAT-CN-derived materials possibly undergoes a hysteresis due to pore condensation. It can also be indicated that  $NH_3$  is adsorbed within the pore system due to strong donor-acceptor interactions of the C-HAT-CN materials towards  $NH_3$  gas. Highly symmetric sorption curves in the case of TiC-CDC indicate weaker interactions due to the absence of nitrogen-containing binding sites.

Mass-related and  $V_{\text{micro}}$ -related thermal response peak areas of 363, 241, and 74  $\text{mg}^{-1} \text{cm}^{-3}$  for C-HAT-CN-550, C-HAT-CN-700, and TiC-CDC, respectively, underlines the strong affinity of C-HAT-CN-550 towards  $\text{NH}_3$  gas (**Figure 31d**).

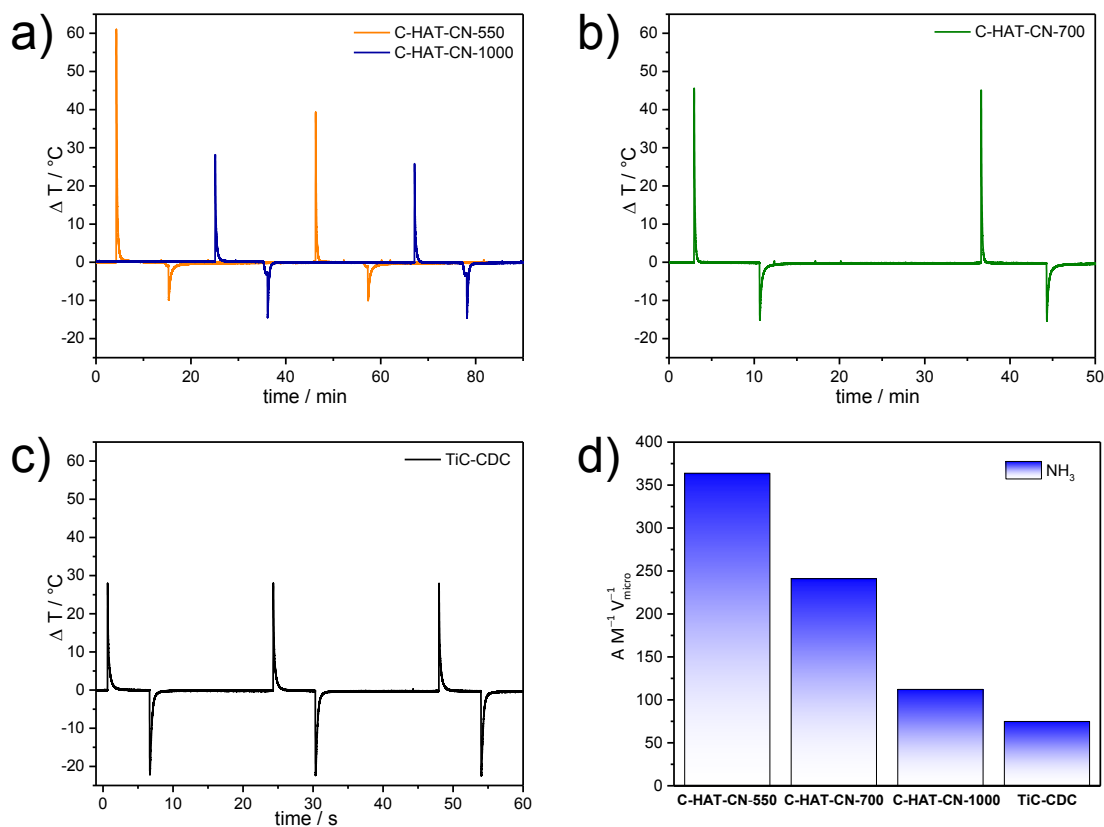


**Figure 31:** Thermal response measurements of  $\text{NH}_3$  adsorption/desorption (1 bar, 298 K) over two cycles of C-HAT-CN-550, and C-HAT-CN-1000 (a), C-HAT-CN-700 (b), over three cycles of TiC-CDC (c), and mass-related thermal response peak areas ( $\text{A m}^{-1}$ ) of the adsorption peak normalized by  $V_{\text{micro}}$  (d).

Further, the stability of the HAT-CN-derived carbon materials and TiC-CDC was tested regarding the repeated sorption of  $\text{NH}_3$  gas over several cycles (**Figure S 22a** and **Figure S 22b**). A fully reversible adsorption capacity and strength can be observed for C-HAT-CN-700 (**Figure S 22a**) and TiC-CDC (**Figure S 22b**) over fourteen and twelve cycles, respectively. It can thus be concluded that the exposure of  $\text{NH}_3$  gas towards the C-HAT-CN materials has no major influence on their sorption capability over several cycles.

The sorption kinetics of C-HAT-CN-700 were investigated using thermal response measurements with  $\text{NH}_3$  gas over six sorption cycles with increasing desorption times from 10 sec, 1 min, 10 min, 60 min, 90 min, to overnight ( $\sim 13$  h) using  $\text{N}_2$  (**Figure S 22c**). The fully activated sample C-HAT-CN-700 exhibited a temperature signal of  $\sim 55$  °C upon  $\text{NH}_3$  adsorption. With increasing desorption times, the adsorption capacity, and thus, temperature

release of the sample can be increased. Already after 10 min desorption time, a temperature signal of  $\sim 35$  °C can be obtained that corresponds to a recovery of  $\sim 64$  % to the initial adsorption curve. The asymmetry of the adsorption and desorption curves indicate that the  $\text{NH}_3$  desorption is the rate limiting step and further shows the strong affinity of C-HAT-CN-700 towards  $\text{NH}_3$  gas. A longer duration up to 60 min with  $\text{N}_2$  of the material is necessary to recover  $\sim 77$  % ( $\sim 12$  °C lower compared to the initial adsorption curve). The initial temperature release signal, and thus adsorption capacity of the fully activated C-HAT-CN-700 can also not be obtained by flushing the material for  $\sim 13$  h with  $\text{N}_2$ . Hence, the filled pores with residual  $\text{NH}_3$  gas within the material can only be emptied using high vacuum and sufficient activation temperature.

To conclude this chapter,  $\text{H}_2\text{O}$  vapor physisorption measurements at different temperatures allowed to calculate the  $Q_{\text{st}}$  of  $\text{H}_2\text{O}$  adsorption, thus to interpret the interaction of the C-HAT-CN materials with  $\text{H}_2\text{O}$  molecules. The interactions between the materials and  $\text{H}_2\text{O}$  are stronger than between liquid  $\text{H}_2\text{O}$  itself. The physicochemical environments of the  $\text{H}_2\text{O}$  molecules within the pores of the C-HAT-CN materials were investigated by  $^1\text{H}$  MAS ssNMR spectroscopy.  $\text{NH}_3$ -TPD and thermal response measurements using  $\text{NH}_3$  gas revealed an outstanding affinity of the HAT-CN-derived carbon materials compared to pristine carbon materials. The chemical and physical compatibility of the materials with  $\text{NH}_3$  was nicely shown with repeated sorption cycles. Overall, the structure-related properties of the HAT-CN-derived materials make these kinds of materials promising for vapor compression refrigeration applications.

### 3.4 Nitrogen-doped Carbon Materials derived by Conjugated Microporous Polymer

As it was exemplified in the first chapter (**Chapter 3.1**), the usage of preorganized molecular precursors is a suitable approach towards highly functional frameworks. Nitrogen can be incorporated into the carbon backbone significant in number, well-distributed, and as accessible functionalities. It was shown that the molecular construction of ultrahydrophilic carbon materials leads to enhanced performances in gas adsorption of polar molecules (**Chapter 3.2** and **Chapter 3.3**). But, for example carbon-based molecular CO<sub>2</sub>/N<sub>2</sub> sieves where the pore size has to be precisely adjusted are rather difficult to synthesize due to the amorphous character of carbon materials. Functional carbon materials synthesized by promising precursors that get more aligned than HAT-CN during condensation, are conjugated microporous polymers. The properties of CMPs will be explained in detail and their influences on the structure-related performances for an application beyond gas adsorption, namely electrochemical energy storage in sodium-ion batteries, will be presented. The ever-increasing demand of portable electronic devices and electrified transportation vehicles/systems makes the research work on the electrochemical topic of great importance.

#### 3.4.1 Background and State-of-the-Art

CMPs can be, for instance, manufactured by cross-coupling approaches *via* palladium-catalyzed cross-coupling or homo-coupling organic synthesis.<sup>[102-104]</sup> CMPs stand out due to an inherent porous nanostructure, comparably (for polymers) high thermal/chemical stability, and a carbon-rich  $\pi$ -conjugated skeleton that is built up by rigid aromatic rings (**Chapter 1.5**).<sup>[101]</sup> The  $\pi$ -conjugation throughout the backbone favors the graphitization process during carbonization, which is contributing to higher electrical conductivity. The nanostructure and the properties of CMPs can be translated into carbon materials by simple direct carbonization, due to ideal precursor qualities with the carbon-rich, stable skeleton.<sup>[101]</sup> The electronic and chemical properties of the CMP-derived carbon materials can be easily tuned by the construction of the corresponding nitrogen-containing CMPs, which are synthesized by the selection of appropriate nitrogen-containing monomers. Due to the aforementioned reasons, CMPs are a powerful class of material that have been widely studied as light-emitting/<sup>[105]</sup>-harvesting<sup>[106]</sup> materials, heterogeneous catalysts,<sup>[107]</sup> optoelectronic materials,<sup>[234]</sup> photocatalysts,<sup>[235]</sup> as well as adsorbents (namely, for CO<sub>2</sub> capture).<sup>[236]</sup> Especially, CMPs have been targeted as promising materials for energy storage applications.<sup>[109]</sup> The void volume within the materials provides short diffusion pathways and large contact surface areas

for ion charge carries, which results in good electrochemical performances and fast kinetics.<sup>[237, 238]</sup> Furthermore, the cross-linked structure of the polymers prevents the easy dissolution of the CMPs in organic electrolytes, resulting in higher cycling stability.<sup>[239, 237]</sup>

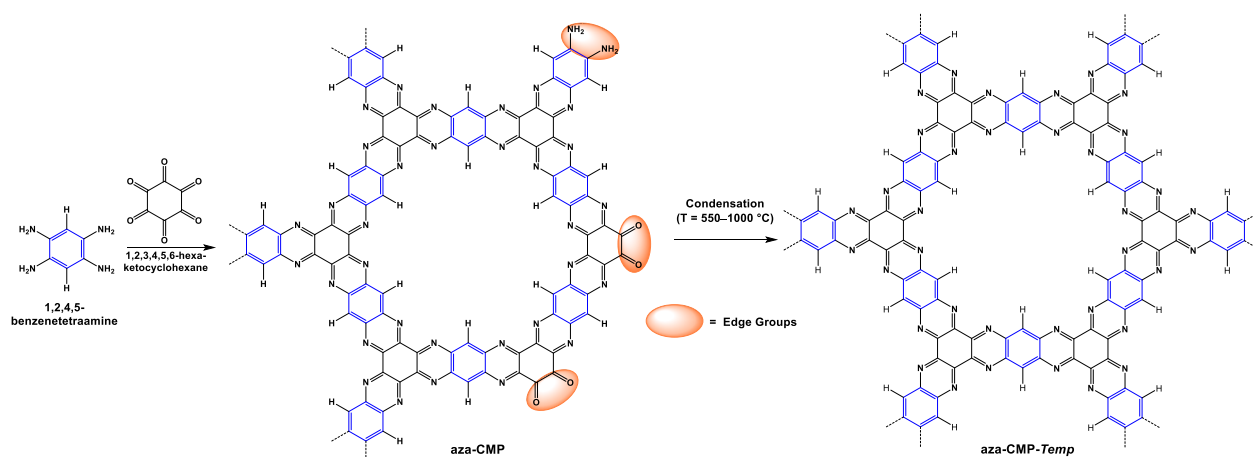
Electrochemical energy storage using rechargeable lithium-ion batteries is employed in numerous portable devices like cell phones, tablets, laptops, and cameras. In addition, the immense effort that is put into the electrification of the transport sector is further consuming the world-wide rare lithium resources.<sup>[141, 142]</sup> Therefore, an alternative to lithium needs to be employed and sodium is experiencing a comeback as a competitive substitution for lithium in the research field of batteries (**Chapter 1.6.2**). Sodium is widely abundant,<sup>[145, 146]</sup> low in cost,<sup>[147]</sup> and offers similar electrochemical properties like lithium.<sup>[147, 148]</sup> Unfortunately, the larger ionic radius of Na<sup>+</sup> ion (102 pm) compared to Li<sup>+</sup> ion (76 pm),<sup>[240]</sup> implicates some problems for the electrochemical performance.<sup>[241]</sup> Namely, it is more difficult to insert Na<sup>+</sup> ions into and extract them from graphite, which is often used as electrode within LIBs, because of its small interlayer distance.<sup>[149]</sup> A lot of research work has been done towards a suitable anode material, as the energy and power density of batteries are highly dependent on the properties of the electrode materials.<sup>[147]</sup> Nitrogen-doping of carbon materials creates active sites for enhanced specific capacities and their integration into a graphitic network increases the electric conductivity, which leads to a better rate performances. So far, a range of CMPs has been applied as electrode materials for LIBs<sup>[239]</sup> and SIBs.<sup>[242, 243]</sup>

In the last chapter of this thesis, a series of nitrogen-doped carbon materials derived from nitrogen-containing conjugated microporous polymer was prepared by high temperature treatment (**Chapter 3.4.2**). The nitrogen content, porosity, and the degree of graphitization were controlled *via* the condensation temperature (**Chapter 3.4.3** and **Chapter 3.4.4**). The influence of the chemical and electronic structure of the aza-CMP-derived carbon materials on their electrochemical performance as anode materials for SIB was investigated in terms of reversible specific capacity, rate capability, and cycling stability (**Chapter 3.4.5**).

### 3.4.2 Thermal treatment of Pyrazine-Fused Conjugated Microporous Polymer

It has been shown that the condensation of preorganized organic molecules as precursors can guide to simplified synthesis routes towards nitrogen-doped porous carbon materials with well-defined structures and unique properties, such as ultrahydrophilicity and nobility. In search of an even higher degree of pre-organization that can result in a more homogeneous and crystalline structure, an appropriate candidate has been found with pyrazine-fused

conjugated microporous polymer (aza-CMP).<sup>\*</sup> In a recently published work, aza-CMP was obtained by the cyclo-condensation of 1,2,4,5-benzenetetraamine and 1,2,3,4,5,6-hexaketocyclohexane in a 1:4 mixture of 1,4-dioxane and acetic acid under reflux conditions.<sup>[244]</sup> In the **Scheme 4**, the solvothermal synthesis route towards an idealized structure of aza-CMP, including presence of residual un-polymerized amine and ketone groups on the edges, is shown. A series of nitrogen-doped carbon materials was synthesized by the thermal treatment of aza-CMP under N<sub>2</sub> flow. The direct condensation at 550, 700, 850, or 1000 °C without any template, solvent, or inorganic porogen resulted in the corresponding materials labelled as aza-CMP-*Temp*, where *Temp* defines the synthesis temperature.



**Scheme 4:** Solvothermal synthesis of aza-CMP and subsequent thermal condensation at 550, 700, 850, or 1000 °C.

### 3.4.3 Structural Characterization of the aza-CMP-derived Carbon Materials

Structural characterization was conducted to provide information about chemical and structural composition of the as-synthesized materials. The aza-CMP-derived carbon materials and the aza-CMP precursor show a comparable microscale thornbush-like morphology (**Figure S 23**). A branched network of bigger bubble-like and thinner sticks-like shapes of several hundred nanometers in size is building up their morphology. The morphology of the aza-CMP precursor can be transferred to the condensed products in a conformal manner.

The aza-CMP precursor has a nitrogen content of 12.5 at.%, and condensation at a moderate temperature of 550 °C is leading to an increase up to 16.0 at.% (EA) and 25.4 at.% (EDX) (**Table 7**). Further increase of the condensation temperature leads to a decrease in nitrogen

<sup>\*</sup> Aza-CMP was synthesized and provided by Prof. Dr. Aurelio Mateo-Alonso and Dr. Alberto Riaño Carerero (University of the Basque Country, Basque Center for Macromolecular Design and Engineering, Donostia-San Sebastian, Spain).

content of 14.6 at.% and 12.9 at.% for aza-CMP-700 and aza-CMP-850, respectively. According to EA results, aza-CMP-550 and aza-CMP-700 show  $C_{3.4}N$  and  $C_{4.2}N$  ratios, respectively. Even at 1000 °C synthesis temperature a nitrogen content of 7.2 at.% is preserved. As expected, the highest oxygen content with 16.1 at.% can be found for the precursor material, which is decreasing upon condensation. Good yields were obtained for condensation of aza-CMP at 550 °C and 700 °C with 68 % and 58 %, respectively, and still moderate yields at higher synthesis temperatures of 850 °C and 1000 °C with 47 % and 41 %, respectively. The yields of the aza-CMP-derived carbon materials (~40–70 %, **Table 7**) are higher compared to the yields of the HAT-CN-derived materials (~25–50 %, **Table 1**). The aza-CMP precursor is already more condensed than HAT-CN, subsequently a rather textural and structural change occurs during the condensation of aza-CMP at high temperatures.

**Table 7:** EA, EDX,  $I_D/I_G$  ratio, and experimental yield data summary of aza-CMP, aza-CMP-550, aza-CMP-700, aza-CMP-850, and aza-CMP-1000.

Material	C / at.%		N / at.%		H / at.%		O / at.%		Yield / %	$I_D/I_G$
	EA	EDX	EA	EDX	EA	EDX	EA	EDX		
<b>aza-CMP</b>	41.3	64.3	12.5	25.4	30.2	-	16.1	10.3	-	0.72
<b>aza-CMP-550</b>	53.9	66.4	16.0	29.9	22.6	-	7.4	3.7	68	1.16
<b>aza-CMP-700</b>	61.7	73.8	14.6	24.4	17.6	-	6.1	2.0	58	1.18
<b>aza-CMP-850</b>	72.0	81.9	12.9	16.9	11.9	-	3.1	1.2	47	1.49
<b>aza-CMP-1000</b>	78.4	90.5	7.2	8.1	10.5	-	3.9	1.5	41	2.42

The structural change upon condensation of aza-CMP can be further followed by PXRD measurements (**Figure 32a** and **Figure 32b**). For aza-CMP two peaks at  $11.7^\circ 2\theta$  and  $26.9^\circ 2\theta$  can be seen. Due to the high temperature treatment, the low angle peak at  $11.7^\circ 2\theta$  disappears and the latter peak is shifted to smaller angles  $25.2^\circ$ ,  $25.7^\circ$ ,  $25.6^\circ$ , and  $26.5^\circ 2\theta$  for aza-CMP-550, aza-CMP-700, aza-CMP-850, and aza-CMP-1000, respectively. Furthermore, a peak arises at the angle of  $\sim 43\text{--}44^\circ 2\theta$ . Thus, a structural development can be clearly noted due to the disappearance of bigger channels that can be assigned to the peak at lower angles  $11.7^\circ 2\theta$ . Interestingly, the most intensive peak at  $25\text{--}26^\circ 2\theta$  lost intensity at 550 °C, and gained again intensity the higher the synthesis temperature gets. The appearance of peaks at higher angles  $\sim 25\text{--}26^\circ 2\theta$  and  $\sim 43\text{--}44^\circ 2\theta$  indicates the stacking of carbon materials without channels.

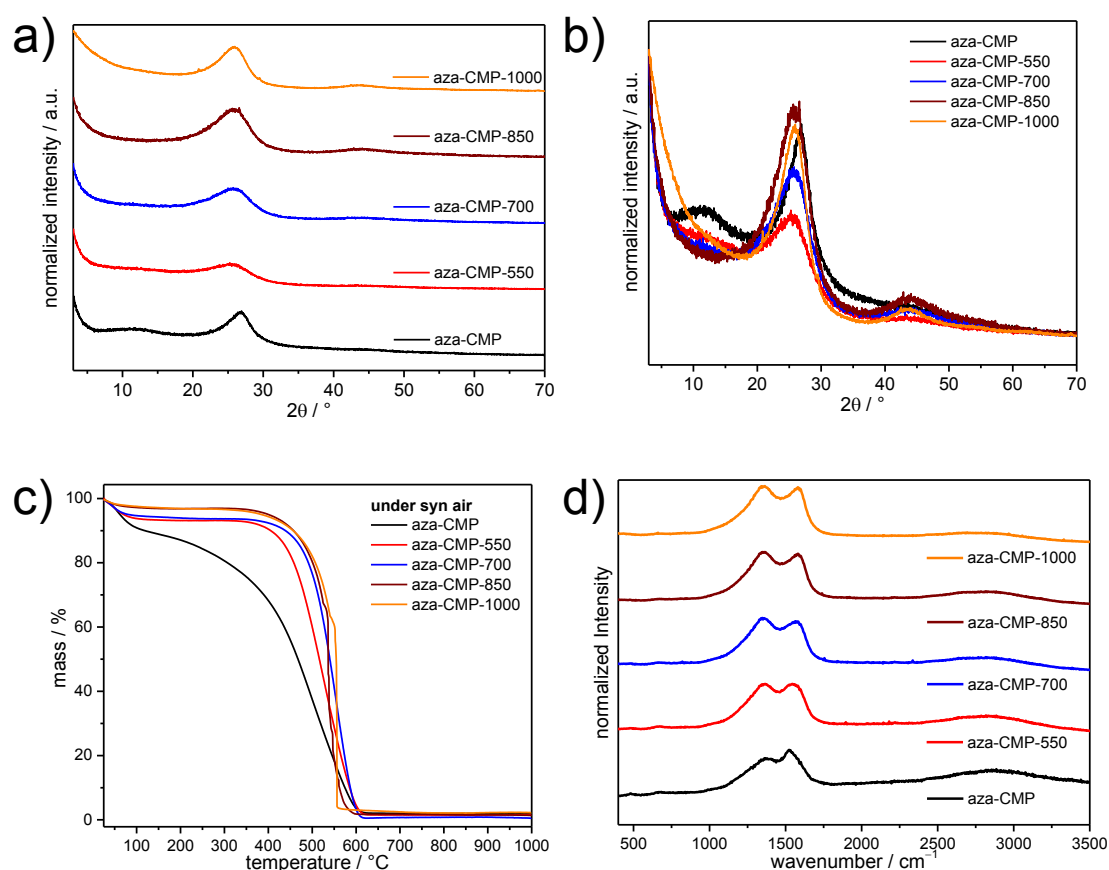


**Figure 32:** PXRD patterns (a) and (b), TGA measured under synthetic air with a heating rate of  $5 \text{ K min}^{-1}$  (c), and Raman spectra (d) of aza-CMP, aza-CMP-550, aza-CMP-700, aza-CMP-850, and aza-CMP-1000.

TGA under synthetic air shows that aza-CMP-850 and aza-CMP-1000 reveals the highest decomposition temperature up  $\sim 550 \text{ }^\circ\text{C}$ , and thus highest oxidation resistance (**Figure 32c**). Aza-CMP itself exhibits a continuous decomposition beginning from  $100 \text{ }^\circ\text{C}$  over the whole range until full combustion at  $600 \text{ }^\circ\text{C}$ . No impurities or residual inorganic compounds can be found in the precursor and aza-CMP-derived carbon materials.

Raman spectroscopy helps to evaluate the degree of graphitization by analyzing the ratio of the full width half maximum of the D-band and G-band (**Figure 32d**, **Table 7**, and **Figure S 24a–e**). The Raman spectra were fitted using a four-peak-model with a full Gaussian function (Figure S 24). The four bands were assigned to D1 (breathing mode of  $\text{sp}^2$ -carbon atoms in aromatic rings), D2 (*trans*-polyacetylene-like chains at layer edges), G1 (disordered  $\text{sp}^2$ -carbon organized in chains or rings), and G2 (ordered  $\text{sp}^2$ -carbon organized in chains or rings). The  $I_{\text{D}}/I_{\text{G}}$  ratio increases from 0.72, 1.16, 1.18, 1.49, and 2.42 according to the synthesis temperature for aza-CMP, aza-CMP-550, aza-CMP-700, aza-CMP-850, and aza-CMP-1000, respectively (**Table 7**). This is due to the on-going formation of a pristine carbon phase with the smaller amount of pyrazinic nitrogen atoms and favored organization in  $\text{sp}^2$ -

bonded carbon atoms in six rings. This should result in a higher electric conductivity for the high temperature samples.

HRTEM images (**Figure 33a–c**) were applied for a more detail investigation of the carbon microstructure of the aza-CMP-derived materials. Aza-CMP and aza-CMP-550 show a more uniform disordered nanostructure confirming their amorphous nature. While the influence of higher condensation temperature for aza-CMP-1000 clearly show local ordered parallel laminar nanostructure characterized by graphitic nanodomains. The HRTEM findings are in good agreement with PXRD patterns and Raman spectroscopy.

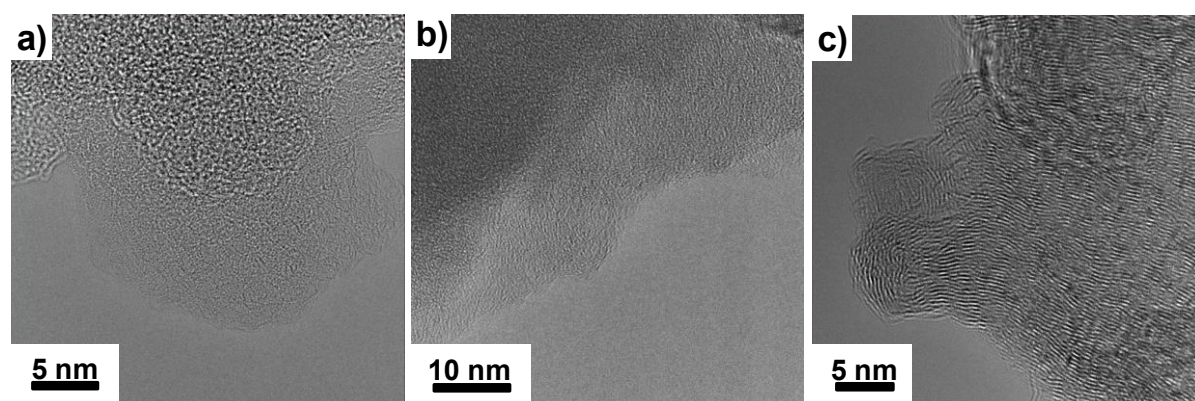


**Figure 33:** HRTEM images of aza-CMP (a), aza-CMP-550 (b), and aza-CMP-1000 (c).

XPS measurements (**Figure S 25a–d**) were conducted to determine the chemical and the electronic states of carbon and nitrogen atoms in the aza-CMP-derived materials. Deconvolution of the N1s line scans (**Figure 34a–d**, **Table S 7**, **Table S 8**, and **Table S 9**) show the appearance of pyrazinic and pyrrolic nitrogen atoms at binding energies of  $\sim 398$  eV and  $\sim 400$  eV, respectively. The small peak at  $\sim 403$  eV corresponds to quaternary nitrogen atoms or oxidized nitrogen species. The nitrogen content of the samples can be controlled by the synthesis temperature from 550 °C (19.4 at.%) to 1000 °C (5.6 at.%). Importantly, the highest pyrazinic nitrogen content compared to other nitrogen species is found in the aza-CMP-550 sample. The temperature increase leads to the depletion of pyrazinic nitrogen atoms, while the content of thermally more stable graphitic nitrogen atoms decreases less.

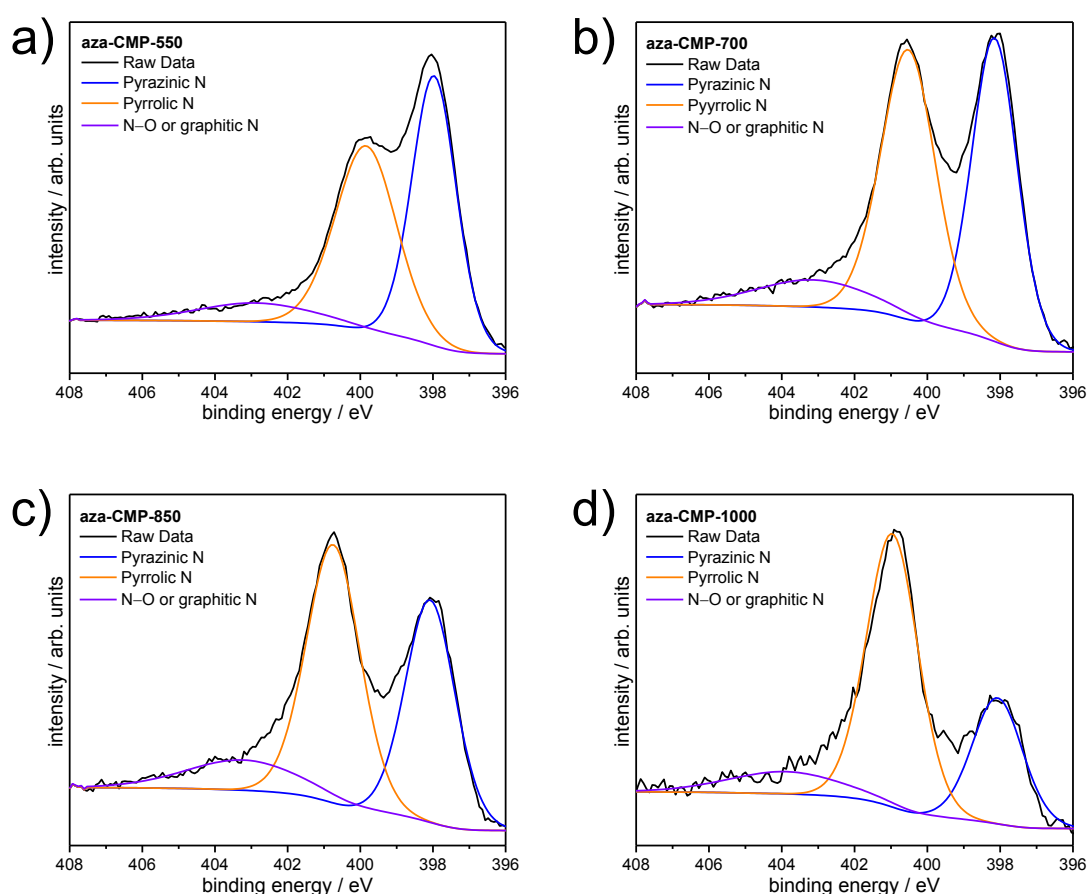


**Figure 34:** Fitted N1s XPS line scans of aza-CMP-550 (a), aza-CMP-700 (b), aza-CMP-850 (c), and aza-CMP-1000 (d).

Deconvolution of the C1s line spectra (**Figure 35a–d**, **Table S 7**, **Table S 8**, and **Table S 9**) exhibits a peak at  $\sim 284$  eV that corresponds to graphitic C=C carbon atoms. Two peaks at  $\sim 286$  eV and  $\sim 287$  eV belong to  $sp^2$ -hybridized carbon atoms that are bonded to nitrogen atoms, while the peaks in the range of  $\sim 288$ – $294$  eV correspond to oxidized carbon atoms. Interestingly, the graphitic C=C carbon content decreases from 550 °C (59.17 at.%), to 700 °C (39.99 at.%) and 850 °C (39.77 at.%), while it increases again at 1000 °C (47.26 at.%). This is indicating a structural change and reorganization. In the aza-CMP-550 sample most of the carbon atoms are in a graphitized state or bonded with nitrogen, while almost no carbon atoms are bonded to oxygen. This means that all the carbon atoms can contribute to the electron transport throughout the materials backbone for sufficient electric conductivity and good charge transport towards the nitrogen adsorption sites, both favoring the electrochemical performance of the material.

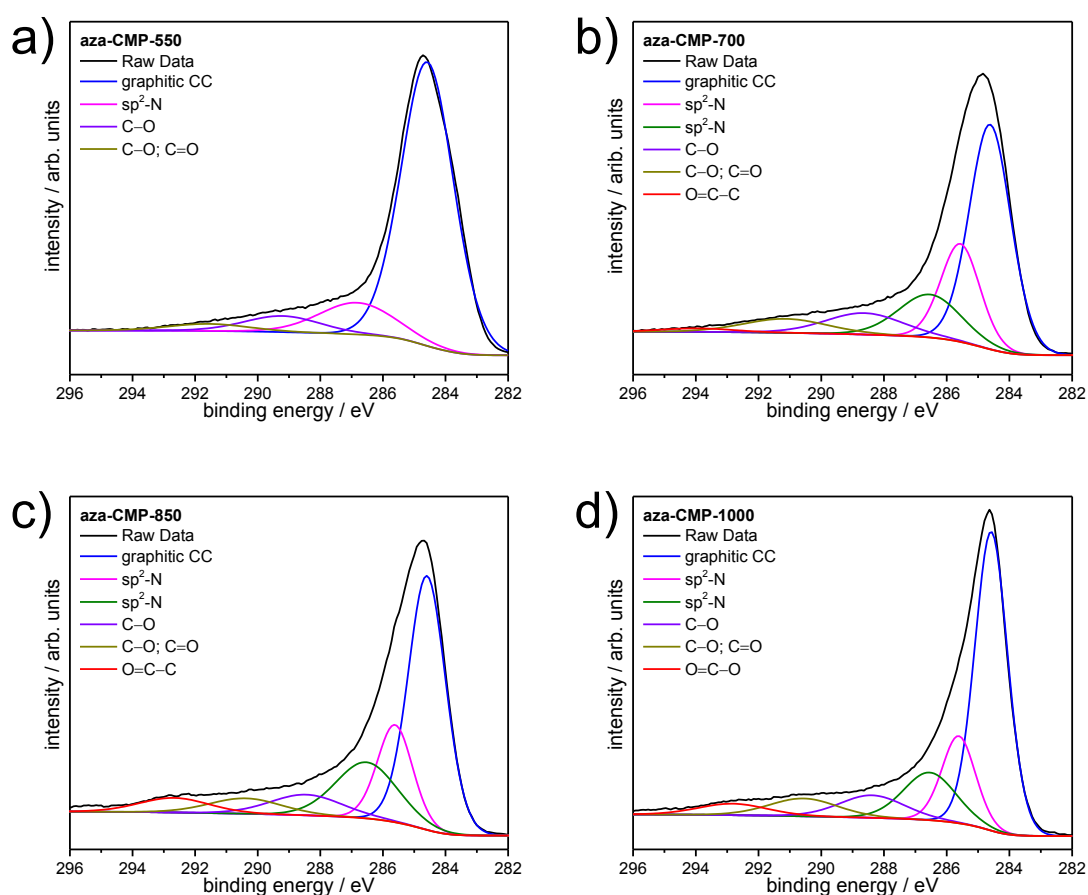


**Figure 35:** Fitted C1s XPS line scans of aza-CMP-550 (a), aza-CMP-700 (b), aza-CMP-850 (c), and aza-CMP-1000 (d).

Deconvolution of the O1s line spectra (**Figure S 26a–d**, **Table S 7**, **Table S 8**, and **Table S 9**) reveals two peaks at ~531 eV and ~533 eV that correspond to oxygenated carbon atoms C–O and C=O, respectively. Interestingly, the relative content of C–O decreases compared to the content of C=O from 550 °C to 1000 °C with the C–O/C=O ratios 1.36 and 0.74, respectively. The overall oxygen content is low for all the prepared samples (~2–4 at.%).

The full line scan as well as all single peaks can be found almost on the same binding energies, indicating the same working potential for the electrons throughout the series of samples. This allows drawing conclusions on the influence of the different bonding states of the carbon and nitrogen atoms on their influence on the electrochemical performance of the aza-CMP-derived materials. Aza-CMP-550 reveals the highest amount of graphitic carbon atoms and the highest nitrogen content that is underlining its greatest potential as anode material for SIB within the aza-CMP-derived series. All in all, the XPS measurements are giving insight into well-defined the atomic construction that can be obtained by using CMPs

as precursors, as well on the influence of the different bonding states of the nitrogen and carbon atoms on the electrochemical performance of the materials.

### 3.4.4 Structure-related Physisorption Properties of the aza-CMP-Derived Carbon Materials

$N_2$  physisorption experiments were conducted at 77 K and gave insight into the change in porosity of the condensation process on the precursor aza-CMP (**Figure 36a** and **Table 8**). All isotherms are typical type III isotherms with a slight appearance of a type H3 hysteresis according to IUPAC classifications.<sup>[26]</sup> This means that the precursor and the aza-CMP-derived carbon materials reveal small amounts of adsorbed gas at low relative pressures, and show a step in the gas uptake close to the saturation pressure. The hysteresis affects the desorption branch and is often observed for aggregates of plate-like particles, as can be seen with the morphology of the aza-CMP-derived materials. The condensation at 550 °C leads to an increase in  $SSA_{BET}$  and  $V_{total}$  with  $170 \text{ m}^2 \text{ g}^{-1}$  and  $0.26 \text{ cm}^3 \text{ g}^{-1}$  compared to aza-CMP with  $109 \text{ m}^2 \text{ g}^{-1}$  and  $0.22 \text{ cm}^3 \text{ g}^{-1}$ , respectively. A higher condensation temperature apparently leads to a fusing of the aza-CMP structure towards a graphitic carbon, as well as blocking of pores and pore pathways, which results in lower  $SSA_{BET}$  of 98, 128, and  $107 \text{ m}^2 \text{ g}^{-1}$  for aza-CMP-700, aza-CMP-850, and aza-CMP-1000, respectively (**Figure 36a** and **Table 8**). The idealized structure of the aza-CMP-derived carbon materials shown in **Scheme 4** would lead to an assumption of higher surface areas ( $\sim 1000\text{--}2000 \text{ m}^2 \text{ g}^{-1}$ ), in the range of MOFs or porous organic frameworks. But, already during the synthesis of the aza-CMP precursor the pore size is big enough to host the monomer molecules, leading to blocked pores and pathways. In consequence, by far lower specific surface areas are obtained for the aza-CMP-derived carbon materials upon condensation of the aza-CMP precursor.

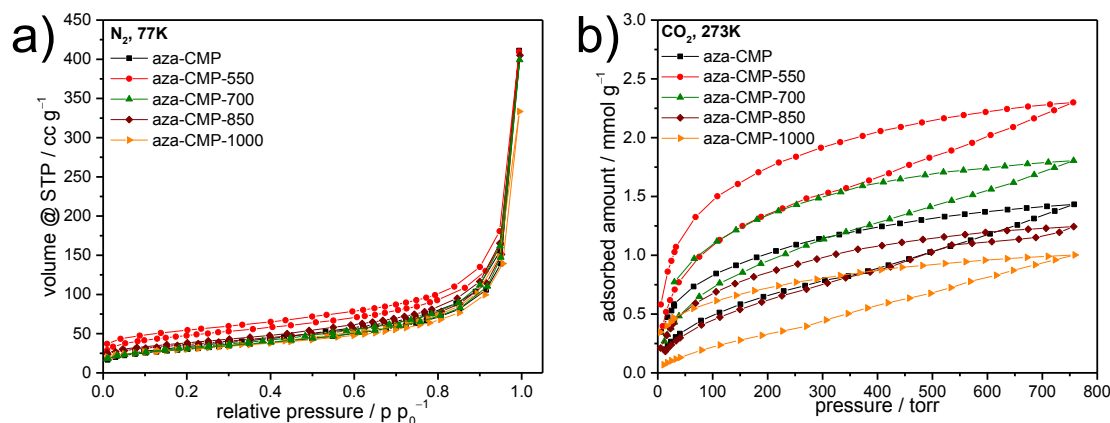


**Figure 36:**  $N_2$  physisorption isotherms (77 K) (a) and  $CO_2$  physisorption isotherms (273 K) (b) of aza-CMP, aza-CMP-550, aza-CMP-700, aza-CMP-850, and aza-CMP-1000.

**Table 8:**  $N_2$  physisorption (77 K) data summary of aza-CMP, aza-CMP-550, aza-CMP-700, aza-CMP-850, and aza-CMP-1000.

Material	$SSA_{BET} / m^2 g^{-1}$	$SSA_{DFT} / m^2 g^{-1}$	$V_{total} / cm^3 g^{-1}$
aza-CMP	109	96	0.22
aza-CMP-550	170	187	0.26
aza-CMP-700	110	97	0.23
aza-CMP-850	128	132	0.23
aza-CMP-1000	107	107	0.22

These structure-related gas adsorption properties of the aza-CMP-derived materials are even more pronounced in  $CO_2$  physisorption measurements recorded at 273 K (**Figure 36b**). Due to the high nitrogen content and low accessible  $SSA_{BET}$  for  $N_2$ , a strong polarization and affinity of the materials towards  $CO_2$  can be expected. And indeed, all isotherms show a rather convex shape with significant uptake at low relative pressures and a hysteresis due to the high energy required for the desorption of  $CO_2$ . Again, moderate synthesis conditions of 550 °C and 700 °C (2.29 mmol  $g^{-1}$  for aza-CMP-550, 1.80 mmol  $g^{-1}$  for aza-CMP-700) leads to increase of the  $CO_2$  gas uptake, while aza-CMP (1.43 mmol  $g^{-1}$ ), aza-CMP-850 (1.24 mmol  $g^{-1}$ ), and aza-CMP-1000 (1.00 mmol  $g^{-1}$ ) reveal a decrease in  $SSA_{BET}$  with higher synthesis temperature, as shown in the same trend with  $N_2$  physisorption isotherms.

### 3.4.5 Aza-CMP-derived Carbon Anode Materials for Sodium-Ion Battery

The electrochemical performance of the aza-CMP-derived carbon materials was tested in a Swagelok-type test cell. The electrolyte was 1 M  $NaClO_4$  in ethylene carbonate/propylene carbonate/fluoroethylene carbonate (45:45:10 by mass), and sodium metal (11 mm in diameter) was used as both counter and reference electrodes. This kind of half-cell setup describes the common testing conditions for sodium-ion hybrid capacitors, but it is also suitable to evaluate the carbon materials as anode materials for SIB.

**Figure 37** shows the cyclic voltammetry (CV) curves of the aza-CMP-derived carbon materials at a scanning rate of 0.1  $mV s^{-1}$  in the voltage range of 0–2.5 V. The irreversible sharp peak around 0.0 V of all samples can be assigned to the reaction of electrolyte with surface functional groups and the formation of solid electrolyte interphase (SEI) layer. Aza-CMP-550 contains a higher number of functional groups due to a lower condensation temperature. Its larger  $SSA_{BET}$  can promote more side reactions that result in a lower initial Coulombic efficiency. The aza-CMP-850 and aza-CMP-1000 electrodes revealed a sharp redox peak around 0.2 V, which can be explained by the reversible sodium insertion into and

extraction from the nanovoids of the hard carbon material. Aza-CMP-550 and aza-CMP-700 show typical battery-type CV curves due to the adsorption of sodium on the abundant nitrogen-containing groups present in the aza-CMP-derived carbon materials.

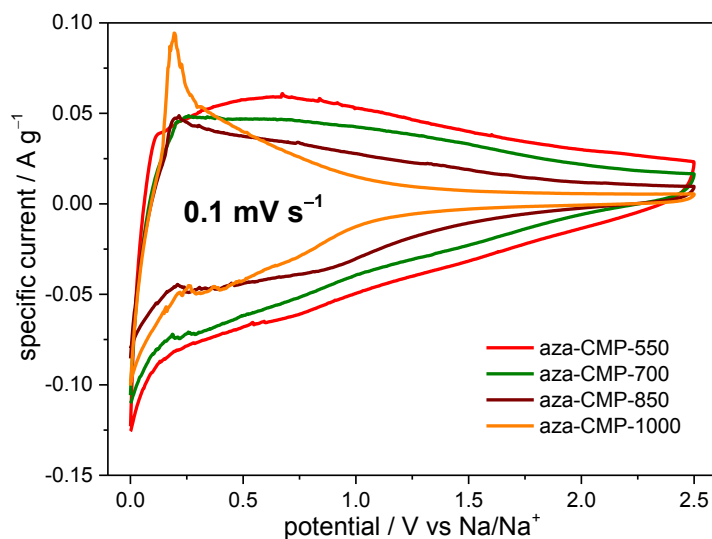


**Figure 37:** Electrochemical performance of the aza-CMP-derived carbon materials. CV curves at a scanning rate of  $0.1 \text{ mV s}^{-1}$  of aza-CMP-550, aza-CMP-700, aza-CMP-850, and aza-CMP-1000.

**Figure 38a–d** shows the galvanostatic charge/discharge curves of the four aza-CMP-derived carbon electrodes at different current densities between  $0.1\text{--}10 \text{ A g}^{-1}$  in the voltage range of  $0\text{--}2.5 \text{ V}$  and allows the quantification of the rate capability. The difference in sodium storage capacity in the plateau and sloping regions is due to the difference in the microstructure between the four materials. The capacity in the steep slope region of high potential range ( $\sim 2.00\text{--}2.50 \text{ V}$ ) can be due to the reaction of sodium with residual sites (e.g., oxygen containing functional groups like carbonyl or ketone groups) on the materials. The capacity in the slope region in the moderate potential range ( $\sim 0.15\text{--}2.00 \text{ V}$ ) can be corresponded to a cooperative mechanism of intercalation and reversible chemical adsorption of sodium ions between the layers of the aza-CMP-derived carbon materials and on the nitrogen-containing sites, and are common capacitive-type curves and not battery-like behavior. As all the materials have relatively low porosity, which shows the importance of heteroatom sites for efficient sodium storage. As expected, all of the aza-CMP-derived carbon materials show a decrease in the specific capacity with increasing current densities. The decrease of capacity in this region of aza-CMP-550, -700, -850, and -1000 can be correlated to the nitrogen content of 16.0, 14.6, 12.9, and 7.2 at.% according to EA, respectively. The capacity in the plateau region in the low potential range ( $\sim 0.00\text{--}0.15 \text{ V}$ ) can be attributed to the increasing repulsion

of negative charges within the backbone of the carbon materials and the positive charges of the adsorbed sodium ions. This leads to the inevitable end of the storage capacity. The plateau region gets more pronounced with decreasing nitrogen content in the series of the aza-CMP-derived carbon materials. The lower nitrogen content of the aza-CMP-1000 leads to a smaller accumulation of sodium ions, and in consequence reaches slower the storage limits due to less charge repulsion.

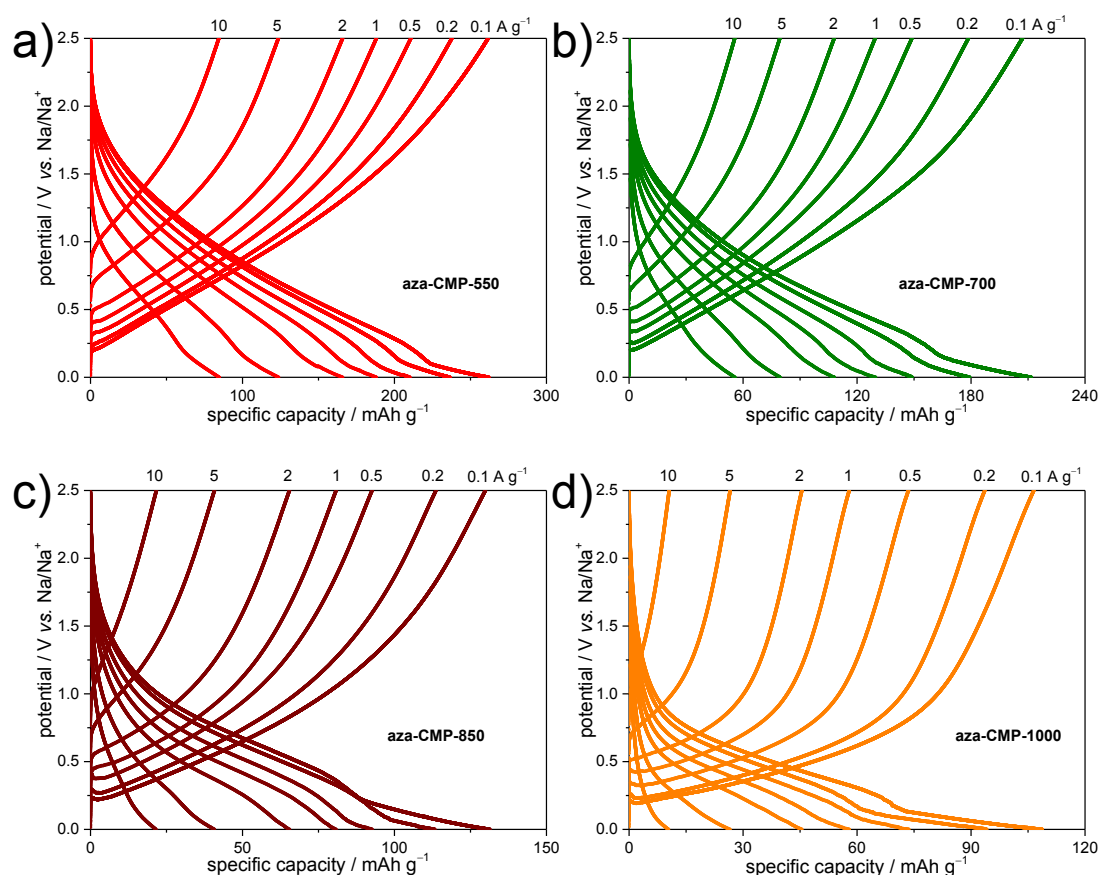


**Figure 38:** Galvanostatic discharge/charge profiles at current rate of  $0.1 \text{ A g}^{-1}$  to  $10 \text{ A g}^{-1}$  of aza-CMP-550 (a), aza-CMP-700 (b), aza-CMP-850 (c), and aza-CMP-1000 (d).

The rate performance was further measured to investigate the kinetic properties of the aza-CMP-derived electrodes condensed at different temperatures (**Figure 39a**). At a low specific current of  $0.1 \text{ A g}^{-1}$ , the initial discharge capacity of aza-CMP-550, -700, -850, and -1000, as well as the aza-CMP precursor reaches 570, 531, 369, 301, and 182  $\text{mAh g}^{-1}$ , while the corresponding initial charge capacity decreases to 281, 240, 145, 122, and 70  $\text{mAh g}^{-1}$ , respectively. At a higher specific current of  $10 \text{ A g}^{-1}$ , the specific capacity of aza-CMP-550, -700, -850, and -1000, as well as aza-CMP precursor obtain again 85, 56, 22, 11, and

1 mAh g<sup>-1</sup>, which corresponds to capacity retention of 32.3, 26.5, 16.7, and 10.1 %, respectively.

The reversible capacity at the specific current of 0.1 A g<sup>-1</sup> of aza-CMP-550, aza-CMP-700, aza-CMP-850, aza-CMP-1000, and aza-CMP precursor are determined after 40 cycles to be around 265, 209, 131, 107, and 68 mAh g<sup>-1</sup>, respectively. This reflects the result of the galvanostatic charge/discharge curves, that is, corresponding to the increase of the nitrogen content at lower condensation temperatures and a higher SSA<sub>BET</sub>, superior rate capability is resulting for aza-CMP-550.

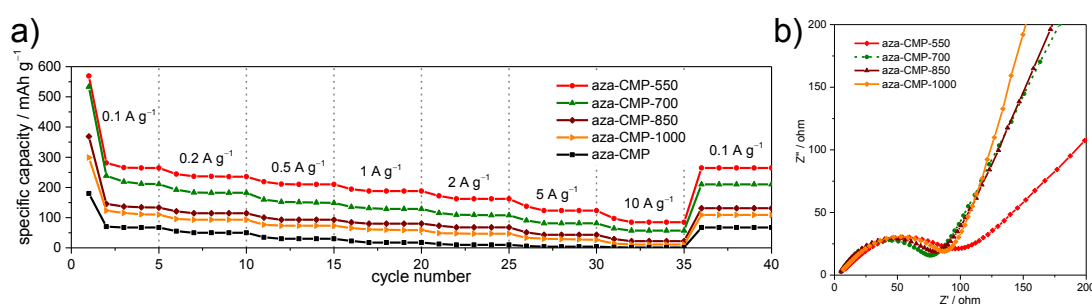


**Figure 39:** Rate capability from 0.1 A g<sup>-1</sup> to 10 A g<sup>-1</sup> (a) of aza-CMP and aza-CMP-derived carbon materials, and EIS (b) of aza-CMP-550, aza-CMP-700, aza-CMP-850, and aza-CMP-1000.

The rate capability can be further analyzed by electrochemical impedance spectroscopy (EIS) measurements, illustrated in the Nyquist Plot (**Figure 39b**). All aza-CMP-derived electrodes show impedance curves of the electrodes that are composed of a semicircle curve in the high frequency range and a straight slope line in the low frequency range. The diameter of the semicircle describes the charge transfer resistance between the electrode and the electrolyte. Aza-CMP-700 and aza-CMP-850 show similar charge transfer resistance, lower than aza-CMP-1000, indicating faster redox reaction kinetics in those electrodes. This is surprising due to the highest degree of  $\pi$ -conjugation and order in the aza-CMP-1000, which should result in the highest electric conductivity. Aza-CMP-550 exhibits with the biggest semicircle the highest electronic and ionic resistance, because of its lower electric conductivity, which is likely a result of the high content of pyrazinic nitrogen. The cycling stability of the aza-CMP-550 sample was tested at 0.5 A g<sup>-1</sup> for 1000 deep charging-discharging cycles, in which 96 % of the initial capacity was recovered. This describes a very high stability that is unusual for battery (**Figure 40**).

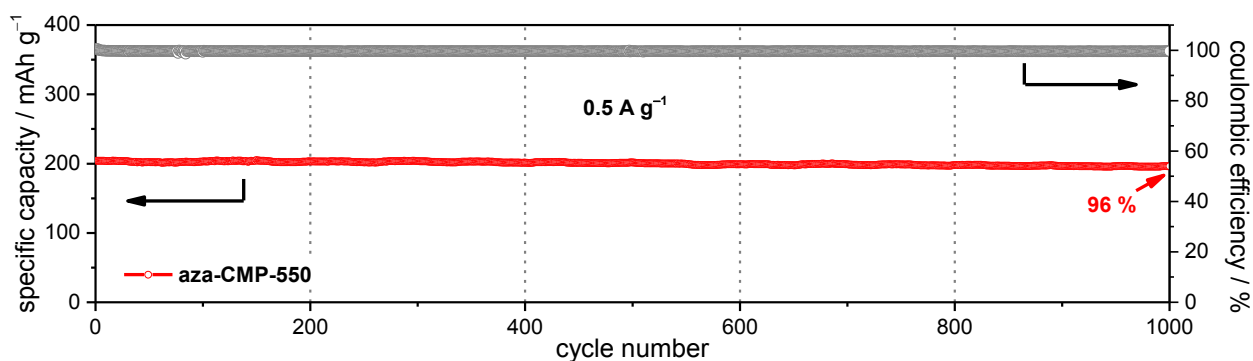


**Figure 40:** Cycling test of aza-CMP-550 at  $0.5 \text{ A g}^{-1}$  for 1000 cycles.

The best overall performance among the aza-CMP-derived carbon materials exhibits aza-CMP-550 with reversible sodium storage capacities of about 265, 188, 125, and  $85 \text{ mAh g}^{-1}$  at current densities of 0.1, 1, 5, and  $10 \text{ A g}^{-1}$ , respectively. Its superior specific capacity and rate capability can be related to the high nitrogen content (16 at.% according to EA), sufficient open nanoporous structure ( $\text{SSA}_{\text{BET}} \sim 170 \text{ m}^2 \text{ g}^{-1}$ ), and a still convenient electric conductivity due to delocalized electrons. The abundant nitrogen-containing active sites provide high energy stabilization sites for the adsorption of sodium ions, while sodium can also intercalate in the available graphitic domains, both favoring a better capacity performance. The aromatic  $\pi$ -conjugation throughout the polymer skeleton provides sufficient electric conductivity, which favors the electron transport, and thus leads to good rate capability.

Within the last chapter in this thesis, a series of nitrogen-doped porous carbon materials was obtained by the direct condensation of a pyrazine-fused conjugated microporous polymer. The precursor aza-CMP has significant nitrogen content in form of pyrazinic nitrogen atoms well-distributed in the polymer framework, and an inherent microporous structure. The aromatic  $\pi$ -conjugation throughout the polymer skeleton results in a desirable electric conductivity. These beneficial properties were transferred by thermal condensation into aza-CMP-derived carbon materials. The remarkable nitrogen content, sufficient graphitization degree, and desirable electric conductivity make the aza-CMP-derived materials appropriate anode materials for sodium-ion batteries and sodium-ion hybrid capacitors. The investigated structure-related performance in the electrochemical tests exhibit remarkable reversible specific capacity, sufficient rate capability, and cycling performance, for the best performing material aza-CMP-550 with the highest nitrogen content and  $\text{SSA}_{\text{BET}}$ . Overall, a new sodium storage mechanism for sodium-ion battery was elaborated that has not been reported so far. The storage capacity of the aza-CMP-derived carbon electrodes is composed of capacitive-type curves in the slope

region with intercalation and chemical adsorption of sodium ions between the layers of the aza-CMP-derived carbon materials and the nitrogen-containing adsorption sites.





## 4 Summary, Conclusions, and Perspectives

The aim of this thesis was the development of novel synthesis pathways towards nitrogen-doped nanoporous noble carbon materials with precise design on a molecular level and understanding of their structure-related performance in energy and environmental applications, namely gas adsorption and electrochemical energy storage. Herein, four main topics were elaborated that are related to synthesis, refinement, and application of novel carbon materials.

The first topic (**Chapter 3.1**) described template-free synthesis approach towards highly nitrogen-doped carbon materials. The thermal condensation of the organic molecule HAT-CN led to purely microporous materials with remarkable  $SSA_{\text{BET}}$  of  $\sim 600\text{--}800\text{ m}^2\text{ g}^{-1}$  and  $V_{\text{total}}$  of  $0.24\text{--}0.32\text{ cm}^3\text{ g}^{-1}$ , without the use of any metal, solvent, or additional washing step. The  $\text{C}_2\text{N}$ -type stoichiometry and pyrazinic nitrogen structure motives are pre-dictated by the structure of HAT-CN. The high thermal stability of the precursor HAT-CN was transferred towards the thermal and oxidation stability of the noble carbon structure, which is exceeding the stabilities of carbon materials obtained by classical carbon precursors, such as carbohydrates or biomaterials. This describes one typical feature of noble carbon materials, which is the thermal decomposition into stable monomers rather than oxidation. The significant nitrogen content (up to 33 at.%) and narrow microporosity in the HAT-CN-derived materials led to high uptake of guest molecules, such as  $\text{H}_2\text{O}$  and  $\text{CO}_2$  at low concentrations. These outstanding gas adsorption properties were so far only achieved by materials like MOFs or zeolites. Nevertheless, the  $\text{CO}_2/\text{N}_2$  selectivities of the HAT-CN-derived carbon materials were comparably low (i.e., C-HAT-CN-550 with 63.8 at 298 K and  $\text{N}_2/\text{CO}_2$  ratio of 90/10). This can be explained by too large pore size that can host remarkable amount of  $\text{N}_2$  and the polar character of the pore wall that are also leading to strong interaction with polarizable  $\text{N}_2$ .

Following up with the enhancement of the  $\text{CO}_2/\text{N}_2$  selectivity, the molecular sieving of  $\text{CO}_2$  *via* kinetic size exclusion of  $\text{N}_2$  was explored by molecularly designed HAT-CN-derived

carbon materials in the **Chapter 3.2**. The precise control over the degree of condensation of HAT-CN led to defined atomic construction and porosity of the resulting materials. At a condensation temperature of 525 °C, pores are large and polarizing enough to host CO<sub>2</sub>, but only negligible amount of N<sub>2</sub> can be adsorbed into the pore system due to size exclusion. This results in high CO<sub>2</sub> adsorption capacities, as well as outstanding CO<sub>2</sub>/N<sub>2</sub> selectivity (C-HAT-CN-525 with 121 at 298 K and N<sub>2</sub>/CO<sub>2</sub> ratio of 90/10) and a high Q<sub>st</sub> of CO<sub>2</sub> adsorption (up to 52 kJ mol<sup>-1</sup>). This material has several anchor points for CO<sub>2</sub>, provided by negatively polarized nitrogen atoms and positively polarized carbon atoms, which ultimately lead to a high CO<sub>2</sub> affinity. This excellent performance is due to the synergy of strong interactions with CO<sub>2</sub> and the narrow pore size of the HAT-CN-derived carbon materials.

The **Chapter 3.3** elucidated the combination of the ultrahydrophilic character of the pore walls and the narrow microporosity of HAT-CN-derived carbon materials and its influence on interface effects with more polar guest molecules than CO<sub>2</sub>, namely H<sub>2</sub>O and NH<sub>3</sub>. The strength of the interactions was determined by H<sub>2</sub>O vapor physisorption experiments at different temperatures. C-HAT-CN-700 reached an impressively high Q<sub>st</sub> of H<sub>2</sub>O adsorption of ~60 kJ mol<sup>-1</sup>. This value is exceeding the heat of liquid H<sub>2</sub>O evaporation. In other words, the hydrogen bonding interactions between HAT-CN-derived materials and H<sub>2</sub>O are stronger than between liquid H<sub>2</sub>O-H<sub>2</sub>O molecules. The extremely high affinity towards NH<sub>3</sub> gas was characterized by NH<sub>3</sub>-TPD and thermal response measurements (+60 °C temperature change upon adsorption, -10 °C upon desorption) using the InfraSORP technique. Mass-related and V<sub>micro</sub>-related thermal response peak area of C-HAT-CN-550 (363 mg<sup>-1</sup> cm<sup>-3</sup>) were outperforming (around five times as high as) the reference heteroatom-free microporous carbon TiC-CDC (74 mg<sup>-1</sup> cm<sup>-3</sup>). The strong temperature decrease during NH<sub>3</sub> desorption and accordingly the sufficient cooling effect is due to the desorption enthalpy of NH<sub>3</sub> from the pores of the HAT-CN-derived materials.

In **Chapter 3.4**, another series of nitrogen-doped carbon materials was synthesized by direct condensation of a pyrazine-fused conjugated microporous polymer. The structure-related performance of the resulting materials as anode materials for sodium-ion batteries and sodium-ion hybrid capacitors was investigated. The content of pyrazinic nitrogen atoms well-distributed in the backbone and the degree of graphitization could be controlled by the condensation temperature. The unique feature of the materials is its  $\pi$ -conjugation throughout the carbon-rich aromatic skeleton, which favors electric conductivity. The nitrogen-containing moieties provide binding sites for sodium that leads to a high reversible specific capacity,

while higher electric conductivity enhances the rate capability. The electrochemical tests with the resulting materials used as anodes for SIBs exhibited sufficient reversible specific capacity and good rate capability for the sample prepared at a temperature of 550 °C, due to a sufficient nitrogen content,  $SSA_{\text{BET}}$ , and electric conductivity.

In conclusion, the results presented in this thesis have demonstrated that the molecular design of nitrogen-doped carbon materials is a valuable approach to fabricate materials with a high concentration of heteroatoms, which are bonded in well-defined structural motives. If the porosity can be fine-tuned at the same time, then these materials can serve as case examples to gain important fundamental knowledge of interactions between nitrogen-doped carbon materials and different guest species.

Some of the open questions include the mechanism of transport of the guest species and the importance of providing additional transport pathways through the pore network of the materials. The additional presence of mesopores in a hierarchical pore system, as well as a smaller particle size could enhance the uptake of the materials in gas adsorption applications but could also lead to lower selectivity. The introduction of cations into the framework could provide an additional anchor points for polar guest molecules, resulting, for example, in enhanced  $\text{CO}_2$  adsorption heat, capacity, and selectivity. Novel precursor molecules with different heteroatoms and functionalities could be beneficial to achieve other interactions between materials and guest molecules. The structure-related performance of such carbon materials could be further employed for the investigation of the separation of other relevant gas mixtures. Furthermore, conductive composites could be created to overcome the limiting electric conductivity of the materials. This could open up a whole new range of applications in electrocatalysis, batteries, or supercapacitors.



## 5 Bibliography

- [1] YaleEnvironment<sup>360</sup> (2019), published at the Yale School of Forestry & Environmental Studies, from <https://e360.yale.edu/features/how-the-world-passed-a-carbon-threshold-400ppm-and-why-it-matters>.
- [2] W.-M. To, and P. K. C. Lee, *Energies* **2017**, *10*, 11, 1883-1896.
- [3] S. Lorek, and J. H. Spangenberg, *J. Clean. Prod.* **2014**, *63*, 33-44.
- [4] T. A. Boden, G. Marland, and R. J. Andres, **2017**, *Global, Regional, and National Fossil-Fuel CO<sub>2</sub> Emissions. Carbon Dioxide Information Analysis Center, Oak Ridge National Laboratory, U.S. Department of Energy, Oak Ridge, Tenn., U.S.A.*
- [5] R. Arango-Miranda, R. Hausler, R. Romero-Lopez, M. Glaus, and S. P. Ibarra-Zavaleta, *Energies* **2018**, *11*, 2668-2684.
- [6] T. C. Michael, J. Paulina, and H. Bri-Mathias, *Environ. Res. Lett.* **2018**, *13*, 1, 014004.
- [7] G. A. Olah, T. Mathew, A. Goeppert, and G. K. Surya Prakash, *Top. Catal.* **2018**, *61*, 7, 522-529.
- [8] I. I. o. Refrigeration, The Role of Refrigeration in the Global Economy, **2015**, *29th Informatory Note on Refrigeration Technologies*,
- [9] Y. Zhao, X. Liu, and Y. Han, *RSC Advances* **2015**, *5*, 38, 30310-30330.
- [10] E. S. Sanz-Pérez, C. R. Murdock, S. A. Didas, and C. W. Jones, *Chem. Rev.* **2016**, *116*, 19, 11840–11876.
- [11] M. Oschatz, and M. Antonietti, *Energy Environ. Sci.* **2018**, *11*, 1, 57-70.
- [12] H. Oberhummer, A. Csótó, and H. Schlattl, *Science* **2000**, *289*, 88-90.
- [13] E. Wiberg, and N. Wiberg, Inorganic Chemistry, *Academic Press*, **2001**.
- [14] H. Sicius, Kohlenstoffgruppe: Elemente der vierten Hauptgruppe: Eine Reise durch das Periodensystem, *Springer Fachmedien Wiesbaden*, **2015**.
- [15] E. Riedel, and C. Janiak, Anorganische Chemie, *De Gruyter*, **2011**.
- [16] V. P. Y. Gogotsi, Carbon Nanomaterials, *CRC Press*, Boca Raton, **2014**.
- [17] L. Dai, D. W. Chang, J.-B. Baek, and W. Lu, *Small* **2012**, *8*, 8, 1130-1166.
- [18] L. Borchardt, M. Oschatz, and S. Kaskel, *Mater. Horiz.* **2014**, *1*, 2, 157-168.
- [19] J. Tang, J. Liu, N. L. Torad, T. Kimura, and Y. Yamauchi, *Nano Today* **2014**, *9*, 3, 305-323.
- [20] R. Yan, T. Heil, V. Presser, R. Walczak, M. Antonietti, and M. Oschatz, *Adv. Sustainable Syst.* **2018**, *2*, 2, 1700128.
- [21] S. V. Mikhalovsky, S. R. Sandeman, C. A. Howell, G. J. Phillips, and V. G. Nikolaev, Chapter 21 - Biomedical Applications of Carbon Adsorbents, Novel Carbon Adsorbents, J. M. D. Tascón, Oxford, *Elsevier*, 639-669, **2012**.
- [22] A. Bhatnagar, W. Hogland, M. Marques, and M. Sillanpää, *Chem. Eng. J.* **2013**, *219*, 499-511.
- [23] R. E. Morris, and P. S. Wheatley, *Angew. Chem., Int. Ed.* **2008**, *47*, 27, 4966-4981.
- [24] M. Oschatz, L. Borchardt, M. Thommes, K. A. Cychosz, I. Senkovska, N. Klein, R. Frind, M. Leistner, V. Presser, Y. Gogotsi, and S. Kaskel, *Angew. Chem., Int. Ed.* **2012**, *51*, 30, 7577-7580.
- [25] J. L. F. P. Serp, Carbon Materials for Catalysis *John Wiley & Sons*, Hoboken, **2009**.
- [26] M. Thommes, K. Kaneko, A. V. Neimark, J. P. Olivier, F. Rodriguez-Reinoso, J. Rouquerol, and K. S. W. Sing, *Pure Appl. Chem.* **2015**, *87*, 9-10, 1051-1069.

- [27] J. C. Palmer, A. Llobet, S. H. Yeon, J. E. Fischer, Y. Shi, Y. Gogotsi, and K. E. Gubbins, *C* **2010**, *48*, 4, 1116-1123.
- [28] W. Li, Q. Yue, Y. Deng, and D. Zhao, *Adv. Mater.* **2013**, *25*, 37, 5129-5152.
- [29] S. Kubo, R. J. White, N. Yoshizawa, M. Antonietti, and M.-M. Titirici, *Chem. Mater.* **2011**, *23*, 22, 4882-4885.
- [30] R. J. White, N. Brun, V. L. Budarin, J. H. Clark, and M.-M. Titirici, *ChemSusChem* **2014**, *7*, 3, 670-689.
- [31] W. Chaikittisilp, K. Ariga, and Y. Yamauchi, *J. Mater. Chem. A* **2013**, *1*, 1, 14-19.
- [32] J. P. Paraknowitsch, and A. Thomas, *Macromol. Chem. Phys.* **2012**, *213*, 10-11, 1132-1145.
- [33] N. Fechler, T.-P. Fellingner, and M. Antonietti, *Adv. Mater.* **2013**, *25*, 1, 75-79.
- [34] M. Sevilla, and R. Mokaya, *Energy Environ. Sci.* **2014**, *7*, 4, 1250-1280.
- [35] S. Osswald, C. Portet, Y. Gogotsi, G. Laudisio, J. P. Singer, J. E. Fischer, V. V. Sokolov, J. A. Kukushkina, and A. E. Kravchik, *J. Solid State Chem.* **2009**, *182*, 7, 1733-1741.
- [36] M. Oschatz, L. Borchardt, I. Senkowska, N. Klein, M. Leistner, and S. Kaskel, *C* **2013**, *56*, 139-145.
- [37] J. Wang, A. Heerwig, M. R. Lohe, M. Oschatz, L. Borchardt, and S. Kaskel, *J. Mater. Chem.* **2012**, *22*, 28, 13911-13913.
- [38] D. Salinas-Torres, D. Lozano-Castelló, M. M. Titirici, L. Zhao, L. Yu, E. Morallón, and D. Cazorla-Amoros, *J. Mater. Chem. A* **2015**, *3*, 30, 15558-15567.
- [39] Y. Xia, Z. Yang, and R. Mokaya, *Nanoscale* **2010**, *2*, 5, 639-659.
- [40] H. Yang, and D. Zhao, *J. Mater. Chem.* **2005**, *15*, 12, 1217-1231.
- [41] A.-H. Lu, and F. Schüth, *Adv. Mater.* **2006**, *18*, 14, 1793-1805.
- [42] M. Kotani, K. Nishiyabu, S. Matsuzaki, and S. Tanaka, *J. Ceram. Soc. Jpn.* **2011**, *119*, 1391, 563-569.
- [43] M. Choi, W. Heo, F. Kleitz, and R. Ryoo, *Chem. Commun.* **2003**, 12, 1340-1341.
- [44] R. Ryoo, S. H. Joo, and S. Jun, *J. Phys. Chem. B* **1999**, *103*, 37, 7743-7746.
- [45] S. Jun, S. H. Joo, R. Ryoo, M. Kruk, M. Jaroniec, Z. Liu, T. Ohsuna, and O. Terasaki, *J. Am. Chem. Soc.* **2000**, *122*, 43, 10712-10713.
- [46] D. Zhao, Q. Huo, J. Feng, B. F. Chmelka, and G. D. Stucky, *J. Am. Chem. Soc.* **1998**, *120*, 24, 6024-6036.
- [47] A. Cruz-Espinoza, V. Ibarra-Galván, A. López-Valdivieso, and J. González-González, *J. Colloid Interface Sci.* **2012**, *374*, 1, 321-324.
- [48] C. Hoffmann, T. Biemelt, A. Seifert, K. Pinkert, T. Gemming, S. Spange, and S. Kaskel, *J. Mater. Chem.* **2012**, *22*, 47, 24841-24847.
- [49] Y. Meng, D. Gu, F. Zhang, Y. Shi, H. Yang, Z. Li, C. Yu, B. Tu, and D. Zhao, *Angew. Chem., Int. Ed.* **2005**, *117*, 43, 7215-7221.
- [50] L. Chuenchom, R. Kraehnert, and B. M. Smarsly, *Soft Matter* **2012**, *8*, 42, 10801-10812.
- [51] C. T. Kresge, M. E. Leonowicz, W. J. Roth, J. C. Vartuli, and J. S. Beck, *Nature* **1992**, *359*, 710.
- [52] R. Yan, M. Antonietti, and M. Oschatz, *Adv. Energy Mater.* **2018**, *8*, 18, 1800026.
- [53] W. Nickel, M. Oschatz, M. v. d. Lehr, M. Leistner, G.-P. Hao, P. Adelhelm, P. Muller, B. M. Smarsly, and S. Kaskel, *J. Mater. Chem. A* **2014**, *2*, 32, 12703-12707.
- [54] W. Nickel, M. Oschatz, S. Rico-Francés, S. Klosz, T. Biemelt, G. Mondin, A. Eychmüller, J. Silvestre-Albero, and S. Kaskel, *Chem. Eur. J.* **2015**, *21*, 42, 14753-14757.
- [55] M. Oschatz, E. Kockrick, M. Rose, L. Borchardt, N. Klein, I. Senkowska, T. Freudenberg, Y. Korenblit, G. Yushin, and S. Kaskel, *C* **2010**, *48*, 14, 3987-3992.
- [56] L. Borchardt, M. Oschatz, M. Lohe, V. Presser, Y. Gogotsi, and S. Kaskel, *C* **2012**, *50*, 11, 3987-3994.
- [57] Y. Gogotsi, A. Nikitin, H. Ye, W. Zhou, J. E. Fischer, B. Yi, H. C. Foley, and M. W. Barsoum, *Nat. Mater.* **2003**, *2*, 591.

- [58] V. Presser, M. Heon, and Y. Gogotsi, *Adv. Funct. Mater.* **2011**, *21*, 5, 810-833.
- [59] Y. Zhao, L. Zhao, K. X. Yao, Y. Yang, Q. Zhang, and Y. Han, *J. Mater. Chem.* **2012**, *22*, 37, 19726-19731.
- [60] T. Lin, I.-W. Chen, F. Liu, C. Yang, H. Bi, F. Xu, and F. Huang, *Science* **2015**, *350*, 6267, 1508-1513.
- [61] L. He, F. Weniger, H. Neumann, and M. Beller, *Angew. Chem., Int. Ed.* **2016**, *55*, 41, 12582-12594.
- [62] S. S. Barton, M. J. B. Evans, E. Halliop, and J. A. F. MacDonald, *C* **1997**, *35*, 9, 1361-1366.
- [63] C. O. Ania, J. B. Parra, and J. J. Pis, *Adsorpt. Sci. Technol.* **2004**, *22*, 4, 337-351.
- [64] Y. El-Sayed, and T. J. Bandosz, *Langmuir* **2002**, *18*, 8, 3213-3218.
- [65] Y. F. Jia, B. Xiao, and K. M. Thomas, *Langmuir* **2002**, *18*, 2, 470-478.
- [66] M. F. R. Pereira, S. F. Soares, J. J. M. Órfão, and J. L. Figueiredo, *C* **2003**, *41*, 4, 811-821.
- [67] M. A. Montes-Morán, D. Suárez, J. A. Menéndez, and E. Fuente, *C* **2004**, *42*, 7, 1219-1225.
- [68] S. Wenzhong, L. Zhijie, and L. Yihong, *Recent Innovations in Chemical Engineering* **2008**, *1*, 1, 27-40.
- [69] K. Jurewicz, K. Babel, A. Ziółkowski, H. Wachowska, and M. Kozłowski, *Fuel Process. Technol.* **2002**, *77-78*, 191-198.
- [70] W. Yang, T.-P. Fellingner, and M. Antonietti, *J. Am. Chem. Soc.* **2011**, *133*, 2, 206-209.
- [71] K. Gong, F. Du, Z. Xia, M. Durstock, and L. Dai, *Science* **2009**, *323*, 5915, 760-764.
- [72] S. M. Mahurin, J. S. Lee, X. Wang, and S. Dai, *J. Membr. Sci.* **2011**, *368*, 1, 41-47.
- [73] J. Wei, D. Zhou, Z. Sun, Y. Deng, Y. Xia, and D. Zhao, *Adv. Funct. Mater.* **2013**, *23*, 18, 2322-2328.
- [74] J. P. Paraknowitsch, J. Zhang, D. Su, A. Thomas, and M. Antonietti, *Adv. Mater.* **2010**, *22*, 1, 87-92.
- [75] J. Lahaye, G. Nansé, A. Bagreev, and V. Strelko, *C* **1999**, *37*, 4, 585-590.
- [76] H. Wang, T. Maiyalagan, and X. Wang, *ACS Catalysis* **2012**, *2*, 5, 781-794.
- [77] R. Czerw, M. Terrones, J. C. Charlier, X. Blase, B. Foley, R. Kamalakaran, N. Grobert, H. Terrones, D. Tekleab, P. M. Ajayan, W. Blau, M. Rühle, and D. L. Carroll, *Nano Lett.* **2001**, *1*, 9, 457-460.
- [78] A. C. M. Carvalho, and M. C. d. Santos, *J. Appl. Phys.* **2006**, *100*, 8, 084305.
- [79] G. Liu, X. Li, J.-W. Lee, and B. N. Popov, *Catal. Sci. Technol.* **2011**, *1*, 2, 207-217.
- [80] S. Chen, J. Bi, Y. Zhao, L. Yang, C. Zhang, Y. Ma, Q. Wu, X. Wang, and Z. Hu, *Adv. Mater.* **2012**, *24*, 41, 5593-5597.
- [81] P. H. Matter, L. Zhang, and U. S. Ozkan, *J. Catal.* **2006**, *239*, 1, 83-96.
- [82] J. R. Pels, F. Kapteijn, J. A. Moulijn, Q. Zhu, and K. M. Thomas, *C* **1995**, *33*, 11, 1641-1653.
- [83] X. Wang, K. Maeda, A. Thomas, K. Takanabe, G. Xin, J. M. Carlsson, K. Domen, and M. Antonietti, *Nat. Mater.* **2008**, *8*, 76.
- [84] A. Thomas, A. Fischer, F. Goettmann, M. Antonietti, J.-O. Müller, R. Schlögl, and J. M. Carlsson, *J. Mater. Chem.* **2008**, *18*, 41, 4893-4908.
- [85] W. Shen, and W. Fan, *J. Mater. Chem. A* **2013**, *1*, 4, 999-1013.
- [86] P. Nowicki, R. Pietrzak, and H. Wachowska, *Energy Fuels* **2009**, *23*, 4, 2205-2212.
- [87] C.-M. Yang, C. Weidenthaler, B. Spliethoff, M. Mayanna, and F. Schüth, *Chem. Mater.* **2005**, *17*, 2, 355-358.
- [88] Y. Deng, Y. Xie, K. Zou, and X. Ji, *J. Mater. Chem. A* **2016**, *4*, 4, 1144-1173.
- [89] N. Baccile, G. Laurent, C. Coelho, F. Babonneau, L. Zhao, and M.-M. Titirici, *J. Phys. Chem. C* **2011**, *115*, 18, 8976-8982.

- [90] M.-M. Titirici, and M. Antonietti, *Chem. Soc. Rev.* **2010**, *39*, 1, 103-116.
- [91] T.-P. Feller, A. Thomas, J. Yuan, and M. Antonietti, *Adv. Mater.* **2013**, *25*, 41, 5838-5855.
- [92] M. Antonietti, and M. Oschatz, *Adv. Mater.* **2018**, *30*, 21, 1706836.
- [93] S. Fukuzumi, and K. Ohkubo, *Org. Biomol. Chem.* **2014**, *12*, 32, 6059-6071.
- [94] Y. Lee, H. Lee, S. Park, and Y. Yi, *Appl. Phys. Lett.* **2012**, *101*, 23, 233305.
- [95] S. Kazemiabnavi, Z. Zhang, K. Thornton, and S. Banerjee, *J. Phys. Chem. B* **2016**, *120*, 25, 5691-5702.
- [96] J. Zhang, J. Sun, K. Maeda, K. Domen, P. Liu, M. Antonietti, X. Fu, and X. Wang, *Energy Environ. Sci.* **2011**, *4*, 3, 675-678.
- [97] L. Lin, H. Ou, Y. Zhang, and X. Wang, *ACS Catalysis* **2016**, *6*, 6, 3921-3931.
- [98] S. Zhang, S. Tsuzuki, K. Ueno, K. Dokko, and M. Watanabe, *Angew. Chem., Int. Ed.* **2015**, *54*, 4, 1302-1306.
- [99] N. Fechner, N. P. Zussblatt, R. Rothe, R. Schlögl, M.-G. Willinger, B. F. Chmelka, and M. Antonietti, *Adv. Mater.* **2016**, *28*, 6, 1287-1294.
- [100] J. Mahmood, E. K. Lee, M. Jung, D. Shin, I.-Y. Jeon, S.-M. Jung, H.-J. Choi, J.-M. Seo, S.-Y. Bae, S.-D. Sohn, N. Park, J. H. Oh, H.-J. Shin, and J.-B. Baek, *Nat. Commun.* **2015**, *6*, 6486.
- [101] F. Xu, D. Wu, R. Fu, and B. Wei, *Materials Today* **2017**, *20*, 10, 629-656.
- [102] J.-X. Jiang, F. Su, A. Trewin, C. D. Wood, N. L. Campbell, H. Niu, C. Dickinson, A. Y. Ganin, M. J. Rosseinsky, Y. Z. Khimyak, and A. I. Cooper, *Angew. Chem., Int. Ed.* **2007**, *46*, 45, 8574-8578.
- [103] F. Vilela, K. Zhang, and M. Antonietti, *Energy Environ. Sci.* **2012**, *5*, 7, 7819-7832.
- [104] Z. Chen, P. Li, and C. Wu, *RSC Adv.* **2015**, *5*, 11791-11796.
- [105] Y. Xu, L. Chen, Z. Guo, A. Nagai, and D. Jiang, *J. Am. Chem. Soc.* **2011**, *133*, 44, 17622-17625.
- [106] L. Chen, Y. Honsho, S. Seki, and D. Jiang, *J. Am. Chem. Soc.* **2010**, *132*, 19, 6742-6748.
- [107] Y. Zhang, and S. N. Riduan, *Chem. Soc. Rev.* **2012**, *41*, 6, 2083-2094.
- [108] C. Gu, N. Huang, J. Gao, F. Xu, Y. Xu, and D. Jiang, *Angew. Chem., Int. Ed.* **2014**, *53*, 19, 4850-4855.
- [109] Y. Kou, Y. Xu, Z. Guo, and D. Jiang, *Angew. Chem., Int. Ed.* **2011**, *50*, 37, 8753-8757.
- [110] Y. Xie, T.-T. Wang, X.-H. Liu, K. Zou, and W.-Q. Deng, *Nat. Commun.* **2013**, *4*, 1960.
- [111] J. P. Paraknowitsch, and A. Thomas, *Energy Environ. Sci.* **2013**, *6*, 10, 2839-2855.
- [112] Q. Pang, J. Tang, H. Huang, X. Liang, C. Hart, K. C. Tam, and L. F. Nazar, *Adv. Mater.* **2015**, *27*, 39, 6021-6028.
- [113] G. Zhou, E. Paek, G. S. Hwang, and A. Manthiram, *Nat. Commun.* **2015**, *6*, 7760.
- [114] X. Feng, Y. Liang, L. Zhi, A. Thomas, D. Wu, I. Lieberwirth, U. Kolb, and K. Müllen, *Adv. Funct. Mater.* **2009**, *19*, 13, 2125-2129.
- [115] Z. Xiang, D. Cao, L. Huang, J. Shui, M. Wang, and L. Dai, *Adv. Mater.* **2014**, *26*, 20, 3315-3320.
- [116] X. Zhu, S. Chai, C. Tian, P. F. Fulvio, K. S. Han, E. W. Hagaman, G. M. Veith, S. M. Mahurin, S. Brown, H. Liu, and S. Dai, *Macromol. Rapid Commun.* **2013**, *34*, 5, 452-459.
- [117] X. Zhu, C. Tian, S. Chai, K. Nelson, K. S. Han, E. W. Hagaman, G. M. Veith, S. M. Mahurin, H. Liu, and S. Dai, *Adv. Mater.* **2013**, *25*, 30, 4152-4158.
- [118] Á. Berenguer-Murcia, J. P. Marco-Lozar, and D. Cazorla-Amorós, *Chem. Rec.* **2018**, *18*, 7-8, 900-912.
- [119] S.-H. Yeon, S. Osswald, Y. Gogotsi, J. P. Singer, J. M. Simmons, J. E. Fischer, M. A. Lillo-Ródenas, and Á. Linares-Solano, *J. Power Sources* **2009**, *191*, 2, 560-567.
- [120] S.-H. Yeon, I. Knoke, Y. Gogotsi, and J. E. Fischer, *Microporous Mesoporous Mater.* **2010**, *131*, 1, 423-428.

- [121] D. M. D'Alessandro, B. Smit, and J. R. Long, *Angew. Chem., Int. Ed.* **2010**, *49*, 35, 6058-6082.
- [122] C. Gouedard, D. Picq, F. Launay, and P. L. Carrette, *Int. J. Greenh. Gas* **2012**, *10*, 244-270.
- [123] B. Dutcher, M. Fan, and A. G. Russell, *ACS Appl. Mater. Interfaces* **2015**, *7*, 4, 2137-2148.
- [124] D. Reichle, J. Houghton, B. Kane, and J. Ekmann, Carbon Sequestration. State of the Science, *U.S. Department of Energy, Office of Science, Office of Fossil Energy: Washington, DC*, **1999**.
- [125] H. A. Patel, J. Byun, and C. T. Yavuz, *ChemSusChem* **2017**, *10*, 7, 1303-1317.
- [126] M. Caplow, *J. Am. Chem. Soc.* **1968**, *90*, 24, 6795-6803.
- [127] P. V. Danckwerts, *Chem. Eng. Sci.* **1979**, *34*, 4, 443-446.
- [128] B. A. Oyenekan, and G. T. Rochelle, **2007**, *53*, 12, 3144-3154.
- [129] A. Sayari, and Y. Belmabkhout, *J. Am. Chem. Soc.* **2010**, *132*, 18, 6312-6314.
- [130] K. Kaneko, *J. Membr. Sci.* **1994**, *96*, 1, 59-89.
- [131] M. Beckner, and A. Dailly, *Int. J. Energ. Res.* **2016**, *40*, 1, 91-99.
- [132] J. C. Meerman, E. S. Hamborg, T. van Keulen, A. Ramirez, W. C. Turkenburg, and A. P. C. Faaij, *Int. J. Greenh. Gas* **2012**, *9*, 160-171.
- [133] K. S. W. Sing, and R. T. Williams, *Part. Part. Syst. Charact.* **2004**, *21*, 2, 71-79.
- [134] J.-M. Gu, W.-S. Kim, Y.-K. Hwang, and S. Huh, *C* **2013**, *56*, 208-217.
- [135] L. Zhang, Z. Su, F. Jiang, L. Yang, J. Qian, Y. Zhou, W. Li, and M. Hong, *Nanoscale* **2014**, *6*, 12, 6590-6602.
- [136] M. Sevilla, P. Valle-Vigón, and A. B. Fuertes, *Adv. Funct. Mater.* **2011**, *21*, 14, 2781-2787.
- [137] Y. S. Bae, and C. H. Lee, *C* **2005**, *43*, 1, 95-107.
- [138] A. Muelleman, J. Schell, S. Glazer, and R. Glaser, *C* **2016**, *2*, 3, 18.
- [139] P. Nugent, Y. Belmabkhout, S. D. Burd, A. J. Cairns, R. Luebke, K. Forrest, T. Pham, S. Ma, B. Space, L. Wojtas, M. Eddaoudi, and M. J. Zaworotko, *Nature* **2013**, *495*, 80.
- [140] O. Shekhah, Y. Belmabkhout, Z. Chen, V. Guillerm, A. Cairns, K. Adil, and M. Eddaoudi, *Nat. Commun.* **2014**, *5*, 4228.
- [141] J. M. Tarascon, and M. Armand, *Nature* **2001**, *414*, 359-367.
- [142] B. Dunn, H. Kamath, and J.-M. Tarascon, *Science* **2011**, *334*, 6058, 928-935.
- [143] N. Yabuuchi, K. Kubota, M. Dahbi, and S. Komaba, *Chem. Rev.* **2014**, *114*, 23, 11636-11682.
- [144] D. Kundu, E. Talaie, V. Duffort, and L. F. Nazar, *Angew. Chem., Int. Ed.* **2015**, *54*, 11, 3431-3448.
- [145] M. D. Slater, D. Kim, E. Lee, and C. S. Johnson, *Adv. Funct. Mater.* **2013**, *23*, 8, 947-958.
- [146] C. Nithya, and S. Gopukumar, *WIREs Energy and Environ.* **2015**, *4*, 3, 253-278.
- [147] B. L. Ellis, and L. F. Nazar, *Current Opinion in Solid State and Materials Science* **2012**, *16*, 4, 168-177.
- [148] H. Pan, Y.-S. Hu, and L. Chen, *Energy Environ. Sci.* **2013**, *6*, 8, 2338-2360.
- [149] M. M. Doeff, Y. Ma, S. J. Visco, and L. C. De Jonghe, *J. Electrochem. Soc.* **1993**, *140*, L169.
- [150] C. Bommier, and X. Ji, *Isr. J. Chem.* **2015**, *55*, 5, 486-507.
- [151] M.-S. Balogun, Y. Luo, W. Qiu, P. Liu, and Y. Tong, *C* **2016**, *98*, 162-178.
- [152] H. Hou, X. Qiu, W. Wei, Y. Zhang, and X. Ji, **2017**, *7*, 24, 1602898.
- [153] D. A. Stevens, and J. R. Dahn, *J. Electrochem. Soc.* **2001**, *148*, A803.
- [154] Y. Li, S. Xu, X. Wu, J. Yu, Y. Wang, Y. S. Hu, H. Li, L. Chen, and X. Huang, *J. Mater. Chem. A* **2015**, *3*, 71-77.

- [155] D. Stevens, and J. Dahn, *J. Electrochem. Soc.* **2000**, *147*, 1271-1273.
- [156] Y. Cao, L. Xiao, M. L. Sushko, W. Wang, B. Schwenzer, J. Xiao, Z. Nie, L. V. Saraf, Z. Yang, and J. Liu, *Nano Lett.* **2012**, *12*, 7, 3783-3787.
- [157] B. Zhang, C. M. Ghimbeu, C. Laberty, C. Vix-Guterl, and J.-M. Tarascon, *Adv. Energy Mater.* **2016**, *6*, 1, 1501588.
- [158] W. Li, M. Zhou, H. Li, K. Wang, S. Cheng, and K. Jiang, *Energy Environ. Sci.* **2015**, *8*, 10, 2916-2921.
- [159] C. Chen, Y. Lu, Y. Ge, J. Zhu, H. Jiang, Y. Li, Y. Hu, and X. Zhang, *Energy Technology* **2016**, *4*, 11, 1440-1449.
- [160] H. G. Wang, Z. Wu, F. L. Meng, D. L. Ma, X. L. Huang, L. M. Wang, and X. B. Zhang, *ChemSusChem* **2013**, *6*, 56.
- [161] J. Xu, M. Wang, N. P. Wickramaratne, M. Jaroniec, S. Dou, and L. Dai, *Adv. Mater.* **2015**, *27*, 12, 2042-2048.
- [162] O. Y. Podyacheva, and Z. R. Ismagilov, *Catal. Today* **2015**, *249*, 12-22.
- [163] M. Li, F. Xu, H. Li, and Y. Wang, *Catal. Sci. Technol.* **2016**, *6*, 11, 3670-3693.
- [164] Z. Wang, L. Qie, L. Yuan, W. Zhang, X. Hu, and Y. Huang, *C* **2013**, *55*, 328-334.
- [165] S. Wang, L. Xia, L. Yu, L. Zhang, H. Wang, and X. W. Lou, *Adv. Energy Mater.* **2016**, *6*, 7, 1502217.
- [166] R. Walczak, B. Kurpil, A. Savateev, T. Heil, J. Schmidt, Q. Qin, M. Antonietti, and M. Oschatz, *Angew. Chem., Int. Ed.* **2018**, *57*, 33, 10765-10770.
- [167] X. Ren, H. Li, J. Chen, L. Wei, A. Modak, H. Yang, and Q. Yang, *C* **2017**, *114*, 473-481.
- [168] G.-P. Hao, G. Mondin, Z. Zheng, T. Biemelt, S. Klosz, R. Schubel, A. Eychmüller, and S. Kaskel, *Angew. Chem., Int. Ed.* **2015**, *54*, 6, 1941-1945.
- [169] J. Zhao, H. Lai, Z. Lyu, Y. Jiang, K. Xie, X. Wang, Q. Wu, L. Yang, Z. Jin, Y. Ma, J. Liu, and Z. Hu, *Adv. Mater.* **2015**, *27*, 23, 3541-3545.
- [170] C. Schneidermann, N. Jäckel, S. Oswald, L. Giebeler, V. Presser, and L. Borchardt, *ChemSusChem* **2017**, *10*, 11, 2416-2424.
- [171] J. K. Ewert, D. Weingarh, C. Denner, M. Friedrich, M. Zeiger, A. Schreiber, N. Jäckel, V. Presser, and R. Kempe, *J. Mater. Chem. A* **2015**, *3*, 37, 18906-18912.
- [172] Y. Gong, M. Li, H. Li, and Y. Wang, *Green Chem.* **2015**, *17*, 2, 715-736.
- [173] M. Oschatz, J. P. Hofmann, T. W. van Deelen, W. S. Lamme, N. A. Krans, E. J. M. Hensen, and K. P. de Jong, *ChemCatChem* **2017**, *9*, 4, 620-628.
- [174] Z. Wen, X. Wang, S. Mao, Z. Bo, H. Kim, S. Cui, G. Lu, X. Feng, and J. Chen, *Adv. Mater.* **2012**, *24*, 41, 5610-5616.
- [175] A. Savateev, S. Pronkin, J. D. Epping, M. G. Willinger, M. Antonietti, and D. Dontsova, *J. Mater. Chem. A* **2017**, *5*, 18, 8394-8401.
- [176] J. L. Segura, R. Juarez, M. Ramos, and C. Seoane, *Chem. Soc. Rev.* **2015**, *44*, 19, 6850-6885.
- [177] B. Kurpil, A. Savateev, V. Papaefthimiou, S. Zafeiratos, T. Heil, S. Özenler, D. Dontsova, and M. Antonietti, *Appl. Catal., B* **2017**, *217*, 622-628.
- [178] T. Chiba, Y.-J. Pu, R. Miyazaki, K.-i. Nakayama, H. Sasabe, and J. Kido, *Organic Electronics* **2011**, *12*, 4, 710-715.
- [179] Y. Dai, H. Zhang, Z. Zhang, Y. Liu, J. Chen, and D. Ma, *J. Mater. Chem. C* **2015**, *3*, 26, 6809-6814.
- [180] R. Walczak, B. Kurpil, A. Savateev, T. Heil, J. Schmidt, Q. Qin, M. Antonietti, and M. Oschatz, *Angew. Chem.* **2018**, *130*, 33, 10926-10931.
- [181] G.-P. Hao, C. Tang, E. Zhang, P. Zhai, J. Yin, W. Zhu, Q. Zhang, and S. Kaskel, *Adv. Mater.* **2017**, *29*, 37, 1702829-n/a.

- [182] M. Oschatz, H. C. Hoffmann, J. Pallmann, J. Schaber, L. Borchardt, W. Nickel, I. Senkowska, S. Rico-Francés, J. Silvestre-Albero, S. Kaskel, and E. Brunner, *Chem. Mater.* **2014**, *26*, 10, 3280-3288.
- [183] P. Wollmann, M. Leistner, W. Grähler, O. Throl, F. Dreisbach, and S. Kaskel, *Microporous Mesoporous Mater.* **2012**, *149*, 1, 86-94.
- [184] M. Leistner, W. Grähler, and S. Kaskel, *Chem. Ing. Tech.* **2013**, *85*, 5, 747-752.
- [185] M. Oschatz, M. Leistner, W. Nickel, and S. Kaskel, *Langmuir* **2015**, *31*, 13, 4040-4047.
- [186] E. S. Sanz-Perez, C. R. Murdock, S. A. Didas, and C. W. Jones, *Chem. Rev.* **2016**, *116*, 19, 11840-11876.
- [187] F. A. Rahman, M. M. A. Aziz, R. Saidur, W. A. W. A. Bakar, M. R. Hainin, R. Putrajaya, and N. A. Hassan, *Renew. Sust. Energ. Rev.* **2017**, *71*, 112-126.
- [188] Y. S. Bae, and R. Q. Snurr, *Angew. Chem., Int. Ed.* **2011**, *50*, 49, 11586-11596.
- [189] X. Lu, D. Jin, S. Wei, Z. Wang, C. An, and W. Guo, *J. Mater. Chem. A* **2015**, *3*, 23, 12118-12132.
- [190] G. P. Hao, W. C. Li, D. Qian, and A. H. Lu, *Adv. Mater.* **2010**, *22*, 7, 853-857.
- [191] Z. Tian, N. Fechner, M. Oschatz, T. Heil, J. Schmidt, S. Yuan, and M. Antonietti, *J. Mater. Chem. A* **2018**, *6*, 39, 19013-19019.
- [192] Y. Zhao, K. X. Yao, B. Teng, T. Zhang, and Y. Han, *Energy Environ. Sci.* **2013**, *6*, 12, 3684-3692.
- [193] H. A. Patel, S. H. Je, J. Park, D. P. Chen, Y. Jung, C. T. Yavuz, and A. Coskun, *Nat. Commun.* **2013**, *4*, 1357.
- [194] F. Akhtar, Q. Liu, N. Hedin, and L. Bergström, *Energy Environ. Sci.* **2012**, *5*, 6, 7664.
- [195] O. Cheung, and N. Hedin, *RSC Advances* **2014**, *4*, 28, 14480.
- [196] F. Gao, Y. Li, Z. Bian, J. Hu, and H. Liu, *J. Mater. Chem. A* **2015**, *3*, 15, 8091-8097.
- [197] M. Abu Ghalia, and Y. Dahman, *Energy Technology* **2017**, *5*, 3, 356-372.
- [198] J. Liu, P. K. Thallapally, B. P. McGrail, D. R. Brown, and J. Liu, *Chem. Soc. Rev.* **2012**, *41*, 6, 2308-2322.
- [199] R. Luebke, J. F. Eubank, A. J. Cairns, Y. Belmabkhout, L. Wojtas, and M. Eddaoudi, *Chem. Commun.* **2012**, *48*, 10, 1455-1457.
- [200] K. Sumida, D. L. Rogow, J. A. Mason, T. M. McDonald, E. D. Bloch, Z. R. Herm, T. H. Bae, and J. R. Long, *Chem. Rev.* **2012**, *112*, 2, 724-781.
- [201] Y. Belmabkhout, V. Guillerm, and M. Eddaoudi, *Chem. Eng. J.* **2016**, *296*, 386-397.
- [202] Y. Zhao, X. Liu, K. X. Yao, L. Zhao, and Y. Han, *Chem. Mater.* **2012**, *24*, 24, 4725-4734.
- [203] Y. K. Kim, G. M. Kim, and J. W. Lee, *J. Mater. Chem. A* **2015**, *3*, 20, 10919-10927.
- [204] T. M. McDonald, J. A. Mason, X. Kong, E. D. Bloch, D. Gygi, A. Dani, V. Crocella, F. Giordanino, S. O. Odoh, W. S. Drisdell, B. Vlasisavljevich, A. L. Dzubak, R. Poloni, S. K. Schnell, N. Planas, K. Lee, T. Pascal, L. F. Wan, D. Prendergast, J. B. Neaton, B. Smit, J. B. Kortright, L. Gagliardi, S. Bordiga, J. A. Reimer, and J. R. Long, *Nature* **2015**, *519*, 7543, 303-308.
- [205] J. W. To, J. He, J. Mei, R. Haghpanah, Z. Chen, T. Kurosawa, S. Chen, W. G. Bae, L. Pan, J. B. Tok, J. Wilcox, and Z. Bao, *J. Am. Chem. Soc.* **2016**, *138*, 3, 1001-1009.
- [206] J. R. Li, J. Yu, W. Lu, L. B. Sun, J. Sculley, P. B. Balbuena, and H. C. Zhou, *Nat. Commun.* **2013**, *4*, 1538.
- [207] N. P. Wickramaratne, and M. Jaroniec, *J. Mater. Chem. A* **2013**, *1*, 1, 112-116.
- [208] Q. Liu, A. Mace, Z. Bacsik, J. Sun, A. Laaksonen, and N. Hedin, *Chem. Commun.* **2010**, *46*, 25, 4502-4504.
- [209] H. T. Chifotides, B. L. Schottel, and K. R. Dunbar, *Angew. Chem., Int. Ed.* **2010**, *49*, 7202-7207.
- [210] S. Kirkpatrick, C. D. Gelatt, and M. P. Vecchi, *Science* **1983**, *220*, 671.

- [211] R. Car, and R. Parrinello, *Phys. Rev. Lett.* **1985**, *55*, 2471.
- [212] T. D. Kühne, M. Krack, F. R. Mohamed, and M. Parrinello, *Phys. Rev. Lett.* **2007**, *98*, 066401.
- [213] T. D. Kühne, *WIREs Comput. Mol. Sci.* **2014**, *4*, 391.
- [214] D. Marx, L. Joss, M. Hefti, R. Pini, and M. Mazzotti, *Energy Procedia* **2013**, *37*, 107-114.
- [215] P. R. Davies, *Top. Catal.* **2016**, *59*, 8, 671-677.
- [216] V. R. Stamenkovic, D. Strmcnik, P. P. Lopes, and N. M. Markovic, *Nat. Mater.* **2016**, *16*, 57.
- [217] S. K. Henninger, S.-J. Ernst, L. Gordeeva, P. Bendix, D. Fröhlich, A. D. Grekova, L. Bonaccorsi, Y. Aristov, and J. Jaenchen, *Renewable Energy* **2017**, *110*, 59-68.
- [218] L. Liu, S. Tan, T. Horikawa, D. D. Do, D. Nicholson, and J. Liu, *Adv. Colloid Interface Sci.* **2017**, *250*, 64-78.
- [219] C. Pierce, and R. N. Smith, *J. Chem. Phys.* **1950**, *54*, 6, 784-794.
- [220] R. P. Sah, B. Choudhury, and R. K. Das, *Renew. Sust. Energ. Rev.* **2016**, *62*, 109-120.
- [221] D. C. Wang, Y. H. Li, D. Li, Y. Z. Xia, and J. P. Zhang, *Renew. Sust. Energ. Rev.* **2010**, *14*, 1, 344-353.
- [222] P. Goyal, P. Baredar, A. Mittal, and A. R. Siddiqui, *Renew. Sust. Energ. Rev.* **2016**, *53*, 1389-1410.
- [223] D. Britt, D. Tranchemontagne, and O. M. Yaghi, *Proceedings of the National Academy of Sciences* **2008**, *105*, 33, 11623-11627.
- [224] P. Camille, and B. T. J., *Adv. Funct. Mater.* **2010**, *20*, 1, 111-118.
- [225] J. F. Van Humbeck, T. M. McDonald, X. Jing, B. M. Wiers, G. Zhu, and J. R. Long, *J. Am. Chem. Soc.* **2014**, *136*, 6, 2432-2440.
- [226] H. M. S., W. A. L., M. Alon, and C. Edward, *AIChE J.* **2012**, *58*, 11, 3526-3532.
- [227] L. Damjanović, and A. Auroux, Zeolite Characterization and Catalysis: A Tutorial, Determination of Acid/Base Properties by Temperature Programmed Desorption (TPD) and Adsorption Calorimetry, A. W. Chester, and E. G. Derouane, *Springer*, 107-167, **2010**.
- [228] F. Sandra, N. Klein, M. Leistner, M. R. Lohe, M. Benusch, M. Woellner, J. Grothe, and S. Kaskel, *Ind. Eng. Chem. Res.* **2015**, *54*, 26, 6677-6682.
- [229] R. Sabbah, A. Xu-Wu, J. S. Chickos, P. L. M. L., M. V. Roux, and K. A. Torres, *Thermochim. Acta* **1999**, *331*, 93-204.
- [230] J. S. Chickos, and W. E. J. Acree, *J. Phy. Chem. Ref. Data* **2003**, *32*, 2, 519-878.
- [231] S. Hayes, L. van Wüllen, H. Eckert, W. R. Even, R. W. Crocker, and Z. Zhang, *Chem. Mater.* **1997**, *9*, 4, 901-911.
- [232] L. Calucci, C. Forte, L. Galleschi, M. Geppi, and S. Ghiringhelli, *Int. J. Biol. Macromol.* **2003**, *32*, 3, 179-189.
- [233] K. Gottschling, L. Stegbauer, G. Savasci, N. A. Prisco, Z. J. Berkson, C. Ochsenfeld, B. F. Chmelka, and B. V. Lotsch, *Chem. Mater.* **2019**, *31*, 6, 1946-1955.
- [234] C. Gu, N. Huang, Y. Chen, H. Zhang, S. Zhang, F. Li, Y. Ma, and D. Jiang, *Angew. Chem., Int. Ed.* **2016**, *55*, 9, 3049-3053.
- [235] Z. Wang, X. Yang, T. Yang, Y. Zhao, F. Wang, Y. Chen, J. H. Zeng, C. Yan, F. Huang, and J.-X. Jiang, *ACS Catalysis* **2018**, *8*, 9, 8590-8596.
- [236] Y. Chen, H. Sun, R. Yang, T. Wang, C. Pei, Z. Xiang, Z. Zhu, W. Liang, A. Li, and W. Deng, *J. Mater. Chem. A* **2015**, *3*, 1, 87-91.
- [237] C. Zhang, X. Yang, W. Ren, Y. Wang, F. Su, and J.-X. Jiang, *J. Power Sources* **2016**, *317*, 49-56.
- [238] C. Zhang, Y. He, P. Mu, X. Wang, Q. He, Y. Chen, J. Zeng, F. Wang, Y. Xu, and J.-X. Jiang, *Adv. Funct. Mater.* **2018**, *28*, 4, 1705432.
- [239] F. Xu, X. Chen, Z. Tang, D. Wu, R. Fu, and D. Jiang, *Chem. Commun.* **2014**, *50*, 37, 4788-4790.

- [240] E. Riedel, and C. Janiak, *Anorganische Chemie*, Berlin, *Walter de Gruyter*, 7. Auflage, **2007**.
- [241] H. Liu, M. Jia, B. Cao, R. Chen, X. Lv, R. Tang, F. Wu, and B. Xu, *J. Power Sources* **2016**, *319*, 195-201.
- [242] S. Zhang, W. Huang, P. Hu, C. Huang, C. Shang, C. Zhang, R. Yang, and G. Cui, *J. Mater. Chem. A* **2015**, *3*, 5, 1896-1901.
- [243] X. Wang, C. Zhang, Y. Xu, Q. He, P. Mu, Y. Chen, J. Zeng, F. Wang, and J.-X. Jiang, *Macromol. Chem. Phys.* **2018**, *219*, 7, 1700524.
- [244] A. B. Marco, D. Cortizo-Lacalle, I. Perez-Miqueo, G. Valenti, A. Boni, J. Plas, K. Strutyński, S. De Feyter, F. Paolucci, M. Montes, A. N. Khlobystov, M. Melle-Franco, and A. Mateo-Alonso, *Angew. Chem., Int. Ed.* **2017**, *56*, 24, 6946-6951.
- [245] S. Brunauer, P. H. Emmett, and E. Teller, *J. Am. Chem. Soc.* **1938**, *60*, 2, 309-319.
- [246] E. P. Barrett, L. G. Joyner, and P. P. Halenda, *J. Am. Chem. Soc.* **1951**, *73*, 1, 373-380.
- [247] A. V. Neimark, Y. Lin, P. I. Ravikovitch, and M. Thommes, *C* **2009**, *47*, 7, 1617-1628.
- [248] K. A. Cychoz, R. Guillet-Nicolas, J. García-Martínez, and M. Thommes, *Chem. Soc. Rev.* **2017**, *46*, 2, 389-414.
- [249] S. Furmaniak, A. P. Terzyk, P. A. Gauden, P. J. F. Harris, and P. Kowalczyk, *J. Phys.: Condens. Matter* **2010**, *22*, 8, 085003.
- [250] H.-J. Wang, A. Kleinhammes, T. P. McNicholas, J. Liu, and Y. Wu, *The Journal of Physical Chemistry C* **2014**, *118*, 16, 8474-8480.
- [251] G. Lippert, J. Hutter, and M. Parrinello, *Mol. Phys.* **1997**, *92*, 3, 477-488.
- [252] J. VandeVondele, M. Krack, F. Mohamed, M. Parrinello, T. Chassaing, and J. Hutter, *Comput. Phys. Commun.* **2005**, *167*, 103.
- [253] J. VandeVondele, and J. Hutter, *J. Chem. Phys.* **2007**, *127*, 11, 114105.
- [254] S. Goedecker, M. Teter, and J. Hutter, *Phys. Rev. B* **1996**, *54*, 1703.
- [255] M. Krack, *Theor. Chem. Acc.* **2005**, *114*, 1, 145-152.
- [256] S. Grimme, *J. Comput. Chem.* **2006**, *27*, 15, 1787-1799.
- [257] J. T. Rademacher, K. Kanakarajan, and A. W. Czarnik, *Synthesis* **1994**, *4*, 378-380.



## 6 Appendix

### 6.1 List of Abbreviations

AC	activated carbon
ADF-STEM	annular dark field scanning transmission electron microscopy
Ar	Argon
BET	Brunauer–Emmett–Teller
calcd.	calculated
CCS	carbon capture and storage
CCU	carbon capture and utilization
CDC	carbide-derived carbon
CFC	chlorofluorocarbon
CMK	carbon mesostructured by KAIST
CMP	conjugated microporous polymer
COF	covalent organic framework
CV	cyclic voltammetry
EA	elemental analysis
EDX	energy-dispersive X-ray spectroscopy
EIS	electrochemical impedance spectroscopy
FT	Fourier transformed
$g\text{-C}_3\text{N}_4$	graphitic carbon nitride
HAB	hexaaminobenzene
HAT-CN	hexaazatriphenylene-hexacarbonitrile
HCFC	hydrochlorofluorocarbons
HFC	hydrofluorocarbons
HKH	hexaketocyclohexane
HRTEM	high resolution transmission electron microscopy
HOMO	highest occupied molecular orbital
IAST	Ideal Adsorption Solution Theory
IL	ionic liquid
IUPAC	International Union of Pure and Applied Chemistry
IR	infrared

KAIST	Korea Advanced Institute of Science and Technology
LIB	lithium ion battery
LUMO	lowest occupied molecule orbital
MAS	magic angle spinning
Me	methyl
MeOH	methanol
MOF	metal organic framework
NdC	nitrogen-doped carbon
NH <sub>3</sub> -TPD	NH <sub>3</sub> -temperature programmed desorption
NMP	<i>N</i> -methyl-2-pyrrolidone
NMR	nuclear magnetic resonance
ppm	parts per million
POP	porous organic polymer
PSD	pore size distribution
PXRD	powder X-ray diffraction
Q <sub>st</sub>	isosteric heat of adsorption
QSDFE	quenched solid density functional theory
RHE	reference hydrogen electrode
SSA <sub>BET</sub>	Brunauer–Emmett–Teller specific surface area
SEI	solid electrolyte interphase
SEM	scanning electron microscopy
SIB	sodium ion battery
ssNMR	solid-state nuclear magnetic resonance
STEM	scanning transmission electron microscopy
TGA	thermogravimetric analysis
V <sub>micro</sub>	micropore volume
V <sub>total</sub>	total pore volume
XPS	X-ray photoelectron spectroscopy
ZIF	zeolitic imidazolate framework

## 6.2 Characterization Methods

### **Gas Physisorption Measurements**

#### *N<sub>2</sub>/Ar Physisorption*

Physical adsorption (physisorption) is an important technique to characterize porous materials and to optimize these materials due to a comprehensive understanding of their textural characterization. Crucial properties, such as specific surface area (SSA), total pore volumes ( $V_{\text{total}}$ ), and pore size distribution (PSD) can be obtained from physisorption analysis. Physisorption is a phenomenon that occurs between a gas (the adsorptive) and the surface of a solid (the adsorbent), in which only weak van der Waals interactions are involved. The physisorption process is based on the strength of fluid-wall and fluid-fluid interactions, as well as pore geometry effects. All these parameters can influence the shape of an adsorption isotherm. In general, pores can be divided into three different groups depending on their pore width ( $d$ ), named as micropores ( $d < 2$  nm), mesopores ( $2 < d < 50$  nm), and macropores ( $d > 50$  nm), based on the classification suggested by the International Union of Pure and Applied Chemistry (IUPAC) in 2015.<sup>[26]</sup> The micropores can also be distinguished into ultramicropores ( $d = 0\text{--}0.7$  nm) and supermicropores ( $d = 0.7\text{--}2.0$  nm). High-resolution experimental data can be obtained using subcritical fluids, such as N<sub>2</sub> at 77.4 K, Ar at 87.3 K, and CO<sub>2</sub> at 273.1 K. The measurements are conducted *via* volumetric or gravimetric methods. Gas adsorption measurements at cryogenic temperatures of N<sub>2</sub> and Ar are primarily used for surface area and pore size characterization. A physisorption isotherm is measured *via* the amount of adsorbed gas on the adsorbent (within this thesis: porous (nitrogen-doped) carbon materials) with respect to the relative pressure ( $p/p_0$ ).  $P_0$  is the saturation pressure of the adsorptive at a given temperature and  $p$  is the absolute pressure.

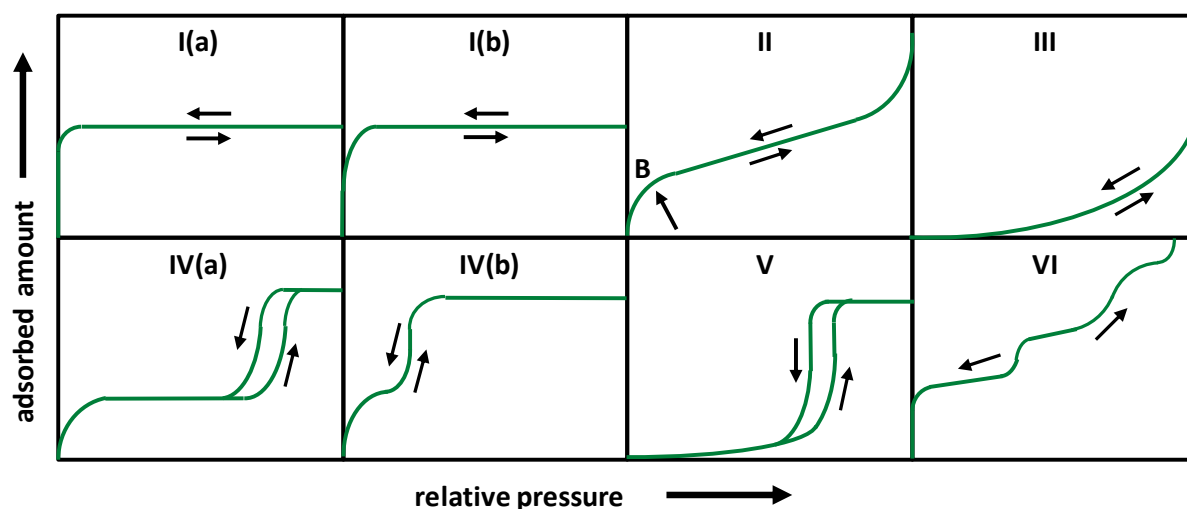


**Figure S 1:** Classification of physisorption isotherms according to IUPAC (adapted from reference <sup>[26]</sup>).

The shape of the isotherms can be classified into eight different types according to IUPAC classification from 2015, as can be seen in **Figure S 1**.<sup>[26]</sup> The isotherms of type I(a) and I(b) are typical for microporous materials, where the filling of ultramicropores and supermicropores corresponds to type I(a) and type I(b) isotherms, respectively. The filling of micropores is a continuous process and occurs for ultramicropores at low relative pressures ( $p/p_0 < 0.01$ ), which is completely based on enhanced solid-gas interactions in such narrow pores. In the case of supermicropores the filling starts at higher relative pressures (e.g.,  $p/p_0 = 0.01-0.15$ ) and an additional cooperative mechanism between the adsorptive molecules becomes important.<sup>[26]</sup> The onset of micropore filling is influenced by the size and kind of adsorbate, pore shape, and width. A type II isotherm refers to non-porous or macroporous materials, in which first monolayer, and then multilayer formation occurs on the surface. Type III and type V isotherms are obtained by materials that reveal relatively weak interactions between adsorbate and adsorbent, i.e., the adsorbate is not entirely wetting the adsorbent surface. This results in very small amounts of adsorbed gas at low relative pressures. Isotherms of the type IV(a) and IV(b) are common for mesoporous materials and are again distinguished by the mesopore size. Type IV(a) isotherms have a hysteresis due to capillary condensation, which can be observed for pore diameters above a certain critical width ( $d > \sim 2$  nm).<sup>[26]</sup> In consequence, adsorbents with mesopores of a smaller width ( $d < \sim 2$  nm) show fully reversible isotherms of type IV(b).<sup>[26]</sup> The filling of mesopores occurs *via* capillary condensation in pores, which describes a gas-liquid transition in confined space. Finally, the type VI isotherm is rarely observed and is characteristic multilayer formation. Several steps in the isotherm stand for the formation of a new adsorbate layer on a smooth, non-porous surface.

The evaluation of the surface area of porous materials is nowadays widely addressed by using the BET method, which was introduced by Brunauer, Emmett, and Teller.<sup>[245]</sup> The BET method assumes multilayer adsorption of a fluid on the pore surface with a different adsorption enthalpy between the first and the following layers, and is thus applicable for micro- and mesoporous materials. The specific surface area is determined by the physisorption isotherms using the BET **Equation S1**, where  $p/p_0$  is the relative pressure,  $V_{ads}$  the total adsorbed volume,  $V_{Mono}$  the volume of a monolayer, and  $C$  the adsorption constant:

$$\frac{p/p_0}{(1 - p/p_0) \times V_{ads}} = \frac{1}{C \times V_{Mono}} + \frac{C - 1}{C \times V_{Mono}} \times \frac{p}{p_0} \quad (\text{Eq. S1})$$

The term on left side of **Equation S1** has to be plotted as a function of the relative pressure  $p/p_0$ , which leads to the volume of adsorbed monolayer  $V_{Mono}$  that can be determined from the slope  $(\frac{C-1}{C \times V_{Mono}})$  of the obtained line and the intersection  $(\frac{1}{C \times V_{Mono}})$  with the y-axis after extrapolation. Using  $V_{Mono}$ , the specific BET surface area ( $SSA_{BET}$ ) (in  $\text{m}^2 \text{g}^{-1}$ ) can be calculated *via* the **Equation S2**, where  $S$  is the  $SSA_{BET}$ ,  $N_A$  is the Avogadro constant,  $\sigma_{N_2}$  the required surface area of a single  $N_2$  molecule in dense package ( $0.162 \text{ nm}^2$ ), and  $m_{Ads}$  the mass of the adsorbent.

$$S = \frac{N_A \times V_{Mono} \times \sigma_{N_2}}{m_{Ads}} \quad (\text{Eq. S2})$$

Furthermore, the pore size distribution of porous materials can be derived by physisorption. The classical macroscopic, thermodynamic methods, like the Barrett-Joyner-Halenda (BJH) method, are based on the Kelvin Equation (**Equation S3**),<sup>[246]</sup> where  $\gamma$  is the surface tension of the gas/fluid interface,  $V_{mol}$  the ideal gas volume,  $\varphi$  the wetting angle,  $R$  the ideal gas constant, and  $T$  the temperature. Capillary condensation (also so-called pore condensation) is correlated to the formation of a meniscus through which the vapor pressure of the fluid is lowered, which leads to sudden condensation and total pore filling. The Kelvin Equation correlates the relative pressure  $p/p_0$  at which pore condensation occurs in a cylindrical pore and the radius  $r_{meniscus}$  of the meniscus (with meniscus is meant the curved liquid-gas interface within the pore) of the condensed liquid in the pore.

$$\ln \frac{p}{p_0} = \frac{-2 \times \gamma \times V_{mol}}{r_{meniscus} \times R \times T} \times \cos \varphi \quad (\text{Eq. S3})$$

According to **Equation S3**, the pore condensation happens at higher relative pressures in pore with a larger diameter, and thus a smaller curvature of the meniscus. The drawback of this

model is that only cylindrical pores and pore diameters above 2.5 nm are considered. The Kelvin Equation does not take the dominant interactions between pore wall and adsorbate in micropores with smaller radius into account. Further improvements that are applicable for micro- and mesopores were made with microscopic methods that are based on the density functional theory (DFT). Advanced quenched solid density functional theory (QSDFT) methods have been developed that take the surface heterogeneity of porous carbon materials and carbon/nitrogen materials into account and were the method of choice to determine the pore size distribution within this thesis.<sup>[247]</sup>

### *CO<sub>2</sub> Physisorption*

CO<sub>2</sub> physisorption at 273 K is an alternative to Ar as adsorbative concerning the analysis of narrowest micropores (i.e., pores with  $d < 0.45$  nm). The problem of diffusion and kinetic restriction at cryogenic temperatures of Ar (87 K) can be overcome. The saturation pressure of CO<sub>2</sub> is very high (26141 torr), and with the measurement temperature of 273 K, CO<sub>2</sub> is around 32 K below its critical temperature. The relative pressure measurements necessary for micropore analysis are obtained within a range of moderate absolute pressures (1–760 torr).<sup>[248]</sup> Hence, micropore size analyses ( $d < 2$  nm) can be performed within a few hours due to faster kinetics by increased temperature and gas uptake at much higher pressures. Due to the quadrupole moment of CO<sub>2</sub>, it is interacting with polar functional groups of micropore-containing adsorbents, such as mesoporous zeolites, silicas, MOFs, or nanoporous heteroatom-containing carbon materials. In consequence, the pore size analysis using CO<sub>2</sub> can get complicated for micropores with significant polar functional groups.<sup>[249]</sup>

### *H<sub>2</sub>O Vapor Physisorption*

Another possibility to investigate the micropore volume, that gained more and more attention in recent years, is the usage of H<sub>2</sub>O vapor physisorption. H<sub>2</sub>O is able to diffuse into very small pores, which cannot be entered by N<sub>2</sub> or Ar at cryogenic temperatures, due to its small kinetic diameter of 0.265 nm.<sup>[133]</sup> On the other hand, H<sub>2</sub>O has a stronger dipole moment, and thus shows higher specific interactions with polar surfaces. In consequence, the combination of H<sub>2</sub>O vapor adsorption with Ar adsorption leads to complementary information about pore structure, porosity, and surface properties/chemistry (e.g., hydrophilicity) of polar adsorbents. H<sub>2</sub>O vapor adsorption on carbonaceous materials is affected by the concentration of functional groups, the arrangement of these groups (topology), measurement temperature, as well as the confined pore structure (pore size/structure) in the adsorbents. There are specific

interactions between H<sub>2</sub>O molecules themselves, as well as to polar functional groups at the surfaces.

In general, H<sub>2</sub>O vapor adsorption on hydrophobic microporous or mesoporous adsorbents exhibit typical S-shaped type V isotherms with a hysteresis loop according to the IUPAC classification. Non-porous adsorbents that contain a low quantity of functional groups result in a type III isotherm, in which the onset point of adsorption is close to the saturation vapor pressure. The presence of functional groups in the adsorbents shifts the initial adsorption and uptake of H<sub>2</sub>O vapor to significantly lower relative pressures, which is reflected by the type I, II or IV isotherms.

Prior to all physisorption measurements, the samples were degassed under vacuum at 150–200 °C for 20 h. Ar, CO<sub>2</sub>, N<sub>2</sub>, and H<sub>2</sub>O vapor physisorption were performed on a Quantachrome Autosorb IQ apparatus. Low pressure physisorption measurements were performed using Ar at 87 K (sample weight ~20 mg). The pore size distributions were calculated using QSDFT method (adsorption branch kernel) for Ar adsorbed on carbon with cylindrical/sphere pore shape at 87 K, integrated into the ASiQwin 3.0 analysis software (Quantachrome). The SSA<sub>BET</sub> were calculated using the multi-point BET model ( $p/p_0 = 0.005–0.05$ ). Total pore volumes ( $V_{total}$ ) were determined at  $p/p_0 = 0.95$ . CO<sub>2</sub> and N<sub>2</sub> physisorption measurements (sample weight ~40–50 mg) were carried out at 273 K and 298 K. The volume of pores with a size below 1.5 nm ( $V_{CO_2 (<1.5 \text{ nm})}$ ) corresponds to the cumulative pore volume at 1.5 nm determined by applying the non-local density functional theory (NLDFT) method to the CO<sub>2</sub> physisorption isotherms measured at 273K. H<sub>2</sub>O vapor physisorption isotherms (sample weight ~50 mg) were measured at 293, 298, and 303 K.

The determination of CO<sub>2</sub> over N<sub>2</sub> selectivity ( $S$ ) (at 298 K; for N<sub>2</sub>/CO<sub>2</sub> ratio of 90/10) followed the ideal adsorption solution theory (IAST) method and was calculated using following equation (**Equation S4**):

$$S_{CO_2/N_2} = \frac{X_{CO_2}}{X_{N_2}} \times \frac{y_{N_2}}{y_{CO_2}} \quad (\text{Eq. S4})$$

where  $x$  is to the molar ratio of CO<sub>2</sub> or N<sub>2</sub> in the adsorbed phase and  $y$  is the molar ratio in the gas phase.

The strength of the interaction of the adsorbent and the test gas (within this thesis CO<sub>2</sub> and H<sub>2</sub>O) can be expressed by the isosteric heat of adsorption ( $Q_{st}$ ). It can be determined by measuring more than one sorption isotherms measured at different temperatures and can be

calculated by the Clausius-Clapeyron equation (**Equation S5**), where  $T$  is the temperature,  $R$  is the ideal gas constant ( $8.3144 \text{ J mol}^{-1} \text{ K}^{-1}$ ),  $p$  is the partial pressure of the test gas,  $p_0$  is the saturation pressure of the test gas, and  $q_a$  is the adsorption capacity of the test gas (in  $\text{mmol g}^{-1}$ ):

$$-\frac{Q_{st}}{R} = \left( \frac{\partial(\ln p/p_0)}{\partial(1/T)} \right)_{q_a} \quad (\text{Eq. S5})$$

The constant loading of test gas  $q_a$  at the corresponding partial pressures  $p$  at different temperatures  $T$  is plotted as  $\ln P$  against  $1/T$ , subsequently the adsorption heat  $Q_{st}$  can be obtained from the slope of the resulting straight line.

### **Thermal Response Measurement using InfraSORP Technique**

Thermal response measurements, using the so-called InfraSORP technique,<sup>[183, 184]</sup> are a useful method for the rapid analysis of porous materials. This screening technique is equipped with an infrared sensor that enables the optical detection of the temperature of the adsorbent during gas adsorption that provides information about several materials properties, such as porosity or capacity for the adsorption gases.

Within the InfraSORP device, the sample is exposed to a continuous flow of test gas and the change of material's temperatures is measured in real-time using an optical temperature sensor. This temperature change is due to the release of the heat of adsorption (thermal response). Upon the dynamic flow conditions, the temperature reaches the original state after the maximum due to cooling by the continuous supply of gas. The integral of the thermal response curve can be correlated to the total heat released during adsorption of the test gas. A wide variety of different test gases (e.g.,  $\text{CO}_2$ ,  $n$ -butane, or  $\text{NH}_3$ ) can be used. The extent of temperature change is depending on the amount of adsorbed gas molecules, pore size distribution, adsorption kinetics, heat capacity, chemical composition, and surface properties of the adsorbents. It is possible to measure different points of a common gas physisorption isotherm, that is, at different relative pressures. Under measurement conditions using  $n$ -butane as test gas (298 K, 1 bar), the relative pressure  $p/p_0^{-1}$  is close to 0.4, which means it fills micropores that would correspond to the plateau/saturation in a type I isotherm.

Thermal response measurements were performed on an optical calorimeter, so called InfraSORP Technology by Fraunhofer/Rubotherm. For the adsorption/desorption measurements, the C-HAT-CN-X materials (~20–30 mg) were placed in the sample holder, and the whole sample cell was purged under  $\text{N}_2$  flow (72 sccm, 1 bar, 99.999 %) until a

constant sample temperature was observed. Then, the sample was exposed to the test gas (e.g., CO<sub>2</sub> or NH<sub>3</sub>) (72 sccm, 1 bar) for 100 seconds, resulting in a temperature increase due to gas adsorption detected by the optical calorimeter. Subsequently, the by-pass was purged with N<sub>2</sub> for 200 s to remove the test gas from the lines. Finally, the N<sub>2</sub> flow was directed to the sample cell for 200 s causing a decrease in temperature due to desorption of the test gas from the C-HAT-CN-X materials. The uptake capacity of the samples was obtained by the peak areas ( $A$ ) of the thermal response curve, which was integrated using OriginPro2015 software. The peak area was divided by the sample mass (mg<sup>-1</sup>) used for the measurements, and is also normalized to the  $V_{\text{total}}$  of the sample material. The sorption kinetics of a sample were investigated using test gas (NH<sub>3</sub>, 72 sccm, 1 bar, 298 K) over repeated cycles with increasing desorption times (e.g., 10 sec, 1 min, 10 min, 60 min, 90 min, and overnight (~13 h)).

The thermal response measurements using the InfraSORP technique with NH<sub>3</sub> gas (**Chapter 3.3.4**) were performed by M.Sc. Michelle Wöllner (Technical University Dresden/Fraunhofer Institute for Material and Beam Technology IWS, Dresden).

### ***NH<sub>3</sub>-Temperature-Programmed Desorption***

Temperature-Programmed Desorption (TPD) is one of the most widely used and flexible techniques for characterizing the acidic sites on zeolite and oxide surfaces. This method is useful to determine the quantity and strength of the acidic sites present in the sample, which is crucial for example to understand and predict the performance of the material as a catalyst. One of the commonly used molecular probes for characterizing acidic sites using TPD is NH<sub>3</sub>. Due to the simplicity of NH<sub>3</sub>-TPD, it is widely established for the characterization of the amount and strength of acidic sites in solid materials. The small molecular size of NH<sub>3</sub> allows its diffusion into all pores of the sample and its basicity is capable of titrating weakly acidic sites. After degassing and temperature activation, the test gas is adsorbed on the cooled sample. The TPD is performed by ramping the sample temperature not higher than the maximum temperature used in the synthesis of the sample, otherwise additional species from the specimen can lead to misleading results. A thermal conductivity detector (TCD) within the device is monitoring the concentration of desorbed NH<sub>3</sub> during the measurement.

NH<sub>3</sub>-TPD was conducted using Belcat Basic instrument (Bel Japan Inc.). Prior to the measurements ~25 mg of the sample was activated at 200 °C for 24 h. The dried sample inside the measuring device was heated up to 500 °C with a heating rate of 10 K min<sup>-1</sup> under helium flow (50 mL min<sup>-1</sup>) and was hold for 1 h at 500 °C. Afterwards, it was cooled to

100 °C and was kept at 100 °C for 30 min under NH<sub>3</sub> flow (100 %, 50 mL min<sup>-1</sup>) to initiate chemisorption of NH<sub>3</sub> on the samples. The samples were purged at 100 °C for 3 h under helium flow (50 mL min<sup>-1</sup>) to get rid of the NH<sub>3</sub> that was physisorbed. The desorption of NH<sub>3</sub>, which was adsorbed by chemisorption, was initialized by heating up to 550 °C with a heating rate of 10 K min<sup>-1</sup> under helium flow (20 mL min<sup>-1</sup>) and the desorbed NH<sub>3</sub> was detected by a thermal conductivity detector.

The NH<sub>3</sub>-TPD measurements (**Chapter 3.3.4**) were conducted by M.Sc. Carolin Selzer (Technical University Dresden, Inorganic Chemistry).

### ***Raman Spectroscopy***

Raman spectroscopy is a vibrational spectroscopy method used to gain information about molecular vibrations and crystal structures. Within this technique, a sample is illuminated with a laser beam in the ultraviolet, visible, or near-infrared range. Raman scattered light is collected with a lense, is subsequently sent through an interference filter or spectrophotometer, and is detected by a charge-coupled device, to obtain a Raman spectrum of a sample. It is possible to investigate the samples concerning their local crystallinity, orientation, and stress.

When light is scattered by a molecule most photons are elastically scattered. The incident photons have the same wavelength, and thus, the same energy (frequency) as the scattered photons. Only an infinitesimal amount of light that is scattered also differs from the optical frequencies of the incident photons (e.g., different (usually lower) optical frequencies). This process leads to the inelastic scattering, which describes the so-called Raman Effect. Raman scattering goes along with a change in vibrational, rotational, or lower frequency of a molecule. The difference in energy between the Raman scattered photon and the incident photon is equal to the energy of a vibration of the scattering molecule.

The huge majority of scattered photons has exactly the same wavelength as the incident photons and is called elastic Rayleigh scattering. In a scattering process, an electron gets excited by the incident photons to a higher energy level. As the electron decays back to a lower level, a scattered photon gets emitted. In the case of Rayleigh scattering, the electron falls back to the original energy level and the scattering is thus being considered as elastic.

The Raman Effect is generated by the interaction of the incident photons with the electric dipole of the molecule that interferes with the molecule's electric field. It can be considered as

electronic spectroscopy, in which the spectrum does contain vibrational frequencies. The process can be described as the decay of the excited electron in the virtual state to a state of lower energy than the real electronic transition including coincident de-excitation and a change in vibrational energy. Hence, the excited electron in the Raman Effect within this scattering process decays to a different level as its original level, and is defined as inelastic scattering.

The wavelength (or energy difference) between the incident and scattered light from a material is represented in **Figure S 2**. The Raman shift in wavenumbers ( $\text{cm}^{-1}$ ) can be calculated *via* the **Equation S6**, using the wavelengths of the incident  $\frac{1}{\lambda_{\text{incident}}}$  and Raman scattered  $\frac{1}{\lambda_{\text{scattered}}}$  photons, respectively, which describes the energy difference  $\bar{\nu}$  between the incident and final vibrational levels.

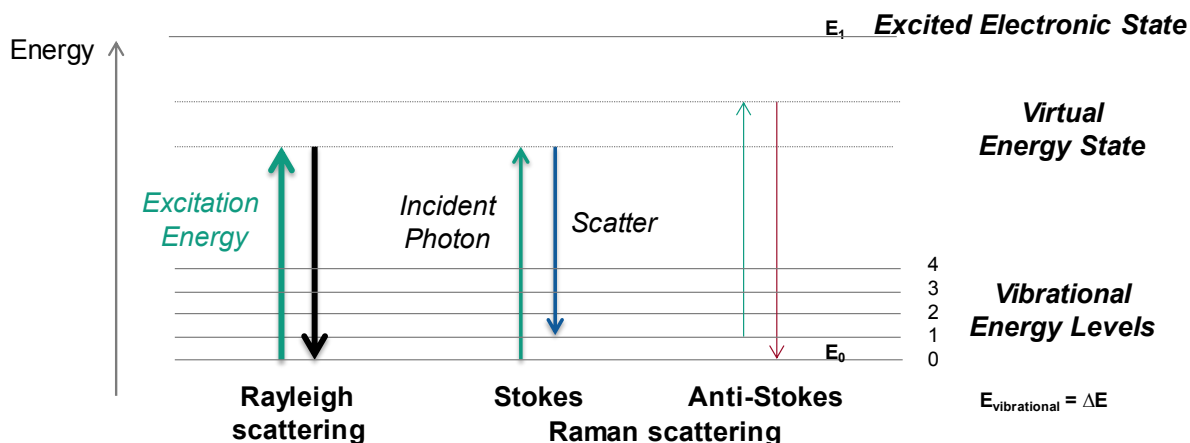


**Figure S 2:** Energy level diagram with involved states in Raman measurements: Rayleigh scattering, Stokes Raman scattering, and Anti-Stokes Raman scattering (b).

$$\bar{\nu} = \frac{1}{\lambda_{\text{incident}}} - \frac{1}{\lambda_{\text{scattered}}} \quad (\text{Eq. S6})$$

Raman spectra were recorded using a Witec (focus innovations) Raman Microscope operating with an objective (Nikon (Japan), LWD 10x/0.25,  $\infty$ - WD 6.1), an excitation wavelength of 532 nm (green laser) with an intensity of 3.5 mW, and accumulations of 100 scans with 10 sec per scan.

### **Scanning Electron Microscopy with Energy-Dispersive X-Ray Spectroscopy**

In both scanning electron microscopy (SEM) and transmission electron microscopy (TEM), the electrons of a beam interact with the sample, which are producing various signals that can be used to obtain information about the surface topography or composition of the sample. In general, electrons are generated by an electron gun, accelerated by an electromagnetic field, and vertically directed, as well as focused, towards the sample by electromagnetic lenses.

In the case of SEM, the electron gun at the top of the column produces a high-energy incident beam of electrons that is focused on a fine spot of the specimen surface. This incident beam is scanned over the specimen and the interactions between incident electron beam and specimen are monitored. As the electrons interact with the sample X-rays are emitted, as well as three different kinds of electrons: primary backscattered electrons, secondary electrons, and Auger electrons. Secondary electrons and backscattered electrons are commonly used for imaging samples. Secondary electrons are most widely used in SEM for showing the morphology and topography of the samples, whereas backscattered electrons are important for exhibiting contrast in composition of the sample.

Secondary electrons are produced from collisions of the incident electron beam and the valence electrons of the specimen. Since the energy of secondary electrons is very low, only at the top surface of the specimen generated electrons are emitted outside the sample. Thus, secondary electrons are very sensitive to the surface. Depending on the incidence angle of the electron beam (i.e., perpendicular or obliquely) to the surface, a difference in the brightness can be observed and secondary electrons are thus used to observe the topography of the sample. The backscattered electrons possess higher energy than the secondary electrons, and hence contain information about the sample from deeper regions. The quantity of backscattered electrons is depending on atomic number of the elements. This means, heavier atoms will create more electrons, and thus areas with heavier atoms will appear brighter in the image than those with lighter atoms. Thus, this image represents the so-called material-contrast of the sample.

The qualitative and quantitative analysis that identifies which elements are present in the sample can be performed by Energy Dispersive X-ray (EDX) Spectroscopy. In this case, the incident electron beam strikes an atom, which then ejects an electron from an inner shell. Subsequently, this vacancy is filled by an electron from a higher-energy shell. In doing so, the electron releases energy in form of X-rays, which corresponds to the difference in energy

between outer and inner shell. The quantity and energy of the X-rays that are emitted from the sample can be measured and thus the elemental composition of the sample, because the energy of the X-ray is characteristic to the atomic structure of the element which it is emitted from. Finally, EDX-mapping is widely used to illustrate the local distribution of elements in the sample.

SEM was carried out on a LEO 1550-Gemini microscope operating at 3.00 kV. The samples were coated with a few nm thin platinum layer *via* sputtering in order to increase the surface conductivity. EDX investigations were conducted using a Link ISIS-300 system (Oxford Microanalysis Group) equipped with a Si(Li) detector and an energy resolution of 133 eV.

SEM with EDX measurements were carried out by Heike Runge and Rona Pitschke.

### ***High-Resolution Transmission Electron Microscopy***

TEM led to even higher magnifications than SEM and the electrons are directed to a very thin area of sample. It can provide information about crystal structure, symmetry, and orientation of materials, as well as the elemental composition of a sample. The electron beam is transmitted (“transmitted” means “passed through”) through the sample, but some electrons are absorbed or deflected. The most common image generated by TEM is the bright field image, in which some areas of the sample scatter or adsorb electrons and therefore appear darker, whereas areas that transmit electrons appear brighter. In this mode, the scattered electrons are excluded from imaging. Thicker regions of the sample or regions with a higher atomic number will appear darker. Thus, lighter elements or regions with no sample will appear brighter, hence, it is called “bright field mode”. The scanning transmission electron microscopy (STEM) allows annular dark field scanning transmission (ADF-STEM) images that are produced by detecting the scattered electrons. The contrast of the image is reversed, and regions with no scattering appear black where the electron beam passes through the sample. It is useful to study crystal defects and imaging crystallographic phases.

HRTEM was performed using a JEOL ARM 200F microscope operating at 200 kV. Prior to analysis, the samples were dispersed in ethanol, and several droplets were cast onto copper TEM grids with a holey carbon film and then dried at room temperature.

For STEM observations, a suspension of the sample in ethanol was sonicated for 10 min and then drop-casted to the copper grid with a lacey carbon support and dried for 5 min. The STEM study was performed using a double Cs corrected JEOL JEM-ARM200F (S)TEM operated at

80 kV and equipped with a cold-field emission gun, a high-angle silicon drift EDX detector (solid angle up to 0.98 steradians with a detection area of 100 mm<sup>2</sup>) and a Gatan Quantum GIF spectroscopy system. ADF-STEM images were collected at a probe convergence semi-angle of 26 mrad. Backscattered electron images (BEI) were obtained in the same microscope using SEI/BEI microplate detector.

The HRTEM measurements were performed by Dr. Tobias Heil (**Chapter 3.1.3**) and Dr. Nadja Tarakina (**Chapter 3.2.2** and **Chapter 3.4.3**), as well as Bolortuya Badamdorj for help with collecting HRTEM images.

### ***Powder X-Ray Diffraction***

Powder X-ray diffraction (PXRD) is a widely applied X-ray diffraction technique for characterizing materials (e.g., crystalline structures and atomic spacing) and is based on constructive interference of monochromatic X-rays and a sample.

X-rays are produced when a focused electron beam in an X-ray tube is accelerated using a high voltage field and bombarded to a stationary or rotating solid target. The electrons collide with atoms in the target (common targets are copper or molybdenum), subsequently X-rays are emitted. The wavelength of the X-rays is characteristic for that element. The monochromatic X-rays are directed to the sample, the incident X-rays are diffracted (i.e., constructive interference) and collected. An important component of all diffraction methods is the angle between incident and diffracted X-rays.

The peaks in an X-ray diffraction are directly related to the atomic distances. The atom distances in crystals are in a similar distance than the wavelengths of the X-rays. The position of the diffraction peaks are determined by the distance between parallel planes of atoms. According to Bragg's Law (**Equation S7**), the angle can be calculated where the constructive interference from X-rays that are diffracted by parallel planes of atoms will produce a diffraction peak. For parallel planes of atoms with the distance  $d$  between the planes, constructive interference only occurs when the Bragg's Law is satisfied.

$$n\lambda = 2d\sin(\theta) \quad (n \in N) \quad (\text{Eq. S7})$$

The Bragg's Law relates the wavelength  $\lambda$  of the incident X-ray to the diffraction angle  $\theta$  of the X-ray beam (i.e., the angle of incidence is equal to the angle of diffraction) and the lattice spacing  $d$  in a sample (i.e., the  $d$ -spacings), and the integer  $n$  is the order of the diffraction beam. The random orientation of the powdered sample requires the scanning of the sample

through a wide range of  $2\theta$  angles that all possible diffraction directions of the lattice are covered.

All PXRD patterns were collected on a Bruker D8 Advance diffractometer equipped with a scintillation counter detector with  $\text{Cu}_{K\alpha}$  radiation ( $\lambda = 0.1518 \text{ nm}$ ) applying  $2\theta$  in the range of  $3\text{--}70^\circ$  step size of  $0.03^\circ$  and counting time of 1 s per step.

### **X-Ray Photoelectron Spectroscopy**

X-ray Photoelectron Spectroscopy (XPS) is a surface analysis technique using ultra-high vacuum (UHV) technology, which provided valuable quantitative and chemical state information about the surface composition of the samples. It has a typical analysis depth of less than 5 nm. The specimen is irradiated using X-ray photons, and the core level electrons are excited by the photons with the energy  $h\nu$ . The electron is ejected from the atom with a well-defined kinetic energy  $E_{\text{kin}}$ , if the excitation energy is sufficient. This is known as the photoelectric effect. The atom is in an excited, ionized state with a hole in its electron shell. The difference of the energy of the incident photon ( $h\nu$ ) and the detected kinetic energy of the photoelectron ( $E_{\text{kin}}$ ) resulted in the binding energy  $E_{\text{bind}}$  of the electron that can be calculated according the **Equation S8**:

$$E_{\text{bind}} = h\nu - E_{\text{kin}} \quad (\text{Eq. S8})$$

In general, electrons from the inner shell of the atom (core electrons) are evaluated in XPS, because the spectra of valence electrons would be too complicated to get any information. From the binding energy and the intensity of a photoelectron peak, the elemental identity, binding motifs, chemical state, and quantity of the detected element can be determined.

XPS measurements were performed using a Thermo Scientific K-Alpha<sup>+</sup> X-ray Photoelectron Spectrometer. All samples were analyzed using a microfocused, monochromated  $\text{Al}_{K\alpha}$  X-ray source ( $h\nu = 1486.68 \text{ eV}$ ;  $400 \mu\text{m}$  spot size). The K-Alpha<sup>+</sup> charge compensation system was employed during analysis to prevent any localized charge buildup. The samples were mounted on conductive carbon tape and the resulting spectra analyzed using the Avantage software from Thermo Scientific. Elemental compositions were determined using survey scans over a range of  $1350\text{--}0 \text{ eV}$  with a step size of  $1.0 \text{ eV}$  and a pass energy of  $200 \text{ eV}$ .

The XPS measurements (**Chapter 3.1.3**) were performed by Dr. Johannes Schmidt (Technical University Berlin, Institute of Chemistry) and (**Chapter 3.4.3**) Prof. Dr. Aurelio Mateo-

Alonso and Dr. Alberto Riaño Carnerero (University of the Basque Country, Basque Center for Macromolecular Design and Engineering, Donostia-San Sebastian, Spain).

### ***Thermogravimetric Analysis coupled with Mass Spectrometry***

Thermogravimetric analysis (TGA) is a technique in which the mass of a substance is monitored as a function of temperature or time as the sample specimen is subjected to a controlled temperature program in a controlled atmosphere. These instruments can quantify the loss of water or solvent, pyrolysis, oxidation, decomposition, amount of metallic catalytic residue, as well as the adsorption and desorption of gases. The TGA instrument can be coupled with a mass spectrometer (TGA-MS) to analyze the composition of the evolved gases, and thus provides more detailed information about the investigated processes.

TGA measurements were performed using a thermo microbalance TG 209 F1 Libra (Netzsch, Selb, Germany) coupled with a Thermostar Mass spectrometer (Pfeiffer Vacuum; Asslar/Germany) with ionization energy of 75 eV. A platinum crucible was used for the measurement of  $10 \pm 1$  mg of samples in a  $\text{N}_2$  flow of  $10 \text{ mL min}^{-1}$  and a purge flow of  $10 \text{ mL min}^{-1}$  and additional  $5 \text{ mL min}^{-1}$   $\text{O}_2$  flow for the measurements in synthetic air. The samples were heated to  $1000 \text{ }^\circ\text{C}$  with a heating rate of  $5 \text{ K min}^{-1}$ . The data was recorded and analyzed by the Proteus (6.0.0) and Quadstar (7.03) software package. TGA mass spectrometry (TGA-MS) measurement was performed using helium or synthetic air with a flow of  $10 \text{ mL min}^{-1}$  and with a heating rate of  $2.5 \text{ K min}^{-1}$ .

TGA-MS measurements were carried out by Antje Völkel.

### ***Elemental Analysis***

Elemental microanalysis (EA) is the sample combustion for quantifying the elemental composition, specifically carbon, hydrogen, nitrogen, and sulfur content. The process typically involves combustion, reduction to simple gases, and separation of combustion gases and detection. Combustion is performed in a stream of oxygen at around  $1000 \text{ }^\circ\text{C}$  or in the presence of metal oxides. The combustion gases are then exposed to reagents that lead to the formed gaseous products (e.g.,  $\text{CO}_2$ ,  $\text{N}_2$ ,  $\text{SO}_2$ , and  $\text{H}_2\text{O}$ ), which are separated and precisely quantified by thermal conductivity detectors.

C/H/N/S EA was accomplished as combustion analysis using a Vario Micro device.

Elemental analysis was carried out by Antje Völkel and Ursula Lubahn.

### **Nuclear Magnetic Resonance Spectroscopy**

Nuclear magnetic resonance (NMR) spectroscopy is a powerful, non-destructive measurement technique to analyze the content, the purity, and the structure of molecular and solid-state compounds. The basic principle relies on the characteristic spin of the nuclei of many elemental isotopes. Commonly used isotopes are  $^1\text{H}$ ,  $^{13}\text{C}$ ,  $^{19}\text{F}$ , and  $^{31}\text{P}$ , which all have a spin of  $\frac{1}{2}$ . If an external magnetic field is applied on the nucleus, the initial energy level splits up. The energy gap between the level of higher and lower energy corresponds to the frequency of radiation. This specific frequency of the energy transition is depending on the strength of the magnetic field applied on the nucleus and the magnetic properties of the isotopes. The field is influenced by the electron shielding of a nucleus, which is further affected by its electronic and chemical environment. Thus, the resonant frequency results in important information about the chemical environment of a nucleus. Furthermore, the orientation of neighboring nuclei has an influence on the effective magnetic field, which is so-called spin-spin coupling. This effect results in a splitting up of the signals of each specific nucleus in two or more lines. In general, NMR experiments are performed in *liquid* phase with dissolved samples. In this case, the Brownian motion averages the orientation dependency of interactions between isotopes and their electronic environment. In comparison, the NMR experiments in *solid-state* struggle with the anisotropy of these interactions, this results in a broadening of the signals. This problem can be avoided by spinning the sample with high rotatory speed in a specific angle of  $54.7^\circ$ , the so-called magic angle with respect to the external magnetic field, which results in the averaging of the anisotropic isotope interactions. The magic-angle spinning (MAS) NMR still suffers from broadened signals, because of dipolar coupling between nuclear spins. Further optimization brings the cross-polarization (CP) NMR spectroscopy, in which the magnetization transfer from more sensitive nuclei (e.g.,  $^1\text{H}$ ) to less sensitive nuclei (e.g.,  $^{13}\text{C}$ ), which results in stronger signals in solid-state NMR (ssNMR).

ssNMR spectra were recorded with a Bruker Avance 400 MHz spectrometer operating at 100.56 MHz for  $^{13}\text{C}$  and 399.88 MHz for  $^1\text{H}$ .  $^{13}\text{C}^{[250]}$  magic angle spinning (MAS) NMR experiments were carried out at a MAS rate of 10 kHz using 4 mm MAS HX double resonance probe. The  $^1\text{H}$  and  $^{13}\text{C}$   $\pi/2$  pulse length were 4.0 and 3.0  $\mu\text{s}$ , respectively. Two pulse phase modulation (TPPM) heteronuclear dipolar decoupling was used during acquisition and a recycle delay of 20 s was implemented. All  $^{13}\text{C}^{[250]}$  spectra are referenced to external TMS at 0 ppm using solid adamantane as a secondary reference.

The  $^1\text{H}$  and  $^{13}\text{C}$  ssNMR spectroscopy measurements (**Chapter 3.2.2** and **Chapter 3.3.3**) were conducted by Dr. Jan Dirk Epping (Technical University Berlin, Institute of Chemistry).

### ***Fourier-Transform Infrared Spectroscopy***

Infrared spectroscopy is a qualitative analysis to identify and to determine the quality and the consistency of a sample, as well as the amounts of components in a mixture. The preferred method is the so-called Fourier-transform infrared (FTIR) spectroscopy. FTIR spectroscopy is a vibrational spectroscopic technique, which means that it takes advantage of asymmetric molecular stretching, vibration, and rotation of chemical bonds as they are exposed to designated wavelengths of light. When infrared radiation is passed through a sample, then parts of it will be absorbed by the sample or are transmitted (going through) the sample. The resulting infrared spectrum represents the absorption and transmission of a sample, which is creating fingerprint information on the chemical composition of the sample. The absorption peaks are correlated to the vibration frequencies between the bonds of the atoms within the sample and are thus unique for different molecular structures (e.g., existence of functional groups). The absorption peaks arise from molecular vibrations, and absorbed energy causes molecular motions, which create a net change in the dipole moment. However, excitation by electromagnetic radiation is only possible for vibration modes, which lead to a change in the electronic dipole moment of the respective molecular entity. The Fourier transform converts the function's time-domain representation, into the function's frequency domain representation. The FTIR is very rapid spectroscopy technique, due to the simultaneously and smoothly analysis of many frequency components in a single operation. This Fourier-based method is used over the whole IR frequency region and is creating the entire spectrum in the amount of time that a conventional spectrometer would need to scan across just a single line in the spectrum.

The FTIR setup used in this thesis is equipped with an attenuated total reflection (ATR) accessory. The infrared beam is directed onto an optically dense crystal (the best is diamond, due to robustness and durability) with a high refractive index at a certain angle. This internal reflectance creates an evanescent wave, which elongates beyond the surface of the crystal right into the sample. The sample absorbs energy in the infrared region and the evanescent wave will be attenuated or altered. This attenuated energy from each evanescent wave is finally returned to the detector and an infrared spectrum is generated. Solid and liquid samples can be measured with accessory without further preparation of the samples.

FTIR spectra were recorded on a Varian 1000 spectrometer with an attenuated total reflectance setup.

### **Sodium-Ion Battery**

The sodium-ion battery (SIB) is a rechargeable electrochemical cell that consists of a negative (i.e., carbonaceous material, metal oxides, or metal alloys) and positive (i.e., a sodium compound) electrode with a separator in-between. The sodium-ion transfer occurs between the electrodes *via* an ionically conducting electrolyte (i.e., a sodium salt in organic solution). The electrodes are made of active material deposited on an aluminum current collector and the separator is an electrically insulating but ionically conducting layer. The voltage range is usually between 0.0 to ~4.0 Volts (V). The SIB stores energy *via* chemical bond in the anode. During the charging process,  $\text{Na}^+$  ions de-intercalate and migrate from the cathode to the anode. Electrons are balancing simultaneously the charge and thus migrate from the cathode through the external circuit containing the charger and into the anode.

Cyclic voltammetry (CV) is applied to investigate the oxidation and reduction processes of molecular species or to study electron transfer-initiated chemical reactions. The potential of the working electrode is measured against a reference electrode. The reference electrode keeps a constant potential, and the resulting applied potential to the working electrode produces an excitation signal. The slope of the excitation signal correlates to the applied scan rate. Within a CV, the voltage potential is repeatedly swept between two boundary values back and forth, and a cyclic voltammogram is obtained by measuring the current at the working electrode during the potential scans.

During charge/discharge with potential limitation (GCPL), a fixed current is applied and the voltage response is monitored. The performance of a battery is tested as a function of the charge and discharge current that are usually expressed as C-rate, which is calculated from the battery capacity. A C-rate of 1 C corresponds to the necessary current that has to be applied/drained into/from the battery to fully charge/discharge it in 1 h (i.e.,  $\text{C h}^{-1}$ ). C-rates multiples of 1 C are often applied and a common of 0.1 C corresponds to charge and discharge of a battery in 10 h. Since the specific capacity of an interaction electrode material per weight is expressed in Ampere per hour ( $\text{mAh g}^{-1}$ ), and hence, the galvanostatic rate in current per active mass ( $\text{mA g}^{-1}$ ).

The approach in electrochemical impedance spectroscopy (EIS) is to use a small amplitude alternating current (AC) sinusoidal excitation signal to the system under investigation and

measure the response of the current or the voltage. The impedance of a system can be calculated using Ohm's law according to following equation (**Equation S9**), where  $E$  is the voltage and  $I$  the current:

$$Z(\omega) = \frac{E(\omega)}{I(\omega)} \quad (\text{Eq. S9})$$

The impedance of the system,  $Z(\omega)$ , is a complex quantity with a magnitude and a phase shift what is in correlation to the frequency of the signal. In consequence, the variation of the frequency of the used signal leads to the impedance of a system as a function of frequency.  $Z(\omega)$  can be further represented in Cartesian as polar coordinates (**Equation S10**), where  $|Z(\omega)|$  is the magnitude of the impedance and  $\varphi$  is the phase shift.

$$Z(\omega) = |Z(\omega)|e^{j\varphi} \quad (\text{Eq. S10})$$

Finally, in Cartesian coordinates  $Z(\omega)$  is defined by following equation (**Equation S11**):

$$Z(\omega) = Z'(\omega) - j \times Z''(\omega) \quad (\text{Eq. S11})$$

Where  $Z'(\omega)$  is the real part of the impedance and  $Z''(\omega)$  is the imaginary part and  $= \sqrt{-1}$ . To get a quick overview of the data and to conclude qualitative interpretations, the data is plotted according to the Nyquist representation. The Nyquist plot shows the plot of the real part of the impedance  $Z'(\omega)$ , against the imaginary part  $Z''(\omega)$ .

For the electrochemical measurements 80 wt.% of the active materials, 10 wt.% of carbon black (super-P), 5 wt.% of sodium carboxymethyl cellulose (Sigma, average molecular weight (MW) ~250000) and 5 wt.% of poly(acrylic acid) (Sigma, average MW ~450000) were uniformly mixed in Milli-Q water under mechanical stirring. The obtained slurries were transferred onto a copper current collector (10 mm in diameter), dried at 60 °C overnight. The areal loading of an electrode was about 1.5 mg cm<sup>-2</sup>. The half-cell tests were carried out using Swagelok-type cells assembled in an Ar filled glove box (H<sub>2</sub>O < 0.1 ppm, O<sub>2</sub> < 0.1 ppm). Sodium metal (11 mm in diameter) was used as both counter and reference electrodes. Glass fibers (Whatman GF/C, 13 mm in diameter) were employed as the separators. The electrolyte was 1 M NaClO<sub>4</sub> in ethylene carbonate/propylene carbonate/fluoroethylene carbonate (45:45:10 by mass). The Swagelok cell was assembled using the working and counter electrodes sandwiching the separator, with 300 μL electrolyte and a copper foil as the current collector for the working electrode. A Biologic MPG-2 galvanostat/potentiostat was used for electrochemical characterization. All measurements were performed at room temperature. EIS was performed at open circuit potential with a sinusoidal signal over a frequency range from

20 kHz to  $10^{-2}$  Hz at an amplitude of 10 mV. CV tests were performed at scan rates of  $0.1 \text{ mV s}^{-1}$ . GCPL tests were applied at specific currents between 0.1 and  $10 \text{ A g}^{-1}$  in a voltage range from 0 to +2.5 V. The specific capacity,  $Q$  ( $\text{mAh g}^{-1}$ ), was calculated according to the following equation (**Equation S12**):

$$Q = \frac{Q_{\text{dis}}}{m} \quad (\text{Eq. S12})$$

Where  $Q_{\text{dis}}$  (mAh) is the charge of the discharging cycle, and  $m$  (g) is the mass of the active material in a single electrode.

The electrochemical measurements on the sodium-ion battery (**Chapter 3.4.5**) were performed by M.Sc. Runyu Yan and M.Sc. Konstantin Schutjajew (Max Planck Institute of Colloids and Interfaces, Colloid Chemistry, Potsdam).

### **Computational Calculations**

Computational Details Periodic density functional theory calculations were carried out using the hybrid Gaussian and plane wave approach,<sup>[251]</sup> as implemented in the CP2K/Quickstep code.<sup>[252]</sup> The Kohn-Sham orbitals were described by an accurate molecularly optimized double-zeta basis set with one additional set of polarization function, while the charge density was represented by plane waves with a density cutoff of 500 Ry.<sup>[253]</sup> Separable norm-conserving pseudopotentials were used to mimic the interactions between the valence electrons and the ionic cores.<sup>[254, 255]</sup> The B97-D exchange and correlation functional, which is based on Becke's power-series *Ansatz*, plus a damped atom-pairwise dispersion correction to account for long-range van der Waals interactions was employed.<sup>[256]</sup> The  $\text{C}_2\text{N}$  structure was modeled using a supercell with  $a=b=16.8$ ,  $c=12.3 \text{ \AA}$  and  $\alpha=\beta=90.0$  and  $\gamma=16.0$ , which consists of four  $\text{C}_2\text{N}$  layers. Optimized structures were obtained by globally minimizing the potential energy, while varying the atomic positions by dynamical simulated annealing<sup>[210, 211]</sup> based on the second-generation Car-Parrinello approach of Kühne *et al.*<sup>[212, 213]</sup>

The computational calculations (**Chapter 3.2.4**) were performed by Prof. Dr. Thomas Kühne (Paderborn University, Theoretical Chemistry).

## 6.3 Experimental Part

### 6.3.1 List of used Chemicals and Gases

#### Gases

**Table S1:** Overview of the purity and supplier of the used gases in this thesis on hand.

Gas	Purity	Supplier
Ar 5.0	99.999 %	Westfalen AG
N <sub>2</sub>	≥ 99.999 %	Air Liquide
CO <sub>2</sub> (Schutzgas ISO)	99.8 %	Westfalen AG
Helium 5.0	99.999 %	Westfalen AG
<i>n</i> -Butane 2.5 (MINICAN®)	≥ 99.5 %	The Linde Group
NH <sub>3</sub>	99 % (for InfraSORP) 100 % (for NH <sub>3</sub> -TPD)	The Linde Group
H <sub>2</sub> O	distilled H <sub>2</sub> O	-

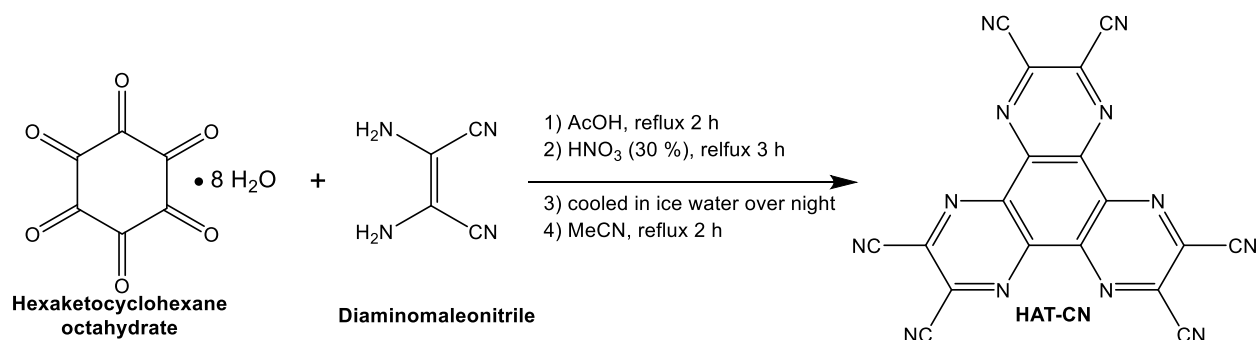
#### Chemicals

**Table S2:** Overview of the chemical formula, purity grade, and supplier of the used chemicals in the thesis on hand.

Substance	Chemical formula	Purity grade	supplier
Acetic Acid (AcOH)	C <sub>2</sub> H <sub>4</sub> O <sub>2</sub>	100 %	Merck
Acetonitrile (MeCN)	C <sub>2</sub> H <sub>3</sub> N	HPLC Plus, ≥ 99.9 %	Sigma-Aldrich
Diaminomaleonitrile	C <sub>4</sub> H <sub>4</sub> N <sub>4</sub>	98 %	Alfa Aesar
Dimethyl sulfoxide- <i>d</i> <sub>6</sub> (DMSO- <i>d</i> <sub>6</sub> )	C <sub>2</sub> D <sub>6</sub> OS	99% 99.5 at.% D	Sigma-Aldrich
Hexaketocyclohexane octahydrate	C <sub>6</sub> O <sub>6</sub> •8H <sub>2</sub> O	97 %	Arcos Organics
Nitric Acid	HNO <sub>3</sub>	65 %	Merck

### 6.3.2 Synthesis of Materials

The *synthesis of hexaazatriphenylene-hexacarbonitrile (HAT-CN)* was carried out according the procedure stated in literature (**Scheme S 1**).<sup>[257, 177]</sup> Synthesis of HAT-CN: Hexaketocyclohexane octahydrate (4 g, 12.6 mmol) and diaminomaleonitrile (10.88 g, 100.8 mmol) were refluxed in AcOH (150 mL) for 2 h. The black suspension was filtered off while hot and washed with hot AcOH (3 × 25 mL) resulting in a black solid. The solid was suspended in 30 % HNO<sub>3</sub> (60 mL) and heated at 100 °C for 3 h. The hot dark brown suspension was poured into ice water (200 mL) and cooled over night. The suspension was filtered and the solid was refluxed in MeCN (400 mL) for 2 h and was filtered. The filtrate was evaporated in vacuo to give an orange solid (2.4 g, yield 50 %). <sup>13</sup>C NMR (DMSO-*d*<sub>6</sub>, 101 MHz): δ 142.0, 135.8, 114.6 (**Figure S 3**).



Scheme S 1: Synthesis of HAT-CN via hexaketocyclohexane and diaminomaleonitrile.

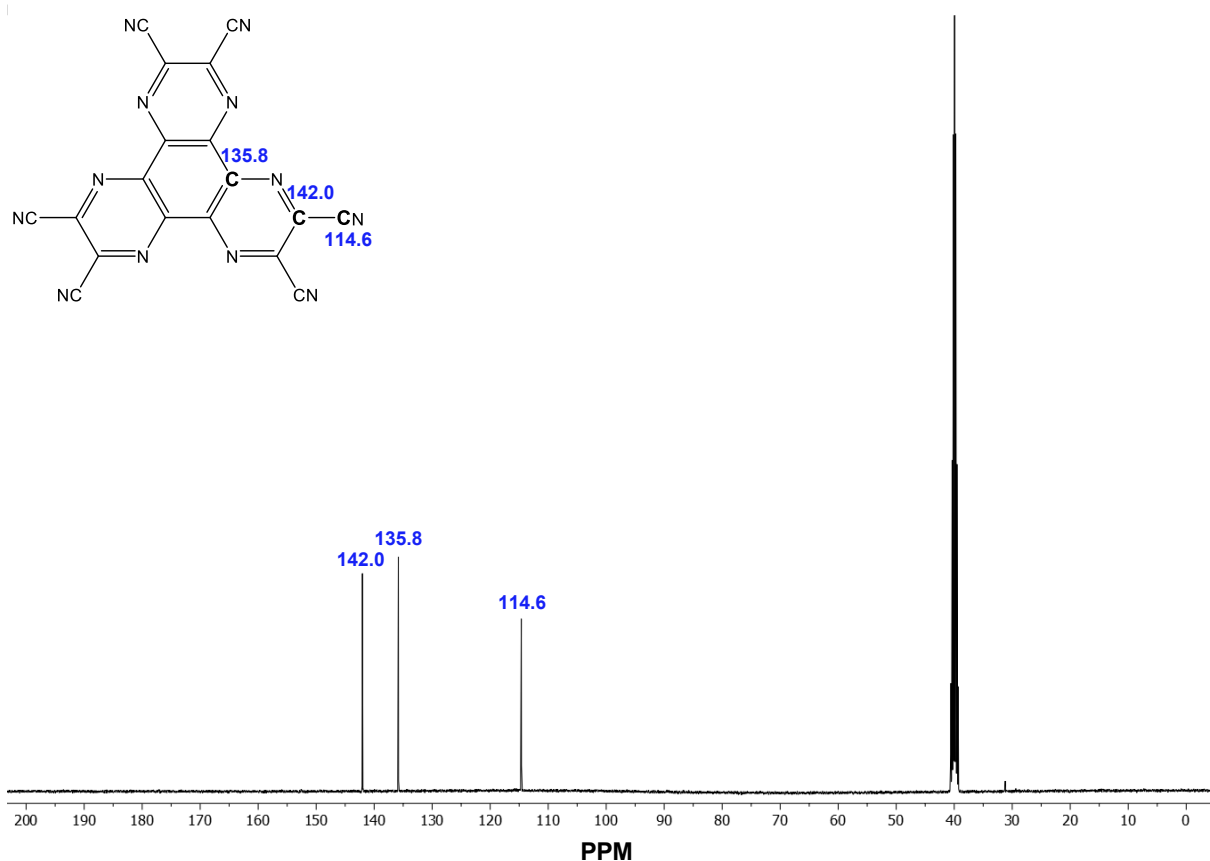


Figure S 3: <sup>13</sup>C NMR spectrum of HAT-CN in DMSO-*d*<sub>6</sub>.

The **synthesis of C-HAT-CN-X**: In a typical procedure, C-HAT-CN-X was prepared using HAT-CN (500 mg) for condensation in a horizontal tubular furnace at different temperatures for 1 h under N<sub>2</sub> gas flow. The heating ramp was set up to be 2 °C min<sup>-1</sup> from room temperature to 80 °C, and 4 °C min<sup>-1</sup> from 80 °C to 500, 525, 550, 700, 850, or 1000 °C, respectively. The described resulting materials are labelled as C-HAT-CN-X, where C stands for condensed and X as the synthesis temperature.

The *synthesis of hexaazatriphenylene-hexacarbonitrile (aza-CMP)*<sup>\*</sup> was carried out according to the procedure stated in literature.<sup>[244]</sup> Synthesis of aza-CMP: To a *Schlenk* flask with hexaketocyclohexane octahydrate (124.8 mg, 0.4 mmol) and 1,2,4,5-benzenetetraamine chlorohydrate (170.4 mg, 0.6 mmol), a mixture of dioxane/acetic acid (1:4 v v<sup>-1</sup>, 20 mL) was added. The mixture was sonicated for five min, and subsequently degassed by three cycles of freeze-pump-thaw. Once finished the degassing process, the mixture was heated at 135 °C and stirred for 7 days under nitrogen. After this time, reaction was cooled to room temperature and filtered off, washing the resulting dark solid with water, HCl aq. 0.2 N, methanol and THF. The solid was *Soxhlet* extracted with water (48 h), methanol (48 h), THF (48 h) and CH<sub>2</sub>Cl<sub>2</sub> (48 h). The compound was then sonicated in the presence of methanol (20 min), THF (20 min), CH<sub>2</sub>Cl<sub>2</sub> (20 min) and Et<sub>2</sub>O (20 min), before being dried under vacuum at 150 °C for 24 h, yielding **aza-CMP** as a black solid (73 mg, 68 %). SS-<sup>1</sup>H-NMR (δ) (ppm): 7.24. SS-<sup>13</sup>C-NMR (δ) (ppm): 170-76, 131, 111. ATR-FTIR (cm<sup>-1</sup>): 3001 (C-H, st); 1597, 1508 (C=N/C=C); 1459 (C-C, st); 1354, 1216 (C-N, st). Elemental Analysis: calculated: C (63.16 %), N (29.46 %) H (1.77 %); observed: C (54.33 %), N (22.96 %), H (2.54 %).

**Synthesis of aza-CMP-X:** In a typical procedure, aza-CMP-X was prepared using aza-CMP (500 mg) for condensation in a horizontal tubular furnace at different temperatures for 1 h under N<sub>2</sub> gas flow. The heating ramp was set up to be 4 °C min<sup>-1</sup> from room temperature to 80 °C, and 4 °C min<sup>-1</sup> from 80 °C to 550, 700, 850, or 1000 °C, respectively. The described resulting materials are labelled as aza-CMP-X, where *X* stands for as the synthesis temperature.

---

\* Aza-CMP was synthesized and provided by Prof. Dr. Aurelio Mateo-Alonso and Dr. Alberto Riaño Carnerero (University of the Basque Country, Basque Center for Macromolecular Design and Engineering, Donostia-San Sebastian, Spain).

## 6.4 Supporting Figures and Tables

### 3.1 Synthesis of Nitrogen-Rich Nanoporous Noble Carbon Materials from a Preorganized Hexaazatriphenylene Precursor

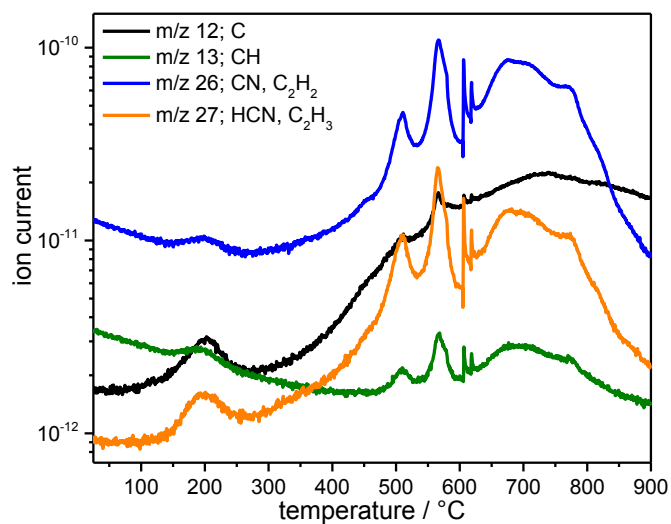


**Figure S 4:** TGA-MS measurement of HAT-CN under helium with a heating rate of  $2.5 \text{ K min}^{-1}$ .

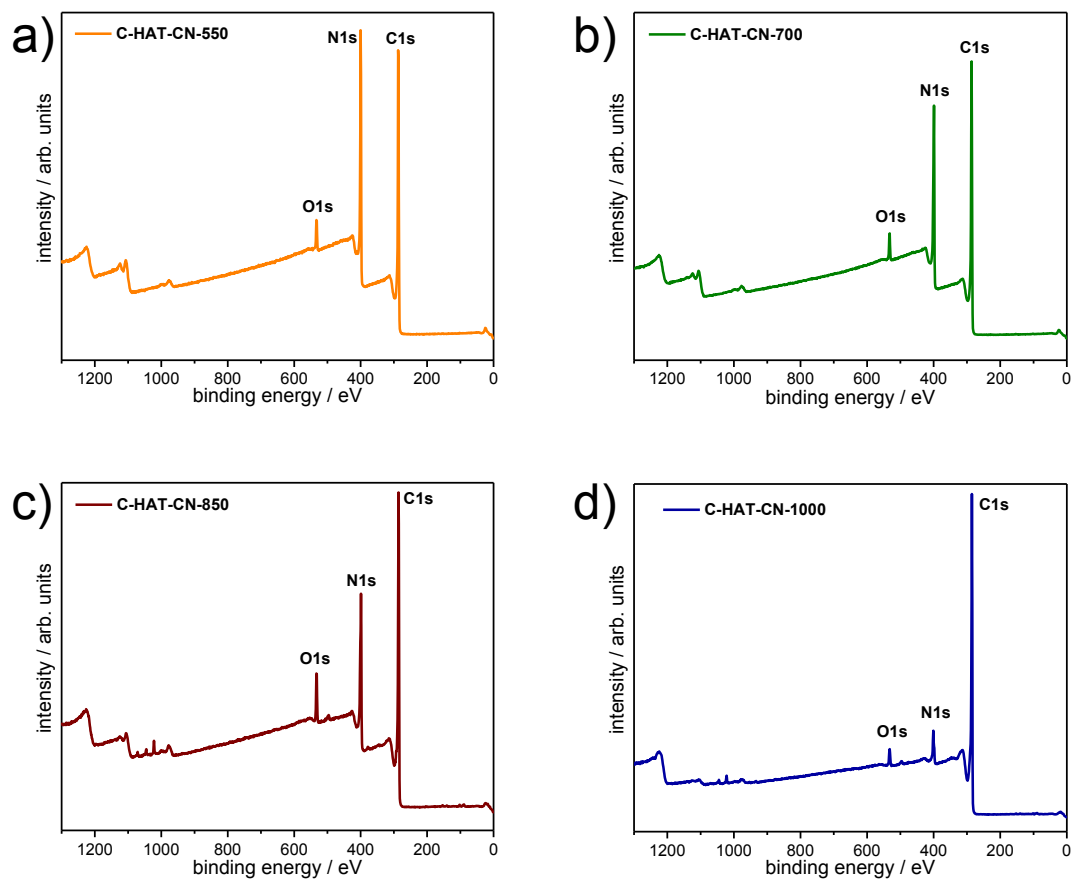


**Figure S 5:** XPS survey spectra of C-HAT-CN-550 (a), C-HAT-CN-700 (b), C-HAT-CN-850 (c), and C-HAT-CN-1000 (d).

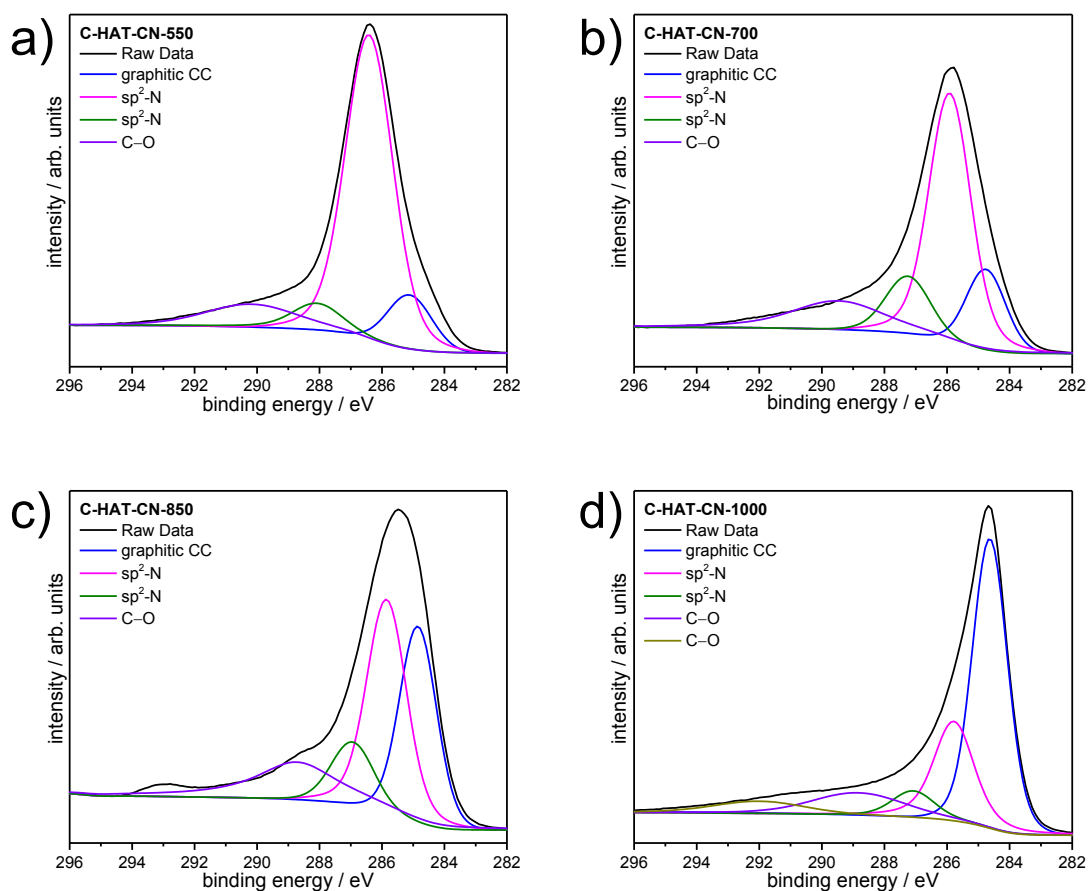


**Figure S 6:** Fitted C1s XPS line scans of C-HAT-CN-550 (a), C-HAT-CN-700 (b), C-HAT-CN-850 (c), and C-HAT-CN-1000 (d).

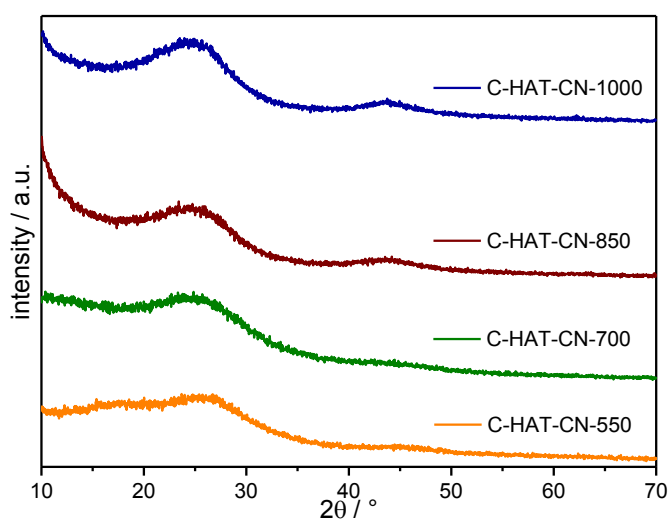


**Figure S 7:** PXRD patterns of C-HAT-CN-550, C-HAT-CN-700, C-HAT-CN-850, and C-HAT-CN-1000.

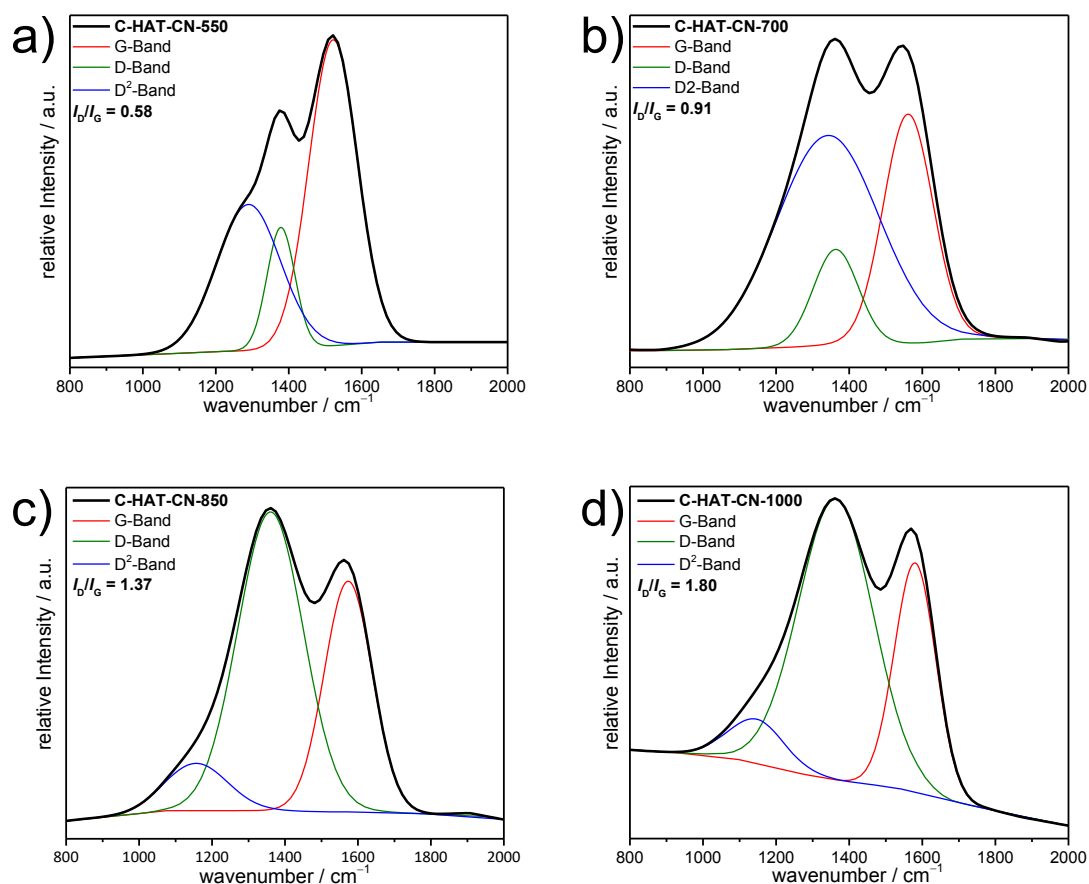


**Figure S 8:** Fitted Raman spectra of C-HAT-CN-550 (a), C-HAT-CN-700 (b), C-HAT-CN-850 (c), and C-HAT-CN-1000 (d).

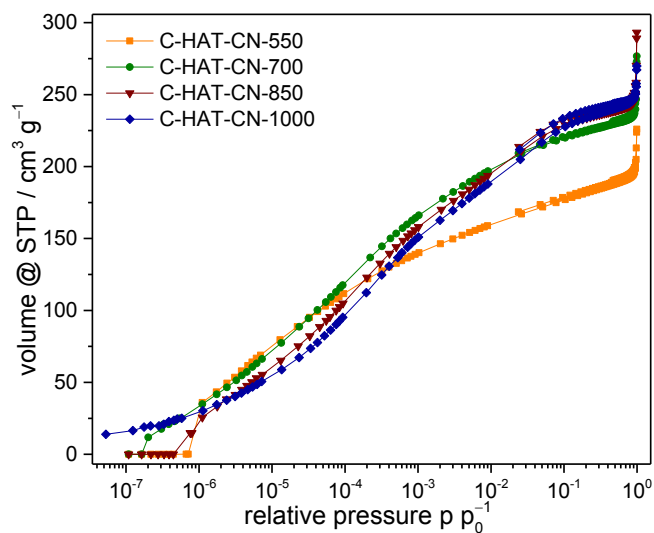


**Figure S 9:** Semi-logarithmic plots of Ar physisorption isotherms (87 K) of C-HAT-CN-550 (orange circles), C-HAT-CN-700 (green squares), C-HAT-CN-850 (wine triangles), and C-HAT-CN-1000 (blue diamonds).

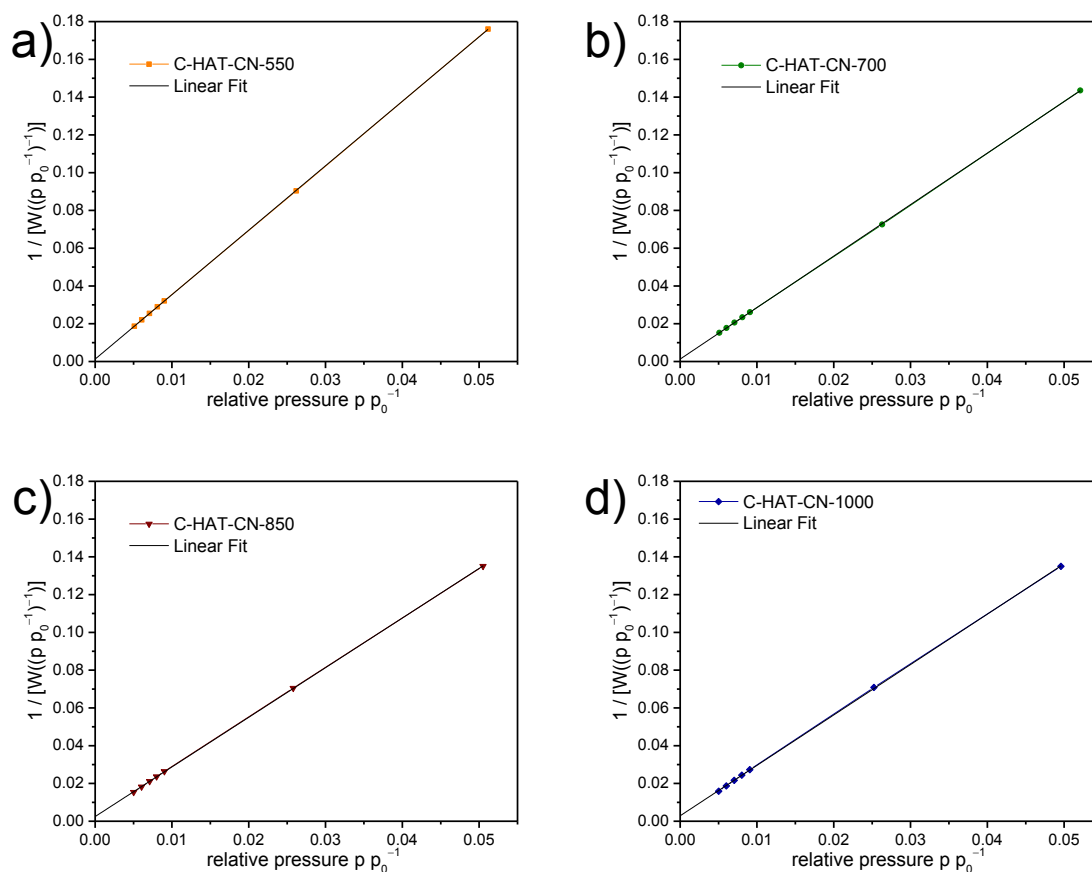


**Figure S 10:** Multipoint-BET plots of C-HAT-CN-550 (a), C-HAT-CN-700 (b), C-HAT-CN-850 (c), and C-HAT-CN-1000 (d).

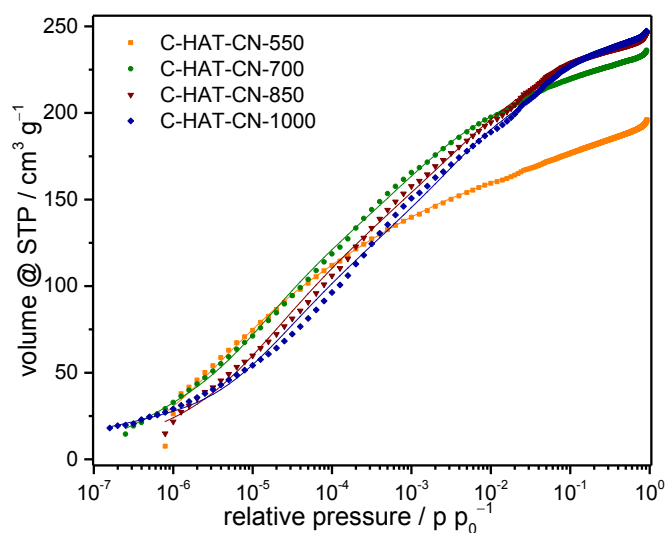


**Figure S 11:** QSDFT fits between the used carbon (cylindrical/spherical pores) adsorption branch kernel and the experimental data (Ar physisorption at 87 K). The good fit between the DFT kernel and the experimental data indicates that this kernel calculates reliable pore size distributions.

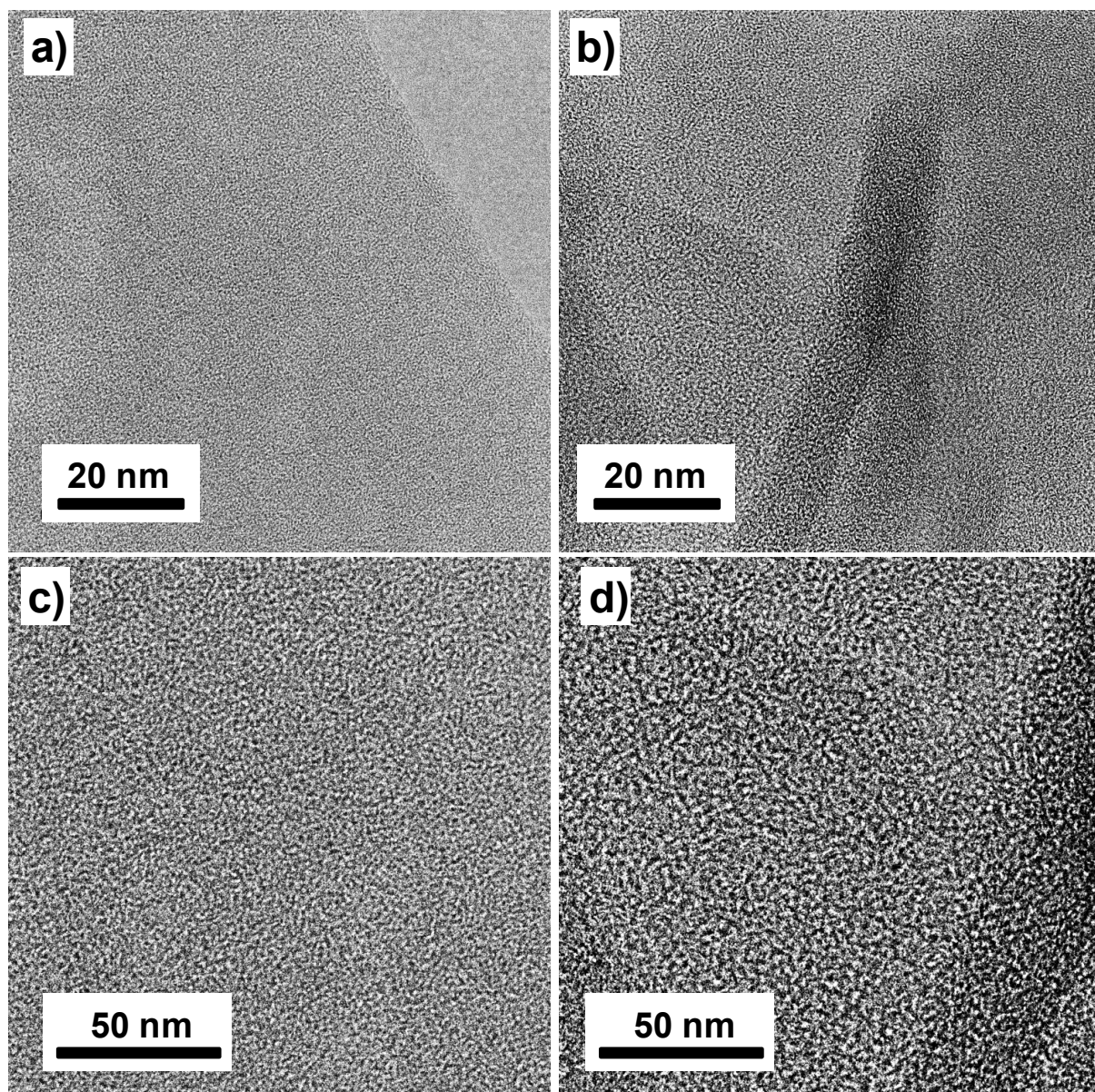


**Figure S 12:** HRTEM images of C-HATCN-550 (a and c) and C-HAT-CN-700 (b and d).

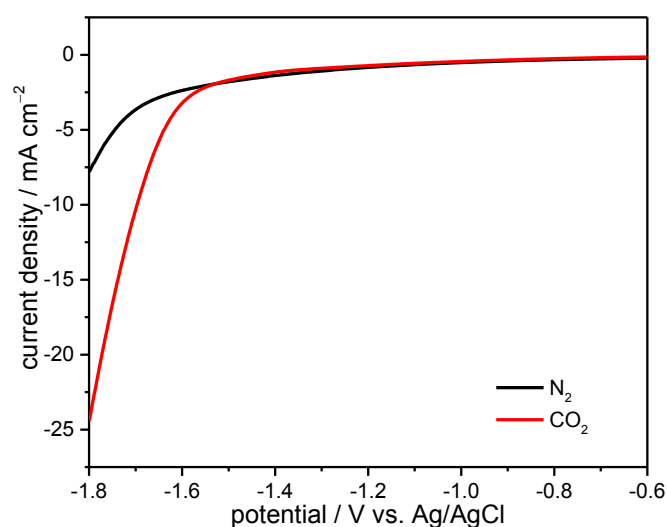


**Figure S 13:** Linear sweep voltammetry (LSV) test for C-HAT-CN-700 performed in  $\text{CO}_2$  and  $\text{N}_2$ -saturated 0.1 M  $\text{NaHCO}_3$  solution ( $\text{pH} = 6.8$ , 298 K). C-HAT-CN-700 was loaded onto a carbon paper electrode as a working electrode. The curves showed a significant current enhancement in  $\text{CO}_2$ -saturated solution.

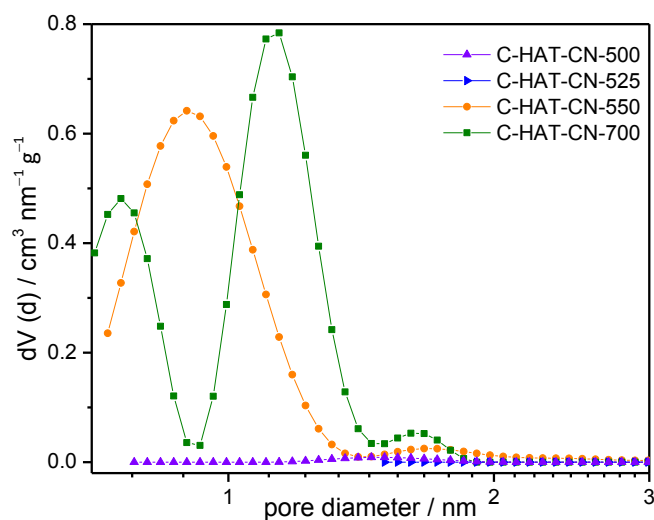
**Table S 3:** Peak assignment (binding energies in eV) of the deconvoluted C1s and N1s XPS spectra of C-HAT-CN-550, C-HAT-CN-700, C-HAT-CN-850, and C-HAT-CN-1000.

Peak	C-HAT-CN-550	C-HAT-CN-700	C-HAT-CN-850	C-HAT-CN-1000
	/ binding energies in eV			
graphitic CC	284.91	284.76	284.85	284.63
sp <sup>2</sup> -N	286.41	285.91	285.85	285.78
sp <sup>2</sup> -N	288.08	287.25	286.95	287.08
C–O	290.17	289.47	288.71	288.84
C–O	-	-	-	291.98
Cyano or Pyrazine	399.74	398.53	398.24	398.10
Cyano or Pyrazine	399.10	398.80	398.65	398.74
quaternary N	401.01	400.82	400.78	400.92
Higher oxides N–O or terminal N	402.75	403.36	403.18	402.90

**Table S 4:** Peak assignment (contribution in at.%) of the deconvoluted C1s and N1s XPS spectra of C-HAT-CN-550, C-HAT-CN-700, C-HAT-CN-850, and C-HAT-CN-1000.

Peak	C-HAT-CN-550	C-HAT-CN-700	C-HAT-CN-850	C-HAT-CN-1000
	contribution / at.%			
graphitic CC	6.95	10.60	22.12	46.42
sp <sup>2</sup> -N	44.78	36.59	26.80	20.19
sp <sup>2</sup> -N	4.52	8.67	8.11	5.64
C–O	6.82	10.23	11.94	9.92
C–O	-	-	-	5.44
Cyano or Pyrazine	10.84	3.16	5.00	1.33
Cyano or Pyrazine	14.61	15.06	9.57	0.51
quaternary N	4.75	9.83	8.85	4.62
Higher oxides N–O or terminal N	3.68	2.81	2.78	1.43

### 3.2 Towards Enhanced CO<sub>2</sub>/N<sub>2</sub> Molecular Sieving with Nitrogen-Doped Carbon Materials Prepared by Molecular Design

**Figure S 14:** Differential pore size distribution plot calculated with QSDFT (Ar on carbons with cylindrical/sphere pores at 87 K, adsorption branch kernel) of C-HAT-CN-500, of C-HAT-CN-525, of C-HAT-CN-550, and C-HAT-CN-700.

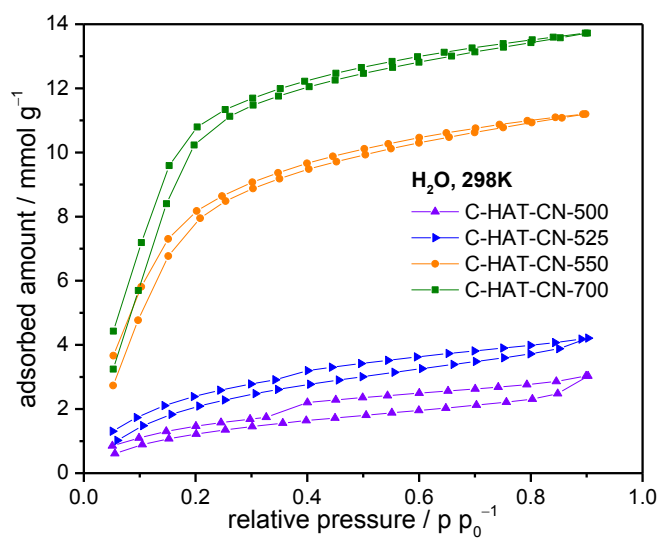


**Figure S 15:** *H<sub>2</sub>O* vapor physisorption isotherms (at 298 K) of C-HAT-CN-500, C-HAT-CN-525, C-HAT-CN-550, and C-HAT-CN-700.

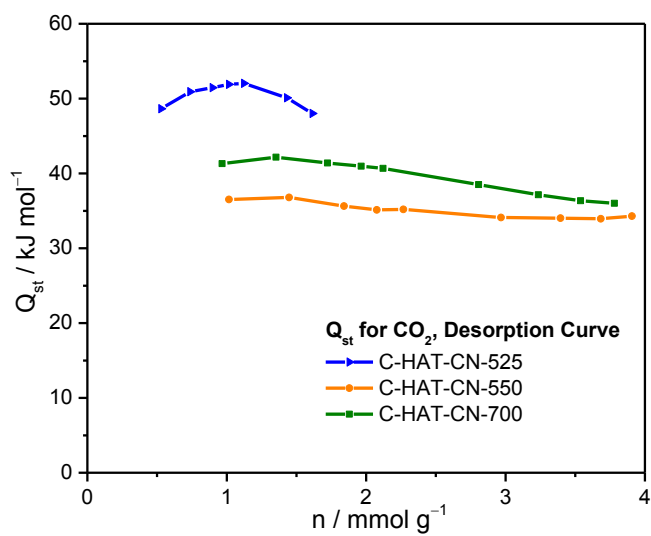


**Figure S 16:** Isosteric heat ( $Q_{st}$ ) of CO<sub>2</sub> adsorption of C-HAT-CN-525, C-HAT-CN-550, and C-HAT-CN-700.

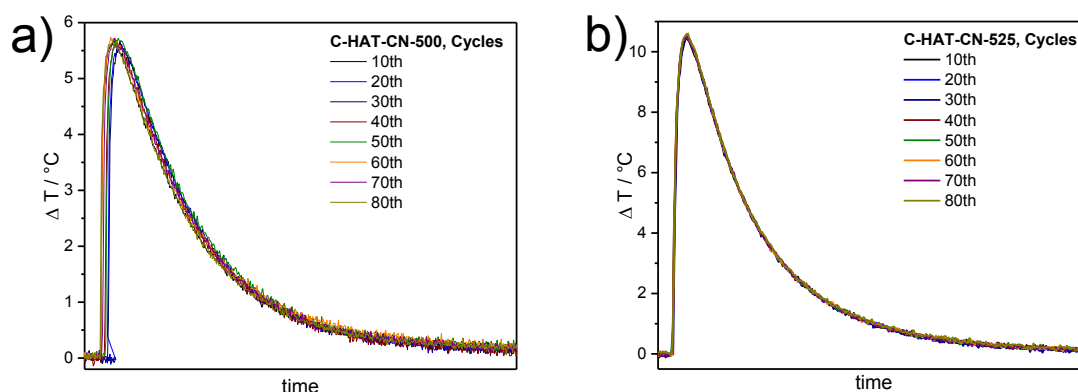


**Figure S 17:** Thermal response curves during cycling experiments on C-HAT-CN-500 (a) and C-HAT-CN-525 (b) using  $\text{CO}_2$  as test gas at 1 bar at 298 K over 80 cycles.

**Table S 5:** Atomic coordinates of  $\text{CO}_2$  in  $\text{C}_2\text{N}$ .

C	C	C	C	C	C	C	C	C	C
7.656810	7.656810	7.656810	7.656810	11.852940	11.852940	11.852940	11.852940	16.054180	16.054180
6.102780	6.102780	6.102780	6.102780	13.381050	13.381050	13.381050	13.381050	6.099530	6.099530
0.000000	3.300000	6.600000	9.900000	0.000000	3.300000	6.600000	9.900000	0.000000	3.300000
C	C	C	C	C	C	C	C	C	C
16.054180	16.054180	20.258350	20.258360	20.258350	20.258360	7.686130	7.686130	7.686130	7.686130
6.099530	6.099530	13.383060	13.383070	13.383060	13.383070	3.579330	3.579330	3.579330	3.579330
6.600000	9.900000	0.000000	3.300000	6.600000	9.900000	0.000000	3.300000	6.600000	9.900000
C	C	C	C	C	C	C	C	C	C
11.880620	11.880620	11.880620	11.880620	16.085279	16.085279	16.085279	16.085279	20.290470	20.290470
10.852770	10.852770	10.852770	10.852770	3.574160	3.574160	3.574160	3.574160	10.853490	10.853500
0.000000	3.300000	6.600000	9.900000	0.000000	3.300000	6.600000	9.900000	0.000000	3.300000
C	C	C	C	C	C	C	C	C	C
20.290470	20.290470	9.143310	9.143310	9.143310	9.143310	13.341710	13.341710	13.341710	13.341710
10.853490	10.853500	6.102960	6.102960	6.102960	6.102960	13.382940	13.382940	13.382940	13.382940
6.600000	9.900000	0.000000	3.300000	6.600000	9.900000	0.000000	3.300000	6.600000	9.900000
C	C	C	C	C	C	C	C	C	C
17.545759	17.545759	17.545759	17.545759	21.747110	21.747110	21.747110	21.747110	6.939080	6.939080
6.099740	6.099740	6.099740	6.099740	13.381060	13.381060	13.381060	13.381060	-0.013080	-0.013080
0.000000	3.300000	6.600000	9.900000	0.000000	3.300000	6.600000	9.900000	0.000000	3.300000
C	C	C	C	C	C	C	C	C	C
6.939080	6.939080	11.138050	11.138050	11.138050	11.138050	15.342950	15.342950	15.342950	15.342950
-0.013080	-0.013080	7.255910	7.255910	7.255910	7.255910	-0.017140	-0.017140	-0.017140	-0.017140
6.600000	9.900000	0.000000	3.300000	6.600000	9.900000	0.000000	3.300000	6.600000	9.900000
C	C	C	C	C	C	C	C	C	C
19.544519	19.544519	19.544519	19.544519	7.685170	7.685170	7.685170	7.685170	11.880700	11.880700
7.253750	7.253750	7.253750	7.253750	1.275290	1.275290	1.275290	1.275290	8.546250	8.546250
0.000000	3.300000	6.600000	9.900000	0.000000	3.300000	6.600000	9.900000	0.000000	3.300000
C	C	C	C	C	C	C	C	C	C
11.880700	11.880700	16.086380	16.086380	16.086380	16.086380	20.290520	20.290510	20.290520	20.290510
8.546250	8.546250	1.270130	1.270130	1.270130	1.270130	8.545420	8.545420	8.545420	8.545420
6.600000	9.900000	0.000000	3.300000	6.600000	9.900000	0.000000	3.300000	6.600000	9.900000
C	C	C	C	C	C	C	C	C	C
9.113630	9.113630	9.113630	9.113630	13.309480	13.309480	13.309480	13.309480	17.514830	17.514830
3.579490	3.579500	3.579490	3.579500	10.853510	10.853510	10.853510	10.853510	3.574340	3.574340
0.000000	3.300000	6.600000	9.900000	0.000000	3.300000	6.600000	9.900000	0.000000	3.300000
C	C	C	C	C	C	C	C	C	C
17.514830	17.514830	21.719299	21.719299	21.719299	21.719299	9.857060	9.857060	9.857060	9.857060
3.574340	3.574340	10.852620	10.852620	10.852620	10.852620	4.866760	4.866760	4.866760	4.866760
6.600000	9.900000	0.000000	3.300000	6.600000	9.900000	0.000000	3.300000	6.600000	9.900000
C	C	C	C	C	C	C	C	C	C
14.055510	14.055510	14.055510	14.055510	18.260910	18.260910	18.260910	18.260910	22.461910	22.461910
12.145130	12.145130	12.145130	12.145130	4.862720	4.862710	4.862720	4.862710	12.142960	12.142960
0.000000	3.300000	6.600000	9.900000	0.000000	3.300000	6.600000	9.900000	0.000000	3.300000
C	C	C	C	C	C	C	C	C	C
22.461910	22.461910	3.458300	3.458300	3.458300	3.458300	7.656690	7.656690	7.656690	7.656690
12.142960	12.142960	6.015930	6.015930	6.015930	6.015930	13.295860	13.295860	13.295860	13.295860

6.600000	9.900000	0.000000	3.300000	6.600000	9.900000	0.000000	3.300000	6.600000	9.900000
C	C	C	C	C	C	C	C	C	C
11.852890	11.852890	11.852890	11.852890	16.054260	16.054260	16.054260	16.054260	1.457090	1.457090
6.017840	6.017840	6.017840	6.017840	13.299140	13.299140	13.299140	13.299140	-0.017010	-0.017010
0.000000	3.300000	6.600000	9.900000	0.000000	3.300000	6.600000	9.900000	0.000000	3.300000
C	C	C	C	C	C	C	C	C	C
1.457090	1.457090	5.662030	5.662030	5.662030	5.662030	9.860900	9.860900	9.860900	9.860900
-0.017010	-0.017010	7.255770	7.255770	7.255770	7.255770	-0.012810	-0.012820	-0.012810	-0.012820
6.600000	9.900000	0.000000	3.300000	6.600000	9.900000	0.000000	3.300000	6.600000	9.900000
C	C	C	C	C	C	C	C	C	C
14.055370	14.055360	14.055370	14.055360	4.947070	4.947070	4.947070	4.947070	9.143190	9.143190
7.253630	7.253630	7.253630	7.253630	6.017840	6.017850	6.017840	6.017850	13.296050	13.296050
0.000000	3.300000	6.600000	9.900000	0.000000	3.300000	6.600000	9.900000	0.000000	3.300000
C	C	C	C	C	C	C	C	C	C
9.143190	9.143190	13.341640	13.341640	13.341640	13.341640	17.545799	17.545799	17.545799	17.545799
13.296050	13.296050	6.015810	6.015810	6.015810	6.015810	13.299350	13.299350	13.299350	13.299350
6.600000	9.900000	0.000000	3.300000	6.600000	9.900000	0.000000	3.300000	6.600000	9.900000
C	C	C	C	C	C	C	C	C	C
6.942900	6.942890	6.942900	6.942890	11.138010	11.138010	11.138010	11.138010	15.339100	15.339100
4.866630	4.866630	4.866630	4.866630	12.143110	12.143110	12.143110	12.143110	4.862450	4.862450
0.000000	3.300000	6.600000	9.900000	0.000000	3.300000	6.600000	9.900000	0.000000	3.300000
C	C	C	C	C	C	C	C	C	C
15.339100	15.339100	19.544600	19.544600	19.544600	19.544600	0.713860	0.713860	0.713860	0.713860
4.862450	4.862450	12.145260	12.145260	12.145260	12.145260	1.270290	1.270290	1.270290	1.270290
6.600000	9.900000	0.000000	3.300000	6.600000	9.900000	0.000000	3.300000	6.600000	9.900000
C	C	C	C	C	C	C	C	C	C
4.919380	4.919380	4.919380	4.919380	9.114710	9.114710	9.114710	9.114710	13.309530	13.309530
8.546090	8.546090	8.546090	8.546090	1.275470	1.275470	1.275470	1.275470	8.545430	8.545430
0.000000	3.300000	6.600000	9.900000	0.000000	3.300000	6.600000	9.900000	0.000000	3.300000
C	C	N	N	N	N	N	N	N	N
13.309530	13.309530	11.192830	11.192830	11.192830	11.192830	15.391840	15.391840	15.391840	15.391840
8.545430	8.545430	4.855230	4.855230	4.855230	4.855230	12.138350	12.138340	12.138350	12.138350
6.600000	9.900000	0.000000	3.300000	6.600000	9.900000	0.000000	3.300000	6.600000	9.900000
N	N	N	N	N	N	N	N	N	N
19.598520	19.598520	19.598520	19.598520	23.798759	23.798759	23.798759	23.798759	5.601510	5.601510
4.852210	4.852210	4.852210	4.852210	12.133260	12.133260	12.133260	12.133260	-0.002520	-0.002520
0.000000	3.300000	6.600000	9.900000	0.000000	3.300000	6.600000	9.900000	0.000000	3.300000
N	N	N	N	N	N	N	N	N	N
5.601510	5.601510	9.801220	9.801220	9.801220	9.801220	14.007170	14.007170	14.007170	14.007170
-0.002520	-0.002520	7.265580	7.265580	7.265580	7.265580	-0.005590	-0.005590	-0.005590	-0.005590
6.600000	9.900000	0.000000	3.300000	6.600000	9.900000	0.000000	3.300000	6.600000	9.900000
N	N	N	N	N	N	N	N	N	N
18.208160	18.208160	18.208160	18.208160	7.008450	7.008450	7.008450	7.008450	11.202890	11.202890
7.260500	7.260500	7.260500	7.260500	2.428200	2.428200	2.428200	2.428200	9.699520	9.699520
0.000000	3.300000	6.600000	9.900000	0.000000	3.300000	6.600000	9.900000	0.000000	3.300000
N	N	N	N	N	N	N	N	N	N
11.202890	11.202890	15.408690	15.408690	15.408690	15.408690	19.616659	19.616659	19.616659	19.616659
9.699520	9.699520	2.421150	2.421150	2.421150	2.421150	9.699380	9.699370	9.699380	9.699370
6.600000	9.900000	0.000000	3.300000	6.600000	9.900000	0.000000	3.300000	6.600000	9.900000
N	N	N	N	N	N	N	N	N	N
2.792820	2.792830	2.792820	2.792830	6.998820	6.998820	6.998820	6.998820	11.198470	11.198470
-0.005670	-0.005670	-0.005670	-0.005670	7.265210	7.265210	7.265210	7.265210	-0.002490	-0.002490
0.000000	3.300000	6.600000	9.900000	0.000000	3.300000	6.600000	9.900000	0.000000	3.300000
N	N	N	N	N	N	N	N	N	N
11.198470	11.198470	15.391670	15.391670	15.391670	15.391670	5.607170	5.607170	5.607170	5.607170
-0.002490	-0.002490	7.260130	7.260130	7.260130	7.260130	4.855310	4.855310	4.855310	4.855310
6.600000	9.900000	0.000000	3.300000	6.600000	9.900000	0.000000	3.300000	6.600000	9.900000
N	N	N	N	N	N	N	N	N	N
9.801190	9.801190	9.801190	9.801190	14.001500	14.001500	14.001500	14.001500	18.208330	18.208330
12.133630	12.133630	12.133630	12.133630	4.852170	4.852170	4.852170	4.852170	12.138730	12.138730
0.000000	3.300000	6.600000	9.900000	0.000000	3.300000	6.600000	9.900000	0.000000	3.300000
N	N	N	N	N	N	N	N	N	N
18.208330	18.208330	9.791330	9.791330	9.791330	9.791330	13.983340	13.983340	13.983340	13.983340
12.138730	12.138730	2.428470	2.428460	2.428470	2.428460	9.699460	9.699460	9.699460	9.699460
6.600000	9.900000	0.000000	3.300000	6.600000	9.900000	0.000000	3.300000	6.600000	9.900000
N	N	N	N	N	N	N	N	C	O
18.191540	18.191540	18.191540	18.191540	22.397110	22.397120	22.397120	22.397120	16.799906	16.799974
2.421420	2.421420	2.421420	2.421420	9.699450	9.699450	9.699450	9.699450	9.699467	9.699486
0.000000	3.300000	6.600000	9.900000	0.000000	3.300000	6.600000	9.900000	6.668839	7.837833
O	C	O	O	C	O	O	C	O	O
16.799999	16.799908	16.799976	16.799999	8.399993	8.436068	8.363932	8.399993	8.436074	8.363925
9.699481	9.699467	9.699486	9.699481	9.699480	9.699453	9.699527	9.699479	9.699453	9.699527
5.501488	0.068839	1.237832	-1.098512	6.600013	7.767787	5.432231	0.000034	1.167809	-1.167746
C	O	O	C	O	O	C	O	O	C
12.616377	12.618105	12.618034	12.616377	12.618105	12.618034	4.249375	4.254428	4.254220	4.249375

## 6 Appendix

2.453383	2.456320	2.456198	2.453383	2.456320	2.456198	2.453409	2.456282	2.456157	2.453409
9.968726	11.137695	8.801399	3.368726	4.537695	2.201400	9.968646	11.137601	8.801332	3.368646
O	O								
4.254428	4.254220								
2.456282	2.456157								
4.537601	2.201333								

Table S 6: Atomic coordinates of  $CO_2$  in  $C_3H$ .

C	C	C	C	C	C	C	C	C	C
7.685840	11.885950	16.085899	20.285879	7.701030	11.901100	16.101101	20.301050	9.114010	13.314110
6.068870	13.343670	6.068990	13.343590	3.621620	10.896260	3.621650	10.896240	6.068970	13.343640
9.900010	9.900130	9.900110	9.900160	9.899970	9.900000	9.900000	9.900060	9.900010	9.900210
C	C	C	C	C	C	C	C	C	C
17.514040	21.714081	6.987030	11.186960	15.387120	19.587021	7.700950	11.901060	16.101160	20.301041
6.069070	13.343720	-0.008880	7.265800	-0.008830	7.265820	1.228010	8.502650	1.228020	8.502630
9.900050	9.900260	9.900180	9.900000	9.900380	9.900140	9.900050	9.900000	9.900230	9.900150
C	C	C	C	C	C	C	C	C	C
9.098780	13.298900	17.498989	21.698879	9.812930	14.013030	18.213020	22.413090	3.485860	7.685950
3.621610	10.896230	3.621620	10.896210	4.858420	12.133000	4.858480	12.133020	6.055320	13.329990
9.900040	9.899930	9.899600	9.899520	9.900030	9.899950	9.899600	9.899530	9.899770	9.899720
C	C	C	C	C	C	C	C	C	C
11.885880	16.085930	1.413050	5.612990	9.813000	14.013030	4.914000	9.114120	13.314070	17.514059
6.055230	13.329890	-0.008760	7.265800	-0.008810	7.265840	6.055120	13.329920	6.055210	13.329810
9.899990	9.899970	9.899870	9.899900	9.899920	9.900000	9.899900	9.899820	9.900000	9.899960
C	C	C	C	C	C	C	C	C	C
6.986980	11.187040	15.387040	19.587000	0.698950	4.898880	9.098880	13.298930	11.184560	15.384680
4.858420	12.133090	4.858480	12.133050	1.228040	8.502630	1.228020	8.502650	4.876130	12.150740
9.900000	9.900050	9.900090	9.900150	9.899780	9.899780	9.899990	9.899990	9.900000	9.899980
C	C	C	C	C	C	C	C	C	C
19.584629	23.784740	5.615270	9.815160	14.015340	18.215219	7.030490	11.230590	15.430650	19.630510
4.876210	12.150850	-0.026600	7.247990	-0.026520	7.248100	2.424830	9.699440	2.424780	9.699410
9.899180	9.899180	9.900610	9.899980	9.900910	9.900110	9.899850	9.900000	9.899970	9.900140
C	C	C	C	C	C	C	C	C	C
2.784680	6.984640	11.184640	15.384690	5.615230	9.815270	14.015270	18.215219	9.769300	13.969430
-0.026470	7.247980	-0.026550	7.248120	4.876110	12.150900	4.876210	12.150760	2.424840	9.699430
9.900160	9.900180	9.899830	9.900060	9.900210	9.900110	9.900060	9.900010	9.900030	9.899950
C	C	C	C	C	C	C	C	C	C
18.169460	22.369360	7.685860	11.885980	16.085930	20.285910	7.701030	11.901100	16.101110	20.301060
2.424790	9.699410	6.068940	13.343740	6.069060	13.343660	3.621600	10.896240	3.621630	10.896220
9.899120	9.899170	6.600000	6.600010	6.600010	6.600020	6.599990	6.600000	6.600000	6.600000
C	C	C	C	C	C	C	C	C	C
9.114030	13.314120	17.514050	21.714100	6.986960	11.186890	15.387050	19.586950	7.700990	11.901100
6.068880	13.343540	6.068980	13.343630	-0.008840	7.265840	-0.008780	7.265860	1.228020	8.502650
6.600000	6.600020	6.600000	6.600030	6.600020	6.600000	6.600040	6.600010	6.600000	6.600000
C	C	C	C	C	C	C	C	C	C
16.101200	20.301081	9.098820	13.298940	17.499029	21.698931	9.812860	14.012960	18.212950	22.413019
1.228030	8.502640	3.621620	10.896240	3.621630	10.896220	4.858470	12.133050	4.858520	12.133070
6.600020	6.600010	6.600000	6.599990	6.599950	6.599950	6.600000	6.600000	6.599960	6.599950
C	C	C	C	C	C	C	C	C	C
3.485880	7.685970	11.885900	16.085951	1.412990	5.612940	9.812940	14.012980	4.914030	9.114140
6.055230	13.329900	6.055150	13.329800	-0.008780	7.265770	-0.008830	7.265820	6.055190	13.329990
6.599970	6.599970	6.600000	6.600000	6.599990	6.600000	6.599990	6.600000	6.600000	6.599990
C	C	C	C	C	C	C	C	C	C
13.314100	17.514080	6.986930	11.186990	15.386990	19.586950	0.698950	4.898880	9.098880	13.298930
6.055280	13.329880	4.858390	12.133070	4.858450	12.133030	1.228020	8.502600	1.227990	8.502630
6.600000	6.599990	6.600000	6.600010	6.600010	6.600020	6.599970	6.599970	6.600000	6.600000
C	C	C	C	C	C	C	C	C	C
11.184630	15.384760	19.584709	23.784821	5.615350	9.815240	14.015420	18.215300	7.030520	11.230620
4.876160	12.150770	4.876240	12.150880	-0.026570	7.248020	-0.026490	7.248130	2.424850	9.699450
6.600000	6.599990	6.599940	6.599930	6.600040	6.600000	6.600070	6.600020	6.599990	6.600000
C	C	C	C	C	C	C	C	C	C
15.430680	19.630550	2.784750	6.984710	11.184710	15.384760	5.615300	9.815340	14.015340	18.215290
2.424800	9.699430	-0.026480	7.247960	-0.026570	7.248110	4.876100	12.150880	4.876200	12.150750
6.600010	6.600020	6.600010	6.600010	6.599990	6.600010	6.600010	6.600000	6.600010	6.600000
C	C	C	C	C	C	C	C	C	C
9.769330	13.969460	18.169491	22.369390	7.685840	11.885950	16.085899	20.285879	7.701030	11.901100
2.424860	9.699450	2.424810	9.699430	6.068870	13.343670	6.068990	13.343590	3.621620	10.896260
6.600000	6.599990	6.599940	6.599940	3.300000	3.300000	3.300000	3.300000	3.300000	3.300000
C	C	C	C	C	C	C	C	C	C
16.101101	20.301050	9.114010	13.314110	17.514040	21.714081	6.987030	11.186960	15.387120	19.587021
3.621650	10.896240	6.068970	13.343640	6.069070	13.343720	-0.008880	7.265800	-0.008830	7.265820
3.300000	3.300000	3.300000	3.300000	3.300000	3.300000	3.300000	3.300000	3.300010	3.300000
C	C	C	C	C	C	C	C	C	C

7.700950	11.901060	16.101160	20.301041	9.098780	13.298900	17.498989	21.698879	9.812930	14.013030
1.228010	8.502650	1.228020	8.502630	3.621610	10.896230	3.621620	10.896210	4.858420	12.133000
3.300000	3.300000	3.300000	3.300000	3.300000	3.300000	3.300000	3.299990	3.300000	3.300000
C	C	C	C	C	C	C	C	C	C
18.213020	22.413090	3.485860	7.685950	11.885880	16.085930	1.413050	5.612990	9.813000	14.013030
4.858480	12.133020	6.055320	13.329990	6.055230	13.329890	-0.008760	7.265800	-0.008810	7.265840
3.300000	3.300000	3.300000	3.300000	3.300000	3.300000	3.300000	3.300000	3.300000	3.300000
C	C	C	C	C	C	C	C	C	C
4.914000	9.114120	13.314070	17.514059	6.986980	11.187040	15.387040	19.587000	0.698950	4.898880
6.055120	13.329920	6.055210	13.329810	4.858420	12.133090	4.858480	12.133050	1.228040	8.502630
3.300000	3.300000	3.300000	3.300000	3.300000	3.300000	3.300000	3.300000	3.300000	3.300000
C	C	C	C	C	C	C	C	C	C
9.098880	13.298930	11.184560	15.384680	19.584629	23.784740	5.615270	9.815160	14.015340	18.215219
1.228020	8.502650	4.876130	12.150740	4.876210	12.150850	-0.026600	7.247990	-0.026520	7.248100
3.300000	3.300000	3.300000	3.300000	3.299990	3.299990	3.300000	3.300000	3.300010	3.300000
C	C	C	C	C	C	C	C	C	C
7.030490	11.230590	15.430650	19.630510	2.784680	6.984640	11.184640	15.384690	5.615230	9.815270
2.424830	9.699440	2.424780	9.699410	-0.026470	7.247980	-0.026550	7.248120	4.876110	12.150900
3.300000	3.300000	3.300000	3.300000	3.300000	3.300000	3.300000	3.300000	3.300000	3.300000
C	C	C	C	C	C	C	C	C	C
14.015270	18.215219	9.769300	13.969430	18.169460	22.369360	7.685860	11.885980	16.085920	20.285910
4.876210	12.150760	2.424840	9.699430	2.424790	9.699410	6.068940	13.343740	6.069060	13.343660
3.300000	3.300000	3.300000	3.300000	3.299990	3.299990	0.000000	0.000010	0.000010	0.000020
C	C	C	C	C	C	C	C	C	C
7.701030	11.901100	16.101101	20.301050	9.114030	13.314120	17.514050	21.714100	6.986960	11.186890
3.621600	10.896240	3.621630	10.896220	6.068880	13.343550	6.068980	13.343640	-0.008830	7.265840
-0.000010	0.000000	0.000000	0.000000	0.000000	0.000020	0.000000	0.000030	0.000020	0.000000
C	C	C	C	C	C	C	C	C	C
15.387050	19.586950	7.700990	11.901100	16.101200	20.301069	9.098820	13.298940	17.499020	21.698919
-0.008780	7.265860	1.228020	8.502650	1.228030	8.502640	3.621620	10.896240	3.621630	10.896220
0.000040	0.000010	0.000000	0.000000	0.000020	0.000010	0.000000	-0.000010	-0.000050	-0.000050
C	C	C	C	C	C	C	C	C	C
9.812860	14.012960	18.212950	22.413019	3.485870	7.685960	11.885900	16.085951	1.412990	5.612940
4.858470	12.133050	4.858520	12.133070	6.055230	13.329900	6.055150	13.329800	-0.008780	7.265770
0.000000	0.000000	-0.000040	-0.000050	-0.000030	-0.000030	0.000000	0.000000	-0.000010	0.000000
C	C	C	C	C	C	C	C	C	C
9.812940	14.012980	4.914020	9.114140	13.314100	17.514080	6.986930	11.186990	15.386980	19.586950
-0.008830	7.265820	6.055190	13.329990	6.055280	13.329880	4.858400	12.133070	4.858460	12.133030
-0.000010	0.000000	0.000000	-0.000010	0.000000	-0.000010	0.000000	0.000010	0.000010	0.000020
C	C	C	C	C	C	C	C	C	C
0.698950	4.898880	9.098880	13.298930	11.184630	15.384760	19.584709	23.784809	5.615350	9.815240
1.228020	8.502600	1.227990	8.502630	4.876160	12.150770	4.876240	12.150880	-0.026570	7.248020
-0.000030	-0.000030	0.000000	0.000000	0.000000	-0.000010	-0.000060	-0.000070	0.000040	0.000000
C	C	C	C	C	C	C	C	C	C
14.015420	18.215300	7.030520	11.230620	15.430670	19.630541	2.784750	6.984710	11.184710	15.384760
-0.026490	7.248130	2.424850	9.699460	2.424800	9.699430	-0.026480	7.247960	-0.026570	7.248110
0.000070	0.000020	-0.000010	0.000000	0.000010	0.000020	0.000010	0.000010	-0.000010	0.000010
C	C	C	C	C	C	C	C	H	H
5.615300	9.815340	14.015340	18.215290	9.769330	13.969460	18.169479	22.369390	15.008020	15.904166
4.876100	12.150880	4.876200	12.150750	2.424860	9.699450	2.424810	9.699430	9.699458	11.251211
0.000010	0.000000	0.000010	0.000000	0.000000	-0.000010	-0.000060	-0.000060	-0.019192	-0.003993
H	H	H	H	H	H	H	H	H	H
17.695791	18.591818	17.695791	15.904205	14.360282	13.480222	11.719739	10.839813	9.295902	10.193801
11.251287	9.699404	8.147600	8.147633	2.424904	3.949252	3.949169	2.424971	8.147410	9.699417
-0.008640	0.004043	-0.008405	-0.003913	0.001293	0.001868	-0.000109	0.001444	-0.023355	-0.069973
H	H	H	H	H	H	H	H	H	H
9.296036	7.503943	5.080368	5.960238	13.480362	11.719834	5.080392	23.406221	24.304045	20.119968
11.251463	8.147390	3.949121	2.424974	0.900653	0.900601	0.900580	9.699437	11.251432	3.949266
-0.023139	0.024146	0.003308	0.001620	0.002759	0.000652	0.001549	0.069461	0.023423	0.000866
H	H	H	H	H	H	H	H	H	H
19.240051	3.319952	15.039849	15.919790	17.680153	18.560099	17.680136	15.919827	14.393227	13.497146
2.424888	0.900671	9.699442	11.223706	11.223715	9.699394	8.175150	8.175140	2.421453	3.978935
0.001078	-0.000650	9.901167	9.901350	9.901296	9.901690	9.901580	9.901342	9.890381	9.893141
H	H	H	H	H	H	H	H	H	H
11.700560	10.809258	9.280028	10.160113	9.280204	7.519808	5.094363	5.995728	13.492427	11.705341
3.976119	2.421523	8.175064	9.699377	11.223796	8.175038	3.981937	2.420956	0.872469	0.875003
9.891408	9.893456	9.899898	9.900213	9.900590	9.900450	9.891177	9.886067	9.897902	9.894488
H	H	H	H	H	H	H	H	H	H
5.090700	23.439842	24.319860	20.098999	19.211752	3.303652	15.008019	15.904164	17.695791	18.591827
0.870027	9.699367	11.223771	3.973715	2.422086	0.877485	9.699457	11.251211	11.251287	9.699405
9.897235	9.898725	9.898786	9.892665	9.892245	9.896215	6.580808	6.596007	6.591360	6.604043
H	H	H	H	H	H	H	H	H	H
17.695793	15.904204	14.360292	13.480221	11.719739	10.839813	9.295902	10.193802	9.296040	7.503945
8.147601	8.147633	2.424907	3.949252	3.949169	2.424971	8.147408	9.699408	11.251462	8.147389
6.591594	6.596087	6.601294	6.601869	6.599892	6.601444	6.576644	6.530026	6.576858	6.624147

H	H	H	H	H	H	H	H	H	H
5.080363	5.960238	13.480361	11.719834	5.080394	23.406221	24.304050	20.119967	19.240059	3.319954
3.949125	2.424976	0.900652	0.900600	0.900577	9.699433	11.251432	3.949264	2.424882	0.900668
6.603308	6.601620	6.602761	6.600652	6.601550	6.669457	6.623426	6.600865	6.601077	6.599350
H	H	H	H	H	H	H	H	H	H
15.039849	15.919790	17.680153	18.560099	17.680136	15.919827	14.393217	13.497147	11.700561	10.809258
9.699442	11.223705	11.223715	9.699394	8.175148	8.175140	2.421454	3.978937	3.976118	2.421524
3.301255	3.301342	3.301425	3.301373	3.301398	3.301256	3.291707	3.292723	3.291643	3.293221
H	H	H	H	H	H	H	H	H	H
9.280028	10.160112	9.280204	7.519808	5.094385	5.995704	13.492440	11.705345	5.090696	23.439842
8.175064	9.699377	11.223795	8.175036	3.981951	2.420946	0.872461	0.875008	0.870020	9.699368
3.300013	3.300226	3.300186	3.299766	3.288222	3.288459	3.293910	3.296102	3.295138	3.300112
H	H	H	H	C	O	O	C	O	O
24.319860	20.099012	19.211761	3.303652	16.799982	16.799789	16.800217	16.799982	16.799789	16.800215
11.223771	3.973714	2.422086	0.877480	9.699406	9.699494	9.699481	9.699405	9.699494	9.699481
3.300013	3.295269	3.294863	3.295360	6.671480	7.845218	5.494851	0.071479	1.245218	-1.105150
C	O	O	C	O	O	C	O	O	C
8.399996	8.435630	8.364381	8.399999	8.435629	8.364379	12.610610	12.616999	12.616683	12.610607
9.699311	9.699464	9.699514	9.699309	9.699465	9.699515	2.443860	2.454438	2.453745	2.443859
6.600009	7.774882	5.425118	0.000010	1.174882	-1.174883	9.971267	11.144994	8.794632	3.371273
O	O	C	O	O	C	O	O		
12.617016	12.616665	4.233090	4.250941	4.249745	4.233086	4.250987	4.249690		
2.454414	2.453769	2.444057	2.454313	2.453500	2.444064	2.454287	2.453526		
4.544990	2.194628	9.970882	11.144579	8.794217	3.370876	4.544582	2.194217		

### 3.3 Structure-Related Properties of HAT-CN-Derived Carbon Materials for the Adsorption of H<sub>2</sub>O and NH<sub>3</sub>

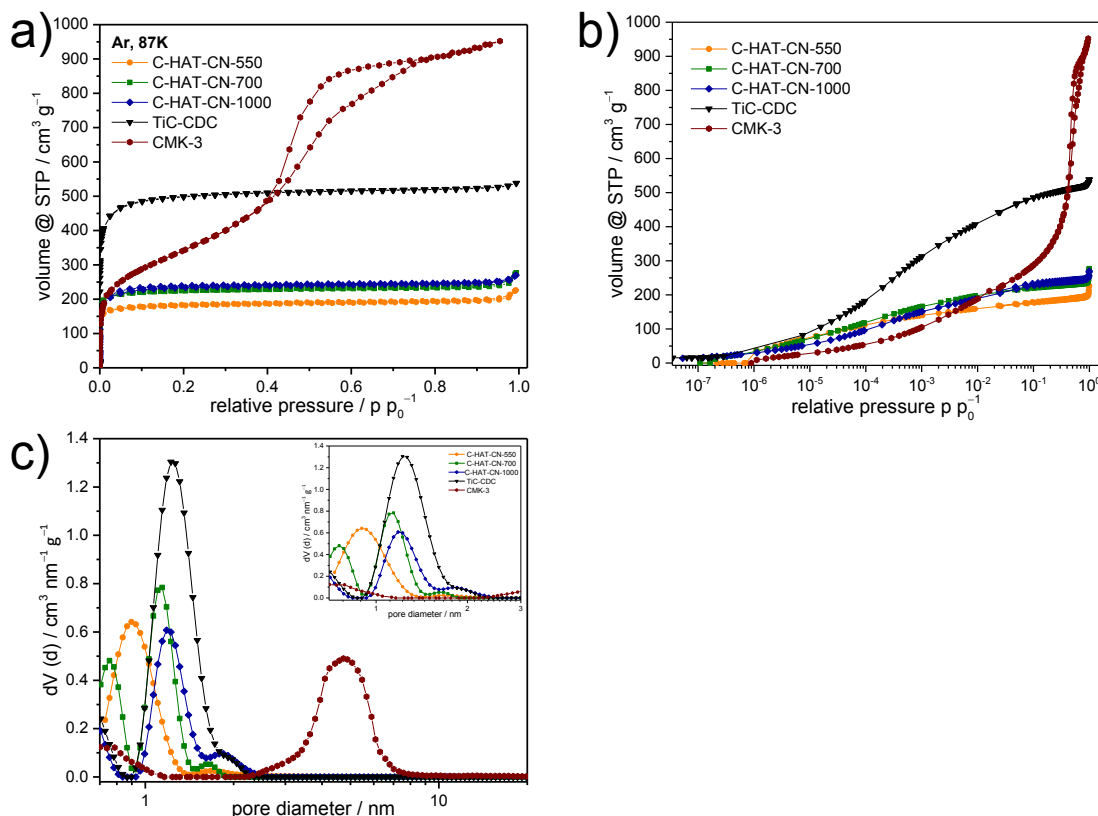


**Figure S 18:** Ar physisorption isotherms (87 K) (a), differential (b), and cumulative (c) pore size distribution plot calculated with QSDFT (Ar on carbons with cylindrical/sphere pores at 87 K, adsorption branch kernel), semi-logarithmic plots of Ar physisorption isotherms (87 K) (d) of C-HAT-CN-550, of C-HAT-CN-700, of C-HAT-CN-1000, and TiC-CDC.

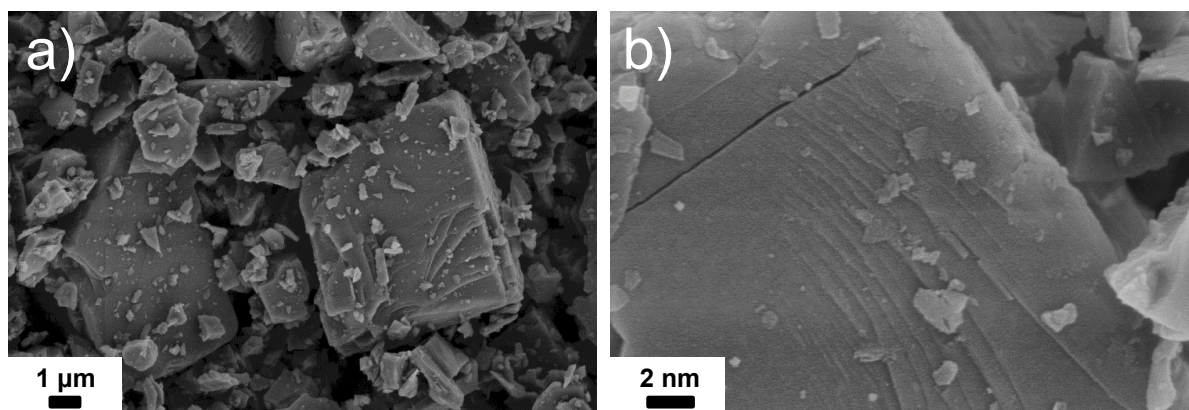


Figure S 19: SEM images of TiC-CDC (a) and (b).

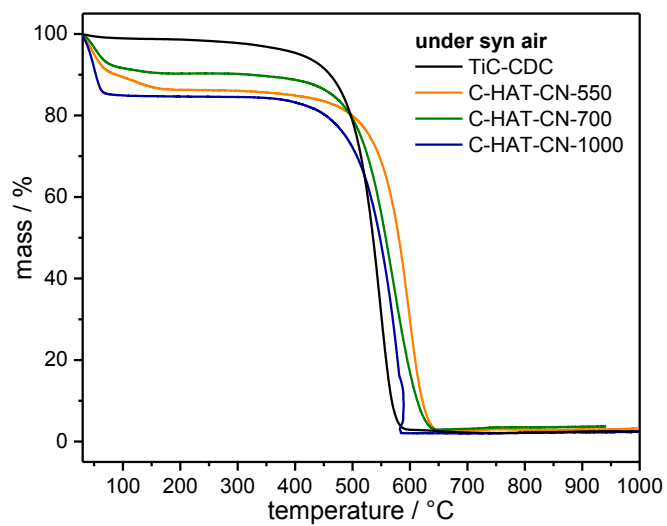
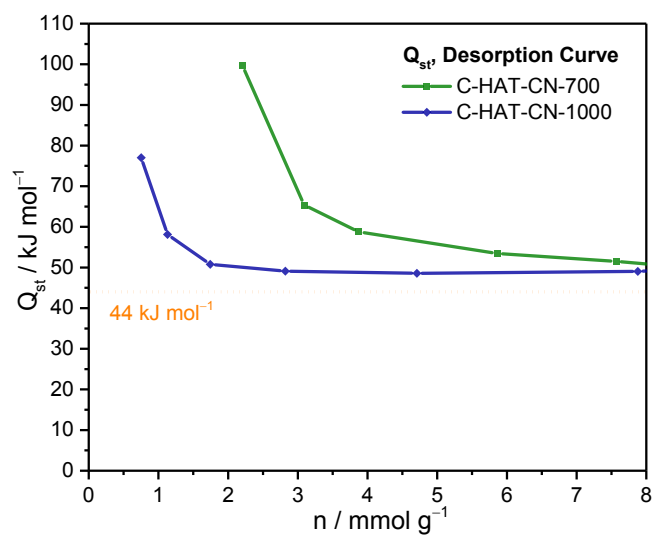
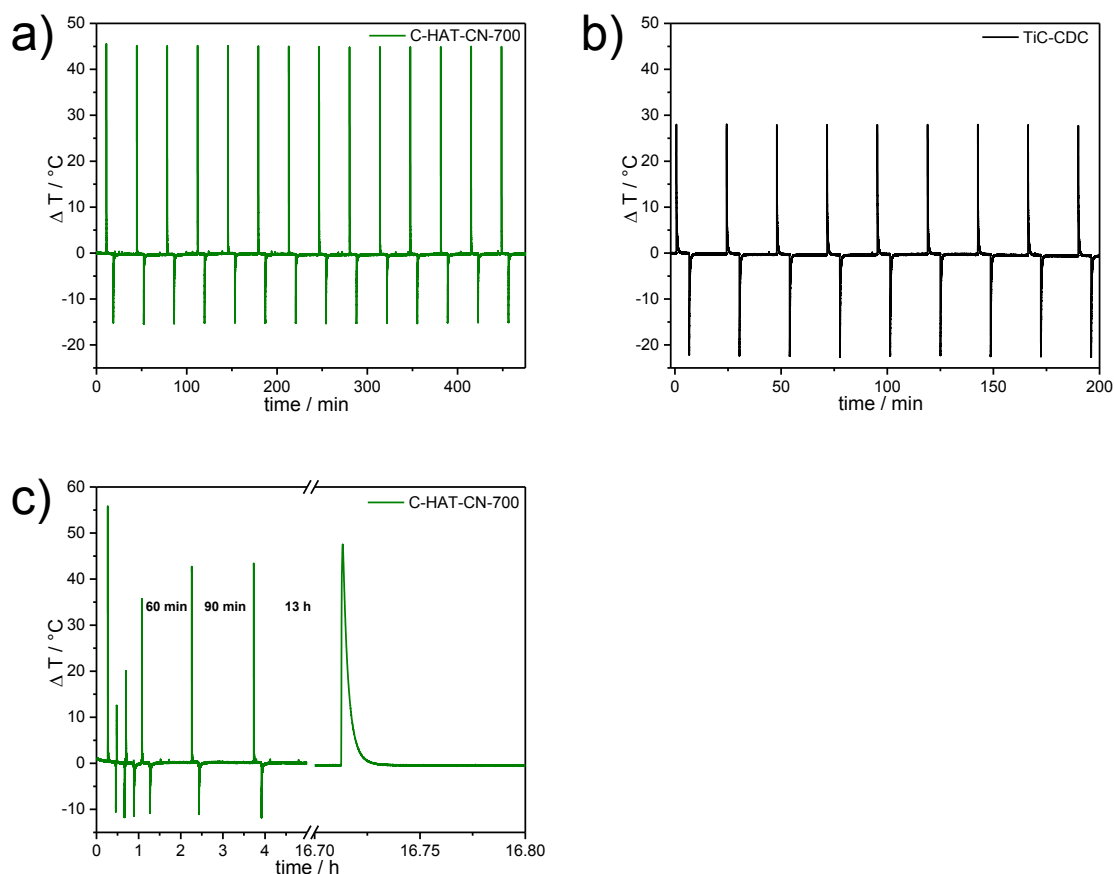


Figure S 20: TGA measurements of C-HAT-CN-550, C-HAT-CN-700, C-HAT-CN-1000, and TiC-CDC measured under synthetic air with a heating rate of  $5 \text{ K min}^{-1}$ .



**Figure S 21:** Isothermic heat ( $Q_{st}$ ) of  $H_2O$  adsorption of C-HAT-CN-700 and C-HAT-CN-1000.



**Figure S 22:** Stability tests under  $NH_3$  adsorption and desorption using InfraSORP technique over nine cycles of C-HAT-CN-700 (a) and TiC-CDC (b), as well as the investigation of sorption kinetics using InfraSORP technique with  $NH_3$  (1 bar, 298 K) of C-HAT-CN-700 over six cycles with increasing desorption times of 10 sec, 1 min, 10 min, 60 min, 90 min, and overnight (~13 h) (c).

### 3.4 Nitrogen-doped Carbon Materials derived by Conjugated Microporous Polymer

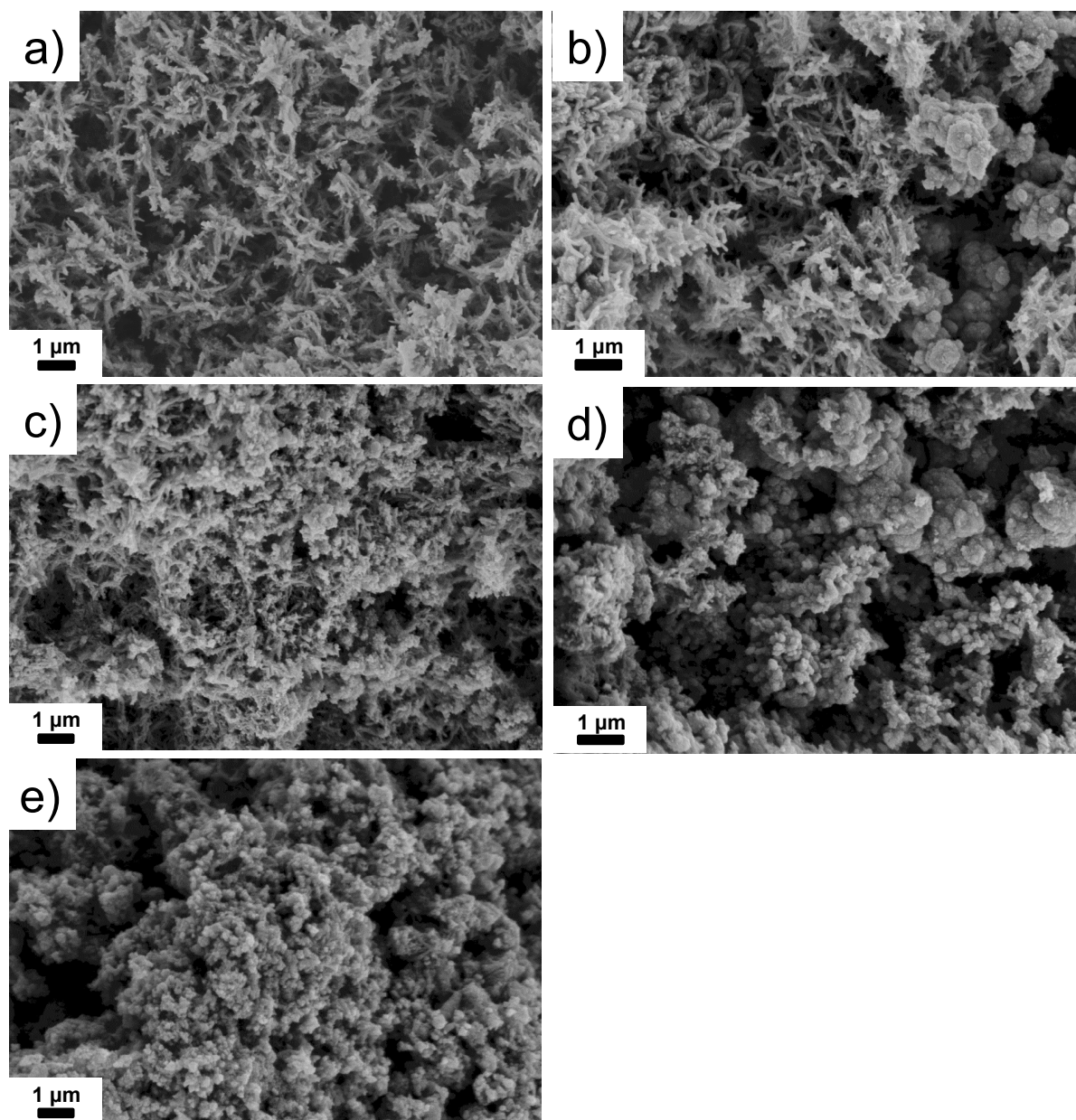


**Figure S 23:** SEM images of aza-CMP (a), aza-CMP-550 (b), aza-CMP-700 (c), aza-CMP-850 (d), and aza-CMP-1000 (e).

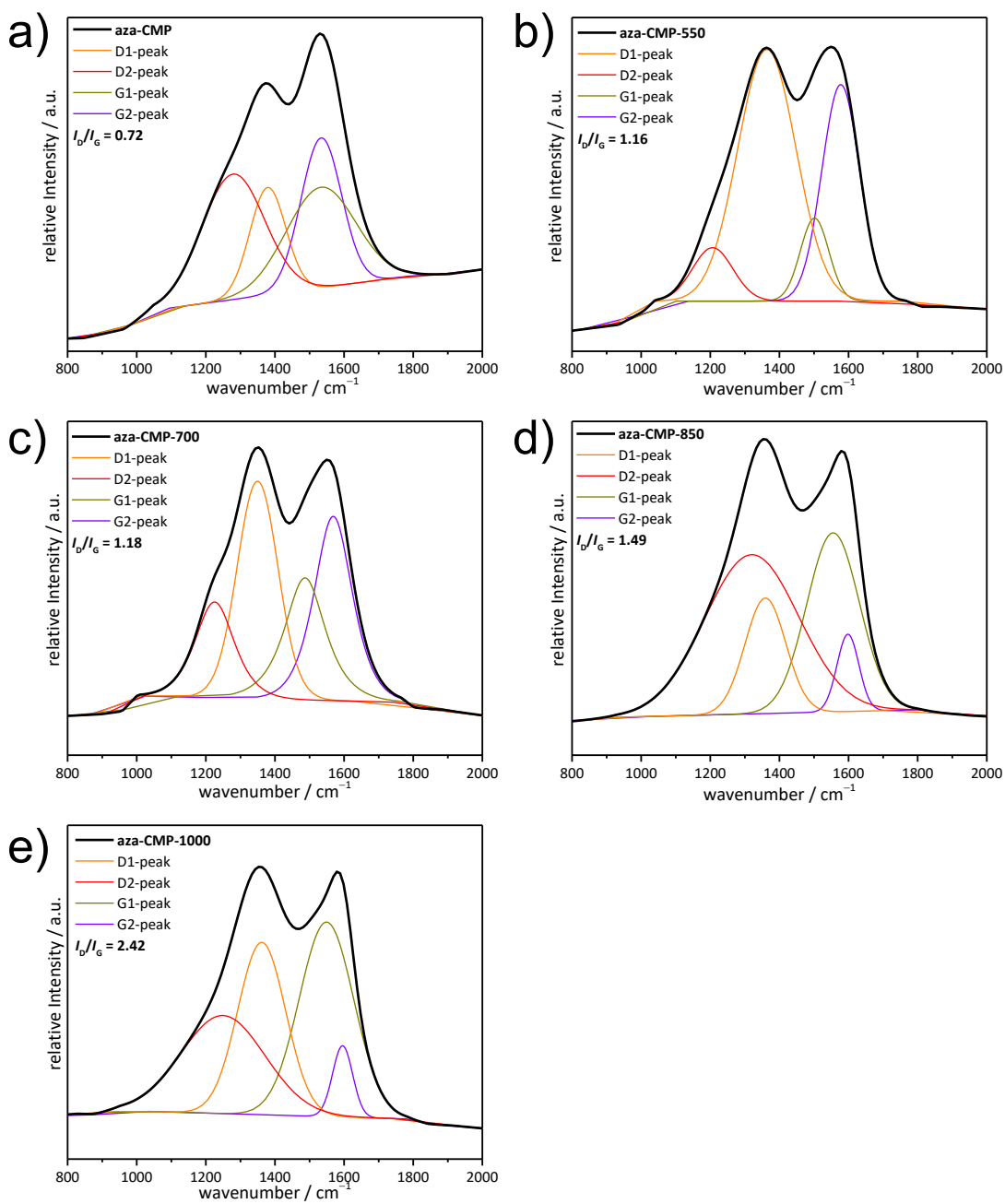


**Figure S 24:** Fitted Raman spectra of aza-CMP (a), aza-CMP-550 (b), aza-CMP-700 (c), aza-CMP-850 (d), and aza-CMP-1000 (e).

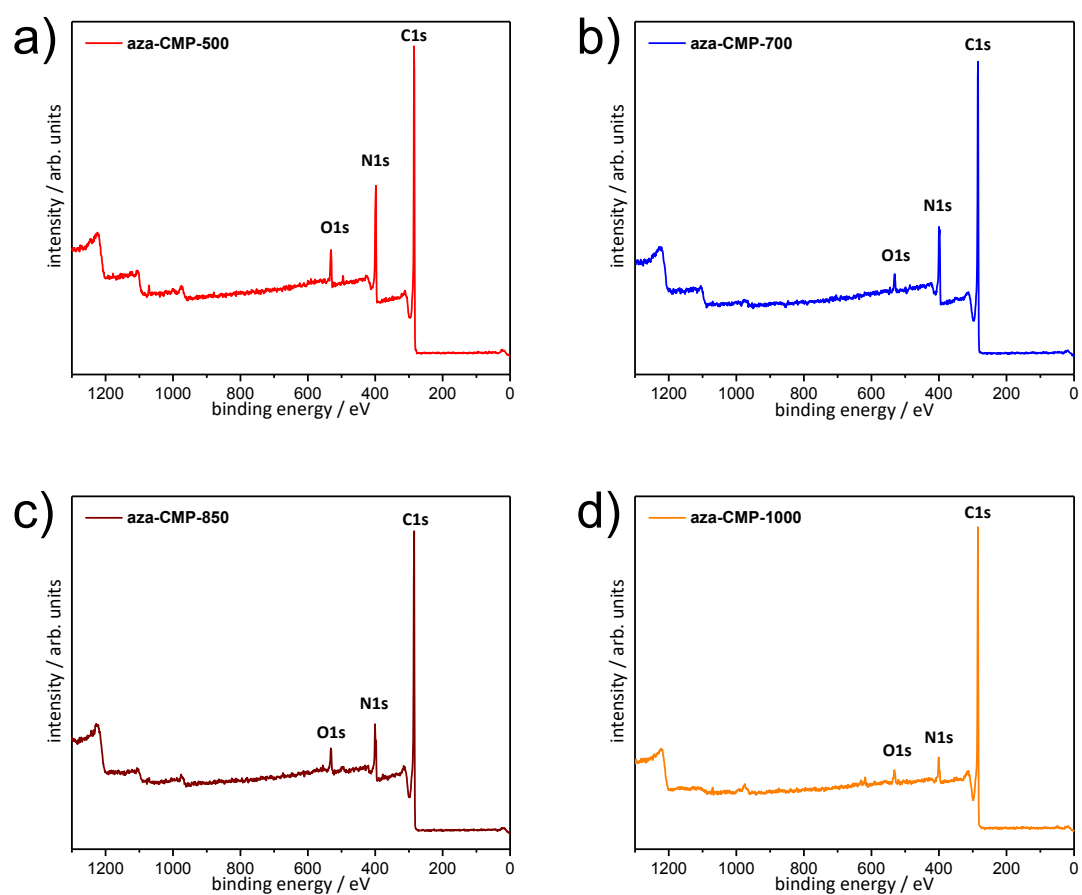


**Figure S 25:** XPS survey spectra of aza-CMP-550 (a), aza-CMP-700 (b), aza-CMP-850 (c), and aza-CMP-1000 (d).

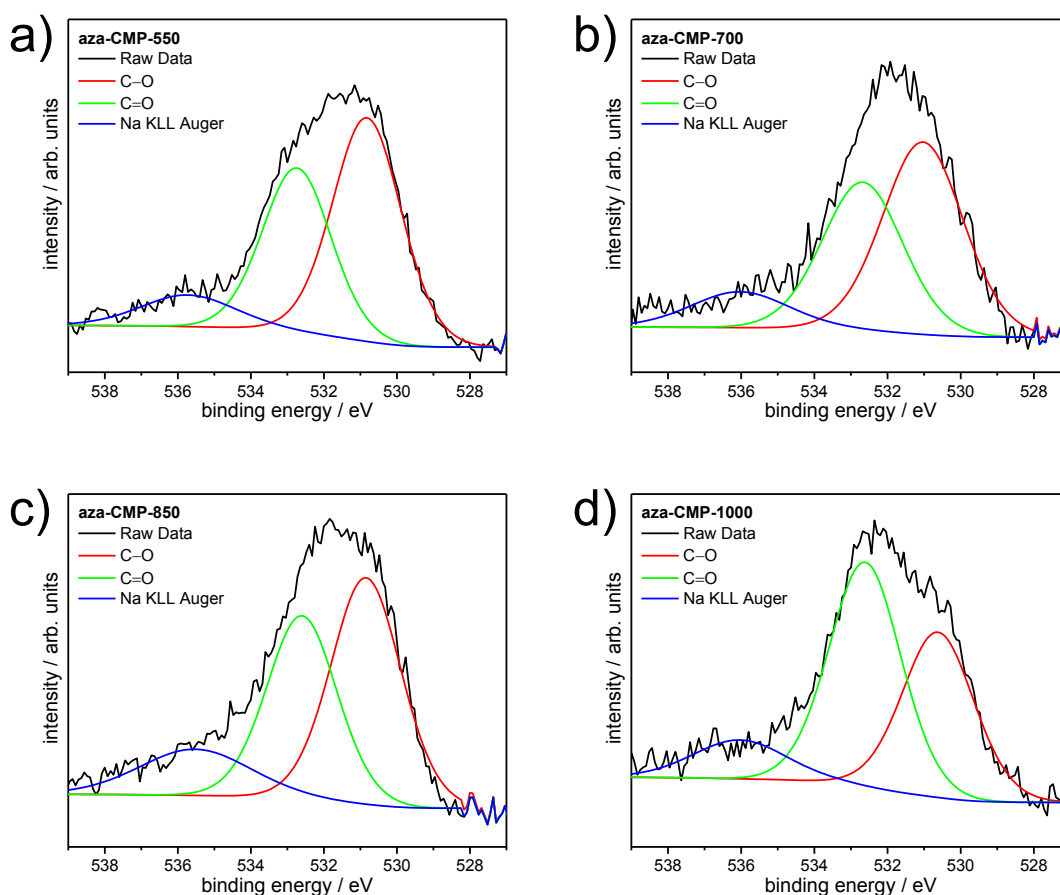


**Figure S 26:** Fitted O1s XPS line scans of aza-CMP-550 (a), aza-CMP-700 (b), aza-CMP-850 (c), and aza-CMP-1000 (d).

**Table S 7:** Peak assignment (binding energies in eV) of the deconvoluted C1s, N1s, O1s, and Na1s XPS spectra of aza-CMP-550, aza-CMP-700, aza-CMP-850, and aza-CMP-1000.

Peak	aza-CMP-550	aza-CMP-700	aza-CMP-850	aza-CMP-1000	binding energies / eV				
graphitic CC	284.6	284.6	284.6	284.6					
sp <sup>2</sup> -N	286.8	285.6	285.6	285.6					
sp <sup>2</sup> -N	-	286.5	286.5	286.5					
C-O	289.2	288.6	288.5	288.4					
C-O or C=O	291.6	291.1	290.4	290.6					
O=C-C	-	294.0	292.7	292.8					
pyrazinic N	398.0	398.2	398.1	398.1					
pyrrolic N	399.8	400.5	400.7	401.0					
higher oxides N-O or graphitic N (quaternary N)	402.9	403.1	403.2	403.9					
C-O	530.8	531.0	530.9	530.6					
C=O	532.7	532.7	532.6	532.6					
Na KLL Auger	535.7	536.0	535.5	536.0					
Na1s	1071.2	-	-	-					

**Table S 8:** Peak assignment (contribution in at.%) of the deconvoluted C1s, N1s, O1s, and Na1s XPS spectra of aza-CMP-550, aza-CMP-700, aza-CMP-850, and aza-CMP-1000.

Peak	aza-CMP-550	aza-CMP-700	aza-CMP-850	aza-CMP-1000
	contribution / at.%			
graphitic CC	59.17	39.99	39.77	47.26
sp <sup>2</sup> -N	9.59	16.47	14.36	14.14
sp <sup>2</sup> -N	4.86	11.54	14.59	12.13
C–O	2.24	7.12	6.22	7.02
C–O or C=O	-	5.04	4.69	5.89
O=C–C	-	1.08	4.27	3.79
pyrazinic N	9.15	6.99	4.34	1.54
pyrrolic N	8.61	7.49	5.45	3.39
higher oxides N–O or graphitic N (quaternary N)	1.67	1.56	1.35	0.62
C–O	2.34	1.36	1.71	1.03
C=O	1.72	1.05	1.39	1.39
Na KLL Auger	0.45	0.31	0.55	0.31
Na1s	0.19	-	-	-

**Table S 9:** Peak assignment (relative contribution in at.%) of the deconvoluted C1s, N1s, O1s, and Na1s XPS spectra of aza-CMP-550, aza-CMP-700, aza-CMP-850, and aza-CMP-1000.

Peak	aza-CMP-550	aza-CMP-700	aza-CMP-850	aza-CMP-1000
	relative contribution / at.%			
C1s	75.9	81.2	85.1	91.6
N1s	19.4	16.0	11.1	5.6
O1s	4.5	2.7	3.7	2.7
Na1s	0.2	-	-	-

### 6.4.1 List of Figures

Figure 1: <i>Development of the global CO<sub>2</sub> emission due to fossil fuel combustion and consequences on the CO<sub>2</sub> concentration in the atmosphere (adapted from reference<sup>[4]</sup>).</i> .....	1
Figure 2: <i>Structures of different carbon allotropes: Cubic diamond (a), graphite (b), carbon nanotube (c), and fullerene (d),<sup>[13]</sup> as well as model atomic construction of nanoporous carbon materials with different degree of carbon ordering (e).((a–d) adapted from reference<sup>[13]</sup>, (e) adapted from reference<sup>[27]</sup>).</i> .....	6
Figure 3: <i>Hard- and soft-templating methods for the synthesis of ordered mesoporous carbon materials.</i> .....	8
Figure 4: <i>Different types of nitrogen-containing functional groups on porous carbon surfaces.</i> .....	10
Figure 5: <i>Concept of carbonization pathways to a non-noble and noble carbons (adapted from reference<sup>[92]</sup>).</i> .....	14
Figure 6: <i>Different CO<sub>2</sub> sorption isotherms with similar uptake at 1 bar illustrate different working capacities for CO<sub>2</sub> adsorption at a relative pressure of 0.1 (adapted from reference<sup>[132]</sup>).</i> .....	22
Figure 7: <i>H<sub>2</sub>O vapor physisorption isotherms of N-doped and non-doped ACs (a),<sup>[75]</sup> nitrogen-dependent change in isosteric heat of CO<sub>2</sub> adsorption of N-doped polypyrrole-based porous carbons at a surface coverage of ~0.6 mmol g<sup>-1</sup> (b).<sup>[136]</sup> ((a) adapted from reference<sup>[75]</sup>, (b) adapted from reference<sup>[136]</sup>).</i> .....	24
Figure 8: <i>The CO<sub>2</sub> capture system at the active sites of Rubisco between the Mg<sup>2+</sup> and the lysine NH<sub>2</sub> group (adapted from reference<sup>[138]</sup>).</i> .....	25
Figure 9: <i>Charge-discharge curves of glucose-derived hard carbon in SIBs (a), and “house of cards” model for sodium storage in hard carbon (b). The “house of cards” model is built up by a big amount of randomly stacked microcrystal carbon layers, several carbon layers are parallel ordered in order to form graphite microcrystals, and others are spread in a disordered fashion to form nanosized micropore areas.<sup>[155]</sup> ((a) and (b) adapted from reference<sup>[155]</sup>).</i> .....	27
Figure 10: <i>Nitrogen-doped carbon materials synthesized in this thesis and their pursued applications in gas adsorption and sodium-ion battery.</i> .....	30
Figure 11: <i>Molecular structure (a), thermogravimetric analysis (TGA) under air (black) and nitrogen (blue) atmosphere (b), scanning electron microscopy (SEM) images (c), and powder X-ray diffraction (PXRD) pattern (d) of the HAT-CN precursor used for condensation.</i> .....	35

Figure 12: Idealized model for the proposed formation of a $C_2N$ structure by condensation of HAT-CN precursor. <sup>[166, 180]</sup> .....	36
Figure 13: SEM images of C-HAT-CN-550 (a), C-HAT-CN-700 (b) and (e), C-HAT-CN-850 (c) and (f), and C-HAT-CN-1000 (d). .....	37
Figure 14: SEM images with elemental mapping (a–d) of N (green), and C (red), as well as HRTEM images (e–h) of C-HAT-CN-550 (a and e), C-HAT-CN-700 (b and f), C-HAT-CN-850 (c and g), and C-HAT-CN-1000 (d and h). .....	38
Figure 15: Fitted N1s XPS line scans of C-HAT-CN-550 (a), C-HAT-CN-700 (b), C-HAT-CN-850 (c), and C-HAT-CN-1000 (d). .....	39
Figure 16: Raman spectra of C-HAT-CN-550, C-HAT-CN-700, C-HAT-CN-850, and C-HAT-CN-1000 (a), TGA measurements of C-HAT-CN-550, C-HAT-CN-700, C-HAT-CN-850, and C-HAT-CN-1000, measured under synthetic air with a heating rate of $5\text{ K min}^{-1}$ (b), and TGA-MS measurements of C-HAT-CN-550 (c) and C-HAT-CN-1000 (d) under synthetic air with heating rates of $2.5\text{ K min}^{-1}$ . .....	41
Figure 17: Ar physisorption isotherms (87 K) (a), corresponding cumulative (b) and differential (c) pore size distribution plots calculated with QSDFT (Ar on carbons with cylindrical/sphere pores at 87 K, adsorption branch kernel), and H <sub>2</sub> O vapor physisorption isotherms at 298 K (d) of C-HAT-CN-550, C-HAT-CN-700, C-HAT-CN-850, and C-HAT-CN-1000. ....	43
Figure 18: CO <sub>2</sub> physisorption isotherms at 273 K (a), thermal response measurements of CO <sub>2</sub> adsorption/desorption (1 bar, 298 K) with inset: Mass-related thermal response peak ( $A\text{ m}^{-1}$ ) of the adsorption peak normalized by the $V_{\text{total}}$ (b), CO <sub>2</sub> physisorption isotherms at 298 K (c), and (d) N <sub>2</sub> physisorption isotherms at 298 K of C-HAT-CN-550, C-HAT-CN-700, C-HAT-CN-850, and C-HAT-CN-1000. ....	45
Figure 19: PXRD patterns (a) and FTIR spectra (b) of HAT-CN, C-HAT-CN-500, C-HAT-CN-525, C-HAT-CN-550, and C-HAT-CN-700. ....	50
Figure 20: <sup>13</sup> C CP-MAS ssNMR spectra of HAT-CN, C-HAT-CN-500, C-HAT-CN-525, C-HAT-CN-550, and C-HAT-CN-700, and the molecule structure of HAT-CN. Green circle is denoting aromatic carbon in the inner benzene ring, orange circle is the pyrazinic carbon, and blue circle is the nitrile carbon. Asterisks (*) denote spinning sidebands. ....	51
Figure 21: Ar physisorption isotherms (87 K) (a) and N <sub>2</sub> physisorption isotherms (77 K) (b) of C-HAT-CN-500, C-HAT-CN-525, C-HAT-CN-550, and C-HAT-CN-700. ....	52

- Figure 22: HRTEM images of C-HAT-CN-700 (a) and (b), C-HAT-CN-550 (c) and (d), C-HAT-CN-525 (e) and (f), and C-HAT-CN-500 (g), and ADF-STEM image of C-HAT-CN-500 (h). ..... 53
- Figure 23: Backscattered electron image of the C-HAT-CN-525 sample (a), ADF-STEM images of the C-HAT-CN-525 sample (b–h), (b) shows the same areas as in (a), dotted lines in (b) and (c) indicate areas enlarged in (c) and (d), respectively. Images (f) and (g) shows inner morphology of the particles, (h) shows morphology of the outer layer of the particles. 54
- Figure 24: CO<sub>2</sub> (a) and (b), as well as N<sub>2</sub> (c) and (d) physisorption isotherms of C-HAT-CN-500, C-HAT-CN-525, C-HAT-CN-550, and C-HAT-CN-700 measured at 273 K (a) and (c) and at 298 K (b) and (d). ..... 55
- Figure 25: Comparison of SSABET (a) and CO<sub>2</sub> capacities at 0.1–0.15 bar (at 298 K) (b) to IAST CO<sub>2</sub>/N<sub>2</sub> selectivities (at 298 K) of the as-synthesized HAT-CN-derived carbon materials (C-HAT-CN-525, C-HAT-CN-550, and C-HAT-CN-700) to nitrogen-containing porous carbon materials, aza-COPs, and CTFs from literature. Inset: SIFSIX materials, MOFs, ZIFs, and zeolite compounds from literature.<sup>[11]</sup> ..... 56
- Figure 26: CO<sub>2</sub> thermal response adsorption and desorption measurements at 1 bar and 298 K (a), integrated adsorption temperature peak area normalized by mass ( $A\ m^{-1}$ ) and  $V_{total}$  (b) of C-HAT-CN-500, C-HAT-CN-525, C-HAT-CN-550, and C-HAT-CN-700, as well as their adsorption (c) and desorption (d) thermal response curves at higher magnifications together with a microporous nitrogen-free carbon material (TiC-CDC) for comparison. .... 57
- Figure 27: Lowest energy structure of the C<sub>2</sub>N network with maximum amount of CO<sub>2</sub> molecules adsorbed (a) and (b). For comparison, the considered control system with C<sub>3</sub>H stoichiometry is also shown (c) and (d). Left: top views; right: side views. .... 59
- Figure 28: H<sub>2</sub>O vapor physisorption isotherms at 298 K of C-HAT-CN-550, C-HAT-CN-700, C-HAT-CN-1000, TiC-CDC, and CMK-3 (a), H<sub>2</sub>O vapor physisorption isotherms at different temperatures (293 K, 298 K, and 303 K) of C-HAT-CN-700 (b), and C-HAT-CN-1000 (c), as well as  $Q_{st}$  of H<sub>2</sub>O vapor adsorption (d). The orange dotted line indicates the heat of evaporation of H<sub>2</sub>O with  $44\ \text{kJ mol}^{-1}$ .<sup>[229, 230]</sup> ..... 65
- Figure 29: <sup>1</sup>H MAS ssNMR spectra of air exposed (a), and H<sub>2</sub>O impregnated (b) samples of C-HAT-CN-500, C-HAT-CN-700, C-HAT-CN-1000, and CMK-3. .... 66
- Figure 30: NH<sub>3</sub>-TPD curve of C-HAT-CN-550. Inset: NH<sub>3</sub>-TPD curves of C-HAT-CN-700, C-HAT-CN-1000, and TiC-CDC. .... 69
- Figure 31: Thermal response measurements of NH<sub>3</sub> adsorption/desorption (1 bar, 298 K) over two cycles of C-HAT-CN-550, and C-HAT-CN-1000 (a), C-HAT-CN-700 (b), over three

cycles of TiC-CDC (c), and mass-related thermal response peak areas ( $A m^{-1}$ ) of the adsorption peak normalized by $V_{micro}$ (d).....	70
Figure 32: PXRD patterns (a) and (b), TGA measured under synthetic air with a heating rate of $5 K min^{-1}$ (c), and Raman spectra (d) of aza-CMP, aza-CMP-550, aza-CMP-700, aza-CMP-850, and aza-CMP-1000.....	76
Figure 33: HRTEM images of aza-CMP (a), aza-CMP-550 (b), and aza-CMP-1000 (c).....	77
Figure 34: Fitted N1s XPS line scans of aza-CMP-550 (a), aza-CMP-700 (b), aza-CMP-850 (c), and aza-CMP-1000 (d).....	78
Figure 35: Fitted C1s XPS line scans of aza-CMP-550 (a), aza-CMP-700 (b), aza-CMP-850 (c), and aza-CMP-1000 (d).....	79
Figure 36: $N_2$ physisorption isotherms (77 K) (a) and $CO_2$ physisorption isotherms (273 K) (b) of aza-CMP, aza-CMP-550, aza-CMP-700, aza-CMP-850, and aza-CMP-1000.....	80
Figure 37: Electrochemical performance of the aza-CMP-derived carbon materials. CV curves at a scanning rate of $0.1 mV s^{-1}$ of aza-CMP-550, aza-CMP-700, aza-CMP-850, and aza-CMP-1000.....	82
Figure 38: Galvanostatic discharge/charge profiles at current rate of $0.1 A g^{-1}$ to $10 A g^{-1}$ of aza-CMP-550 (a), aza-CMP-700 (b), aza-CMP-850 (c), and aza-CMP-1000 (d).....	83
Figure 39: Rate capability from $0.1 A g^{-1}$ to $10 A g^{-1}$ (a) of aza-CMP and aza-CMP-derived carbon materials, and EIS (b) of aza-CMP-550, aza-CMP-700, aza-CMP-850, and aza-CMP-1000.....	84
Figure 40: Cycling test of aza-CMP-550 at $0.5 A g^{-1}$ for 1000 cycles.....	85

#### 6.4.2 List of Tables

Table 1: EA, EDX, XPS, and Raman spectroscopy data summary, as well as experimental yield of C-HAT-CN-550, C-HAT-CN-700, C-HAT-CN-8500, and C-HAT-CN-1000.....	37
Table 2: Ar (87 K) and $CO_2$ (273 K) physisorption data summary of C-HAT-CN-550, C-HAT-CN-700, C-HAT-CN-850, and C-HAT-CN-1000.....	42
Table 3: Elemental analysis data of HAT-CN and the condensed materials, as well as the corresponding condensation yields.....	49
Table 4: Ar physisorption (87 K) data summary, selectivity of $CO_2$ over $N_2$ (at 273 K and 298 K), and $Q_{st}$ of $CO_2$ of C-HAT-CN-500, C-HAT-CN-525, C-HAT-CN-550, and C-HAT-CN-700.....	51

Table 5: <i>Ar</i> physisorption (87 K) data summary of C-HAT-CN-550, C-HAT-CN-700, C-HAT-CN-1000, TiC-CDC, and CMK-3. ....	62
Table 6: Elemental analysis and EDX data summary of C-HAT-CN-550, C-HAT-CN-700, C-HAT-CN-1000, TiC-CDC, and CMK-3. ....	63
Table 7: EA, EDX, $I_D/I_G$ ratio, and experimental yield data summary of aza-CMP, aza-CMP-550, aza-CMP-700, aza-CMP-850, and aza-CMP-1000. ....	75
Table 8: $N_2$ physisorption (77 K) data summary of aza-CMP, aza-CMP-550, aza-CMP-700, aza-CMP-850, and aza-CMP-1000. ....	81

### 6.4.3 List of Schemes

Scheme 1: Electrochemical potentials for some known materials (adapted from reference <sup>[92]</sup> ). .....	13
Scheme 2: Synthesis pathway from cyclohexanone and urea as reactants, over a cross-linked intermediate state, towards a nitrogen-containing carbon material consisting of pyridinic and pyrazinic nitrogen in a defective $C_2N$ manner (adapted from reference <sup>[99]</sup> ). ....	16
Scheme 3: Bottom-up wet-chemical formation of $C_2N$ -h2D crystals via HAB and HKH in the presence of acid. The edge groups of the intermediate $C_6H_2N_3O$ could be thermally (at 700 °C) removed in form of small molecules (e.g., $H_2O$ , $O_2$ , and so on) and resulted in the heat-treated $C_2N$ holey structure (adapted from reference <sup>[100]</sup> ). ....	17
Scheme 4: Solvothermal synthesis of aza-CMP and subsequent thermal condensation at 550, 700, 850, or 1000 °C. ....	74

## 6.5 List of Publications

- 1) **R. Walczak**, B. Kurpil, A. Savateev, T. Heil, J. Schmidt, Q. Qin, M. Antonietti, and M. Oschatz: “Template- and Metal-free Synthesis of Nitrogen-rich Nanoporous Noble Carbon Materials by Direct Pyrolysis of a Preorganized Hexaazatriphenylene Precursor”, *Angewandte Chemie, International Edition* **2018**, *57*, 10765–10770.
- 2) **R. Walczak**, B. Kurpil, A. Savateev, T. Heil, J. Schmidt, Q. Qin, M. Antonietti, and M. Oschatz: “Templat- und metallfreie Synthese stickstoffreicher, nanoporöser und “edler” Kohlenstoffmaterialien durch direkte Kondensation eines vororganisierten Hexaazatriphenylen Vorläufers”, *Angewandte Chemie* **2018**, *130*, 10926–10931.
- 3) S. M. G. Lama, J. Schmidt, A. Malik, **R. Walczak**, D. V. Silva, A. Völkel, and M. Oschatz: “Modification of Salt-Templated Carbon Surface Chemistry for Efficient Oxidation of Glucose with Supported Gold Catalysts”, *ChemCatChem* **2018**, *11*, 2458–2465.
- 4) R. Yan, T. Heil, V. Presser, **R. Walczak**, M. Antonietti, and M. Oschatz: “Ordered Mesoporous Carbons with High Micropore Content and Tunable Structure Prepared by Combined Hard and Salt Templating as Electrode Materials in Electric Double-Layer Capacitors”, *Advanced Sustainable Systems* **2018**, *2*, 1700128.
- 5) M. Oschatz, and **R. Walczak**: “Crucial Factors for the Application of Functional Nanoporous Carbon-Based Materials in Energy and Environmental Applications”, *Carbon* **2018**, *4*, 56.
- 6) R. Yan, E. Josef, H. Huang, K. Leus, M. Niederberger, J. P. Hofmann, **R. Walczak**, M. Antonietti, M. Oschatz: “Understanding the charge storage mechanism to achieve high capacity and fast ion storage in sodium-ion capacitor anodes by using electrospun nitrogen-doped carbon fibers”, *Advanced Functional Materials* **2019**, 1902858, *accepted*.
- 7) Q. Qin, Y. Zhao, M. Schmallegger, T. Heil, J. Schmidt, **R. Walczak**, G. Gescheidt, H. Jiao, and M. Oschatz: “New modes of N<sub>2</sub> fixation by partial anion substitution in titanium oxides for enhanced electrochemical ammonia synthesis”, *Angewandte Chemie, International Edition* **2019**, *submitted*.
- 8) J. Hwang, **R. Walczak**, M. Oschatz, N. Tarakina, and B. V. K. J. Schmidt: „Micro-Blooming: Hierarchically Porous Nitrogen-doped Carbon Flowers derived from Metal-Organic Mesocrystals”, *Small* **2019**, *submitted*.

- 9) **R. Walczak**, M. Antonietti, and M. Oschatz: “Controlling the strength of interaction between carbon dioxide and nitrogen-rich carbon materials by molecular design”, *Sustainable Energy & Fuels* **2019**, *accepted*.
- 10) **R. Walczak**, M. Antonietti, and M. Oschatz: “Approaching Zeolite-like H<sub>2</sub>O Vapor and NH<sub>3</sub> Gas Adsorption Properties with Highly Nitrogen-Doped Carbon Materials”, **2019**, *under preparation*.

## 6.6 Declaration

Die vorliegende Dissertation entstand in dem Zeitraum zwischen Dezember 2016 und Mai 2019 am Max-Planck-Institut für Kolloid- und Grenzflächenforschung unter Betreuung von Prof. Dr. Dr. h.c. Markus Antonietti.

Hiermit erkläre ich, dass die vorliegende Arbeit selbstständig angefertigt wurde und keine anderen als die angegebenen Hilfsmittel und Quelle verwendet wurden.

Die Arbeit wurde bisher weder im Inland noch im Ausland in gleicher oder ähnlicher Form einer anderen Prüfungsbehörde vorgelegt. Es habe bisher keine früheren erfolglosen Promotionsverfahren stattgefunden.

The present work was carried out during the period of December, 2016 to May, 2019 at the Max Planck Institute of Colloids and Interfaces under supervision of Prof. Dr. Dr. h.c. Markus Antonietti.

I declare that I have written this work on my own and used no other than the named aids and references.

This thesis was not submitted to another examination board in this or other countries. There were no unsuccessful examination processes.

Ralf Walczak

Potsdam, den 08.05.2019

